

AN IN-SITU STUDY OF ORGANIC SEMICONDUCTOR
THIN FILMS FOR GAS SENSING

by

MELISSA A. STOKES

A dissertation submitted to the

Graduate School-New Brunswick

Rutgers, The State University of New Jersey

and

The Graduate School of Biomedical Sciences

University of Medicine and Dentistry of New Jersey

In partial fulfillment of the requirements

For the degree of

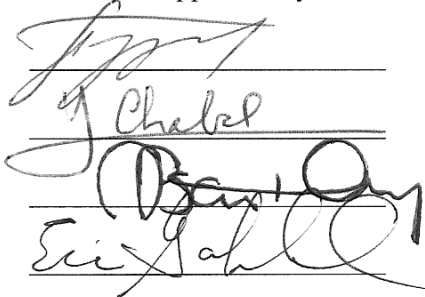
Doctor of Philosophy

Graduate Program in Biomedical Engineering

Written under the direction of

Professor Yves Chabal

And approved by



New Brunswick, New Jersey

October, 2008

ABSTRACT OF THE DISSERTATION

An In-Situ Study of Organic Semiconductor Thin Films for Gas Sensing

By MELISSA A. STOKES

Dissertation Director:
Professor Yves Chabal

Organic semiconductors are an attractive platform for developing chemisensors, because of their customizable surface chemistry. An understanding of the sensing mechanism would help develop surface chemistry design for molecular recognition. We have studied the steric and chemical effects of acetone and ethanol on sublimated and spun organic films, which are used as chemisensor transducers.

We designed deposition and exposure systems to study the surface current and chemistry of rubrene, pentacene, and 5,5'-bis(4-hydroxyhexylphenyl)-2,2'-bithiophene (C6) in response to acetone and ethanol vapors. A rubrene crystal and spun film, as well as sublimated C6 and pentacene films and transistors were exposed under vacuum to saturated vapor pressure acetone gas. The surface current was recorded in real-time, while the infrared absorption (IRAS) signature of the acetone film effect was recorded in-situ.

Some chemical interaction between acetone and the organic substrate was observed, and led to the use of saturated alkyl perfluorinated trichlorosilane (FTS) monolayer coverage of rubrene to prevent acetone degradation and removal of an amorphous spun rubrene film. Acetone removed only 1.5% of the FTS film from

saturated coverage, physisorbed multilayers of FTS on rubrene. Besides this small chemical effect, the main effect on the sensor current is due to the physisorption of acetone itself.

In the cases of pentacene and C6 sublimated films, the surface chemistry and surface current could both be measured on the same film. Acetone intercalation into pentacene and C6 sublimated films perturbed the out-of-plane C-H bending, possibly due to steric interaction. An irreversible reduction in surface current and carrier mobility was found. Acetone caused the thickest pentacene thin film tested (1500 Å) to produce the highest intensity differential peaks, similar to the effect of cooling the film by 3°C - 7°C. However, cooling did not fully account for transistor current reduction. Also, the surface chemistry response decreased upon reuse, and the surface current was not quantitatively reproducible. This behavior may be explained by the fact that the contact adhesive was soluble in acetone. Less surface chemical change occurred for ethanol than for acetone exposures, despite the fact that the C6 molecule has a more reactive hydroxy-hexanol termination.

Dedication

This thesis is dedicated to my family,
whose loving support and belief in me made this work possible.

Acknowledgements

It has been an honor to work with my advisor, Professor Yves Chabal, whose vision for my potential provided me the opportunity to begin my graduate research in his group. Thank you for many research opportunities. Among the members of the Chabal research group, I would like to especially thank Jean-Francois Veyan for inviting and answering my questions with tireless enthusiasm. His training of me in design, machining, and practical solutions helped me to become a more innovative, professional, and confident engineer. I thank Jean-Francois Veyan and Stan Christman for helping me to discover the enjoyment that I will now pursue in a career focused on engineering. I would also like to acknowledge Oliver Seitz for being most available for friendly and candid advice on experiments. I am thankful to Norman Lapin, for helpful discussions and ideas, John Landers for friendly conversation, and Salah Sommakia for working with me through his Master's Degree.

Thank you, Vitaly Podzorov, for teaching me the basics of transistor theory and for inviting me to collaborate in an investigation of rubrene. I would also like to acknowledge the mentoring I received at two internships. Dr. Cherie Kagan and Dr. Ali Afzali provided mentorship at the IBM, TJ Watson Research Center. Dr. Zhenan Bao provided my initial research opportunity in organic transistors at Bell Labs. I am grateful to Refik Kortan for teaching me about powder diffraction and for assisting with my first journal publication. Thank you, Howard Katz and Ali Afzali, for synthesizing organic semiconductor materials.

I would like to thank Nanophysics Lab (NPL) affiliates: Stan Christman, the Bartynski research group, and Leszek Wielunski. Thank you to the Rutgers faculty whose teaching and mentoring I recall fondly: Troy Shinbrot, Kin Cheung, Eric Garfunkel, Nada Boustany, John Semmlow, and Barbara Gaffney. I would like to thank the machine shop members whose discussions lead to design ideas that could not have otherwise been realized. I would like to acknowledge my funding sources at Rutgers University: NSF-IGERT 0333196, and the Rutgers University Bevier Fellowship.

I especially thank my husband, William A. Stokes, whose smiling, helpfulness, encouragement, support, and love contributed greatly to this shared achievement.

Table of Contents

Abstract of the Dissertation	ii
Dedication	iv
Acknowledgements.....	v
Table of Contents	vi
List of Tables	ix
List of Figures	x
List of Structures.....	xiv

1. Introduction 1

1.1 Motivation.....	1
1.2 Background.....	3
1.2.1 Chemisensors	3
1.2.2 Organic Transistors	5
1.2.3 Organic Semiconductor Chemisensors	6
1.2.4 Organic Semiconductor Materials Investigated.....	9
1.3 Thesis Overview	12
1.4 Surface Characterization Techniques	13
1.4.1 Fourier Transform Infrared Spectroscopy	13
1.4.1.1 Introduction.....	14
1.4.1.2 Interferogram	15
1.4.1.3 Single-Beam Spectrum	16
1.4.1.4 Interpreting FTIR Spectra	18
1.4.1.5 Limitations	20
1.4.2 X-ray Diffraction	20
1.4.3 Transistor Characterization	21
1.5 References.....	23

2. Design, Construction, and Operation of Systems Required to Deposit and Study Organic Semiconductor Thin Films 26

2.1 Introduction.....	26
2.2 Bell Jar Sublimating Vacuum System	26
2.2.1 Bell Jar Components	27
2.2.2 Repairs	28
2.2.3 Additions.....	28
2.2.4 Operational Protocol	32
2.2.5 Precautions.....	35
2.2.6 Double-Coating Thin Films	35
2.3 Spin Coating	36
2.4 Gas Cell.....	37
2.4.1 Motivation and Requirements.....	37
2.4.1.1 First-Generation Gas Cell	38
2.4.1.2 Second-Generation Gas Cell.....	44
2.4.1.2.1 Operational Protocol	48
2.4.2 Future Design Improvements.....	50
2.5 Summary	51

3. Characterizing Three Organic Semiconductor Materials	52
3.1 Abstract.....	52
3.2 Introduction	52
3.3 Rubrene.....	53
3.3.1 Rubrene Photo-oxidation Investigation	57
3.3.2 Photooxidation Indicators	60
3.3.3 Photo-oxidation Results.....	61
3.4 Pentacene	67
3.5 C6	69
3.5.1 Studying C6 thin films using FTIR	69
3.5.2 Studying C6 powder and thin films using X-Ray Diffraction	73
3.5.2.1 Experimental details.....	73
3.5.2.2 Results.....	73
3.5.3 AFM	77
3.5.4 I-V Performance.....	78
3.6 Summary	78
3.7 References.....	80
4. An In-situ Investigation of Octyltrichlorosilane Bonding with Rubrene	83
4.1 Abstract.....	83
4.2 Introduction.....	83
4.3 Materials and Methods.....	94
4.3.1 Chemicals	94
4.3.2 Substrates	95
4.3.3 Rubrene Solution Preparation	95
4.3.4 Silane Deposition.....	96
4.3.5 Measurement of Films and Silanes.....	97
4.4 Results and Discussion	98
4.4.1 Gas cell background.....	98
4.4.2 OTS deposition validation	103
4.4.3 OTS-rubrene bonding	105
4.4.4 Surface Coverage Compared With Electrical Enhancement	117
4.5 Conclusions.....	125
4.6 References	127
5. An In-situ Investigation of Perfluorinated Alkyltrichlorosilane Bonding with Rubrene	129
5.1 Abstract.....	129
5.2 Introduction.....	129
5.3 Materials and Methods.....	137
5.3.1 Chemicals	137
5.3.2 Substrates	137
5.3.3 Rubrene Solution Preparation	138
5.3.4 Silane Deposition.....	138
5.3.5 Measurement of Films and Silanes.....	139
5.4 Results and Discussion	140

5.4.1 FTS Bonding to Rubrene	140
5.4.2 FMS Bonding to Rubrene	149
5.4.3 FOH Bonding to Rubrene	152
5.5 Conclusions.....	155
5.6 References.....	157
6. Investigating Organic Semiconductor Ketone and Alcohol Gas Sensing	158
6.1 Abstract.....	158
6.2 Introduction.....	159
6.3 Materials and Methods.....	163
6.3.1 Chemicals	163
6.3.2 Substrates	163
6.3.3 Thin-Film Deposition.....	164
6.3.3.1 Organic Thin-Film Sublimation.....	164
6.3.3.1.1 Pentacene	164
6.3.3.1.2 C6.....	165
6.3.3.2 Sublimated Thin-Film Testing.....	165
6.3.3.3 Spin Coating Rubrene Films.....	166
6.3.4 Rubrene Crystal Preparation	167
6.4 Results and Discussion	167
6.4.1 Investigating Rubrene Sensing Reversibility.....	168
6.4.2 Pentacene	175
6.4.3 Rubrene	193
6.4.4 C6.....	200
6.5 Conclusions.....	205
6.6 References.....	209
7. Conclusion	210
7.1 References.....	217
8. Appendix	218
Curriculum Vita	227

List of Tables

Table 2.1. Channel Width / Length (μm).....	31
Table 3.1. Rubrene High Wavenumber Peak Assignments.....	55
Table 3.2. Rubrene Mid-Wavenumber Peak Assignments.....	55
Table 3.3. Rubrene Low-Wavenumber Peak Assignments	56
Table 3.4. Increasing-Intensity Peak Assignments During Rubrene-Endoperoxide Formation.....	66
Table 3.5. Largest peaks for three pentacene films shift to lower wavenumbers as film thickness decreases	68
Table 3.6. C6 High and Low Wavenumber Peak Assignments	71
Table 3.7. C6 Mid-Wavenumber Peak Assignments.....	71
Table 3.8. C6 Mid-Wavenumber Peak Assignments.....	72
Table 3.9. C6 thin film field-effect mobility.....	78
Table 4.1. Rubrene Surface Current Enhancement Quantification from OTS and OMS	109
Table 4.2. Quantification of the rubrene surface current enhancement from 1.5 hours OTS exposure.....	113
Table 4.3. Details of the OTS Exposure Conditions.....	120
Table 5.1. Rubrene Surface Current Enhancement Quantification From FMS	150
Table 5.2. Rubrene Surface Current Enhancement Quantification from FOH.....	153
Table 6.1. The Effect of Various Solvents and Vacuum on Rubrene Surface Current ..	170
Table 6.2. Field-effect mobility for each pentacene film thickness.....	177
Table 6.3. Peak to peak intensity changes as a result of acetone exposures	178
Table 6.4. The change in source-drain current of pentacene transistors at the start and end of saturated vapor pressure acetone exposures	192
Table 6.5. Sub-monolayer FTS-coated rubrene surface current response and reversibility when exposed to acetone	195
Table 6.6. Saturated-monolayer FTS-coated rubrene surface current response reversibility upon acetone exposure	196

List of Figures

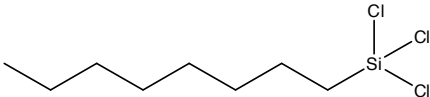
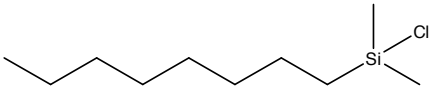
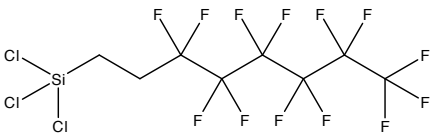
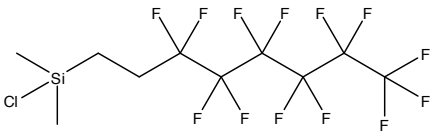
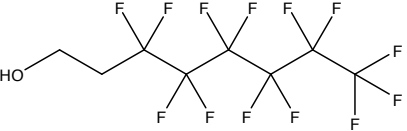
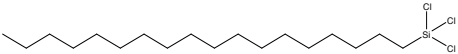
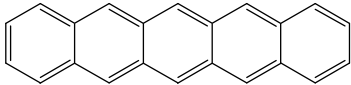
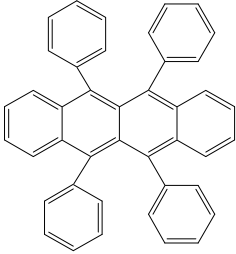
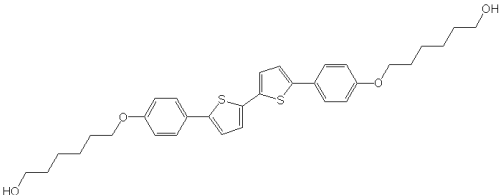
Figure 1.1. Organic Transistor Schematic	5
Figure 1.2. A single-beam spectrum	17
Figure 2.1. Bell jar sublimator	27
Figure 2.2. Bell jar vacuum pumping schematic	28
Figure 2.3. Bell jar scaffolding	29
Figure 2.4. Low-current sublimation power supply	30
Figure 2.5. Molybdenum masks	31
Figure 2.6. Bell jar vacuum system venting schematic	34
Figure 2.7. First gas cell window holder and adapter schematic	39
Figure 2.8. Rotary seal diagram	40
Figure 2.9. Aperture shutters	40
Figure 2.10. First gas cell sample holder	41
Figure 2.11. First gas cell design	42
Figure 2.12. First gas cell integrated	43
Figure 2.13. Second gas cell integrated, 3D design, and sample holder	46
Figure 2.14. Gas cell system schematic	48
Figure 3.1. Rubrene IRAS	54
Figure 3.1A. Rubrene high wavenumber IRAS	54
Figure 3.1B. Rubrene mid-wavenumber IRAS	55
Figure 3.1C. Rubrene low-wavenumber IRAS	56
Figure 3.2. Photo-oxidation progression of a spun rubrene film	62
Figure 3.2A. High-wavenumber region of a photo-oxidation progression	63
Figure 3.2B. Mid-wavenumber region of a photo-oxidation progression	64
Figure 3.2C. Low-wavenumber region of a photo-oxidation progression	65
Figure 3.3. Pentacene IRAS	67
Figure 3.4. C6 IRAS	70
Figure 3.4A. C6 mid-wavenumber IRAS	71
Figure 3.4B. C6 low-wavenumber IRAS	72
Figure 3.5. C6 powder XRD data fit	74
Figure 3.6. C6 powder herringbone arrangement	75
Figure 3.7. C6 powder electrostatic surface potential model	76
Figure 3.8. C6 sublimated film XRD	76
Figure 3.9. C6 sublimated film AFM	78
Figure 4.1. Rubrene oxidation schematic	85
Figure 4.2. Alkyl-trichlorosilane hydrolysis	86
Figure 4.3. Silanol bonding with the substrate SiO ₂ and networking	87
Figure 4.4. Silane self-polymerization (Si-O-Si)	90
Figure 4.5. Silane bonding with the rubrene endoperoxide group (Si-O-C)	91
Figure 4.6. Outgassing under vacuum on thick oxide	99
Figure 4.7. Spun rubrene film stability under vacuum	101
Figure 4.8. KBr pellet stability under vacuum, OTS deposition	102

Figure 4.9. Sub-vapor pressure OTS on thick and thin oxide.....	104
Figure 4.10. Spun rubrene thin film on thick oxide.....	106
Figure 4.11. Validation of rubrene single-crystal contacts	107
Figure 4.12. The rubrene crystal surface current is increased by sub-saturated vapor pressure water plus OTS exposure.....	108
Figure 4.13. The rubrene crystal surface current is increased by sub-saturated vapor pressure water plus OMS exposure.....	109
Figure 4.14. OTS and OMS on spun film of rubrene on SiO ₂ with OTS on SiO ₂	110
Figure 4.15. The rubrene crystal surface current from 1.5 hour OTS exposure	113
Figure 4.16. Different OTS exposure times referenced to spun rubrene films single and double-coated	114
Figure 4.17. Bulk OTS on SiO ₂	116
Figure 4.18. Differential scans of water followed by gradual OTS exposure to rubrene	118
Figure 4.19. Comparison of the peak areas at: 1263 cm ⁻¹ , 1097 cm ⁻¹ , and 1036 cm ⁻¹ after successive OTS exposure to rubrene	119
Figure 4.20. Rubrene crystal surface current response to water, followed by diluted OTS exposures	120
Figure 4.21. The sustained surface current change after OTS exposure	121
Figure 4.22. KBr pellet stability under vacuum, OTS deposition	123
Figure 4.23. OTS on rubrene coated KBr pellet	124
 Figure 5.1. Rubrene oxidation schematic	131
Figure 5.2. Perfluorinated alkyl-trichlorosilane hydrolysis schematic	132
Figure 5.3. Perfluorinated silanol bonding with SiO ₂ and networking schematic.....	133
Figure 5.4. Perfluorinated silane self-polymerization schematic.....	134
Figure 5.5. Perfluorinated Silane bonding with the rubrene endoperoxide schematic ...	135
Figure 5.6. Rubrene, single-crystal surface current increase with FTS exposure.....	140
Figure 5.7. FTS deposition referenced to the spun rubrene film on thin SiO ₂	141
Figure 5.8. Four FTS co-depositions on different films	143
Figure 5.9. Excess FTS deposition on a rubrene-SiO ₂ surface	146
Figure 5.10. FTS depositions on thin chemical SiO ₂ and thick chemical SiO ₂	148
Figure 5.11. Rubrene-crystal-surface current increased as a result of saturated vapor pressure FMS exposure.....	150
Figure 5.12. FMS exposed to a rubrene spun film on thick SiO ₂	151
Figure 5.13. Real-time rubrene crystal surface current enhancement during FOH exposure	153
Figure 5.14. FOH exposed to a rubrene spun film on thick SiO ₂	154
 Figure 6.1. An organic field effect transistor device above the infrared beam-probed region	165
Figure 6.2. Keithley 4200-SCS programs for a: Ids-Vds transistor test and b: Vg-Ids device test.....	166
Figure 6.3. Keithley 4200-SCS program for monitoring changes in drain-source current over time	166

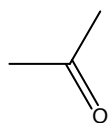
Figure 6.4. Keithley 4200-SCS programs for evaluating: a) rubrene single-crystal contacts and b) surface current over time	167
Figure 6.5. Rubrene crystal surface current perturbation resulting from a series of sub-saturated vapor pressure exposures of acetone, ethanol, pentane	169
Figure 6.6. Spun rubrene film absorption spectrum	170
Figure 6.7. Infrared absorption spectra of rubrene without SAM after a series of sub-saturated vapor pressure exposures to acetone, ethanol, and pentane ...	171
Figure 6.8. Rubrene crystal surface current in response to a series of sub-saturated ethanol and pentane vapor pressure exposures	173
Figure 6.9. Infrared absorption spectra of rubrene without SAM after a series of rubrene sub saturated vapor pressure exposure to ethanol, and pentane	174
Figure 6.10. The infrared absorption spectra of three double-coated pentacene film thicknesses on SiO ₂	176
Figure 6.11. Saturated vapor pressure acetone exposures to different pentacene film thicknesses	178
Figure 6.12. Differential stability of 400 Å and 1500 Å pentacene films exposed to acetone after 50 minutes of N ₂ purge.....	182
Figure 6.13. Differential infrared absorption spectra of 1500 Å pentacene film exposed to saturated-vapor pressure acetone to test reusability	183
Figure 6.14. Drain source current during acetone exposures to 1500Å pentacene.....	184
Figure 6.15. Surface cooling compared with acetone's effect on 1500 Å pentacene film.....	186
Figure 6.16. 1500 Å pentacene organic, thin-film transistor current during N ₂ surface cooling plotted with surface temperature	187
Figure 6.17. Differential infrared absorption spectra of a 400Å pentacene film exposed twice to acetone	188
Figure 6.18. Drain source current response of a 400 Å pentacene transistor to saturated-vapor pressure acetone exposure.....	190
Figure 6.19. Drain source current of 80 Å pentacene transistor response to saturated-vapor pressure acetone exposure	191
Figure 6.20. Surface current for rubrene coated with sub-monolayer FTS in response to a series of saturated acetone vapor exposures	194
Figure 6.21. Surface current of saturated-monolayer, FTS-coated rubrene in response to a series of saturated acetone vapor exposures	196
Figure 6.22. Rubrene coated with sub-monolayer FTS surface chemistry in response to a series of saturated acetone vapor exposures on FTS/Rubrene/SiO ₂ ...	197
Figure 6.23. Acetone removal of saturated, FTS-covered from rubrene on SiO ₂	199
Figure 6.24. The infrared absorption spectra of a 500Å C6 film.....	200
Figure 6.25. Sub-vapor pressure exposure of ethanol to a 500Å C6 film referenced to the C6 film on thick SiO ₂	201
Figure 6.26. Differential infrared absorption spectra of a 500Å C6 film exposed to acetone	203
Figure 6.27. Drain-source current response of 500Å C6 to saturated-vapor pressure acetone exposure using -50V	205

Figure A1. Reproducible infrared absorption spectroscopy of rubrene-spun films referenced to a thick oxide.....	218
Figure A2. Reproducible infrared absorption spectroscopy of OMS referenced to rubrene on thick oxide substrates.....	219
Figure A3. Reproducible infrared absorption spectroscopy of water, OTS deposition referenced to double-coated rubrene on thick SiO ₂ substrates.....	220
Figure A4. Reproducible infrared absorption spectroscopy of OTS referenced to thick and thin SiO ₂ substrates	221
Figure A5. 1500Å Pentacene film transistor performance	222
Figure A6. 1500 Å Pentacene film transistor performance after an acetone exposure...	223
Figure A7. 400 Å Pentacene film transistor performance	224
Figure A8. 80 Å pentacene film transistor performance.....	225
Figure A9. Transistor performance of 500A C6 thin film	226

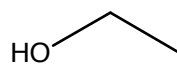
List of Structures

Name	Structure	Abbreviation
n-Octyltrichlorosilane		OTS
n-Octyldimethylchlorosilane		OMS
(tridecafluoro-1,1,2,2-tetrahydrooctyl)trichlorosilane		FTS
(tridecafluoro-1,1,2,2-Tetrahydrooctyl)dimethylchlorosilane		FMS
1H,1H,2H,2H-Perfluoro-1-octanol		FOH
Octadecyltrichlorosilane		OC ₁₈ TS
Pentacene		
Rubrene		
5,5'-bis(4-hydroxyhexyl-phenyl)-2,2'-bithiophene		C6

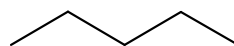
Acetone



Ethanol



Pentane



CHAPTER 1: INTRODUCTION

1.1 Motivation

Organic transistors are an attractive platform for developing sensors, because of their customizable surface chemistry as well as the economic advantages associated with large-scale and low-temperature organic deposition. Organic, transistor-based sensors have been developed for detecting many analytes (Bouvet 2006; Crone, et al. 2001; Huang, et al. 2007; Huang, et al. 2008; Torsi, et al. 2003; Torsi, et al. 2004). Additional sensors for non-invasive diagnosis of blood alcohol level or ketoacidosis would provide affordable consumer products but require a better understanding of ethanol and acetone sensing. However, such chemisensors cannot be easily developed at this time, since current organic transistor sensor research and development is often approached with trial and error (Crone, Dodabalapur, Gelperin, Torsi, Katz, Lovinger and Bao 2001).

The presence of acetone in the breath occurs during ketoacidosis, which is pronounced in patients with diabetes and epilepsy (Musa-Veloso, et al. 2002). Ketoacidosis monitoring via breath analysis is as good an indicator as blood plasma and urine (Musa-Veloso, Likhodii and Cunnane 2002). Non-invasive breath analysis for monitoring acetone provides reduced discomfort, allows increased monitoring, as well as more stable sample and analysis than when using blood or urine analysis (Musa-Veloso, Likhodii and Cunnane 2002). The acetone content of alveolar breath has been measured by using calibrated gas chromatography and a flame ionization detector (Musa-Veloso, Likhodii and Cunnane 2002). However, the cost of analysis equipment in this and other techniques for monitoring acetone including Raman spectroscopy, infrared, near-infrared,

photoacoustic, light scattering, polarization changes, optical emission and cavity ringdown spectroscopies are prohibitive for consumers (Duan and Cao 2008).

The presence of breath ethanol can indicate blood alcohol content and is widely detected with breathalyzer technologies (such as the Intoxilyzer, CMI Inc.). The Intoxilyzer breathalyzer works like a miniature bandpassed infrared spectrometer gas cell. A detector senses the absorption of infrared light generated by a quartz lamp by breath ethanol vapors. All but the portion of the infrared absorption spectrum attributed to ethanol is filtered out. A photocell detects the infrared absorption of ethanol, which is processed by a microchip for display. Breathalyzer technologies detect photocell current from the bandpassed infrared signal of the product of a chemical reaction between exhaled ethanol and sulfuric acid (Menssana Research, Inc. Newark, NJ). These technologies, which rely on infrared absorption detectors are expensive and require non-linear calibration. The linear response of ethanol reaction with fuel cell electrodes is a recent alternative whose drawback is the long time between positive sensing (Intoximeters, Inc.).

A more directed selection (molecular recognition of the transducer functional group by the desired analyte) of the optimal organic semiconductor would be possible if there were a system for characterizing and then understanding the surface chemistry of demonstrated chemical sensors. Addressing the relationship of surface chemistry to the electrical response of a surface has been pursued for decades with various systems. The value of addressing this in the context of organic transistor-based sensors with our system is our insight into the effect physisorbed analytes have on film stability and electrical response. We demonstrate such a system and postulate the surface chemistry response of

rubrene, pentacene, and C6 to acetone and ethanol. This system provides a useful tool for further exploration of the role of organic semiconductor functional groups on chemisensing selectivity. Such an understanding should help improve chemisensor designs. By directing future research toward understanding the selectivity of organic transistor gas sensing, organic chemisensors have the potential to become a platform for future economical, non-invasive, breath-diagnostic products and other chemical sensors.

1.2 Background

A description of why we want to study organic semiconductor transistor sensors is followed by organic transistor construction, and operation. The basis of current organic transistor sensing mechanism ideas is presented below. This motivates our materials selection that follows.

1.2.1 Chemisensors

There are several other chemisensor technologies besides the organic field effect transistors (OFETs) pursued in this thesis. They are discussed below. Briefly, OFETs, amplify the sensing response in real time using the gate voltage which provides larger signal and dynamic range than chemiresistors (Mabeck and Malliaras 2006; Torsi, et al. 2001). Furthermore, custom surface chemistry through organic semiconductor synthesis or reaction with organic semiconductor terminal groups results in a better defined surface bonding chemistry than functionalized inorganic substrates (Huang, Miragliotta, Becknell and Katz 2007).

Chemisensors based on changes in the resistance of carbon black composites with nonpolymeric organic molecules have been demonstrated to sense ethanol vapors using analysis of an array of chemiresistors (Gao, et al. 2006). Similarly, graphene and carbon nanotube resistance changes have been used to detect adsorbed gas molecules; however, the addition of specific gas receptors by coating or chemical reaction is more difficult than with OFETs (Baratona and Merharib 2004; Kong, et al. 2000; Li, et al. 2003; Schedin, et al. 2007; Snow, et al. 2005). Inorganic particles such as TiO_2 and mesoporous SnO_2 , which are used for sensing are undermined by difficulty in coating uniformity and control of pore size (Baratona and Merharib 2004; Li and Kawi 1998). Also, compared to chemiresistors and CHEMFETs (gate-modified FETs), OFETs provide several for analyzing surface changes including field effect mobility and threshold voltage (Torsi, et al. 2000). Reversal of the sensing effect is facilitated in OFETs as opposed to resistors in that applying a reverse bias can enhance OFET reversibility (Bouvet 2006). This may prove advantageous when designing a system to investigate the sensing mechanism of a homogeneous material sensor such as an OFET.

Organic field effect transistors (OFETs), however, can amplify the sensing response in real time using the gate voltage. Customizing the surface chemistry by synthesis of organic semiconductors or by reaction with organic semiconductor terminal groups results in a better defined surface bonding chemistry than functionalized inorganic substrates (Huang, Miragliotta, Becknell and Katz 2007).

In contrast with inorganic devices that use standard lithography techniques, in principle, organic transistors are less expensive because they can be patterned using simple, low-temperature, large-area deposition techniques (Rogers, et al. 2001). Organic

sensors are therefore more suited for large-area sensors. Another advantage of organic transistor chemisensors is that organic semiconductor surface chemistry can be customized to increase sensing selectivity. However, this customization has not been fully utilized due to a lack of understanding of the sensing mechanism.

1.2.2 Organic Transistors

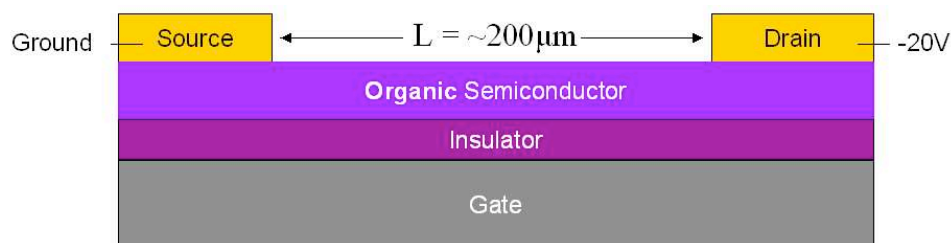


Figure 1.1. Organic Transistor Schematic.

Organic field-effect transistors consist of a doped gate, insulator, semiconductor, and contacts (Figure 1.1). The organic transistors explored in this thesis include only one organic device layer: a p-type organic semiconductor. A doped silicon wafer provides the gate, while the insulator is constructed from thick, thermally grown SiO₂. A negative potential on the gate induces a field across the insulating oxide. Majority hole carriers accumulate at the organic semiconductor-insulator interface. When a potential is applied between the source and drain contacts, a measurable current is produced by charge carriers collected at the drain. Gate-amplified, drain-source current is the signature of a functional field-effect transistor. The figure of merit for organic field effect transistors is the field-effect mobility or source-drain charge carrier drift velocity across a potential per unit area. The calculation of field effect mobility is discussed later in this chapter.

With regard to gas sensing, source-drain current, field-effect mobility, and threshold voltage changes can be used to understand a material's sensing response (Torsi,

Dodabalapur, Cioffi, Sabbatini and Zambonin 2001; Torsi and Dodabalapur 2005).

Demonstrated transistor performance, reasonable field-effect mobility, and at least 10^{-7} - 10^{-6} amps drain-source current are requirements for our study of organic semiconductor and solvent vapor interaction (Torsi, Dodabalapur, Cioffi, Sabbatini and Zambonin 2001).

1.2.3 Organic Semiconductor Chemisensors

Generally, organic field-effect transistors (OFETS) can be made sensitive to 1 ppm gas molecules with a sensor response of 5 - 15% for analyte concentrations of 10 - 100 ppm and a response time of 3 - 5 seconds (Crone, Dodabalapur, Gelperin, Torsi, Katz, Lovinger and Bao 2001; Torsi and Dodabalapur 2005). It is believed that organic film conduction occurs near the buried organic semiconductor-insulator interface (Horowitz 1998). Therefore, the effects of gaseous recognition at the organic semiconductor–environment interface must be translated to the buried conduction channel. Film topology seems to play an important role in chemisensing.

Ethanol sensing decreased alkoxy-substituted conducting polymer drain-source transistor current (Torsi, Tanese, Cioffi, Gallazzi, Sabbatini and Zambonin 2004). The mechanism is thought to involve alcohol interaction with grain boundaries, steric interaction to disrupt the semiconducting molecular arrangement, and electrostatic disruption of charge transfer (Torsi, Tanese, Cioffi, Gallazzi, Sabbatini and Zambonin 2004). Irregular grain nanodomains of oligothiophene transistors with diffuse penetrable grain boundaries (prepared at room temperature) have shown stronger sensing response to 1-pentanol than films with large, regular, flat grains (120°C, 170°C) with lower roughness ($L = 200 \mu\text{m}$) (Torsi, et al. 2002). Transmission electron microscopy (TEM)

images show a decrease in the thickness of grains near the edges of 700 Å-thick films, indicating a penetration of pentanol's effect near the conduction channel (Torsi, Lovinger, Crone, Someya, Dodabalapur, Katz and Gelperin 2002). Although mass uptake is observed with a quartz crystal microbalance (QCM), film swelling has been ruled out by ellipsometry, suggesting the interaction occurs at the surface instead of within the film bulk (Torsi, Lovinger, Crone, Someya, Dodabalapur, Katz and Gelperin 2002).

Dihexylquarter-thiophene films have been shown to be more sensitive to pentanol vapor than single-crystal devices by decreasing the channel length from 45µm to 2.5µm, perhaps isolating the grain boundary effect (Someya, et al. 2002). Crone also observed increased sensing response with smaller grain sizes (Crone, Dodabalapur, Gelperin, Torsi, Katz, Lovinger and Bao 2001). The molecular flexibility gained by increasing alkyl chain length may have increased the grain absorption, surface area, film porosity and increased sensor response (Crone, Dodabalapur, Gelperin, Torsi, Katz, Lovinger and Bao 2001).

Torsi suggests the analyte grain adsorption is dictated by the chemical affinity between the analyte and surface functional groups (Torsi and Dodabalapur 2005). Thickness of the semiconductor material as well as functional group chemistry has been shown to influence sensor performance (Liao, et al. 2005). Solvent gas mass and electronic effect interaction per unit area may determine the magnitude of sensing response (Crone, Dodabalapur, Gelperin, Torsi, Katz, Lovinger and Bao 2001). An alternative mechanism might involve limiting charge injection into the organic semiconductor through gold contact-gas interaction (Torsi, Lovinger, Crone, Someya, Dodabalapur, Katz and Gelperin 2002; Vollmer, et al. 2005). The role of surface

topology or morphology, believed to play a large role in sensing may be less important than organic semiconductor thin-film, terminal functional groups (Huang, Miragliotta, Becknell and Katz 2007). The response of the C6 molecule and a similar molecule without terminal hydroxyl groups showed similar thin-film morphology, yet a larger sensing response to dimethyl methylphosphonate was made by films including the hydroxyl group of the C6 molecule (Huang, Miragliotta, Becknell and Katz 2007).

Reversibility and selectivity may be contradictory goals when designing an analyte-sensing material (Hierlemann, et al. 1999). Strongly selective recognition could be achieved if a chemical bond occurred in a chemisorptive response; however, bond formation will likely be irreversible when compared with a weak physisorption interaction that is less selective but more reversible (Hierlemann, Ricco, Karl Bodenhöfer and Göpel 1999). In this thesis, we study fused aromatic structures and compare their interaction with a molecule that has a polar alkoxyl group believed to have increased interaction with solvents. Since humidity can influence the drain-source current of organic transistors, a vacuum or N₂-purged environment for anhydrous solvents is required (Zhu, et al. 2002).

The mechanism of organic semiconductor sensing is therefore investigated by exploring combinations of different analyte functional groups or organic semiconductor groups and their effects on surface current. The tools for these tests include an exposure system to dose the organic semiconductor, a probe station or ammeter/voltmeter to measure the changes in current, and a synthetic chemist collaboration to try several different functional groups in order to probe the surface chemistry. A gas cell system, such as the one that we have developed, allows us to test all three areas: different

exposure analytes to organic semiconductor films with different terminal groups as a result of an organic chemist collaborator, as well as measuring surface current while probing the surface chemistry with IRAS. Understanding the sensing mechanism as a result of the simultaneous measurements possible in our specialized gas cell can allow future research to focus on the most influential film variables in organic semiconductor design. Chemisensors based on organic transistor materials could then be optimized and evaluated to develop response trends that may direct future sensor design.

Potential influential variables in sensor response include grain boundary, terminal functional group, and film thickness. Distinction of the grain boundary sensing mechanism is difficult due to the large Fourier transform infrared (FTIR) beam sampling area and room temperature deposition system. Analyte oxide response control experiments should provide an indication of insulator response, that is the area between grains whose boundaries reach down to the oxide. Hydrogen bonding of alcohol vapors to the hydroxyl-terminated organic semiconductors could disturb the distribution of charge carriers in the film and will be compared with semiconductors without functionalization. The effect of different film thicknesses will also be explored. The response of three different types of organic semiconductors will be compared. Furthermore, organic transistor aging, stability, degradation with device cycling, the effect of post-annealing, temperature, and real-time response to analytes can be explored.

1.2.4 Organic Semiconductor Materials Investigated

Many conducting organic polymer materials have been used for gas sensing; however, limited sensor lifetime and instability in air, irreversibility, low selectivity, film

swelling, and diffusion-limited response rate present challenges that are also seen in some organic monomers (Bai and Shi 2007; Huang, Miragliotta, Becknell and Katz 2007).

Fortunately, the organic semiconductor monomers can more easily be deposited as thin films. This allows for greater control of the surface topology, which is known to play a role in sensor response (Torsi, Lovinger, Crone, Someya, Dodabalapur, Katz and Gelperin 2002). We therefore study monomer organic semiconductors including pentacene, rubrene, and C6. Pentacene is a well-studied, standard organic semiconductor with reliable transistor performance for room temperature sublimation on SiO₂.

Therefore, a reasonable sensing signal is predicted. However, pentacene lacks reactive functional groups for selective sensitivity, except for possible quinone impurities (Jurchescu, et al. 2004). For comparison, we explored a hydroxy-terminated C6 molecule, which has been demonstrated as an OFET whose terminal hydroxyl group has contributed to its sensitivity to dimethyl methylphosphonate (Huang, Miragliotta, Becknell and Katz 2007; Huang, Sun and Katz 2008). A recent demonstration of large rubrene sensing response to polar analytes coated with a perfluorinated self-assembled monolayer merited interest in our study of rubrene (Calhoun, et al. 2008).

Pentacene is a model organic semiconductor because it is one of the most robust materials to sublime and usually exhibits good field-effect mobility. The deposition of pentacene by sublimation is well understood and can be performed at a low rate with a substrate at room temperature (Zhu, Mason, Dieckmann and Malliaras 2002). The sensing responses of several pentacene film thicknesses will be compared.

Rubrene has been demonstrated as one of the highest mobility organic semiconductor materials (Podzorov, et al. 2003; Sundar, et al. 2004). Recently, self-

assembled monolayer pretreatments have been shown to increase rubrene single-crystal surface current, allowing acetone and solvent vapor sensing (Calhoun, Sanchez, Olaya, Gershenson and Podzorov 2008). However, the surface chemistry of the rubrene pretreatments as well as the surface chemistry of sensing are not fully understood. Therefore, the sensing mechanism of self-assembled monolayer (SAM) vapors, as well as the subsequent sensing of acetone vapors will be explored in this thesis.

A new phenylene-thiophene organic semiconductor, 5,5'-bis(4-hydroxyhexyloxy-phenyl)-2,2'-bithiophene (C6), will be investigated to determine the role of its hydroxyl terminal groups on chemisensing. Hydroxyl groups were initially incorporated into aromatic structures and oligomer length was decreased to four rings in order to increase molecular solubility for solution casting, an economical alternative to vacuum sublimation (Katz, et al. 1998; Wei, et al. 1996). Due to difficulty in identifying the optimal solvent, we sublime this material. This new molecule could demonstrate oxygen-enhanced charge transfer capabilities and reduce the insulating effects of the otherwise mobility-enhancing alkyl side chains (Katz, et al. 1995). Terminal hydroxyl groups could also improve the initial monolayer interaction with the similarly terminated SiO₂ insulator surface and thus improve the molecular ordering at this sensitive charge-carrier channel interface.

The hydroxyl group of C6 contributed to its sensing capability in a mixed film for sensing dimethyl methylphosphonate (DMMP), a nerve agent simulant (Huang, Miragliotta, Becknell and Katz 2007; Huang, Sun and Katz 2008). Similar polymer structures (Poly DPOT) have also been used for transistor-based alcohol sensing that increased drain-source current by ~10% (Torsi, Tafuri, Cioffi, Gallazzi, Sassella,

Sabbatini and Zambonin 2003). Torsi proposed the Poly DPOT sensing mechanism involves the facilitated interaction of long-chain alcohols by the alkyl chains in the polymer. The stronger dipole moment of the alkoxy chain may facilitate detecting shorter, more polar molecules, such as ethanol (Torsi, Tafuri, Cioffi, Gallazzi, Sassella, Sabbatini and Zambonin 2003). Therefore, C6 is likely capable of producing a sensing response, especially with hydroxyl-terminated alkyl chains.

1.3 Thesis Overview

We created an experimental system for in-situ and real-time investigation of organic semiconductor chemisensing in order to study organic transistor sensing mechanisms. Infrared measurements are correlated with current measurements to study the surface chemistry associated with device response to acetone and ethanol. This required developing an organic thin-film deposition system, which we describe in Chapter 2. A gas cell system for exposing thin-films to analyte vapors, which allows for both infrared and current measurements, was designed, machined, and integrated into a spectrometer as described in Chapter 2. The starting surface chemistry of organic semiconductor thin-films is explored in Chapter 3. The surface current of rubrene is an alternative to organic transistor sensor devices, because the surface current can be enhanced with self-assembled monolayers. The surface chemistry mechanism of this enhancement is explored in Chapters 4 and 5. Sensing, using enhanced rubrene surfaces and pentacene and C6 organic transistors, is explored in Chapter 6. A concluding discussion is presented in Chapter 7. X-ray diffraction, atomic force microscopy, current-voltage analysis, and Fourier transform infrared spectroscopy were used to characterize the surface chemistry and material structure of semiconductors as a basis for

understanding the potential for, and the mechanisms of, organic transistor-based acetone and ethanol sensors. The rationale and background for those techniques are discussed below.

1.4 Surface Characterization Techniques

Several techniques were used to characterize the properties of the organic semiconductor thin films including: Fourier Transform Infrared Spectroscopy (FTIR), X-ray diffraction (XRD) and current-voltage (I-V) analysis. Background information for these concepts is presented below.

1.4.1 Fourier Transform Infrared Spectroscopy

Infrared absorption spectroscopy is a technique that provides both chemical and structural information. However, quantitative information is not easily extracted. A technique to indicate mass uptake such as surface acoustic waves or quartz crystal microbalance would help to quantify the real-time changes in the organic semiconductor film upon analyte exposure (Hierlemann, Ricco, Karl Bodenhöfer and Göpel 1999). Although x-ray photoelectron spectroscopy (XPS) is a very sensitive to elemental analysis technique, integration with our in-situ system would be in excess of the satisfactory functional group information obtained using FTIR. Also, differences between fragmented molecules are not easily apparent. Depth profile analysis is also not obtainable with FTIR. The transmission geometry is favored over reflection due to typical distortions of the low wavenumber region near the spectral molecular fingerprint. However, reflection FTIR has been used to evaluate molecular recognition, although use of this geometry in the gas cell would be difficult (Hierlemann, Ricco, Karl Bodenhöfer

and Göpel 1999). Also, coating both sides of the wafer with organic films allows us to increase the interaction signal, which would otherwise be an advantage of multiple internal reflections.

In-situ FTIR experiments allow us to avoid environmental influences on the sample such as light induced photo-oxidation, conduction, or degradation (Podzorov and Gershenson 2005). Also, environmental humidity, sample position, and temperature changes during transport may influence organic films (Torsi, Dodabalapur, Cioffi, Sabbatini and Zambonin 2001; Zhu, Mason, Dieckmann and Malliaras 2002). Therefore, the in-situ analysis of organic semiconductor thin films is merited. Although gas chromatography or mass spectroscopy would be useful to correlate material removal associated with some negative peaks, in this system, the use of 5 mTorr vacuum precludes the use of such vapor analysis techniques. However, a downstream gas analysis chamber using FTIR would allow analysis at this vacuum level.

Through comparison to a reference scan, positive peaks in infrared absorption spectra indicate the presence of new bonds, negative peaks indicate bond removal, and peak shifting can indicate changes in the bond environment. We introduce the basic operation of a spectrometer, then describe raw data processing, basic interpretation of infrared spectra guidelines, as well as acknowledge the limitations of the technique.

1.4.1.1 Introduction

Fourier Transform Infrared Spectroscopy (FTIR) is a non-destructive technique that can be used to identify the molecular and bond composition of a material as well as to observe surface-environment interactions. This technique has been shown to be useful in studying well-understood silicon wafers in many conditions and incident beam

geometries without requiring vacuum conditions. It is attractive for studying organic semiconductors and their interaction with analyte vapors due to the Nicolet Magna-IR Model 860 spectrometer's sample compartment, which can accommodate a suitable, customized gas cell. Also, since the conduction region of the organic semiconductor is at the bottom of the film at the substrate oxide interface, FTIR is an advantageous technique to study the film chemistry because the sample is oriented in the transmission geometry, allowing us to evaluate the entire film.

To record the light absorption signature of a solid, liquid, or gas, an infrared beam transmitted through the interferometer is directed through the sample chamber before reaching the detector. Atoms in a molecule whose native vibration matches the frequency of the incident light absorb discrete energy, while the rest of the spectrum is transmitted unchanged. Absorption increases the amplitude of specific, native molecular vibration. Negative features in the single beam indicate frequencies where beam absorption occurred.

1.4.1.2 Interferogram

A spectrometer's signal, the interferogram, represents the intensities of all of the beam frequencies as a result of passing through the sample compartment. OMNIC computer software (Version 7.1, Thermo Electron Corporation) was used to apply a Fourier transform to the interferogram in order to find the intensity at each frequency. A reference scan of the substrate background is removed from a subsequent spectrum of a film on the substrate by logarithmic division to produce a film absorbance spectrum. A Thermo Electron Corporation spectrometer, Magna 860, was used for most measurements. Its operation is described below.

Black body radiation emitted by a source is sent through an aperture on its way to a beam splitter. At the beam splitter, approximately half of the beam is transmitted to a moving mirror, while the other half is reflected off a stationary mirror. The moving mirror path-length differences are calculated precisely, using a laser interference pattern time reference. The position of the moving mirror determines the difference in the phase of the two beam components when recombined at the beamsplitter where constructive and destructive interference occurs due to phase differences. Then it is transmitted through the sample and finally reaches the detector.

Total intensity of infrared beam reaching the detector is recorded over time by converting from the electrical response measured several times per second. This allows the spectrometer to generate an interferogram containing the entire set of frequencies emitted from the source. An interferogram is a plot of the total detected incident infrared intensity for each moving mirror position. The x-axis is converted to time, given the known laser wavelength, wavenumber range and resolution of the mirror path. To identify the contribution of each frequency in a single-beam spectrum, the time course is fitted to a summation of sine and cosine functions at various intensities for a range of frequencies. This is the basis for the Fourier transform that converts the intensity versus time of every point (since the source emits more than one frequency) in the interferogram to a bell-shaped single beam format of intensity versus frequency spectrum – single beam (Bell 1972). The computer, however, utilizes the fast Fourier transform (FFT). A derivation of the data processing is described by Bell.

1.4.1.3 Single-Beam Spectrum

The single-beam spectrum is a plot of the intensity versus wavenumber. The shape of this basic curve (Figure 1.2) can be explained by three prominent factors: the detector, the infrared source, and the KBr beamsplitter. Objects in the beam path, such as: mirrors, windows (KBr or CaF), the ambient environment, and the sample, have minimal effect on the beam shape.

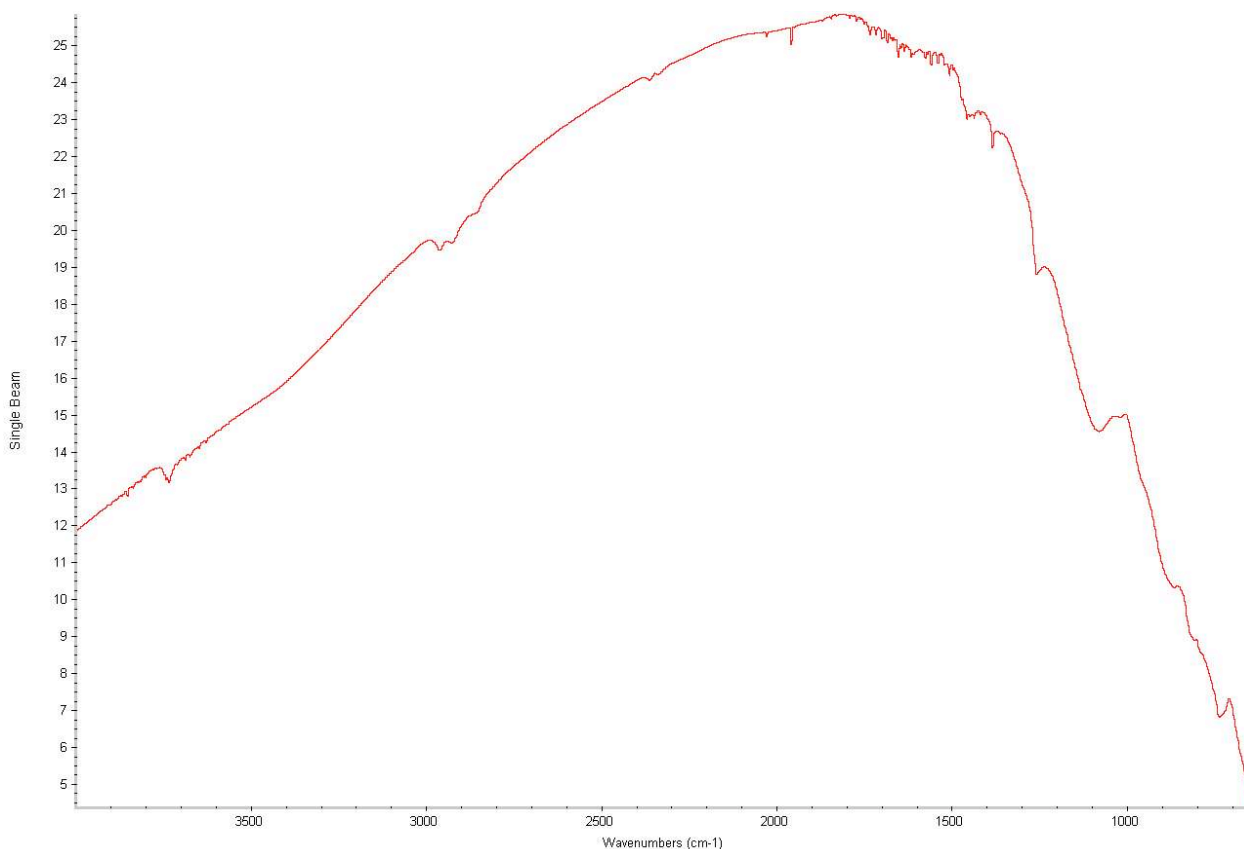


Figure 1.2. The single-beam spectrum of a clean Si (100) sample, using a Magna 750 spectrometer and a MCT/A detector.

The most dominant factor in the single-beam shape is the beamsplitter. The beamsplitter is composed of two highly polished KBr plates sandwiching a thin germanium film. Transmission efficiency is determined by the thickness of the germanium film. Reflectivity of germanium is a function of wavelength. This imposes a high-frequency limitation on the single beam. Resistive heating of the silicon carbide

source produces black body radiation that determines the slope of the single beam low wavenumber region.

Several different types of detectors can be used. MCT and Indium Antimonide detectors utilize photon-induced conduction. A and B types of MCT detectors have different band gaps, according to their alloy composition, which determines the minimum energy for beam sensing. Therefore, the detector imposes the low-frequency limit on the spectra.

1.4.1.4 Interpreting FTIR Spectra

Simply, positive peaks in an infrared absorption spectrum represent bond formation, while negative peaks represent bond removal. Absorption spectrum features can be assigned to stretching (symmetric or asymmetric) vibrations and deformation (in-plane or out-of-plane) motions (bending and twisting). Understanding the following general trends can allow general peak assignment. Less energy is required to bend a bond than to stretch it. Therefore, stretching vibrations should occur at higher wavenumbers than bending or bond deformations, based on a direct relationship between energy and frequency. Stretching vibrations generally occur at twice the frequency or wavenumber as deformation modes (Bloggs 2008). Also, one can expect an asymmetric vibration to require slightly more energy than a symmetric vibration. Generally, if a surface group has less coverage, its peak will shift to lower wavenumber (Coates 2000). If an atom in a molecule is more electron withdrawing, the strength of a functional group bond can increase, increasing rigidity, and the affiliated wavenumber (Bloggs 2008).

Since the beam travels through the atmosphere as well as the sample, the most common single-beam negative features are those attributable to atmospheric gases purged

from the spectrometer while scanning, such as CO₂ and water vapor. Scans with a sample or experimental condition must be compared to a reference in order to determine the desired absorbance spectra. In order to reduce background influences in the resulting spectrum, a single-beam is taken with a control sample, which does not contain the film(s) of interest. This allows removal of substrate and atmospheric spectral peaks from the final absorbance spectrum. The absorbance spectrum is obtained by taking the negative log of the ratio of the single-beam spectrum of the sample to the background.

An absorbance spectrum shows positive peaks for energy absorption between 400 cm⁻¹ or 600 cm⁻¹ and 4000 cm⁻¹, according to the type of detector used: deuterated triglycine sulfate (DTGS) or mercury cadmium telluride (MCT). Infrared light at 1000 cm⁻¹ has a wavelength 0.001 cm (10 μm), which is approximately half the width of a human hair (25 μm) (Thermo Nicolet, OMNIC Tutorial). Wavenumber is used in FTIR because it is proportional to energy (the energy of light increases with decreasing wavelength).

$$Energy = h \cdot \frac{c}{\lambda}$$

$$wavenumber = \frac{1}{\lambda}$$

where h is Planck's constant (6.626068×10^{-34} m² kg / s), c is the speed of light (299,792,458 m / s), and λ is wavelength (m). Wavenumber represents the number of waves within a centimeter (thus the units, cm⁻¹) (Thermo Nicolet, OMNIC Tutorial)¹. Strong vibrations absorb more energy than they transmit and thus produce larger infrared peaks. Also, peak intensity can increase as the number of each bond per molecule as well as the number of molecules increases. Narrow peak line widths, up to 8 - 10cm⁻¹

¹ (wavelength in meters) * 10⁸ = (wavenumber in cm⁻¹). 0.005 cm (50 μm) is 200 cm⁻¹.

(approximately twice the set spectrometer resolution, 4 cm^{-1}), indicate homogeneous bonding (Reutt-Robey, et al. 1988).

Samples are exposed to a transmitted infrared beam at 74° relative to the surface normal, also known as the Brewsters angle for optimized surface sensitivity in the transmission geometry. Spectrum peak assignment is based on similar molecular structure infrared spectra and the general trends for basic spectral features; such as the hydrocarbon and aromatic regions. The National Institute of Standards and Technology (NIST) has an online database of reference molecules (<http://webbook.nist.gov/chemistry/>) that was often used in this thesis to match peaks to molecular modes.

1.4.1.5 Limitations

Generally, one drawback of FTIR is that a fairly large surface area is probed. Microscopic information can only be inferred if long-range ordering is known (Reutt-Robey, et al. 1989). Surface coverage is also difficult to extrapolate from infrared feature intensity. Peak assignment of complex molecules is most valid with theoretical derivations. A separate reference is required for surface analysis. At times, several features of interest can be difficult to separate from each other or atmospheric peaks, such as water or CO_2 . Finally, the intensity of silicon substrate phonon modes can be problematic, if the experimental temperature is different than the reference temperature.

1.4.2 X-Ray Diffraction

X-ray diffraction (XRD) can be used to model atom arrangement by measuring the periodic separation distance of molecular planes. Due to the wavelength of X-rays

(0.1 Å - 100 Å), X-ray diffraction is used to evaluate the periodicity of atomic crystal structures on the same scale, according to Bragg's Law:

$$n\lambda = 2d \sin\theta$$

where n is an integer, λ is the incident wavelength (Å), d is the periodic crystal layer spacing (Å), and θ is the incidence angle with respect to the scattering planes (degrees).

The layer spacing that allows the incident beam with wavelength λ and reflected beams to remain in phase allows the constructively interfering diffracted beams to be detected. Given a sweep of incident beam angles versus detected beam intensity and constant incident beam wavelength, one can calculate the layer spacing, d , using the first prominent peak. By scanning the incident angle, the other scattering planes in the crystal structure give rise to the additional peaks. These additional peaks can be transformed from reciprocal space Bravais lattices to match the expected peaks of known unit cell structures in real space.

A four-circle goniometer was used to control the sample orientation with respect to the beam at the X22A beam line of Brookhaven National Laboratories. The data output is normally 2θ , which when divided by 2 can be used as θ in the above Bragg's law when comparing with beam intensity.

1.4.3 Transistor Characterization

The electrical performance of organic semiconductor field-effect transistors was tested, using a three-point probe station. A shielded probe station is used to connect to the gate and gold contacts. Probes are connected to ports of a HP4155 semiconductor parameter analyzer. It was necessary to grind through the insulating oxide with a diamond knife to form a contact with the doped gate. Swept potentials for the gate and

contacts are performed according to analyzer parameters. The resulting current between the gate, source, drain and source were measured. When the drain is more negative than the gate, the source-drain current will saturate due to a pinch-off in the accumulation layer (Dimitrakopoulos and Mascaro 2001). The relationship between drain-source current and field-effect mobility is given in the saturation regime as:

$$I_{ds} = \frac{W}{2L} \cdot C_i \cdot \mu \cdot (V_{gs} - V_t)^2$$

where L is the channel length, W is the channel width, C_i is the capacitance per unit area of the gate dielectric, V_t is the threshold voltage, V_{gs} is the gate-source voltage, and μ is the field-effect mobility (cm^2/Vs).

C_i can be calculated from the following relationship:

$$\frac{C}{A} = C_i = \frac{k \cdot \epsilon_o}{t}$$

where k is the material dielectric constant, ϵ_o is the permittivity of free space ($8.854 \times 10^{-12} \text{ F/m}$) and t is the material thickness.

For 3000 \AA of thermally deposited SiO_2 , $k=3.78$,

$$C_i = \frac{3.78 \cdot 8.854 \times 10^{-12} \text{ F/m}}{3000 \times 10^{-10} \text{ m}}$$

$$C_i = 1.1156 \times 10^{-4} \text{ F/m}^2 \cdot (.01 \text{ m}/1 \text{ cm})^2 = 1.1156 \times 10^{-8} \text{ F/cm}^2$$

Field-effect mobility, μ , can be related to the slope of the square root of I_{ds} versus V_g by manipulating the above equation:

$$\mu = \frac{1}{C_i} \cdot \frac{2L}{W} \cdot \left(\frac{\sqrt{I_{ds}}}{V_{gs} - V_t} \right)^2$$

Field effect mobility is the ease with which accumulated charge can move under the influence of an electric field (Brown, et al. 1997). Other parameters often used to

characterize organic transistors include the threshold voltage (V_t) and the on/off ratio.

The threshold voltage is the voltage at which half of the maximum drain-source current is achieved (Schroeder, et al. 2003). The on/off ratio is the maximum current at the maximum gate voltage divided by the minimum current at the maximum gate voltage.

This can give a measure of the switching speed of a device. We focus on only the saturation regime mobility of the transistor and the real-time drain-source current response to analyte sensing in this thesis.

1.5 References

1. Bai, H.; Shi, G., Gas Sensors Based on Conducting Polymers. *Sensors* **2007**, 7, 267-307.
2. Baratona, M.-I.; Merharib, L., Surface chemistry of TiO₂ nanoparticles: influence on electrical and gas sensing properties. *Journal of the European Ceramic Society* **2004**, 24, 1399–1404.
3. Bell, R. J., *Introductory Fourier Transform Spectroscopy*. Academic Press: New York, London, 1972.
4. Bloggs, J. R. The Internet Journal of Vibrational Spectroscopy.
5. Bouvet, M., Phthalocyanine-based field-effect transistors as gas sensors. *Analytical Bioanalytical Chemistry* **2006**, 384, 366-373.
6. Brown, A. R.; De Leeuw, D. M.; Matters, M.; Jarrett, C. P., Field-effect transistors made from solution-processed organic semiconductors *Synthetic Metals* **1997**, 88, (1), 37-55.
7. Calhoun, M. F.; Sanchez, J.; Olaya, D.; Gershenson, M. E.; Podzorov, V., Electronic functionalization of the surface of organic semiconductors with self-assembled monolayers. *Nature Materials* **2008**, 7, 84 - 89.
8. Coates, J., *Interpreration of Infrared Spectra, A Practical Approach*. John Wiley & Sons: Chichester, 2000; p 10815-10837.
9. Crone, B.; Dodabalapur, A.; Gelperin, A.; Torsi, L.; Katz, H. E.; Lovinger, A. J.; Bao, Z., Electronic sensing of vapors with organic transistors. *Applied Physics Letters* **2001**, 78, 2229.
10. Dimitrakopoulos, C. D.; Mascaro, D. J., Organic thin-film transistors: A review of recent advances. *IBM Journal of Research and Development* **2001**, 45, (1), 11-27.
11. Duan, Y.; Cao, W. Apparatus and method for monitoring breath acetone and diabetic diagnostics. 2008.
12. Gao, T.; Woodka, M. D.; Brunschwig, B. S.; Lewis, N. S., Chemiresistors for Array-Based Vapor Sensing Using Composites of Carbon Black with Low Volatility Organic Molecules. *Chemistry of Materials* **2006**, 18, 5193-5202.

13. Hierlemann, A.; Ricco, A. J.; Karl Bodenhofer; Göpel, W., Effective Use of Molecular Recognition in Gas Sensing: Results from Acoustic Wave and in Situ FT-IR Measurements. *Analytical Chemistry* **1999**, 71, (15), 3022 - 3035.
14. Horowitz, G., Organic Field-Effect Transistors. *Advanced Materials* **1998**, 10, (5), 365 - 377.
15. Huang, J.; Miragliotta, J.; Becknell, A.; Katz, H. E., Hydroxy-Terminated Organic Semiconductor-Based Field-Effect Transistors for Phosphonate Vapor Detection. *Journal of the American Chemical Society* **2007**, (129), 9366-9376.
16. Huang, J.; Sun, J.; Katz, H. E., Monolayer-Dimensional 5,5'-Bis(4-hexylphenyl)-2,2'-bithiophene Transistors and Chemically Responsive Heterostructures. *Advanced Materials* **2008**, 20, 2567-2572.
17. Jurchescu, O. D.; Baas, J.; Palstra, T. T. M., Effect of impurities on the mobility of single crystal pentacene. *Applied Physics Letters* **2004**, 84, (16), 3061.
18. Katz, H. E.; Dodabalapur, A.; Torsi, L.; Elder, D., Precursor Synthesis, Coupling, and TFT Evaluation of End-Substituted Thiophene Hexamers. *Chemistry of Materials* **1995**, 7, (12), 2238 - 2240.
19. Katz, H. E.; Laquindanum, J. G.; Lovinger, A. J., Synthesis, Solubility, and Field-Effect Mobility of Elongated and Oxa-Substituted ,-Dialkyl Thiophene Oligomers. Extension of "Polar Intermediate" Synthetic Strategy and Solution Deposition on Transistor Substrates. *Chemistry of Materials* **1998**, 10, (2), 633 - 638.
20. Kong, J.; Franklin, N. R.; Zhou, C.; Chapline, M. G.; Peng, S.; Cho, K.; Dai, H., Nanotube Molecular Wires as Chemical Sensors. *Science* **2000**, 287, 622-625.
21. Li, G.-J.; Kawi, S., Synthesis, characterization and sensing application of novel semiconductor oxides. *Talanta* **1998**, 45, 759-766.
22. Li, J.; Lu, Y.; Ye, Q.; Cinke, M.; Han, J.; Meyyappan, M., Carbon Nanotube Sensors for Gas and Organic Vapor Detection. *Nano Letters* **2003**, 3, (7), 929-933.
23. Liao, F.; Chen, C.; Subramanian, V., Organic TFTs as gas sensors for electronic nose applications. *Sensors and Actuators B: Chemical* **2005**, 107, (2), 849-855.
24. Mabeck, J. T.; Malliaras, G. G., Chemical and biological sensors based on organic thin-film transistors. *Analytical Bioanalytical Chemistry* **2006**, 384, 343-353.
25. Musa-Veloso, K.; Likhodii, S. S.; Cunnane, S. C., Breath acetone is a reliable indicator of ketosis in adults consuming ketogenic meals. *American Journal of Clinical Nutrition* **2002**, 76, 65-70.
26. Podzorov, V.; Sysoev, S. E.; Loginova, E.; Pudalov, V. M.; Gershenson, M. E., Single-crystal organic field effect transistors with the hole mobility $\sim 8 \text{ cm}^2/\text{V s}$. *Applied Physics Letters* **2003**, 83, 3504.
27. Podzorov, V.; Gershenson, M. E., Photoinduced Charge Transfer across the Interface between Organic Molecular Crystals and Polymers. *Physical Review Letters* **2005**, 95, 016602.
28. Reutt-Robey, J. E.; Doren, D. J.; Chabal, Y. J.; Christman, S. B., Microscopic Co Diffusion on a Pt(111) Surface by Time-Resolved Infrared Spectroscopy. *Physical Review Letters* **1988**, 61, 2778 - 2781.
29. Reutt-Robey, J. E.; Chabal, Y. J.; Doren, D. J.; Christman, S. B., CO diffusion on Pt(111) by time-resolved surface infrared spectroscopy *Journal of Vacuum Science and Technology A* **1989**, 7, (3), 2227

30. Rogers, J. A.; Bao, Z.; Baldwin, K.; Dodabalapur, A.; Crone, B.; Raju, V. R.; Kuck, V.; Katz, H.; Amundson, K.; Ewing, J.; Drzaic, P., Paper-like electronic displays: Large-area rubber-stamped plastic sheets of electronics and microencapsulated electrophoretic inks *Proceedings of the National Academy of Sciences of the United States of America* **2001**, 98, (9), 4835-4840
31. Schedin, F.; Geim, A. K.; Morozov, S. V.; Hill, E. W.; Blake, P.; Katsnelson, M. I.; Novoselov, K. S., Detection of individual gas molecules adsorbed on graphene. *Nature Materials* **2007**, (Preprint at <http://arxiv.org/abs/cond-mat/0610809>).
32. Schroeder, R.; Majewski, L. A.; Grell, M., A study of the threshold voltage in pentacene organic field-effect transistors. *Applied Physics Letters* **2003**, 83, 3201.
33. Snow, E. S.; Perkins, F. K.; Houser, E. J.; Badescu, S. C.; Reinecke, T. L., Chemical Detection with a Single-Walled Carbon Nanotube Capacitor *Science* **2005**, 307, (5717), 1942 - 1945.
34. Someya, T.; Katz, H. E.; Gelperin, A.; Lovinger, A. J.; Dodabalapur, A., Vapor sensing with alpha,omega-dihexylquarterthiophene field-effect transistors: The role of grain boundaries. *Applied Physics Letters* **2002**, 81, 3079.
35. Sundar, V. C.; Zaumseil, J.; Podzorov, V.; Menard, E.; Willet, R. L.; Someya, T.; Gershenson, M. E.; Rogers, J. A., Mobility Anisotropy in Rubrene Single Crystals Probed by Monolithic Elastomeric Stamps. *Science* **2004**, 303, 1644.
36. Torsi, L.; Dodabalapur, A.; Sabbatini, L.; Zambonin, P. G., Multi-parameter gas sensors based on organic thin-film-transistors. *Sensors and Actuators B* **2000**, 67, 312–316.
37. Torsi, L.; Dodabalapur, A.; Cioffi, N.; Sabbatini, L.; Zambonin, P. G., NTCDA organic thin-film-transistor as humidity sensor: weaknesses and strengths. *Sensors and Actuators B* **2001**, 77, 7-11.
38. Torsi, L.; Lovinger, A. J.; Crone, B.; Someya, T.; Dodabalapur, A.; Katz, H. E.; Gelperin, A., Correlation between Oligothiophene Thin Film Transistor Morphology and Vapor Responses. *Journal of Physical Chemistry B* **2002**, 106, (48), 12563 - 12568.
39. Torsi, L.; Tafuri, A.; Cioffi, N.; Gallazzi, M. C.; Sassella, A.; Sabbatini, L.; Zambonin, P. G., Regioregular polythiophene field-effect transistors employed as chemical sensors *Sensors and Actuators B* **2003**, 93, (1), 257-262.
40. Torsi, L.; Tanese, M. C.; Cioffi, N.; Gallazzi, M.; Sabbatini, L.; Zambonin, P. G., Alkoxy-substituted polyterthiophene thin-film-transistors as alcohol sensors. *Sensors and Actuators B* **2004**, 98, 204-207.
41. Torsi, L.; Dodabalapur, A., Organic Thin Film Transistors as Plastic Analytical Sensors. *Analytical Chemistry A-Pages* **2005**, 77, (19), 380A-387A.
42. Vollmer, A.; Jurchescu, O. D.; Arfaoui, I.; Salzmann, I.; Palstra, T. T. M.; Rudolf, P.; Niemax, J.; Pflaum, J.; Rabe, J. P.; Koch, N., The effect of oxygen exposure on pentacene electronic structure *European Physical Journal E - Soft Matter* **2005**, 17, (3), 339-343
43. Wei, Y.; Yang, Y.; Yeh, J.-M., Synthesis and Electronic Properties of Aldehyde End-Capped Thiophene Oligomers and Other Substituted Sexithiophenes. *Chemistry of Materials* **1996**, 8, (11), 2659 - 2666.
44. Zhu, Z.-T.; Mason, J. T.; Dieckmann, R.; Malliaras, G. G., Humidity sensors based on pentacene thin-film transistors. *Applied Physics Letters* **2002**, 81, 4643.

CHAPTER 2: DESIGN, CONSTRUCTION, AND OPERATION OF SYSTEMS REQUIRED TO DEPOSIT AND STUDY ORGANIC SEMICONDUCTOR THIN FILMS

2.1 Introduction

To study the interaction of organic semiconductor thin films with various gases, a deposition system, gas cell and associated protocols had to be developed. A bell-jar vacuum sublimator system for depositing thin films was adapted, repaired, and improved. A schematic and operational protocol was developed. A method for sublimating pentacene and C6 organic semiconductor thin films on both sides of a sample with gold contacts was developed. To test the film response to sensing vapors with infrared and electrical measurements, a vacuum gas cell prototype and second-generation gas cell were designed, machined, and integrated into an infrared spectrometer and an operational protocol was established.

2.2 Bell Jar Sublimating Vacuum System

Organic thin film deposition by sublimation of insoluble organic semiconductors required a 10^{-6} torr bell jar vacuum system. The clean vacuum prevents variable gaseous environmental contaminants such as water and oxygen from impeding the deposition path from the source to the sample or contaminating the film with defects or charge carrier traps. Parameters important for the resulting organic and gold film quality and reproducibility such as source temperature, film thickness, and deposition rate, can be monitored and controlled in our vacuum deposition system.

A Denton Vacuum bell jar sputtering vacuum system was repaired, adapted for organic sublimation, and an operational protocol was established. Pentacene and HOC6PTTPC6OH films were sublimated on silicon wafers. Since infrared transmission

probes both sides of a silicon wafer, vacuum sublimation sample holders for single-side depositions, and their associated protocols, had to be adapted.



Figure 2.1. Bell jar sublimating vacuum system.

2.2.1 Bell Jar Components

The vacuum sublimator system shown in Figure 2.1 is a Denton Vacuum system from 1989, model DV-602 (Job 9631), previously used for metal sputtering. The system components include a 14" diameter, 18" high Pyrex bell jar attached to a stainless steel plate with a vacuum-greased rubber seal. The vacuum system valves include the following: a high vacuum poppet valve above a liquid nitrogen trap, a Leybold Heraeus Model TMP-150 140 lps turbo pump, an Alcatel Model ZM2008A 7 cfm mechanical pump, and roughing and foreline valves. Pneumatic valves were controlled using 80 psi house compressed dry air. Vacuum gauges include a DVI cold cathode ionization gauge for measuring pressure between 10^{-2} - 10^{-7} torr and two thermocouple gauges for mechanical pump foreline and bell jar roughing pressure monitoring. Pairs of filaments facilitate resistive heating, in order to sublime organic materials from molybdenum crucible holders and evaporate gold from boats. Nitrogen gas (5 psi prepurified) was

used to backfill the jar before opening. System components and their configuration are shown in Figure 2.2.

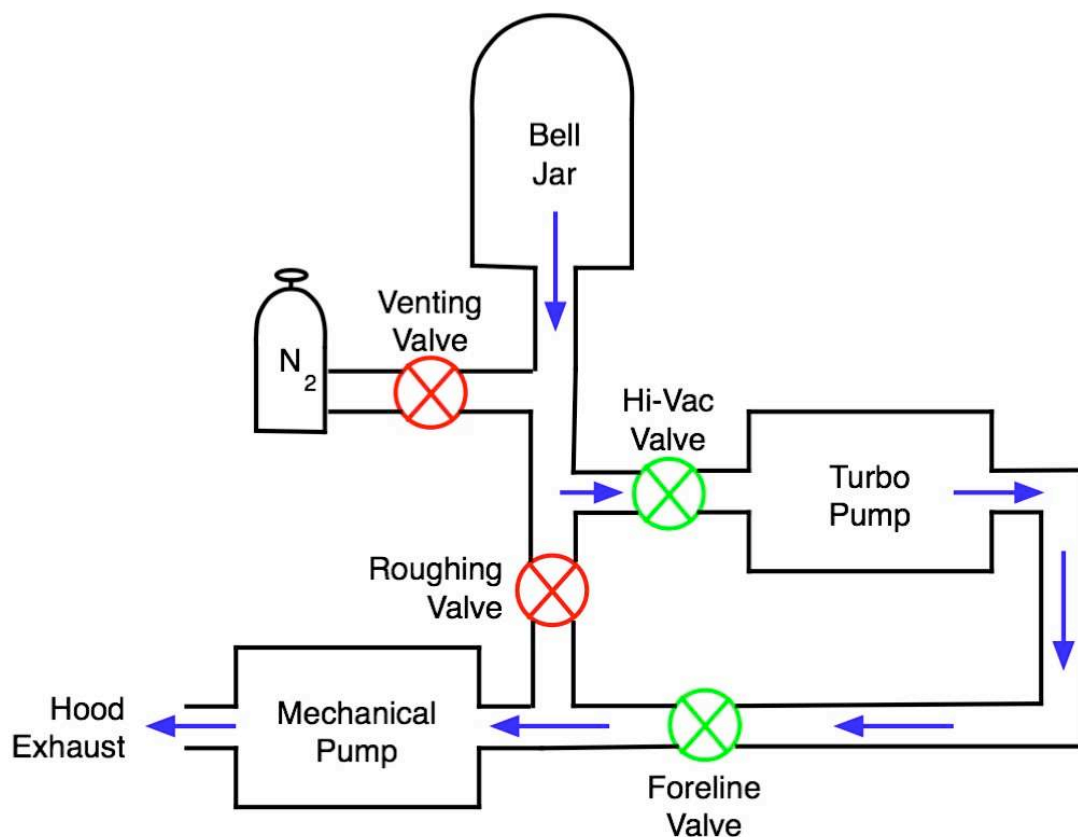


Figure 2.2. Bell jar vacuum pumping schematic.

2.2.2 Repairs

The system mechanical pump and Leybold XTM (quartz crystal microbalance readout) were refurbished through Hickory Hill Designs. The pneumatic controls for the Hi-vac, foreline, and roughing valves were replaced and their flow rates were adjusted to prevent valve jamming. The rubber seal for the glass bell jar was also replaced.

2.2.3 Additions

Several components of the bell jar vacuum system were modified to control and monitor the deposition of gold and organic semiconductors. Deposition rate and thickness were controlled by adding a quartz crystal microbalance (QCM), using a feedthrough connected to an XTM readout. Z-ratio and density calibration settings of the XTM for gold and HOC6PTTPC6OH films were validated by RBS film thickness analysis. In order to monitor substrate, boat and QCM temperatures, two K-type thermocouples were installed through an additional feedthrough for monitoring substrate, boat, and QCM temperatures. A sample-holder scaffolding system was constructed to elevate samples above the material source as shown in Figure 2.3.



Figure 2.3. Scaffolding elevates the sample above the source for line-of-sight deposition of sublimated and evaporated materials.

A thermocouple was wedged between the crucible and crucible holder to monitor the temperature of sublimated organics. When depositing gold, this thermocouple was moved to monitor the sample temperature. A second thermocouple was used to

simultaneously monitor the quartz crystal temperature, since if heated differently between runs, deposition rate and thickness reliability could be compromised.

Standard high current controls normally used for sputtering metals, do not provide the fine low current control required for sublimating organic materials. Terminals from a low-current range (0-70AC amps) external power supply (Figure 2.4) were connected to one of two pairs of bell jar filaments. This allowed stable and reproducible control of the deposition rate of organic semiconductor materials, which was not possible using the bell jar filament controller whose scale was not annotated below 100AC amps and had a maximum current of 500AC amps.



Figure 2.4. Low-current sublimation power supply used to sublimate organic materials

Glass slides¹ provided easily cleanable, sturdy surfaces for attachment of silicon substrates and masks. These were mounted to the bell jar scaffolding by alligator clips. Silicon wafers were first coated with organic semiconductor, and then masks were attached to a glass slide for patterning gold top contacts (Figure 2.5). Kapton tape, which was easily removed after a deposition, prevented organic semiconductor material from

¹ Glass slides were pre-cleaned with a series of acetone, methanol, de-ionized water, and piranha washes.

shorting around the sample edge. Kapton tape was also used to block the gate. A barrier between patterned organic transistors was carved using a plastic pipette tip. This prevented cycling of one device from possibly influencing the material properties of adjacent devices.

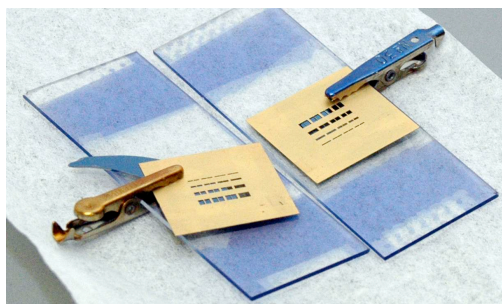


Figure 2.5. Molybdenum masks used to pattern gold top contacts on the silicon wafers coated with organic semiconductor on the topside. After gold deposition, the samples were flipped, elevated, and organic semiconductor was deposited on the other side.

Gold electrodes with micron-order spacing are generally used to test standard organic devices. Dr. Cherie Kagan (IBM) provided molybdenum masks (Figure 2.5) for gold patterning. Channel sizes, as verified with a light microscope, are shown in Table 2.1. Gold masks were consistently anchored to the sample with alligator clips in such a way that masks laid flat against the sample. If not flat, the mask shadow will result in smaller dimensions and possible shorting.

	1	2	3	4
A	1638 / 198	1089 / 198	531 / 180	261 / 178
B	1620 / 139	1080 / 135	535 / 130	252 / 117
C	1665 / 87	1053 / 81	537 / 72	261 / 63
D	1683 / 45	1098 / 45	540 / 40	261 / 36

Table 2.1. Channel Width / Length (μm) as Measured by a Light Microscope.

2.2.4 Operational Protocol

Vacuum components and electronic controls were not previously described or diagrammed in the system's manual. The basic start-up and shut-down procedures provided did not allow the turbo pump to vent to atmospheric pressure. This would cause the bearing lubricant to degas and degrade over time. Also, the manual did not describe how to use the foreline vent to prevent oil suckback into the system. Therefore, various system modifications and a complete operational procedure were developed.

Boats were cleaned with boiling acetone and methanol washes. When used for the first time, boats were then heated alone under vacuum. Organic materials stored in a nitrogen-purged, light-filtering box were loaded into the crucible. Finally, vacuum grease on the bell jar o-ring seal was removed and re-applied. Cleaned samples were positioned approximately 14 inches above the crucible onto the scaffold attached to a glass slide. A shutter blocked line-of-sight material deposition during initial material warming.

A turbo pump started at atmospheric pressure was used to pump on the bell jar contents through an opened poppet valve. The foreline valve was opened to allow the mechanical pump, running briefly in advance, to minimize backstreaming oil and to remove the turbo pump exhaust. Density and Z-ratio values were set to calibrate the XTM. The density and z-ratio values of organic films such as pentacene and HOC6PTTPC6OH are 1.740 g/cm^3 and 1.610 (unitless), respectively. The density and z-ratio of gold are 19.3 g/cm^3 and 0.381 (unitless), respectively. Suitable deposition vacuum (5×10^{-6} torr) was achieved after pumping on the bell jar contents for approximately three hours.

Once suitable deposition vacuum was obtained, the filament was slowly warmed through resistive heating. For slow pentacene preheating, the external power supply was set to 30 AC amps for the first 13 minutes, 45 AC amps for the next ten minutes, and finally, 55 AC amps for 15 minutes in order to achieve a consistent slow deposition rate of 0.1-0.3 Å/s at ~317°C. The sublimation temperature of HOC6PTTPC6OH was ~374°C at 60 AC amps for a high rate of deposition (~1.0 Å/s). Stable deposition rates were achieved by maintaining constant current and thus external crucible temperature. A built-in controller using 160AC amps, at 0.9-1.1 Å/s, controlled gold heating. By moving the shutter out of the sample's line of sight, material was deposited onto the substrate. 250Å or 500Å of organic material and 250Å gold were deposited. Once the desired thickness was obtained, the shutter was closed and the filament power was turned off. The substrate temperature increased to at most 40°C and 80°C during organic and gold material depositions, respectively. The shutdown procedure is discussed below as shown in Figure 2.6.

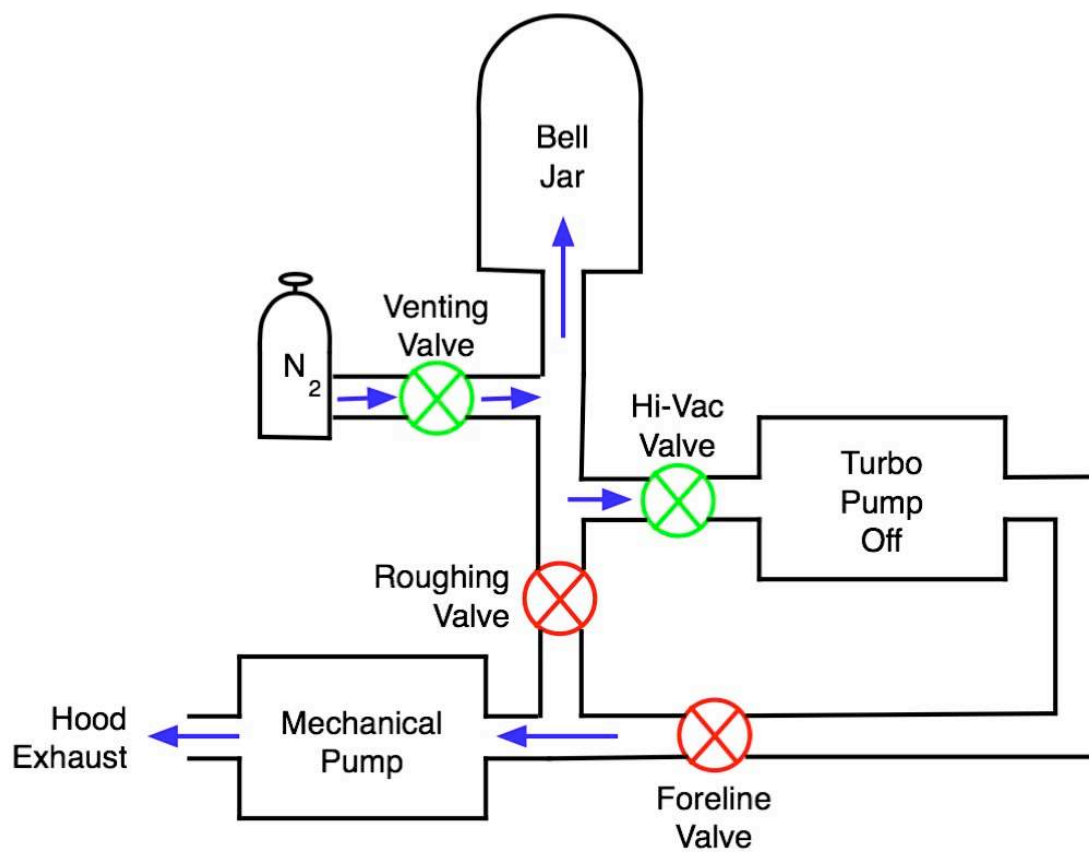


Figure 2.6. Bell jar vacuum system venting schematic.

After organic deposition, the system was allowed to cool for 30 minutes. With the poppet valve in front of the turbo pump still open, the foreline valve behind the turbo pump was closed and the turbo was turned off and allowed to slow down for 20 minutes. This allowed the turbo pump to completely decelerate so that incident nitrogen did not damage the internal balance and condition of the pump blades. Since the system computer controller does not allow the venting valve to open when the poppet valve is open, regardless of the turbo pump status, the venting valve control had to be redirected to an external power supply set at 24V. Opening this valve allowed preset, 5 psi pre-purified nitrogen to backfill the bell jar to atmospheric pressure as shown in Figure 2.6.

The foreline vent controller was opened manually to allow atmospheric pressure to backfill the foreline with air. The mechanical pump was turned off and the foreline vent controller was manually closed. Before opening the bell jar to remove the samples, the poppet valve was closed to prevent dust from reaching the turbo pump.

2.2.5 Precautions

Since the sublimator pneumatic valves were held in their open and closed positions using house air, valves were cycled before operating the system at atmospheric pressure to prevent detrimental leakage whenever air pressure decreased below 50 psi. The valve action rate was calibrated by adjusting the pneumatic controllers to avoid jamming, which, if not properly addressed, would cause detrimental leakage.

Before turning the mechanical pump off, the roughing line was vented by an external controller in order to prevent suck-back of mechanical pump oil. In the future, an additional valve in front of the mechanical pump, which closes in the case of a power failure, could also be added. Optional roughing of the bell jar using the mechanical pump, was limited to 0.1 torr to prevent oil particle backstreaming into the chamber.

2.2.6 Double-Coating Thin Films

Since transmission probes both sides of a sample, both of which can interact with exposure vapors, both sides of each sample were coated with organic films. For electrical measurements, we performed on FTIR-probed samples; gold contacts were deposited on a single side near the corner of the sample through a patterned mask. The rest of the sample was covered with an additional Teflon mask to prevent gold from blocking the infrared beam path through the film. Finally, the sample was flipped over and elevated by narrow, clean Teflon pieces where the gas cell sample holder would normally touch

before the organic deposition was repeated. Film elevation prevented damage or contamination by the glass slide. We assume a nominal amount of organic film deposits underneath the elevated sample.

2.3 Spin Coating

Spin coating was performed with a Laurell Technologies spin coater (model WS-400B-6NPP-LITE). A small o-ring vacuum supported the center of the sample. A dissolved solution of rubrene was dispensed from a glass pipette until it fully covered the sample. Samples were spun at 3000 rpm for one minute before decelerating. Samples were then flipped and spun coat again. To protect samples from photo-oxidation, sample holders were wrapped in foil.

2.4 Gas Cell

In order to investigate the interaction surface chemistry of alcohol vapors with organic semiconductor crystals and thin films, prototype and subsequent second-generation gas cells were designed and built. A fundamental design requirement was allowing infrared scanning without prior removal of alcohol vapors, since doing so might reverse any unknown gas-organic interactions. Electrical measurements in the literature suggested alcohol-surface interactions were reversible. In order to verify this, we performed coupled, real-time infrared and electrical measurements without redirecting the original infrared beam path.

2.4.1 Motivation and Requirements

The unknown mechanism of the reversible and non-specific interaction of gases with organic transistors, as indicated by drain-source current suppression, has prevented the development of selective gas sensors based on organic electronics. An in-situ, infrared analysis of gas interacting with organic films within a closed system could be used to study the factors influencing surface interaction of alcohol vapors. A gas cell was designed to provide a sample chamber for chemical analysis of alcohol interaction with organic thin films without requiring alcohol vapor removal before infrared scanning, which might otherwise reverse any unknown gas-organic interactions.

The requirements for the gas cell design for in-situ monitoring of gas interaction with organic films in a closed system include the following:

1. Fitting the cell within the spectrometer sample chamber
2. The infrared spectrometer must be isolated from the exposure gas

3. Infrared transparent KBr windows must be protected from reactive analytes and moisture
4. The sample holder should facilitate sample: rotation, temperature monitoring, and resistive heating
5. Electrically-insulated feedthroughs should allow applied voltage to the sample device and monitoring of induced sample current
6. Nitrogen and experimental vapor inlets
7. A vacuum port for cell evacuation

2.4.1.1 First-Generation Gas Cell

A gas cell was designed to fit inside a spectrometer sample chamber. By sealing the gas cell to the spectrometer walls, the beam path is enclosed. A cylindrical, NW-50 stainless steel tee was selected because of its compatible dimensions with the sample chamber. The long axis of the tee passed the beam while the other axis provided sample access. The NW-50 tee inner diameter (1.87" or ~50mm) allowed sample rotation. Polished stainless steel was selected because it is resistant to corrosion. The material strength and high vapor pressure are advantageous for machining and for use in a moderate vacuum system.

The KBr windows (49 mm x 6 mm) were held in place by o-rings sandwiched around the machined lip, providing a firm, vacuum-sealed, yet scratch-free mounting (Figure 2.7). Each window holder allowed alternate screws to hold the aluminum ring on opposite sides of the KBr together so that the windows could be easily removed without

disassembling the sandwich. The alternate screws provided attachment to the tee body while evenly compressing a centering O-ring.

Both sides of each hygroscopic KBr window required a nitrogen purge. Welded inlets on the tee and a threaded hole on the window adapter provided nitrogen purging. Window adapters sealed the window holders using compressed O-rings. An O-ring with an inner diameter slightly smaller than the window holder diameter was used. Window adapters mated with spectrometer walls using recessed O-rings.

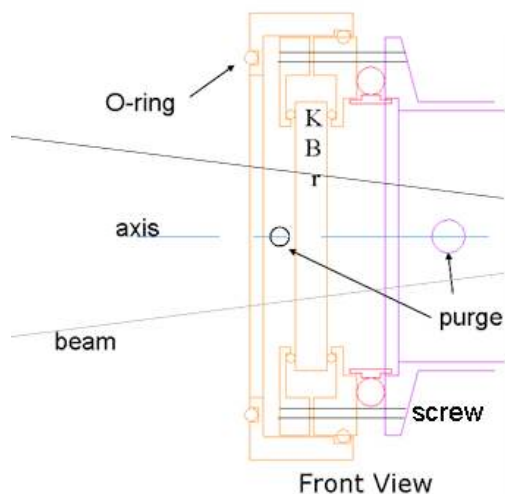


Figure 2.7. Front view schematic of the window holder and adapter.

The KBr windows must be protected from experimental gases in the sample exposure chamber. Since commercial gate valves would not fit inside the tee, we designed a customized shutter that can be operated manually. The challenge was how to vacuum seal the rotating shutter rod to the cell. Stainless steel was selected as the rod material to withstand the torsion forces required during use. A stretch-fit, rotary-shaft ring seal was found from McMaster (Figure 2.8).

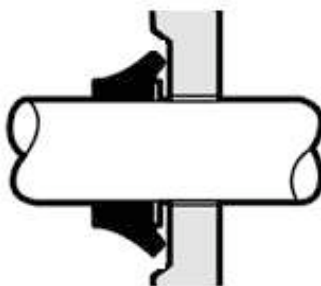


Figure 2.8. Rotary seal diagram

A ring seal stretched over the rod with a flexible, hinged lip provided a good seal to the mating surface. The ring seal material (carboxylated Buna-N) was checked for its resistance to abrasion, water and alcohol, and compatible temperature range with tee baking (up to 225°F). The sealed shaft was compressed against the aperture body by a pin holding the shutter arm to a groove in the rod shown (Figure 2.9).

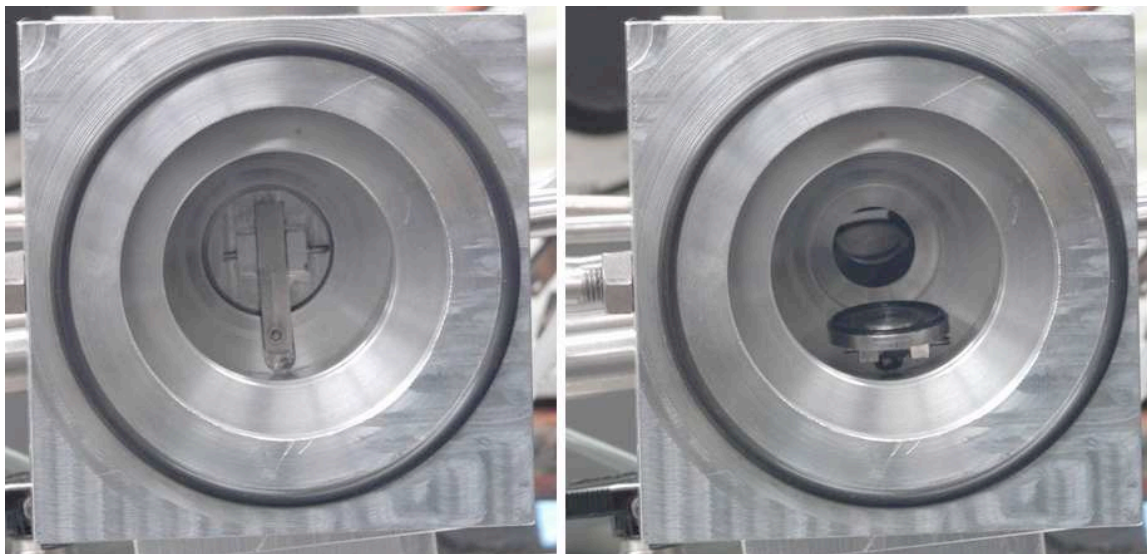


Figure 2.9. One of two customized aperture shutters shown in the closed and opened positions.

A blank flange was adapted for mounting the sample holder and electrical feedthroughs (Figure 2.10). A rod suspended a Teflon sample holder to center the sample

in the infrared beam. The interferogram peak-to-peak maximum identified the maximum sample-beam transmission position ($\sim 74^\circ$ with respect to the sample normal). Tantalum plates with arched fingers attached to the sample arms enhanced electrical contact for heating through power feedthroughs. The sample holder accommodated a standard ~ 1.47 " by 0.6 " silicon sample size. Weldable power feedthroughs were glued with Torr-Seal epoxy and connected to the sample-holder arms with screws. Voltage was applied and current through the sample was monitored to the sample through three female BNC coaxial connectors (vacuum-sealed with O-rings). To monitor the sample temperature, a thermocouple (sealed through the blank flange by Torr-Seal epoxy) was spot-welded to the flat face of a tantalum sample clip.

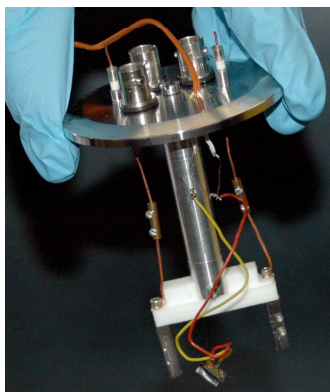


Figure 2.10. First-generation sample holder.

Nitrogen and experimental gas were delivered through welded, $1/4$ " stainless steel pipe connected to three openings on the front and backsides of the tee. The first-generation design was developed using Autocad 2007 (Figure 2.11). A photograph of the integrated system is shown in Figure 2.12.

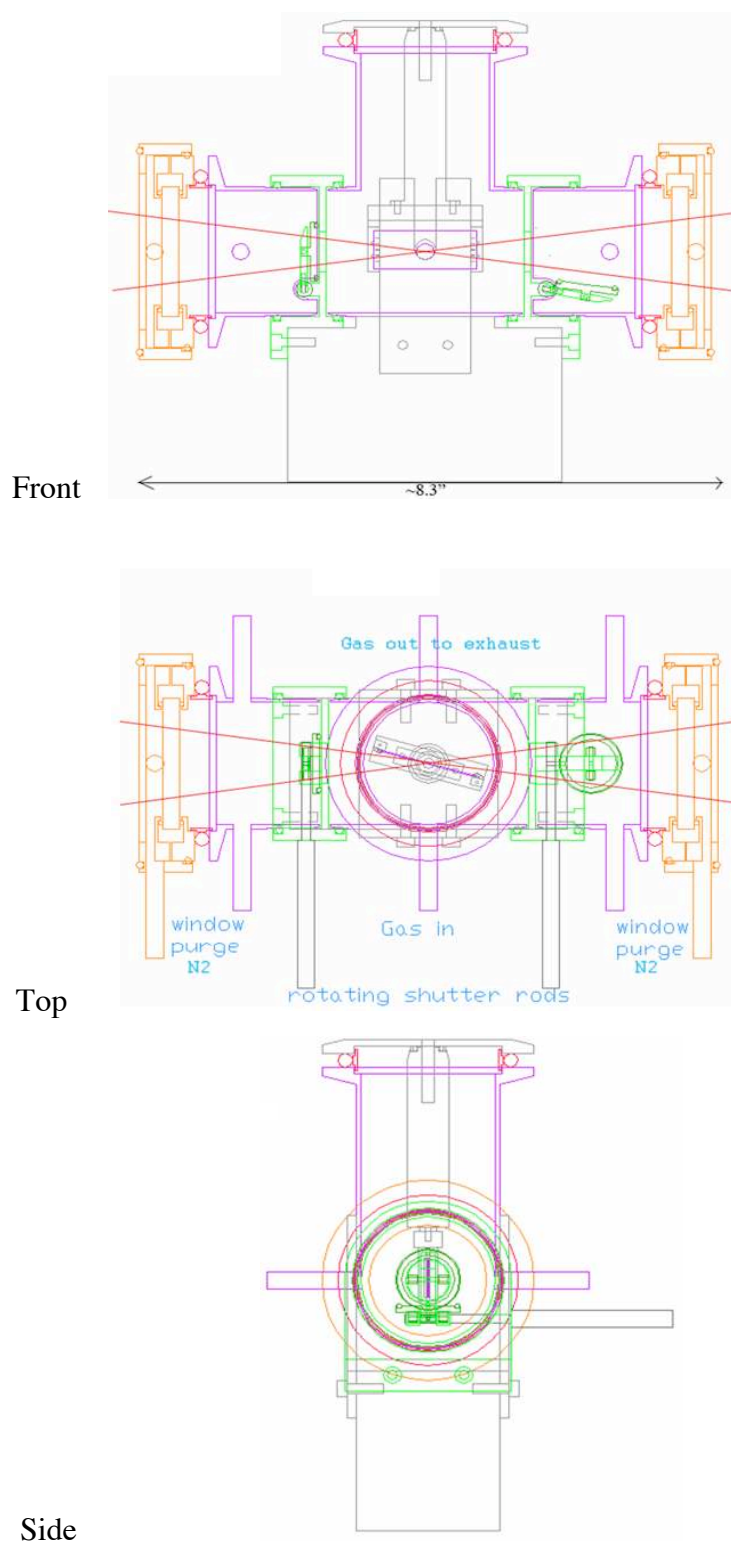


Figure 2.11. Three prospective views of the first-generation gas cell design.

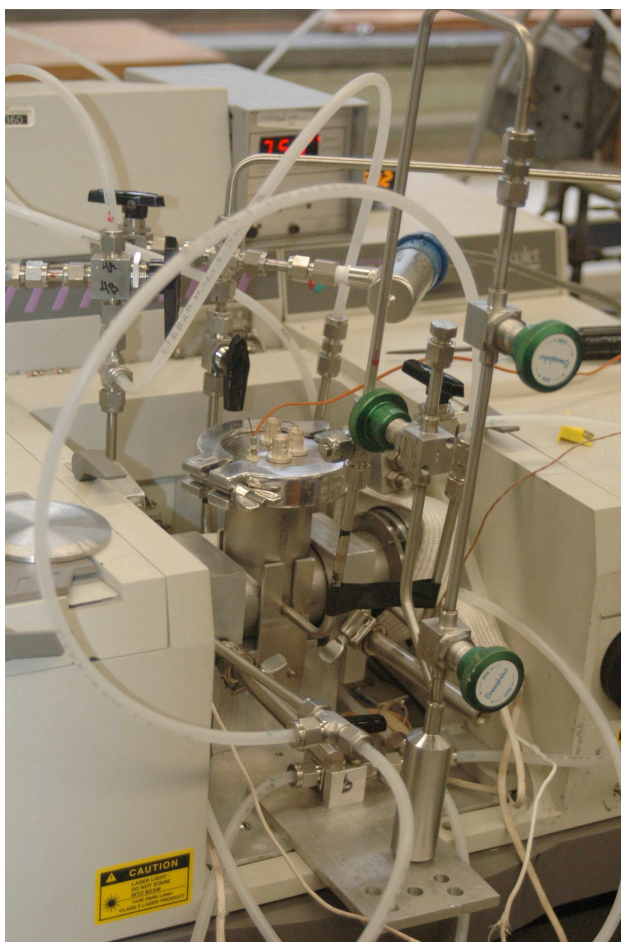


Figure 2.12. The integrated first-generation gas cell.

A Granville-Phillips Convectron Model 275 vacuum gauge was calibrated at atmospheric pressure and used to measure gas cell pressure from 1 millitorr to 1000 torr. At pressures above 1 torr the gauge monitors pressure by convective cooling, using gas circulated with gravity. At pressures below 1 torr, the sensor uses a temperature-compensated, heat-loss sensor for conduction cooling.

If the KBr windows are not sufficiently tightened to the tee, they can move when valves are operated. Slight changes in window position affect beam path-length and can

result in a dramatic baseline oscillation. Baseline oscillation was avoided by sufficiently tightening the window-mounting screws.

Since the trichlorosilane SAM material was corrosive and quite sensitive to water, it was important to be sure its container connections were leak-proof. Swagelok connections near the SAM source were not resistant to corrosion and leakage. Therefore, weldable stainless steel bellows valves connected the material cylinder to the welded exposure line.

The SAM vapor removal required three hours of sorption pumping, with nitrogen flushing into the pump every ten minutes. This was done to expedite the pumping, since the vacuum rate was limited by the 1/4" tubing. Flushing caused the sample chamber to increase from ~50mtorr to ~470torr and may have allowed material to leak past the shutters and contaminate the KBr windows. Constant pressure on the rotary shutter valves, while cumbersome, addressed this problem. A second-generation cell was designed with a commercial gate valve priority from VAT.

Since the sorption pump was loaded with N₂ after every SAM vapor removal, it had to be regenerated under the hood before each experiment. To clean the cell, heating tape and a Variac transformer were used to heat the gas cell and exposure line to 75 - 90°C for approximately one hour, using static heating (no nitrogen flowing). A check valve on the exhaust line prevented overpressure or back-streaming.

2.4.1.2 Second-Generation Gas Cell

To reduce the required time to pump down the cell, extend the sorption pump lifetime, achieve a better vacuum, and reduce the chance of SAM material reacting with

the windows or moisture, we designed a second-generation gas cell. Accommodating commercial gate valves from VAT was a design priority.

Jean-Francois Veyan, a post-doctoral member of the Chabal group, assisted in the design, machining, and troubleshooting of the first gas cell. As a result of these efforts, Jean-Francois designed the basis for a second-generation gas cell machined by the university shop (Figure 2.13). Weldable BNC connectors for vacuum use were integrated into the new design. These reduced the number of possible leaks and provided a durable connection for electrical cables. Larger-diameter tubing of shorter length improved sorption pumping efficiency and lifetime between regeneration. Sorption pump lifetime was extended by the use of a dry pump for roughing the gas cell, such that the sorption pump could start pumping at a better vacuum (20 torr). Commercial gate valves resolved KBr window contamination. O-rings mated the gate valves with the cell and sealed the KBr window holders to the spectrometer walls. The KBr window attachment was improved, using a threaded design that allowed screwing onto the cell housing. While this worked well, it was difficult to compress O-rings between the housing and the spectrometer window adaptors while avoiding cross-threading the window holders.

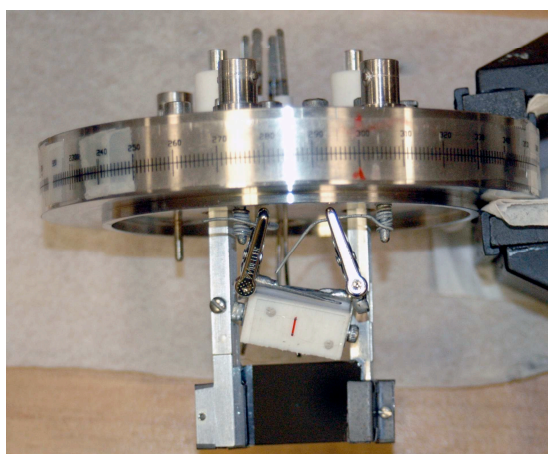
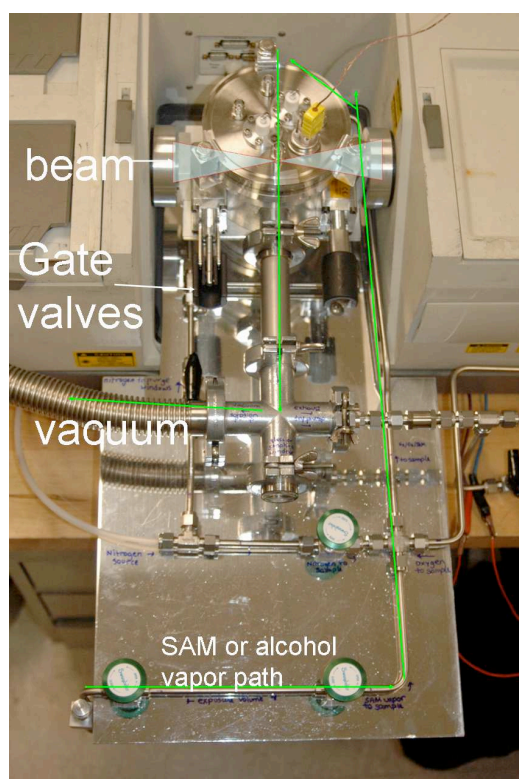
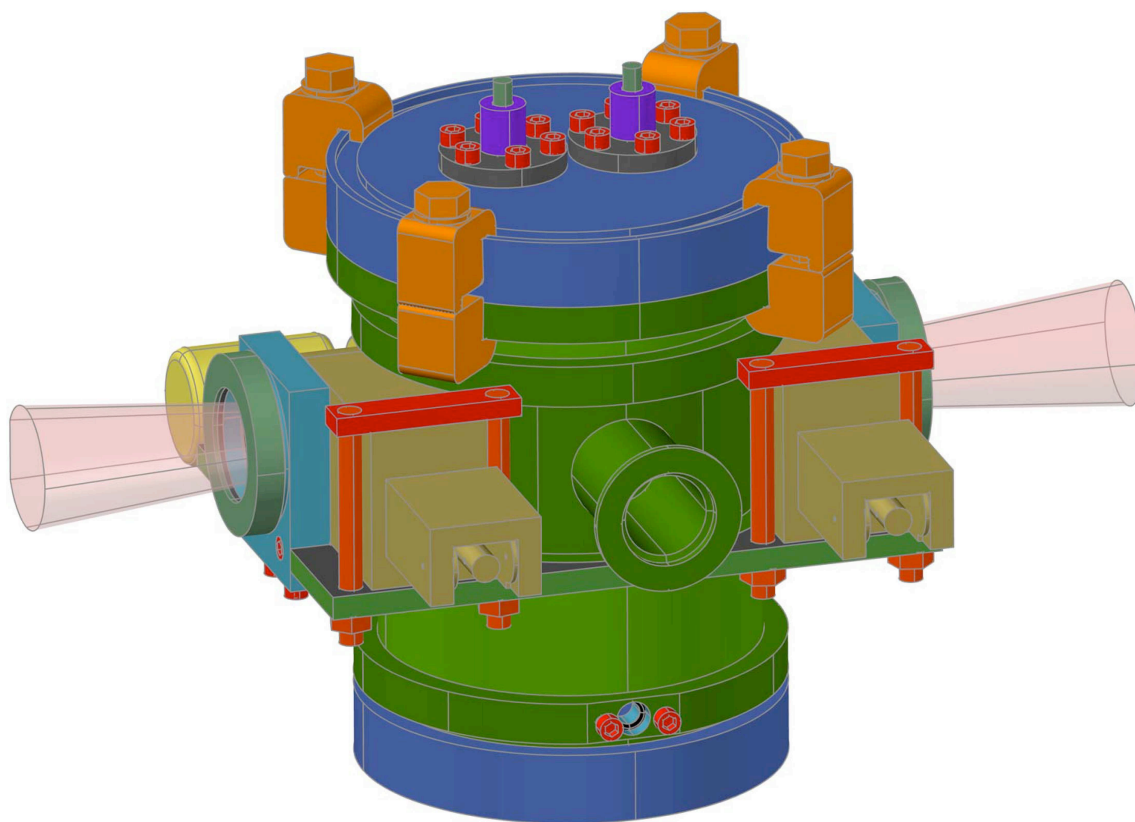


Figure 2.13. Integrated, second-generation gas cell and sample holder.

A single crystal holder was needed to suspend a crystal above the sample for electrical measurement in the same conditions as those of the silicon sample. This required an insulating surface attached to the crystal, providing connectivity between the crystal electrodes and the BNC connectors, and easy attachment/removal of the holder to the gas cell.

A small Teflon block was chosen as an insulating substrate for the crystal connections. Threaded holes at opposing ends of the block provided screw attachment to a metal plate to the ends of the block. The metal plate provided an attachment site for gold wires coming from the crystal, as well as an attachment point for soldered alligator clips shown integrated into the sample holder (Figure 2.13). Wires wrapped around the BNC-feedthrough pin provided an attachment point for the clips.

The gas cell was integrated into the spectrometer and assembled with stainless steel gas lines. A flexible stainless steel line with a ~1" inner diameter and a minimal length connected the sorption pump to the gas cell through a connecting tee of equal diameter. This increased the pumping speed of the sorption pump dramatically. The operation of the integrated system shown in Figure 2.14 is discussed next.

2.4.1.2.1 Operational Protocol

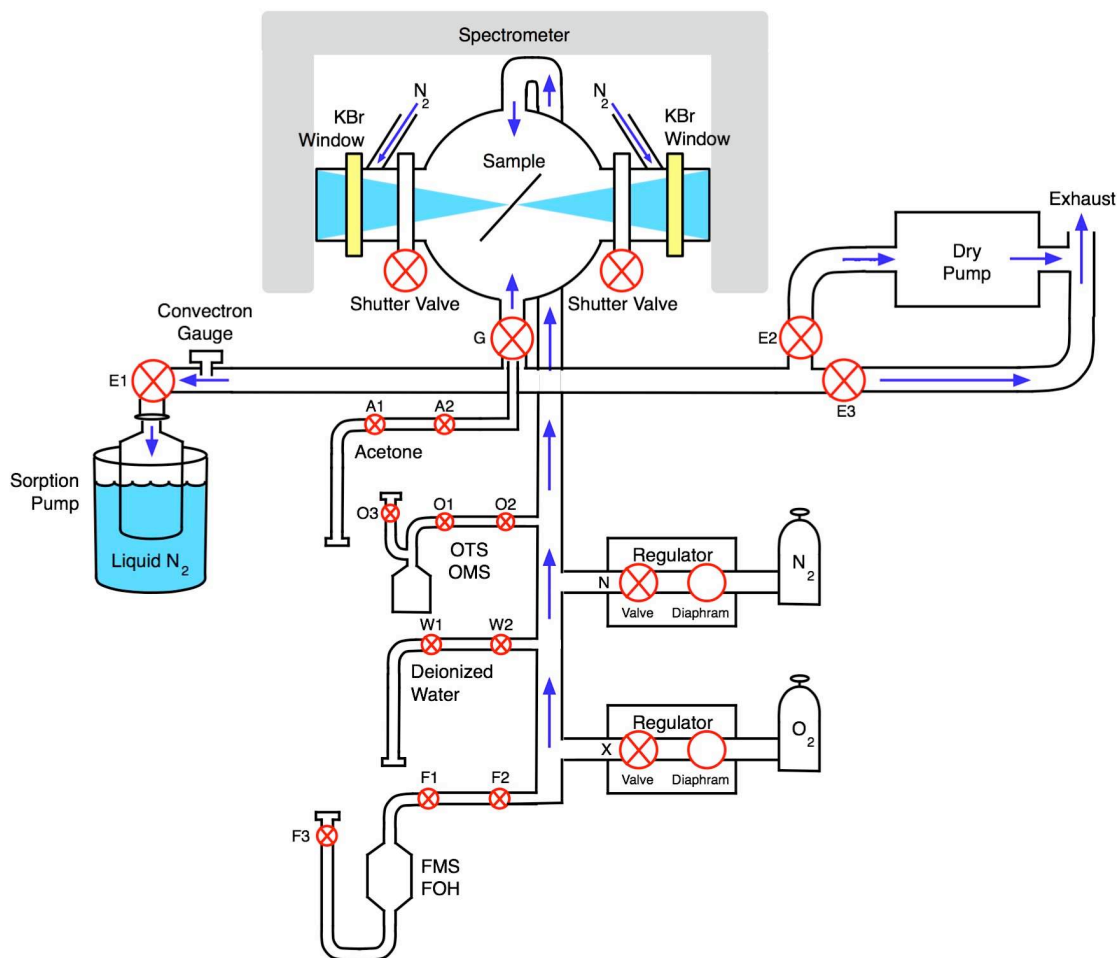


Figure 2.14. Gas cell system schematic (not to scale).

The procedure for preparing the source material vessels, scanning, and exposures are described. Desired materials for thin-film SAM depositions were loaded into stainless steel vessels. The procedure for loading the liquids began with baking a vessel while vacuuming with a sorption pump. Heating continued for approximately 1.5 hours until the vacuum had dropped to 10 mtorr. The vacuum within the vessel was between closed valves before turning off the heat. Vessels were filled with SAM by opening the valve F3 or O3. The vacuum pulled in SAM liquid loaded into an attached line of 3/8"

tubing within the glove box. The valve F3 or O3 was closed, then the 3/8" tubing was removed, and the valve opening was capped. Exposure systems were then re-attached to the gas cell system.

Scanning Under N₂ Purge: The E3, G, and shutter valves were opened while N₂ purge was flowing.

Pumping Down the Sample Area: The E3 valve was closed, followed by the closure of the shutter valves surrounding the sample area. The dry pump was turned on and E2 was opened until the cell vacuum reached ~25 torr. Finally, E2 was closed and E1 was opened.

SAM Exposure: Two types of SAM exposures were made. Sub-vapor pressure exposures give an idea of the sensitivity level of the material, while saturated-vapor pressure exposures give an idea of the maximal material response.

Sub-Vapor Pressure SAM exposure: The vacuumed exposure line (between O1 and O2 or F1 and F2) was filled with SAM vapor by opening F1 or O1 for 30 seconds. Materials instantly boiled, since the vacuum was below the vapor pressure at room temperature for the SAM materials used. By keeping the cell pressure below the vapor pressure, gases in the exposure line backfilled the gas cell and caused an increase in the closed-system pressure. E1 was then closed. With F1 or O1 closed, F2 or O2 was opened for the duration of the exposure. Vapors soaked the sample for 15 minutes while electrical measurements were recorded.

SAM Vapor Removal: E1 was opened to remove exposed vapors for 25 minutes. F2 or O2 were closed once the system pressure reached 10 mtorr. To flush the system, E1 was closed and the N₂ source valve was opened until the cell pressure reached ~300 mtorr. The N₂ source valve was then closed and E1 opened. This process was repeated three times before allowing the final N₂ backfill to return the system to atmospheric pressure.

Solvent Exposures: The same procedure used to perform SAM exposures was used with solvents, except A1 and A2 were opened instead of O1 and O2. For saturated vapor pressure exposures, both A1 and A2 were opened.

2.4.2 Future Design Improvements

Future cell designs should allow N₂ to flow past the KBr windows out dedicated exhausts instead of relying on positive pressure to remove moisture from the sealed compartment in the current design. This would allow N₂ to displace any moisture or contaminants while the gate valves are in the closed position. Additional modifications to facilitate baking out the exposure vessel include replacement of the empty chamber below the gas cell with posts to allow heating tape to be wrapped under the sample exposure area and minimize heat transfer to the spectrometer. Replacement of additional nut and ferrules with welded connections could eliminate possible leak points. However, permanent connections would make the system less modular. Future designs might minimize leak-stressing movements by mounting all valves to the supporting plate.

2.5 Summary

A vacuum sublimation system was repaired, adapted, and improved for the deposition of organic, thin-film sublimation and gold evaporation. Solution casting and vacuum sublimation were used to make samples on SiO₂ for the thin-film analysis described in Chapters 4 - 6. Prototype and more advanced gas cell systems were built and integrated into the sample compartment of an infrared spectrometer. Finally, operation procedures used to conduct various experiments on organic thin films (Chapters 4-6) were diagrammed.

CHAPTER 3: CHARACTERIZING THREE ORGANIC SEMICONDUCTOR MATERIALS

3.1 Abstract

The infrared absorption spectroscopy (IRAS) of rubrene, pentacene, and 5,5'-bis(4-hydroxyhexylphenyl)-2,2'-bithiophene (C6) materials are interpreted as a reference point for further experiments in this thesis. The photo-oxidation of rubrene thin films revealed peaks attributed to endoperoxide group formation and is predicted to be a reactive site for the trichlorosilane bonding explored in Chapters 4 and 5. The peaks for pentacene thin films have been identified as a basis for understanding peak changes that occur with solvent sensing in Chapter 6. X-ray diffraction (XRD) analysis of C6 powders indicates distorted hexagonal arrays where the thiophene group is tilted toward a phenyl group. Hexanol tails were interdigitated between layers. The C6 thin-film peaks were different than those with the powder form, indicating the substrate oxide influences film packing. However, layer spacing indicates a tilt that corresponds to the nearly perpendicular orientation predicted by IRAS. The molecular packing indicates the C6 film surface termination presented for sensing, while the peak interpretation helps to understand film perturbation by solvent sensing in Chapter 6.

3.2 Introduction

Using the vacuum sublimator introduced in Chapter 2, thin films of pentacene and C6 were investigated, using IRAS to identify their spectral peaks. This provides a basis for understanding film perturbation upon exposure to gas vapors, which will be described in Chapter 6. 0.5 weight % rubrene dissolved in xylene was spun cast and studied with IRAS. A photo-oxidation study was performed by illuminating samples with a visible

spectrum quartz tungsten halogen (QTH) lamp. This required line-of-sight access, achieved by exchanging the acetone feedthrough with a glass window.

The organic semiconducting materials investigated in this thesis (rubrene, pentacene, and C6) are evaluated in this chapter, using IRAS, XRD, and electronic characterization as a basis for understanding the film purity, chemistry, structure, and conduction before subsequent gas exposures. Fourier transform infrared spectroscopy was used to verify the integrity of organic semiconductor functional groups and to confirm the absence of contaminants.

3.3 Rubrene

The high mobility of rubrene single crystals ($8 \text{ cm}^2/\text{Vs}$) make them an attractive material for sensing small changes in surface current (Podzorov, et al. 2003; Sundar, et al. 2004). Vitaly Podzorov's research group provided rubrene single crystals grown under the vapor phase in a horizontal reactor. Bumsu Lee selected large, smooth crystals and painted colloidal graphite electrical contacts (spaced $\sim 1\text{-}3\text{mm}$ apart and $\sim 0.5\text{mm}$ wide) for attaching gold wires. Rubrene single crystals absorbed too much of the infrared beam to be studied in the transmission geometry. Since sublimation would also produce an amorphous film at room temperature, spin casting was chosen as the deposition method due to the ease of the technique (Käfer and Witte 2005). Therefore, a 0.5 weight % rubrene in xylene solution was spun-cast on silicon wafers and exposed in tandem with single crystals in order to later correlate electrical measurements with infrared data. Infrared features (after subtracting the substrate) of a typical rubrene spun-cast film are presented in Figures 3.1A-C. Spectral interpretations are presented in Tables 3.1 - 3.3.

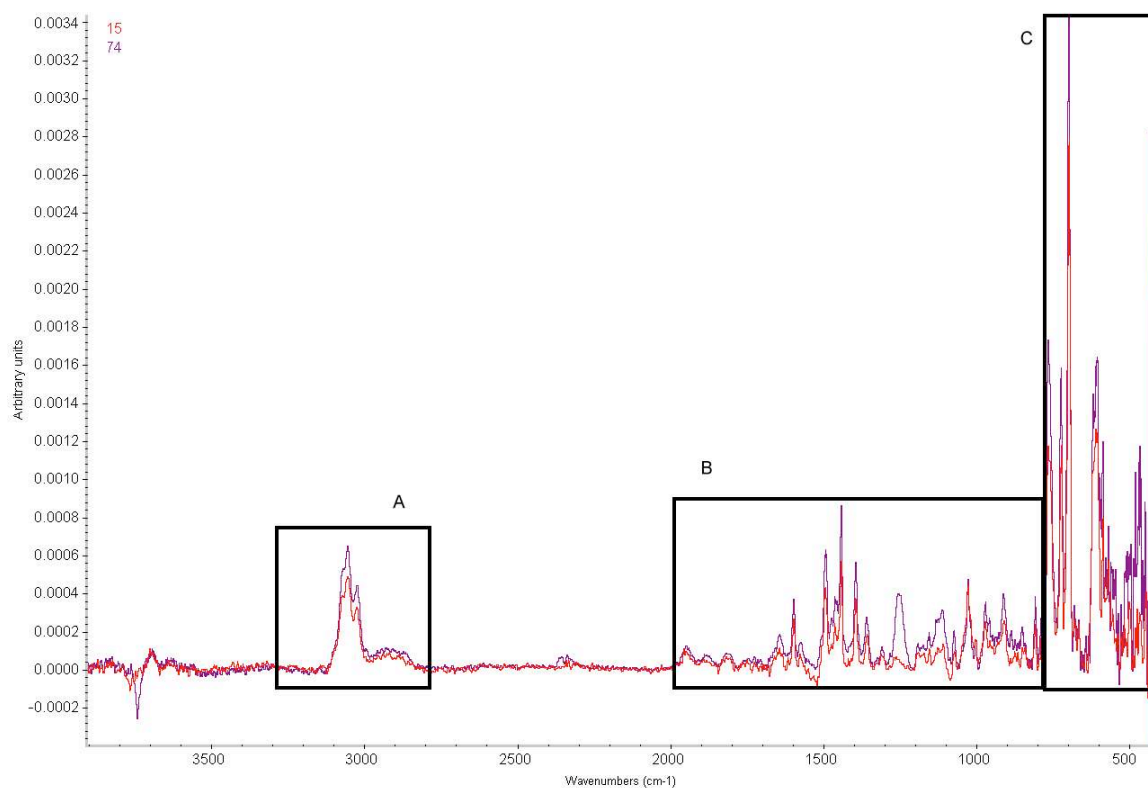


Figure 3.1. The infrared absorption spectra of a typical spun-cast rubrene film referenced to (subtracted by) its clean native oxide silicon substrate. The beam angle of incidence was 15° and 74° from the substrate surface normal.

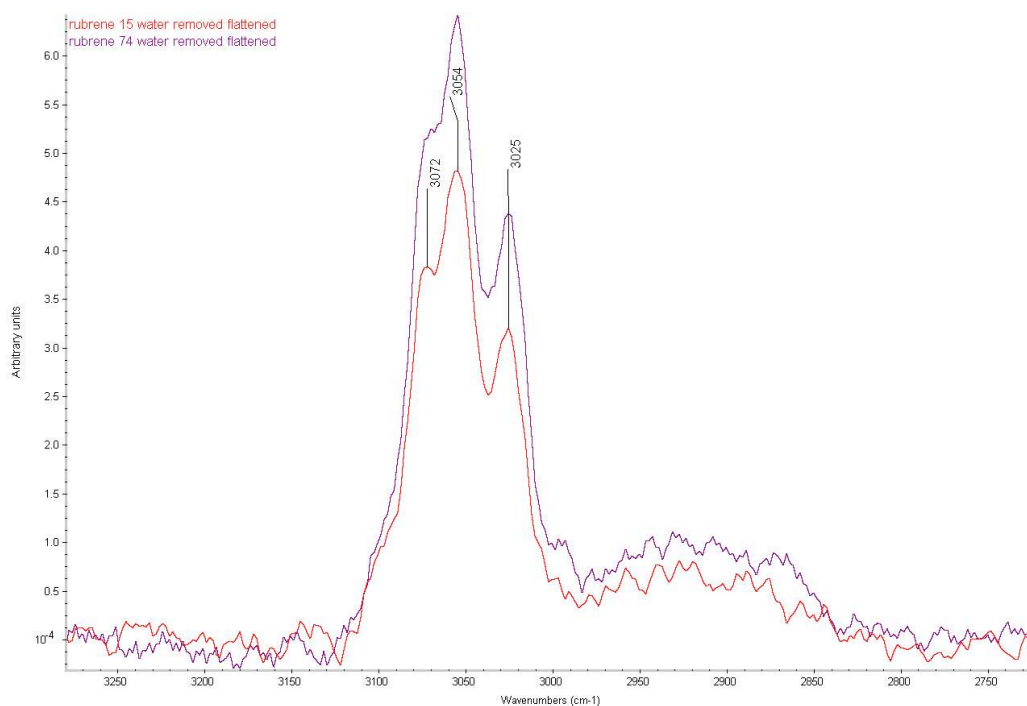


Figure 3.1A. The high wavenumber region (box A in Figure 3.1) of a typical rubrene infrared absorption spectrum referenced to its clean native oxide silicon substrate.

Wavenumber	Interpretation	Reference
3072 3054 3025	CH aromatic stretch	(Socrates 2001), p. 157)
2861-2958	C-H stretch	(Socrates 2001)

Table 3.1 Rubrene High Wavenumber Peak Assignments

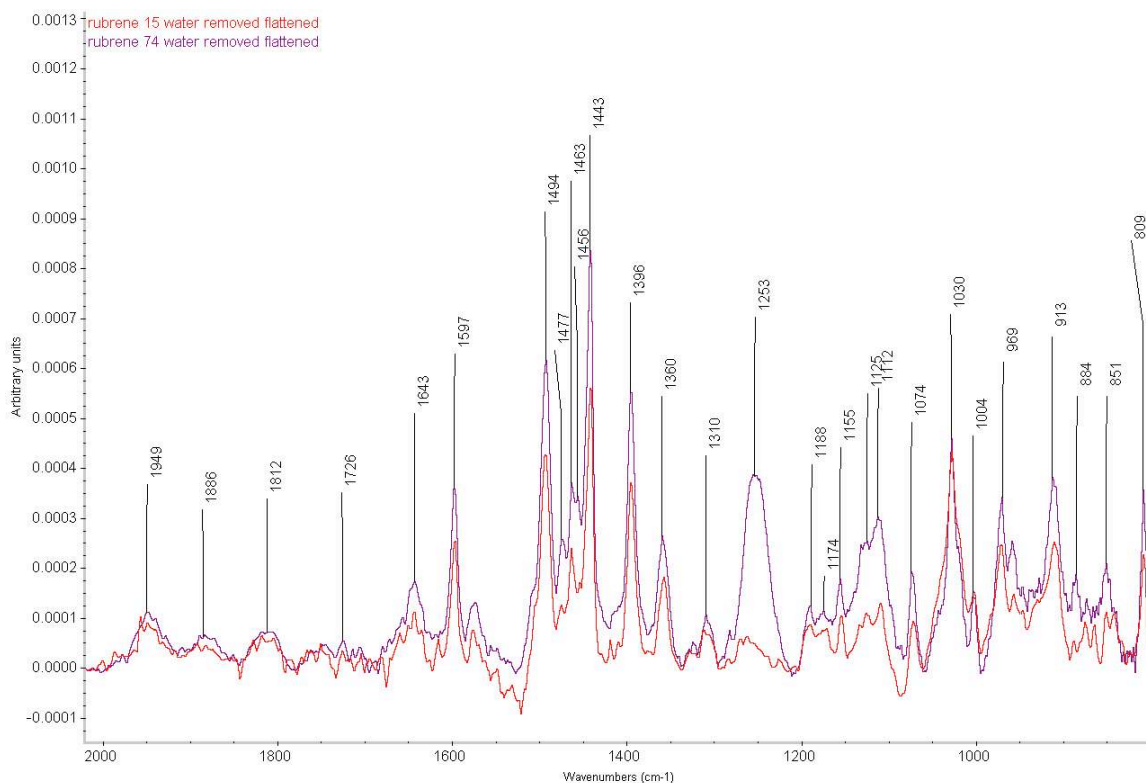


Figure 3.1B. The mid-wavenumber region (box B in Figure 3.1) of a typical rubrene infrared absorption spectrum referenced to its clean native oxide silicon substrate.

Wavenumber	Interpretation	Reference
1643-2000	Ring overtone, combination	(Socrates 2001), p. 157)
1430-1625	Ring C=C stretching	(Socrates 2001), p. 157)
1494, 1577, 1597	Skeletal vibration	(Socrates 2001), p. 160)
900-1290	Ring C-H in plane bending	(Socrates 2001), p. 159)

Table 3.2 Rubrene Mid-Wavenumber Peak Assignments

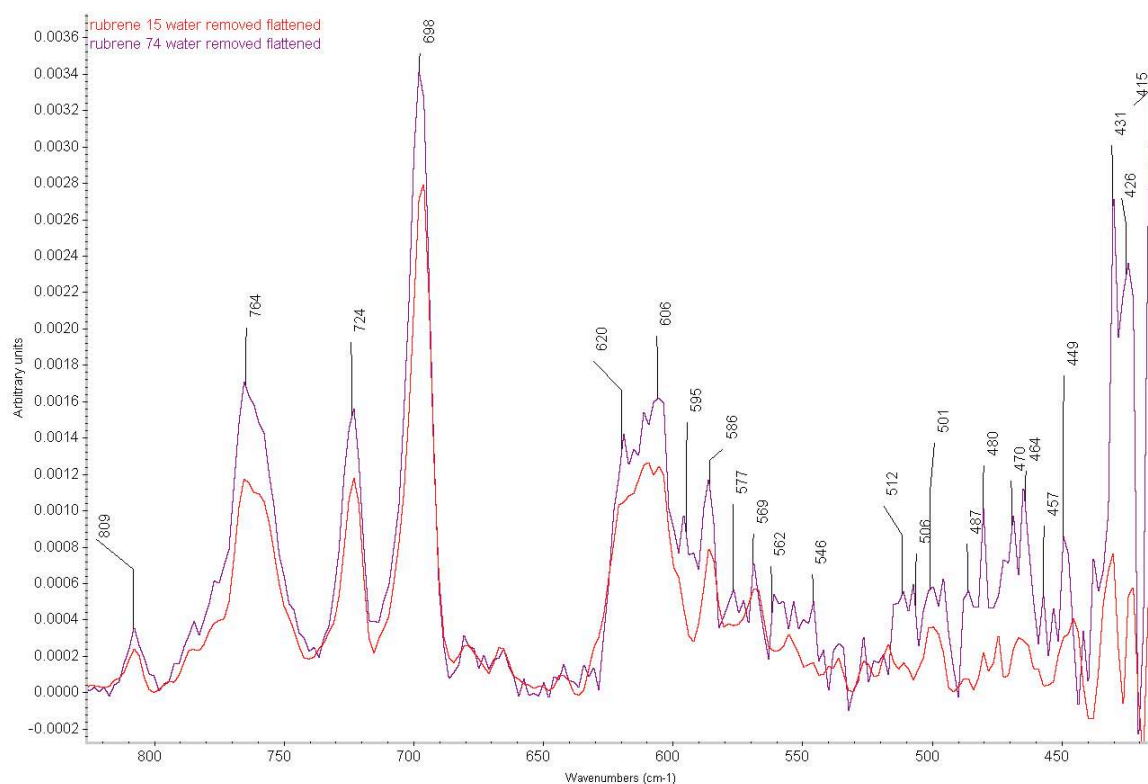


Figure 3.1C. The low-wavenumber region (box C in Figure 3.1) of a typical rubrene infrared absorption spectrum referenced to its clean native oxide silicon substrate.

Wavenumber	Interpretation	Reference
650-900	C-H out of plane aromatic ring bending	(Socrates 2001), p. 157, 159)

Table 3.3 Rubrene Low-Wavenumber Peak Assignments

Peak intensity decreased the most at 1253 cm^{-1} when the incident angle was changed from 74° to 15° . This indicates in-plane aromatic C-H bending, located within rubrene ring planes, are nearly perpendicular to the substrate surface. This is also supported by the high wavenumber polarization effect on aromatic C-H stretching modes. Although we expected the spun film to be amorphous, there must have been sufficient film ordering within the beam path to have caused a polarization effect at 1253 cm^{-1} .

3.3.1 Rubrene Photo-oxidation Investigation

Now that we understand the spectral features of spun-cast rubrene thin films, we can begin to investigate possible rubrene-reactive sites presumed responsible for the sustained increase in rubrene surface current upon exposure to trichlorosilane self-assembled monolayers (SAMs) that will be discussed in Chapters 4 and 5. We hypothesize that both the surface of rubrene crystals and spun-cast rubrene films are terminated with rubrene endoperoxide as a result of exposure to ambient light and atmospheric oxygen. The amorphous spun film with possible diffusion channels and more molecular motion in a loosely packed film may be more reactive than the rubrene single crystal (Käfer and Witte 2005). Only the spun film was characterized here. On an otherwise unreactive surface, the endoperoxide group provides a likely reactive site for the trichlorosilane molecules used to enhance the rubrene surface current. Bonding to rubrene through the surface endoperoxide should decrease peaks affiliated with the broken endoperoxide and increase peaks associated with the formation of new bonds.

In order to validate the position of endoperoxide infrared absorption peaks, the intensity of the affiliated infrared absorption features were increased by exaggerating the conditions required for endoperoxide formation. Once exposed to ambient conditions, the surface of rubrene crystals and spun-cast films may contain many endoperoxide groups (Käfer and Witte 2005). One method for forming additional endoperoxide is to allow a rubrene-xylene solution to oxidize in an illuminated hood overnight. Oxidation is assumed once the solution becomes clear. A more controlled approach for endoperoxide formation is by illuminating a rubrene spun film in the presence of oxygen with a white light. Because endoperoxide formation requires ambient exposure for many hours, and

oxidation sites can be preserved by storing rubrene crystals and solutions under N₂ and protecting them from light.

The process by which rubrene is oxidized and the molecular structure that results are well understood. Rubrene reversibly traps oxygen during photooxidation (IUPAC 1997). Specifically, oxidation is a chemical reaction where one or more electrons are lost when a molecule is excited by light with oxygen exposure. In order for oxidation to take place, a molecule's electronic absorption spectrum must overlap with the spectral range of the incident light (Atkins 1982).

The oxidation of rubrene at the 1,4-ring positions requires the simultaneous excitation of rubrene and oxygen. This simultaneous reaction is required, because singlet state molecular oxygen is relatively unreactive toward ground-state organic molecules (Nardello, et al. 1999). Triplet, ground-state oxygen (³O₂) can be excited to a reactive diradical by photo-oxidation. Photo-oxidation rearranges two opposite-spin oxygen electrons into a degenerate π^* molecular orbital, converting the molecule to the electrophilic singlet state (¹O₂) (Nardello, Marti, Pierlot and Aubry 1999). Oxygen excitation can be catalyzed by a photosensitizer or by reaction with hydrogen peroxide and sodium molybdate. Examples of photosensitizers studied in the literature include: α -terthienyl, tetraphenylporphine, methylene blue and rose Bengal (Hamon, et al. 2007; Nardello, Marti, Pierlot and Aubry 1999; Otomo, et al. 2002). Excitation of the photosensitizer and intersystem crossing form the triplet-excited sensitizer (Hamon, Stensaas, Sugar, Tumminello and Allred 2007). This triplet sensitizer converts triplet oxygen to singlet oxygen and regenerates the sensitizer (Hamon, Stensaas, Sugar, Tumminello and Allred 2007).

The signatures' aromatic molecules undergoing oxidation have been studied with ultraviolet-visible (UV), infrared, and Raman spectroscopy. Rubrene absorption is known to occur within the visible range at 367 nm, 436 nm, and 546 nm (Bowen and Steadman 1934; Otomo, Otomo, Yokoyama and Mashiko 2002). Therefore, photo-oxidation should be initiated by illuminating rubrene thin films cast from xylene, using a white lamp through a quartz window. M-Xylene does not react with rubrene during the oxidative process (Hochstrasser and Ritchie 1956). The photo-oxidation of a rubrene n-hexane solution in oxygen and ambient light starts after five hours with decreased absorption at 300 nm, 520 nm, and an increase at 205-212 nm and 244 nm outside of the UV spectrum (Ristic 1985). Colorless rubrene photo-peroxide reversibly decomposes at 180°C to oxygen and the original molecule (Karyakin 1961). Seventy percent of rubrene peroxide decomposes in benzene at 118°C after 25 minutes (Hochstrasser and Ritchie 1956).

Rubrene crystal surface defects (vacancy, grain boundary, and dislocation) may promote oxidation and support observations of oxidation concentration decreasing away from the crystal surface into the bulk (Käfer and Witte 2005; Mitrofanov, et al. 2006). Thus, there should be many reactive sites for oxidation in polycrystalline spun-cast films if stored under N₂ and used within an hour. A density functional theory (DFT) model of rubrene-peroxide revealed a 55° bend that may decrease the conductivity of a rubrene crystal due to a disruption in pi-bond overlap while providing a reactive site for trichlorosilanes (Käfer and Witte 2005).

3.3.2 Photo-oxidation Indicators

The symmetrical structure of the C-O-O-C peroxy group generally does not produce a large change in dipole moment and thus should have a weak infrared signature (Karyakin 1961). However, X-ray and DFT analysis of the hydrogen peroxide structure indicate H-O-O-H and C-O-O-C are non-planar (Käfer and Witte 2005; Karyakin 1961). The angle between the bonds can prevent the transfer of vibrational energy such that infrared spectrum peaks will be visible (Karyakin 1961).

Generally, aromatic carbon peaks are sensitive to the mass of substituents, such as a 1,4-disubstituted benzene. Out-of-plane bending peaks occur at $680\text{--}710\text{ cm}^{-1}$ and $780\text{--}860\text{ cm}^{-1}$, while other peaks are observed at $445\text{--}520\text{ cm}^{-1}$ and $615\text{--}650\text{ cm}^{-1}$ (Socrates 2001), p. 163). The in-plane bending modes of 1,4-disubstituted benzene occur at $975\text{--}995\text{ cm}^{-1}$, $1005\text{--}1025\text{ cm}^{-1}$, $1110\text{--}1130\text{ cm}^{-1}$, $1165\text{--}1185\text{ cm}^{-1}$, $1215\text{--}1230\text{ cm}^{-1}$, and $1250\text{--}1270\text{ cm}^{-1}$ and may be intensified by a polar ring substitution, such as oxygen (Socrates 2001), p. 164). Aryl and alkyl peroxide structures generally have O-O stretch peaks at $840\text{--}900\text{ cm}^{-1}$ (Socrates 2001), p. 25, 105). Alkyl and aryl peroxides have a C-O peak at $1030\text{--}1155\text{ cm}^{-1}$ and $940\text{--}1030\text{ cm}^{-1}$, respectively. (Socrates 2001), p. 25, 105). The peaks of pentacene, although aromatic, may be different due to additional aromatic groups.

Rurbene endoperoxide, formed in a KBr pellet, showed peaks at approximately: 580 cm^{-1} , 600 cm^{-1} , 630 cm^{-1} , 690 cm^{-1} , 730 cm^{-1} , 1190 cm^{-1} , and 1510 cm^{-1} (Ristic 1985). Anthracene photo-oxidation causes a shift in out-of-plane bending modes at $739\text{ cm}^{-1}\text{--}757\text{ cm}^{-1}$ (Bratschkov 2001; Karyakin 1961). In polycyclic aromatic hydrocarbons, such as anthracene, the peak at 894 cm^{-1} is attributed to O-O, while peaks at 1245 cm^{-1} and 1260 cm^{-1} are attributed to C-O (Karyakin 1961). Kapetanaki and

Varotsis utilized oxygen¹⁸ to identify the oxygen-sensitive modes in the decomposition of the anti-malarial drug artemisinin, a seven-membered ring with an endoperoxide. After a 532 nm laser was flashed at endo-peroxide-containing artemisinin, negative peaks formed at 724 cm^{-1} , 832 cm^{-1} , and 885 cm^{-1} , which are attributed to the O-O, C-O, and O-O-C, respectively (Kapetanaki and Varotsis 2001).

3.3.3 Photo-oxidation Results

To identify rubrene endoperoxide peaks in spun-cast films, photo-oxidation was performed while rubrene surfaces were monitored in real time with infrared spectroscopy. Clean samples were coated with fresh rubrene solution and loaded into the gas cell. Films were stable in the cell under a nitrogen purge. The cell was backfilled with scientific grade molecular oxygen, raising the pressure from 20 mTorr to 880 Torr. A 10 Watt white quartz tungsten halogen (QTH) lamp (Newport Oriel model 6318) was powered with 6.0V and 1.73 amps. The incident QTH white light emits shorter wavelengths than rubrene will absorb (560 nm). A mirror was placed behind the lamp to maximize the amount of light reaching the sample. A total of five loops of 1000 scans (20 minutes each) were averaged over an hour. The resulting single-beam spectra, representing several time points along the photo-oxidation progress, are compared back to the clean reference (Figure 3.2).

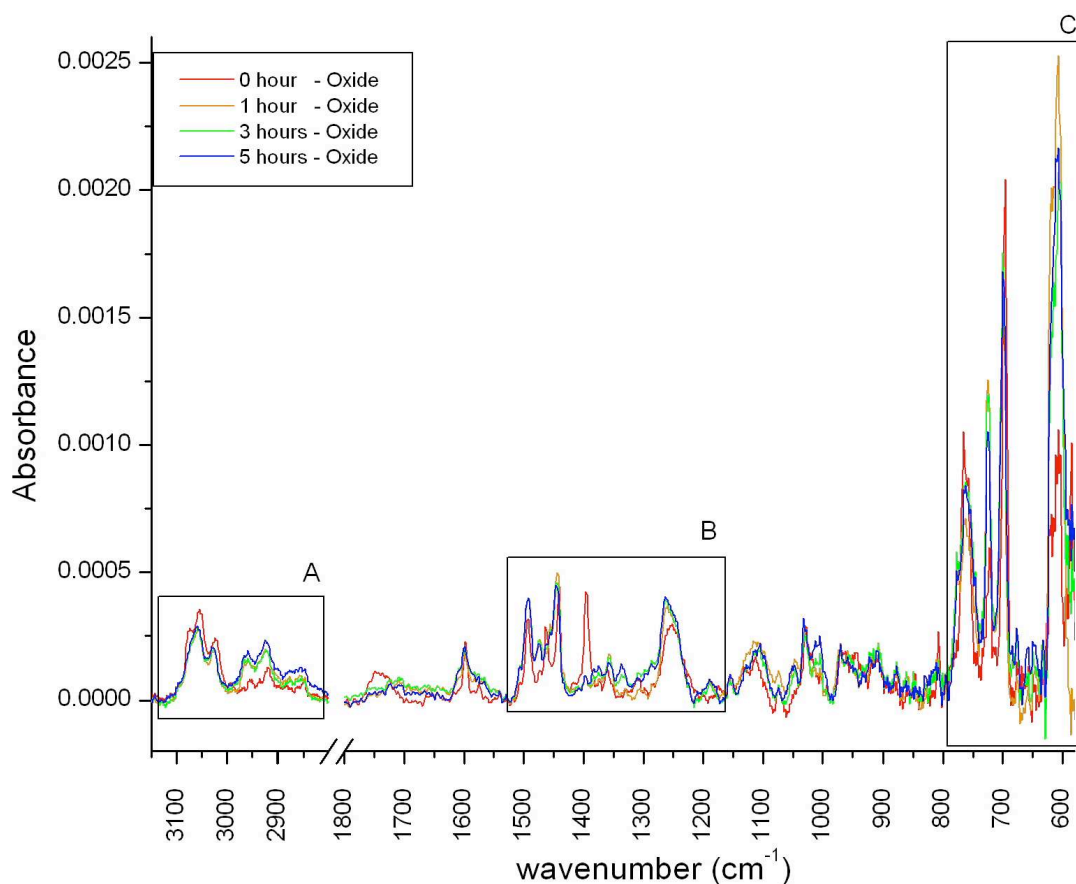


Figure 3.2. Photo-oxidation progression of a spun rubrene film. All spectra are referenced to the same substrate oxide.

Boxed regions in Figure 3.2 are enlarged for clarity (Figures 3.2A - 3.2C). The red line represents the rubrene film before oxidation conditions, while the orange, green, and blue lines represent the rubrene film at different time points throughout photo-oxidation. We hypothesize peak changes that indicate an accumulation of endoperoxide groups on the rubrene-spun film. We therefore look for evidence of: 1,4-disubstituted aromatic molecules, C-O-O-C bond formation, and a decrease in aromatic features.

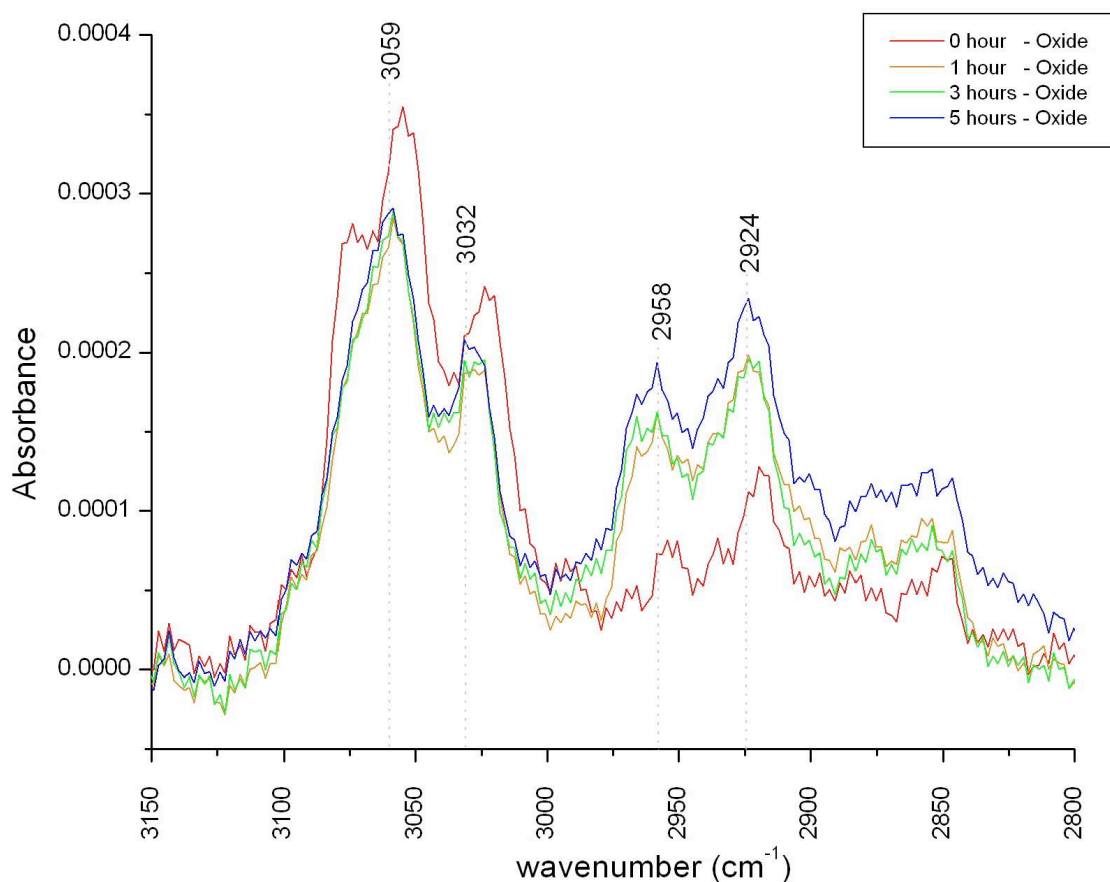


Figure 3.2A. High-wavenumber region of a photo-oxidation progression.

Peaks at 3031 cm^{-1} and 3058 cm^{-1} decreased in intensity and shifted to higher wavenumbers (Figure 3.2A). These changes are attributed to a decrease in CH aromatic stretching with oxygen insertion. The aromatic molecule must lose two sp^2 hybridized C=C double bonds and become a cyclic sp^3 C-C alkyl chain for oxygen insertion to take place. Increasing high-wavenumber peaks support the formation of cyclic alkyl chains observed at 2924 cm^{-1} (alkyl CH_2 asymmetric stretch) and 2958 cm^{-1} (alkyl CH_3 asymmetric stretch). The corresponding symmetric mode (usually less intense than the asymmetric mode) is presumed in the broad growing peaks at 2850 cm^{-1} and 2870 cm^{-1} .

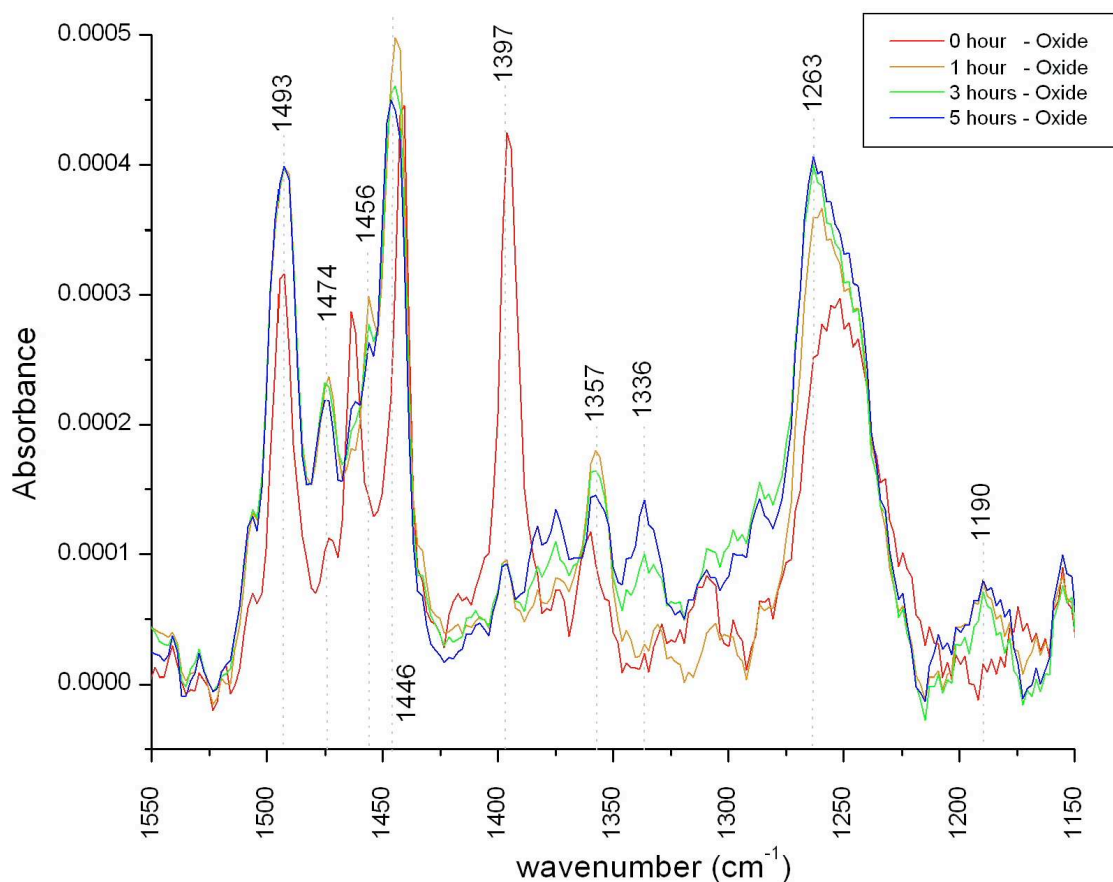


Figure 3.2B. Mid-wavenumber region of a photo-oxidation progression.

Increasing wavenumbers at 1190 cm^{-1} and 1262 cm^{-1} (a region indicative of aromatic ring in-plane bending) as photo-oxidation takes place can be attributed to a polar ring substitution (Socrates 2001), p. 164). Peaks at 1190 cm^{-1} and $1466\text{--}1493\text{ cm}^{-1}$ generally agree with those in a previous study (Ristic 1985). According to a study of anthracene oxidation, the peak at 1262 cm^{-1} and a shoulder at 1245 cm^{-1} are assigned to C-O stretching (Karyakin 1961). The decrease in 1392 cm^{-1} may be due to CH_2 wagging (NIST, dioxane, 1397 cm^{-1}) associated with the loss of the aromatic double bonds.

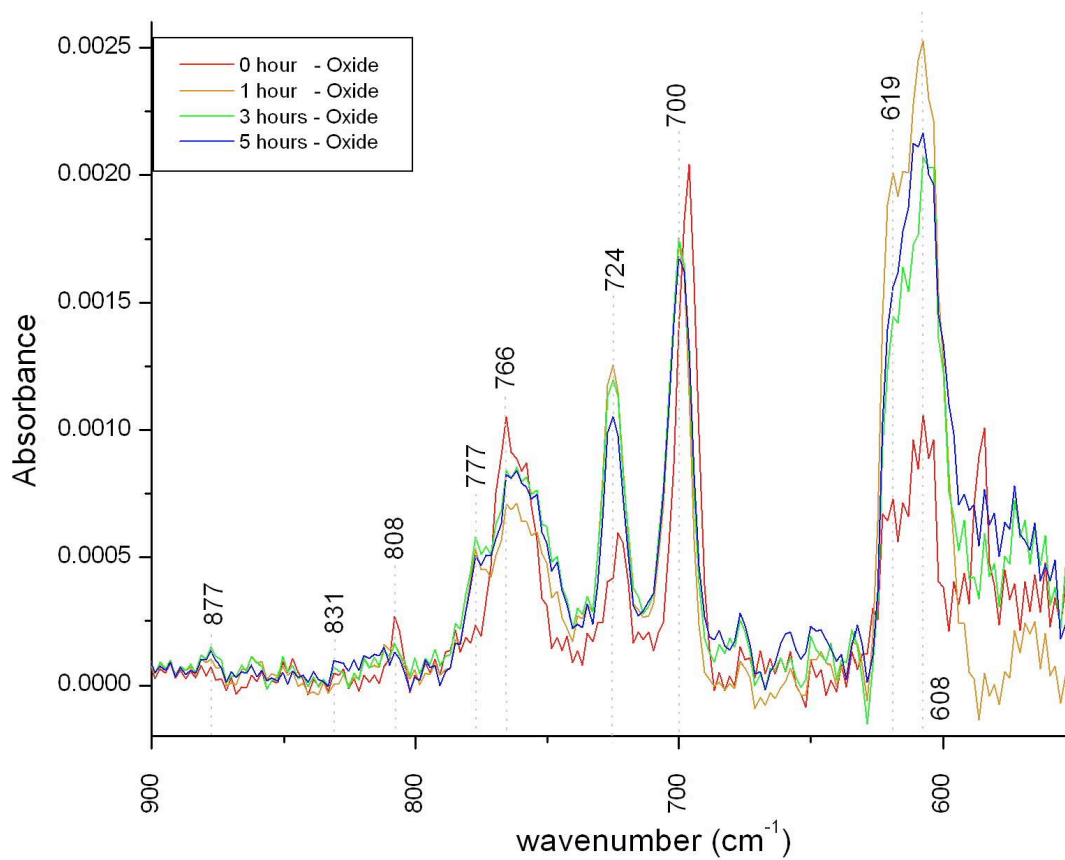


Figure 3.2C. Low-wavenumber region of a photo-oxidation progression.

Out-of-plane C-H deformation peaks in the low wavenumber region decrease at 700 cm^{-1} and 766 cm^{-1} and increase at 608 cm^{-1} , 619 cm^{-1} , 700 cm^{-1} , and 724 cm^{-1} . The increasing peaks at 608 cm^{-1} and 619 cm^{-1} are due to the polar aromatic 1,4-disubstituted benzene ring substitution (Socrates 2001), p. 164). Decreasing peaks at 700 cm^{-1} and 766 cm^{-1} may be due to a reduction of aromatic C-H out-of-plane bending as a result of the kink formed in the molecule upon oxygen insertion (Käfer and Witte 2005). Increasing peaks at 724 cm^{-1} (O-O), 832 cm^{-1} (C-O), and 877 cm^{-1} (O-O-C) agree with the results of Kapetanaki and Varotsis (Kapetanaki and Varotsis 2001). Our results are summarized in Table 3.4.

Wavenumber	Assignment	Reference
2924, 2958	Cyclic hydrocarbon	(Socrates 2001)
1190, 1262	Aromatic ring in-plane bending with polar ring substitution	(Socrates 2001), p. 164)
1245, 1260	C-O stretching	(Karyakin 1961)
877	O-O-C, out-of-plane C-H bending	(Kapetanaki and Varotsis 2001)
832	C-O bend, out-of-plane C-H bending	(Kapetanaki and Varotsis 2001)
724	O-O stretch, out-of-plane C-H bending	(Kapetanaki and Varotsis 2001)
608, 619	Aromatic ring out-of-plane bending with polar ring substitution	(Socrates 2001), p. 164)

Table 3.4 Increasing-Intensity Peak Assignments During Rubrene-Endoperoxide Formation

Evidence of endoperoxide formation indicates that there were oxidation sites available on a spun rubrene surface. We hypothesize that when rubrene endoperoxide bonds with trichlorosilane, these peaks will reverse their formation trend. The peaks in Table 3.4 will be a reference for understanding rubrene-silane bonding that will be explored in Chapters 4 and 5.

3.4 Pentacene

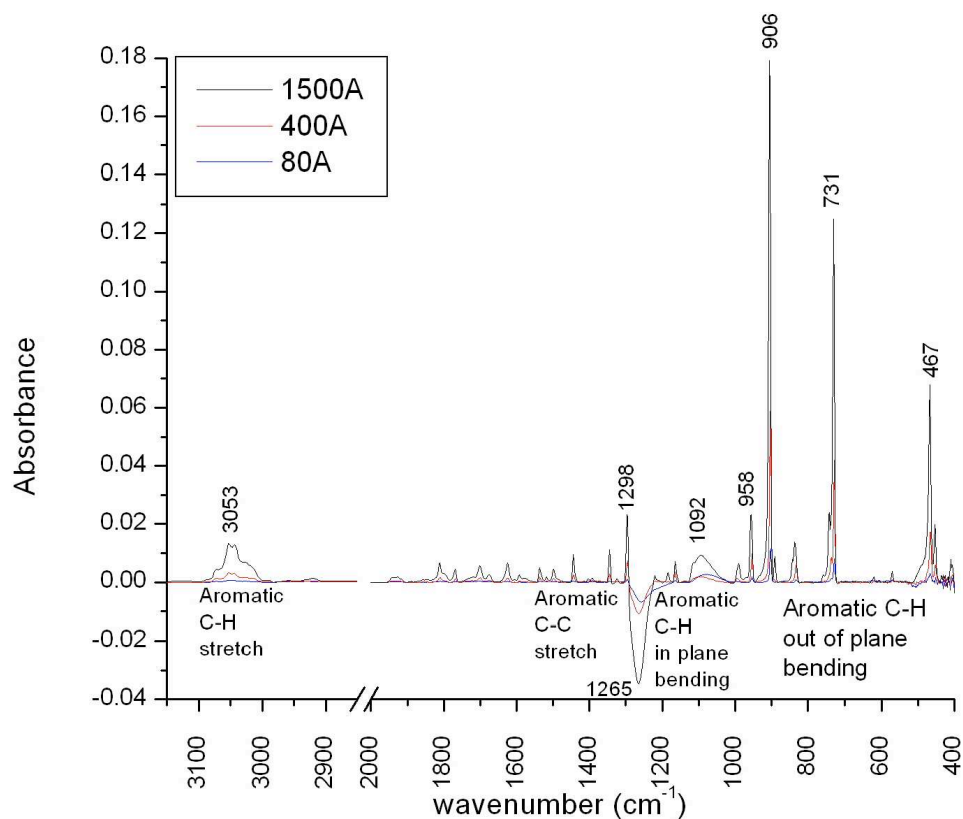


Figure 3.3. Infrared absorption spectra of several pentacene films referenced to their substrate oxide.

Double-side polished, moderately doped silicon (111) wafers (0.75" by 1.46") with 1218 Å of thermally deposited silicon dioxide (SiO_2) were cleaned with acetone, methanol, water, and a 90°C piranha solution soak (7:3 sulfuric acid: hydrogen peroxide) for ten minutes before being used as pentacene and C6 substrates. Pentacene thin films were deposited on both sides of the wafers, using successive room temperature depositions at 0.1-0.3 Å/s. The infrared spectra show scaling peak intensity with increasing film thickness (Figure 3.3). Peaks are labeled for the 1500 Å film. The same general assignments are made as with rubrene. Pentacene peaks previously shown in the literature at 907 cm^{-1} , 1296 cm^{-1} , 1443 cm^{-1} , 3053 cm^{-1} , and 3073 cm^{-1} match the spectra

we observe (Hosoi, et al. 2005; Weidkamp, et al. 2003). Largest peaks seem to shift with film intensity (Table 3.5).

1500 Å	400 Å	80 Å
906 cm^{-1}	904 cm^{-1}	903 cm^{-1}
731 cm^{-1}	729 cm^{-1}	729 cm^{-1}
467 cm^{-1}	465 cm^{-1}	467 cm^{-1}

Table 3.5. Largest peaks for three pentacene films shift to lower wavenumbers as film thickness decreases.

The peak at 906 cm^{-1} decreased more during a polarization experiment than those at 467 cm^{-1} and 731 cm^{-1} . These out-of-plane CH aromatic bending modes decrease more dramatically than with rubrene in a polarization study. Out-of-plane aromatic C-H bending was then presumed fairly perpendicular to the surface, meaning that the molecular axis was fairly parallel to the surface.

Poly-crystalline grains forming $\sim 150 \text{ nm}$ macroscopic dendrites (containing herringbone-arranged molecules) are typically produced by pentacene sublimation on room temperature samples (Knipp, et al. 2003; Ruiz, et al. 2004).

3.5 C6

Organic materials containing phenyl and thiophene aromatic groups have been demonstrated as functional semiconducting layers in organic field-effect transistors. Studies on the effects of terminal alkyl substitutions on aromatic molecular orientation and field-effect mobility have demonstrated that terminal hexyl substitutions enhance long-range order (Garnier, et al. 1993). We investigated the molecular packing of a similar molecule containing a bithiophene core and hexanol termination. We anticipated overlap of the rigid π -conjugated aromatic cores; however, the effects of polar hydroxyl termination on molecular structure is uncertain (Jiang and et 2003). We are particularly interested in such effects, because of their anticipated role in sensing applications. Also, hexyl end-groups on phenylene-thiophene aromatic cores have been shown to enhance long-range molecular ordering and thus increase organic transistor field-effect mobility (Jiang and et 2003; Mushrush, et al. 2003; Uslu, et al. 2004). Therefore, it would be interesting to determine the crystal structure of this class of molecules to determine the effect of adding peripheral substituents to a core molecule. We study the bonds of 5,5'-bis(4-hydroxyhexyl-phenyl)-2,2'-bithiophene (C6) sublimated films, using Infrared absorption spectroscopy (IRAS) and then the structure of its powder with X-ray diffraction (XRD).

3.5.1 Studying C6 Thin Films using FTIR

The previously uncharacterized C6 material was initially designed by Dr. Howard Katz at Bell Laboratories and later synthesized again by Ali Afzali at IBM. Howard Katz's synthesis scheme utilized a stille-coupling reaction that produced a toxic

heavy metal byproduct. Dr. Afzali proposed an alternative Suzuki coupling and hydrolysis reaction.

Characteristic functional group peaks were validated in sublimated C6 thin-film spectra, using FTIR. A total of 500Å of C6 was sublimated on both sides of a silicon wafer, using the same vacuum and preheating procedure as for pentacene. The sublimation temperature of HOC6PTTPC6OH was $\sim 374^{\circ}\text{C}$ at 60AC amps for a high rate of deposition ($\sim 1.0 \text{ Å/s}$).

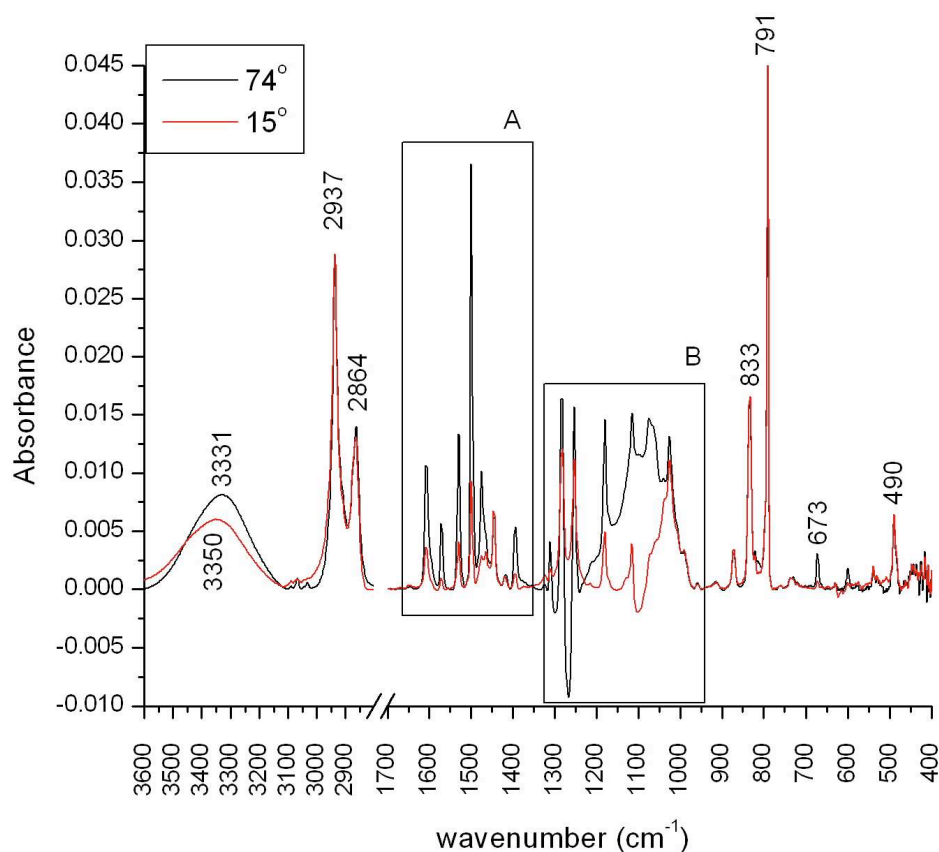


Figure 3.4. Infrared absorption spectrum of a C6 film referenced to their substrate oxide at two angles of incidence: 74° and 15° with respect to the surface normal.

Wavenumber	Interpretation	Reference
3331	OH stretch	NIST, methanol, 3328 NIST, phenol, ~3350
2937	CH ₂ asymmetric stretch	(Socrates 2001)
2864	CH ₂ symmetric stretch	(Socrates 2001)
833	C-O stretch in-plane ring bend	NIST, dioxane, 837 NIST, thiophene, 839
791	CH out-of-plane bending	(Socrates 2001)
490	O-C-C bending	NIST, dioxane, 490

Table 3.6 C6 High and Low Wavenumber Peak Assignments

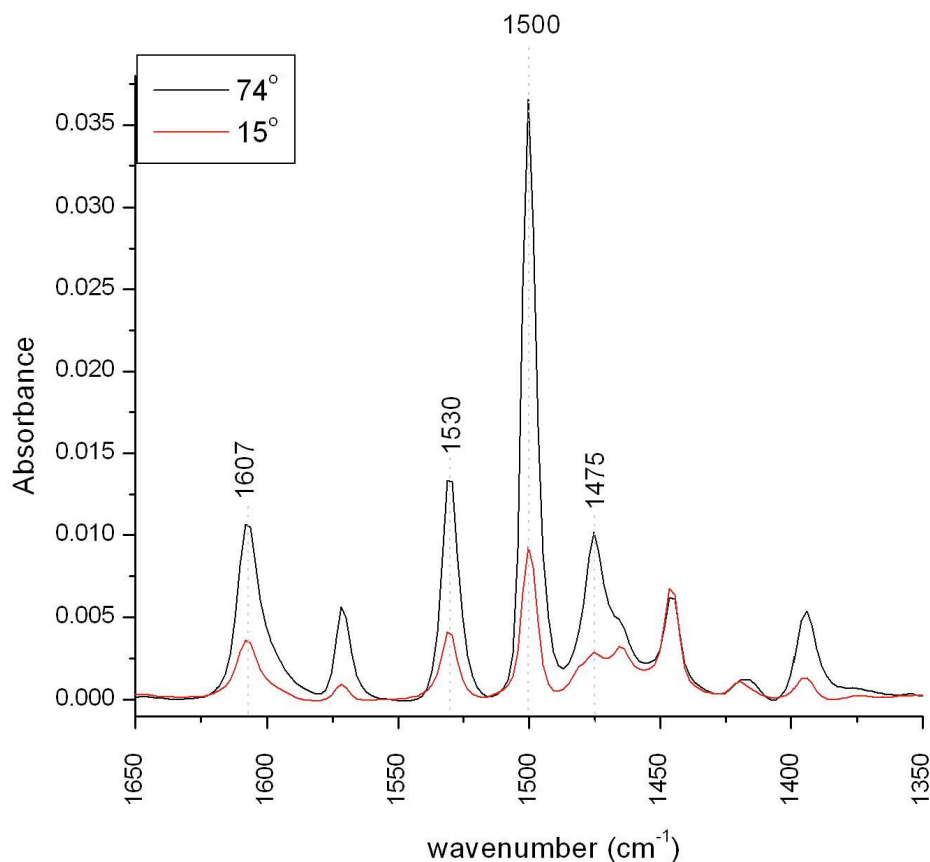


Figure 3.4A. Box A of the infrared absorption spectrum of a C6 film referenced to their substrate oxide at two angles of incidence: 74° and 15° with respect to the surface normal.

Wavenumber	Interpretation	Reference
1607-1530	C=C aromatic stretching or overtone band	(Socrates 2001)
1500	In-plane thiophene bend	NIST, thiophene, 1504 NIST, phenol, ~1500
1475	CH ₃ bending	NIST, methanol, 1477

Table 3.7 C6 Mid-Wavenumber Peak Assignments

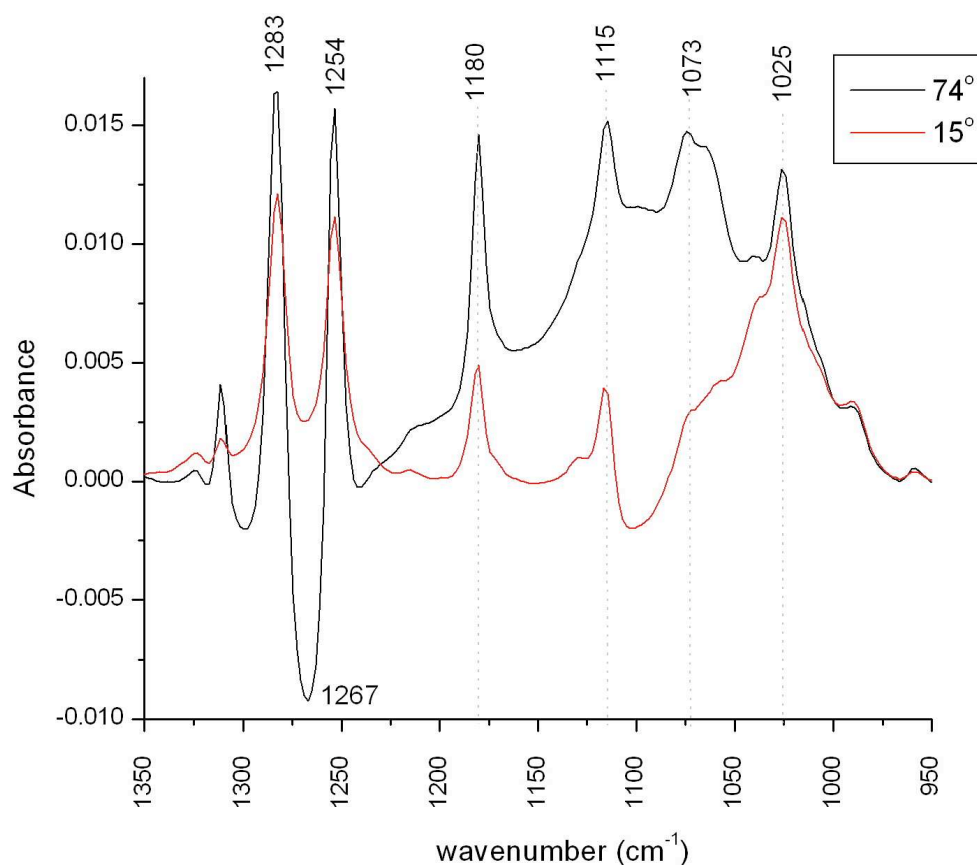


Figure 3.4B. Box B of the infrared absorption spectrum of a C6 film referenced to their substrate oxide at two angles of incidence: 74° and 15° with respect to the surface normal.

Wavenumber	Interpretation	Reference
1283-1254	CH ₂ twist	NIST, butane, 1257
1290-1025	Aromatic ring C-H bending	(Socrates 2001), p. 159

Table 3.8 C6 Mid-Wavenumber Peak Assignments

The differences in polarization intensity from 1073 cm^{-1} to 1180 cm^{-1} may be due to baseline correction, since sharp peaks appear on top of a broad base. Therefore, it appears that the most dramatic polarization effect is visible from 1475 cm^{-1} - 1607 cm^{-1} and can be attributed to in-plane C-H aromatic bending or skeletal vibrations. Therefore, the molecular axis is probably nearly perpendicular to the surface, although extensive calculation is necessary to determine the exact angle.

3.5.2 Studying C6 Powder and Thin Films With X-Ray Diffraction

The structural implications of extensive alkyl and/or polar, end-group functionalization have not yet been uncovered due to the difficulty involved in preparing single crystals. Structure analysis is difficult, because unlike smaller unsubstituted molecules, which readily crystallize and can be analyzed by single-crystal XRD, longer molecules require powder XRD and a more complex analysis. Therefore, we utilized powder X-ray methods to solve the crystal structure of the longer molecule, C6, not available in their single-crystal form. Powder spectra are used to assign a unit cell, index Bragg peaks, find layer spacing, and determine the molecular ordering that takes place within the unit cell. The layer spacing is then compared with that of a sublimated thin film.

3.5.2.1 Experimental Details

The C6 powder diffraction data were collected at the Brookhaven National Laboratories National Synchrotron Light Source (NSLS), with beam line X22A, a wavelength of $\lambda=1.2084\text{\AA}$, and a four-circle goniometer. A powder pellet sample was mounted on a glass cover slip. Diffraction data were acquired at different beam intensities. Exposure time was used to verify that the beam did not damage the sample. Powder averaging was achieved while each two-theta data point was collected.

3.5.2.2 Results

Refik Kortan used the Crysfire, Fox, and PowderCell programs to analyze the collected data shown in Figure 3.5 (Favre-Nicolin and Cerny 2002; Reck, et al. 1994; Shirley 1984; Stokes, et al. 2007). The unit cell predicted by peak fitting were as

follows:

$a = 33.1 \text{ \AA}$, $b = 7.5 \text{ \AA}$, $c = 5.9 \text{ \AA}$, and $\beta = 96.2^\circ$ (Figure 3.6). The difference data and the expanded range inset show that the observed differences are mainly due to peak profile shapes. The data exhibit non-uniform peak broadening, indicating the presence of characteristic defects or frozen alkyl chain disorder. For instance, the (020) peak at 18.576° is significantly broader than predicted, suggesting a specific defect that disrupts the long-range order along this axis. The first Bragg peak of the powder diffraction, used to calculate a layer spacing of 33.1 \AA , was larger than our predicted length of 32 \AA , based on a basic molecular model. This may be due to trapped solvent in the powder.

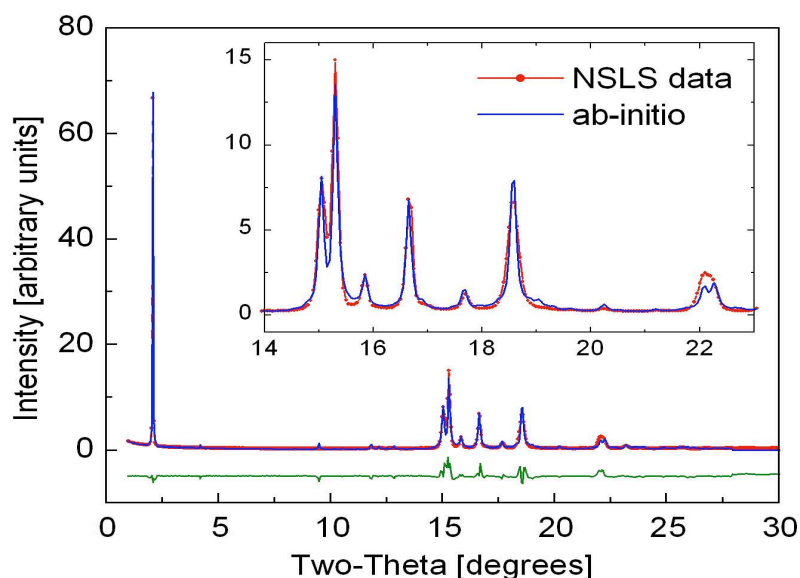


Figure 3.5. NSLS data fit, using Monte Carlo modeling. Six rigid groups, two alkyls and four rings modeled the structure to fit the line. The bottom curve shows the difference of the fit and experimental data.

A herringbone molecular arrangement was also found from the data fitting. The herringbone structure revealed by Monte Carlo analysis of the C6 powder is similar to that found in $\alpha\omega$ DH6T thin films (Garnier, Yassar, Hajlaoui, Horowitz, Deloffre, Servet, Ries and Alnot 1993). The 2PTTP2 crystal, evaluated by Theo Siegrist, shows a similar

distorted hexagonal array whose neighboring molecules are displaced along the long axis (Stokes, Kortan, Amy, Katz, Chabal, Kloc and Siegrist 2007). Close packing in the powder form, possibly in a herringbone arrangement, may allow for increased orbital overlap that would promote enhanced conductivity.

Molecular packing within the unit cell predicts phenyl and thiophene neighboring rings point toward one another. Our modeling predicted unusually short distances between neighboring molecules. The bond lengths of $\text{H-S} = 2.18\text{\AA}$, $\text{H-C} = 2.67\text{\AA}$, and $\text{C-S} = 3.25\text{\AA}$, indicate possible H-bonds between the molecules.

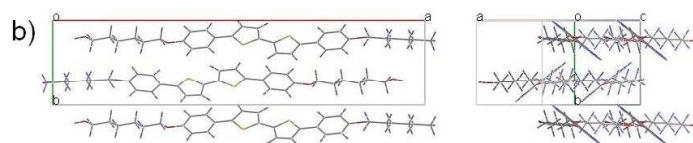


Figure 3.6. A herringbone arrangement predicted by ab-initio Monte Carlo simulations.

The distorted hexagonal array structure of C6 is shown in Figure 3.6 (Stokes, Kortan, Amy, Katz, Chabal, Kloc and Siegrist 2007). Molecules in neighboring (101) planes are shifted along the long axis of the molecule such that one of the thiophene rings of molecules in one layer is approximately aligned with one of the phenyl rings of the neighboring layers. The molecules are interdigitated, with partial mixing of the aliphatic and aromatic groups. X-ray diffraction comparing alkoxy-substituted (oxygen near core aromatics) alpha 6T showed that oxygen substitution into the side chain does not influence the intermolecular packing or molecular length of edge on molecules nearly perpendicular to the substrate, with smooth interconnected microcrystalline grains of 20-50 nm (Katz, et al. 1998).

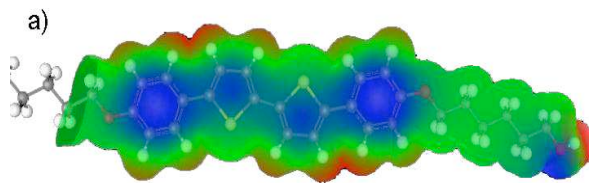


Figure 3.7 Model of the C6 electrostatic surface potential.

The calculated electrostatic potential of a planar molecule, as shown in Figure 3.7, finds a charge distribution on the aromatic part similar to that of 2PTTP2 (Stokes, Kortan, Amy, Katz, Chabal, Kloc and Siegrist 2007). In the ab-initio-calculated structure, some of the most electronegative phenyls are aligned with the hydrogen atoms of the neighboring thiophenes, strongly suggesting that the most electropositive part is now shifted towards the thiophene rings. This can be explained by the separation of phenyl hydrogen atoms from the plane of the thiophene hydrogen atoms, or a rotation of the phenyl rings.

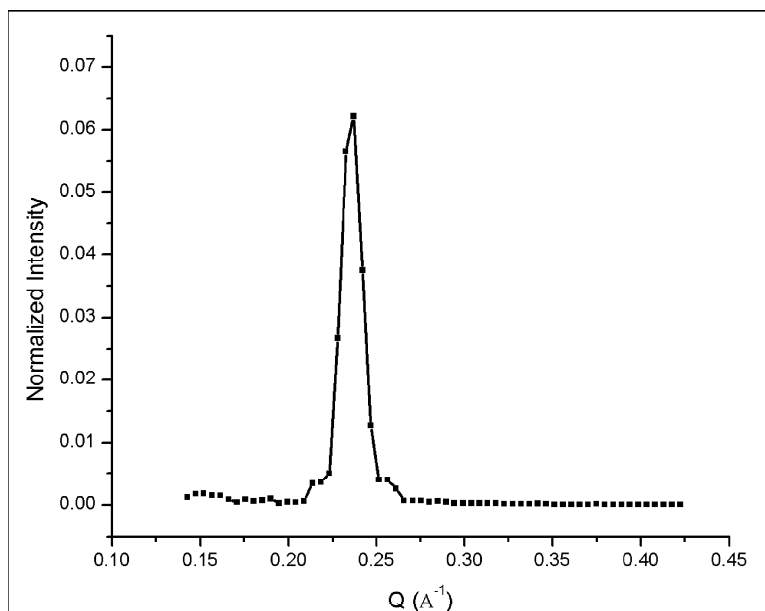


Figure 3.8. X-ray diffraction of a 250Å C6-sublimated film. The low-angle peak is shown with the incident beam attenuated.

Now that we had an idea of the type of packing found in the powder form, the material was sublimated onto silicon wafers for thin-film analysis. Thin, sublimated films of the organic semiconductor were studied with XRD. The C6 layer spacing was calculated by analyzing the first prominent peak $d=2\pi/Q$ as 26.5\AA , which was smaller than that predicted by the powder diffraction data (Figure 3.8 (Stickle, et al. 2005)). This may be explained by the removal of trapped solvent during the vacuum sublimation process. Assuming an end-to-end arrangement and some in-plane ordering, we estimated the tilt angle from the surface normal to be 34.2° . A second peak (not shown) not found in the powder spectrum was present in the organic thin film at $q=0.471\text{\AA}^{-1}$. This suggests that the substrate and/or sublimation process is causing different film morphology compared with the powder form.

3.5.3 Atomic Force Microscopy

We evaluated C6 thin-film topology because morphology could play a role in the organic semiconductor vapor sensitivity. The top of a 500\AA C6 film deposited at 1\AA/s exhibits polycrystalline islands, when analyzed with close-contact vibrating mode AFM (Figure 3.9).

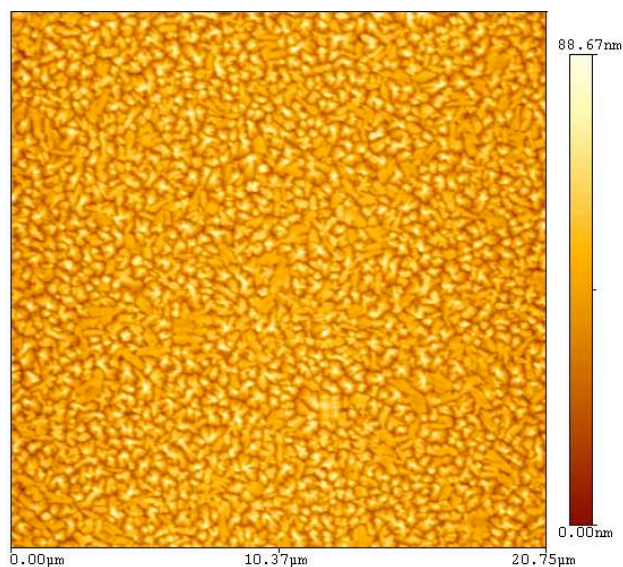


Figure 3.9. Two-dimensional AFM images of 500 Å C6 film deposited at 1 Å/s (Sommakia 2007).

3.5.4 Current - Voltage Performance

Average field-effect mobility, using various C6 thin-film thicknesses and deposition rates are summarized in Table 3.9 (Sommakia 2007). 500 Å C6 films, deposited at ~ 1 Å/s, were chosen for their highest field-effect mobility (Sommakia 2007).

Thickness (Å)	Deposition Rate (Å/sec)	Field-Effect Mobility ($\text{cm}^2\text{V}^{-1}\text{s}^{-1}$)
250	0.13	0.0017 ± 0.0007
250	0.72	0.0022 ± 0.0007
500	0.18	0.0017 ± 0.0009
500	0.8	0.0023 ± 0.0008

Table 3.9. Field-effect mobility of C6 thin films at two thicknesses and deposition rates.

3.6 Summary

Infrared absorption spectroscopy analysis of rubrene thin-film peaks indicates the expected aromatic modes including: C-H bending, C-H stretching, skeletal vibrations, and overtone combinations. Polarization experiments indicated skeletal and in-plane C-H aromatic bending modes were fairly perpendicular to the surface. Although we expected the rubrene film to be amorphous, the polarization result suggests core rubrene ring

planes were fairly perpendicular to the substrate. The exact angle requires further calculation, since the absorption intensity was not completely removed at normal incidence.

Rubrene photo-oxidation requires molecular excitation of rubrene and molecular oxygen. Using a white lamp and oxygen overpressure revealed growing, shifting, and decreasing rubrene peak intensities over time. Aromatic C-H stretching peaks at 3031 cm^{-1} and 3058 cm^{-1} decrease as double bonds are broken by oxygen insertion, forming cyclic aryl groups indicated by growing peaks at 2850 cm^{-1} and 2870 cm^{-1} . Polar oxygen ring substitution caused an increase in wavenumber for peaks at 1190 cm^{-1} and 1262 cm^{-1} . The peak at 1262 cm^{-1} with a shoulder at 1245 cm^{-1} might be related to C-O stretching during endoperoxide formation, according to a single study on anthracene photo-oxidation (Karyakin 1961). Some out-of-plane C-H aromatic bending peaks (700 cm^{-1} and 766 cm^{-1}) decrease, perhaps due to a rubrene-plane kink, while others increase (608 cm^{-1} , 619 cm^{-1} , 700 cm^{-1} , and 724 cm^{-1}), most likely due to polar aromatic 1,4 di-substitution. Increasing peaks at 724 cm^{-1} (O-O), 832 cm^{-1} (C-O), and 877 cm^{-1} (O-O-C) agree with the results of Kapetanaki and Varotsis.

Pentacene thin film peaks occurred in regions with similar assignments to rubrene. Polarization studies indicate that pentacene is fairly parallel to the surface.

A C6 thin-film peak analysis reveals the expected thiophene, hexanol, and phenyl functional groups. A polarization study of the film indicates that skeletal and out-of-plane vibrations are nearly perpendicular to the substrate surface. This was supported by XRD measurements of the sublimated thin-film layer spacing. Comparing the layer spacing with the expected molecular length estimated the tilt angle from the surface

normal to be 34.2° . Experimental powder XRD data fitting revealed C6 and 2PTTP2 molecules show a similar distorted hexagonal array whose neighboring molecules are displaced along the long axis according to ab-initio Monte-Carlo structure simulations. This shows that the hydroxyl substitution does not greatly influence the packing structure of a molecular powder. Molecular layers were interdigitated with partial mixing of the aliphatic and aromatic groups.

Now that rubrene's infrared spectra have been interpreted, we can use these findings as a basis for understanding the functionalization of rubrene films with trichlorosilane films in Chapters 4 and 5. Rubrene, C6 and pentacene film interpretations provide a basis for understanding film perturbations upon exposure to solvents, which we explore in Chapter 6.

3.7 References

1. Atkins, P., *Physical Chemistry*. 2 ed.; WH Freeman & Co.: San Francisco, 1982.
2. Bowen, E. J.; Steadman, F., The photo-oxidation of rubrene. *Journal of the Chemical Society (Resumed)* **1934**, 1098-1101.
3. Bratschkov, C., FTIR spectroscopy study of the UV irradiation induced changes in an anthracene containing copolymer. *European Polymer Journal* **2001**, 37, 1145-1149.
4. Favre-Nicolin, V.; Cerny, R., *Journal of Applied Crystallography* **2002**, 35, 734.
5. Garnier, F.; Yassar, A.; Hajlaoui, R.; Horowitz, G.; Deloffre, F.; Servet, B.; Ries, S.; Alnot, P., Molecular engineering of organic semiconductors: design of self-assembly properties in conjugated thiophene oligomers. *Journal of the American Chemical Society* **1993**, 115, (19), 8716 - 8721.
6. Hamon, M. A.; Stensaas, K. L.; Sugar, M. A.; Tumminello, K. C.; Allred, A. K., Reacting soluble single-walled carbon nanotubes with singlet oxygen. *Chemical Physics Letters* **2007**, 447, (1-3), 1-4.
7. Hochstrasser, R. M.; Ritchie, M., The photoformation and thermal decomposition of rubrene peroxide. *Transactions of the Faraday Society* **1956**, 52, 1363 - 1373.
8. Hosoi, Y.; Okamura, K.; Kimura, Y.; Ishii, H.; Niwano, M., Infrared spectroscopy of pentacene thin film on SiO₂ surface. *Applied Surface Science* **2005**, 244, (1-4), 607-610.
9. IUPAC, *Compendium of Chemical Terminology*. 2 ed.; 1997.
10. Jiang, W.; et, a., *Polymer Preprints* **2003**, 44, 372.
11. Käfer, D.; Witte, G., Growth of crystalline rubrene films with enhanced stability. *Physical Chemistry Chemical Physics* **2005**, 7, 2850 - 2853.

12. Kapetanaki, S.; Varotsis, C., Fourier Transform Infrared Investigation of Non-Heme Fe(III) and Fe(II) Decomposition of Artemisinin and of a Simplified Trioxane Alcohol *Journal of Medicinal Chemistry* **2001**, 44, (19), 3150-3156.
13. Karyakin, A. V., Spectroscopic Determination of Peroxy Compounds During Photochemical Oxidation. *Russian Chemical Reviews* **1961**, 30, (8), 460-469.
14. Katz, H. E.; Laquindanum, J. G.; Lovinger, A. J., Synthesis, Solubility, and Field-Effect Mobility of Elongated and Oxa-Substituted π -Dialkyl Thiophene Oligomers. Extension of "Polar Intermediate" Synthetic Strategy and Solution Deposition on Transistor Substrates. *Chemistry of Materials* **1998**, 10, (2), 633 - 638.
15. Knipp, D.; Street, R. A.; Völkel, A.; Ho, J., Pentacene thin film transistors on inorganic dielectrics: Morphology, structural properties, and electronic transport. *Journal of Applied Physics* **2003**, 93, (1), 347.
16. Mitrofanov, O.; Lang, D. V.; Kloc, C.; Wikberg, J. M.; Siegrist, T.; So, W.-Y.; Sergent, M. A.; Ramirez, A. P., Oxygen-Related Band Gap State in Single Crystal Rubrene. *Physical Review Letters* **2006**, 97, 166601.
17. Mushrush, M.; Facchetti, A.; Lefenfeld, M.; Katz, H. E.; Marks, T. J., Easily Processable Phenylene-Thiophene-Based Organic Field-Effect Transistors and Solution-Fabricated Nonvolatile Transistor Memory Elements. *Journal of the American Chemical Society* **2003**, 125, (31), 9414 - 9423.
18. Nardello, V.; Marti, M.-J.; Pierlot, C.; Aubry, J.-M., Photochemistry without Light: Oxidation of Rubrene in a Microemulsion with a Chemical Source of Singlet Molecular Oxygen (1O_2 , 1Dg). *Journal of Chemical Education* **1999**, 76, 1285.
19. Otomo, A.; Otomo, S.; Yokoyama, S.; Mashiko, S., Photochemical stability of encapsulated laser dyes in dendritic nanoboxes against singlet oxygen. *Optics Letters* **2002**, 27, (11), 891-893.
20. Podzorov, V.; Sysoev, S. E.; Loginova, E.; Pudalov, V. M.; Gershenson, M. E., Single-crystal organic field effect transistors with the hole mobility $\sim 8 \text{ cm}^2/\text{V s}$. *Applied Physics Letters* **2003**, 83, 3504.
21. Reck, G.; Kraus, W.; Nolze, G. *GECEM-15*, Dresden, Germany. Munich: R. Oldenbourg, Verlag, 1994.
22. Ristic, The endoperoxide form of rubrene and spectrochemical investigation of its formation kinetics. *Journal of the Serbian Chemical Society* **1985**, 50, (6), 307 - 311.
23. Ruiz, R.; Mayer, A. C.; Malliaras, G. G.; Nickel, B.; Scoles, G.; Kazimirov, A.; Kim, H.; Headrick, R. L.; Islam, Z., Structure of pentacene thin films. *Applied Physics Letters* **2004**, 85, 4926.
24. Shirley, R., *Measurement and Analysis of Powder Data from Single Solid Phases*. Clarendon Press: Oxford, 1984; p 411-437.
25. Socrates, G., *Infrared and Raman Characteristic Group Frequencies Tables and Charts*. 3 ed.; John Wiley & Sons Ltd.: West Sussex, England, 2001; p 347.
26. Sommakia, S. Electrical and Topological Characterization of Thin Film Transistors Based on a Novel Organic Semiconductor for Biosensing Applications. Rutgers, the State University of NJ, New Brunswick, 2007.
27. Stickle, M.; Rivillon, R. K. S.; Bao, Z.; Katz, H.; Chabal, Y. In *Structural Characterization of a Functionalized Organic Semiconductor*, MRS Proceedings, San Francisco, CA, 2005; San Francisco, CA, 2005; p I3.16.

28. Stokes, M. A.; Kortan, R.; Amy, S. R.; Katz, H. E.; Chabal, Y. J.; Kloc, C.; Siegrist, T., Molecular Ordering in Bis(phenylenyl)bithiophenes. *Journal of Materials Chemistry* **2007**, 17, 3427-3432.
29. Sundar, V. C.; Zaumseil, J.; Podzorov, V.; Menard, E.; Willet, R. L.; Someya, T.; Gershenson, M. E.; Rogers, J. A., Mobility Anisotropy in Rubrene Single Crystals Probed by Monolithic Elastomeric Stamps. *Science* **2004**, 303, 1644.
30. Uslu, F.; Ingebrandt, S.; Mayer, D.; Böcker-Meffert, S.; Odenthal, M.; Offenhäusser, A., Label-free fully electronic nucleic acid detection system based on a field-effect transistor device. *Biosensors and Bioelectronics* **2004**, 19, (12), 1723-1731.
31. Weidkamp, K. P.; Hacker, C. A.; Schwartz, M. P.; Cao, X.; Tromp, R. M.; Hamers, R. J., Interfacial Chemistry of Pentacene on Clean and Chemically Modified Silicon (001) Surfaces. *Journal of Physical Chemistry B* **2003**, 107, (40), 11142 -11148.

CHAPTER 4: AN IN-SITU INVESTIGATION OF OCTYLTRICHLOROSILANE BONDING WITH RUBRENE

4.1 Abstract

In-situ Infrared Absorption Spectroscopy (IRAS) and real-time electrical measurements are used to study rubrene bonding with octyltrichlorosilane (OTS) responsible for rubrene, single-crystal surface current enhancement. The rubrene-silane bond was investigated, with IRAS of rubrene thin films spun-cast on SiO₂-terminated silicon wafers and KBr pellets exposed to OTS vapors in a vacuum cell. Monitoring the rubrene, single-crystal surface current increase during the co-deposition validated the OTS exposure method. To distinguish SiO₂-silane bonding peaks from silane networking and silane-rubrene bonding peaks, the infrared absorption spectra of OTS on rubrene and OTS on SiO₂ were compared. In-situ chemical and real-time electrical saturation were loosely correlated.

4.2 Introduction

Self-assembled monolayers are often used to modify interfaces in organic electronic devices. For example, alkyl or perfluorinated SAMs produce hydrophobic surfaces that are used to avoid cellular adhesion, protein adsorption and movable MEMS component sticking in humid environments (Bhushan, et al. 2006; Knieling, et al. 2007). The bonding of trichlorosilanes to organic semiconductors determines the proximity of the SAM tail to the underlying surface. The proximity of electron- withdrawing groups in the SAM, such as perfluorinated-alkyltrichlorosilane (FTS) deposited by gas phase bonded to rubrene single crystals, is thought to be responsible for the increase in crystal surface current (Calhoun, et al. 2008). However, validation of rubrene-silane bonding

has not been fully explored. A greater understanding of silane bonding events can allow further optimization of their influence on rubrene crystal surface current. A recent demonstration of enhanced rubrene crystal surface current, using FTS SAMs, allowed sufficient surface current for vapor sensing (Banga and Yarwood 1995; Calhoun, Sanchez, Olaya, Gershenson and Podzorov 2008). Since the reversible polar solvent vapor sensing was only possible with enhanced surface current, the study of the trichlorosilane bonding with the rubrene crystal could contribute to an understanding of both the surface current enhancement mechanism and subsequent chemisensing applications (Calhoun, Sanchez, Olaya, Gershenson and Podzorov 2008).

Although the surface charge accumulation is dominated by the SAM tail dipole, it is not sufficient for a sustained current enhancement effect (Calhoun, Sanchez, Olaya, Gershenson and Podzorov 2008). Therefore, covalent bonding through the FTS and OTS trichlorosilane group is a hypothesized requirement for surface current enhancement which has not yet been fully explored (Calhoun, Sanchez, Olaya, Gershenson and Podzorov 2008). The silane bonding of FTS and OTS with SiO₂ substrates and silica has been determined using Infrared Absorption Spectroscopy (IRAS) (Banga and Yarwood 1995; Banga, et al. 1996; Dong, et al. 2006; Kulkarni and Vijayamohanan 2007; Li 2007; Wen, et al. 2008). FTS and OTS monolayers on SiO₂ have been characterized by ellipsometry to reveal monolayer thicknesses of 1.6nm and 2.6nm, respectively (Geer, et al. 1994; Wasserman, et al. 1989). FTIR-ATR and X-ray diffraction (XRD) have characterized the area covered per OTS molecule: $0.21 \pm 0.03\text{nm}^2$, and 0.30nm^2 for FTS (F8) (Banga, Yarwood, Morgan, Evans and Kells 1996; Wasserman, Tao and Whitesides 1989). IRAS has not yet been applied to extend FTS and OTS studies to understand

rubrene bonding with OTS or FTS. IRAS should have sufficient sensitivity for silane-rubrene bonding, since it has revealed submonolayer-bonding events on silicon surfaces that typically support $10^{15} \text{ cm}^{-2} \text{ monolayer}^{-1}$ absorbing molecules (Michalak, et al. 2006).

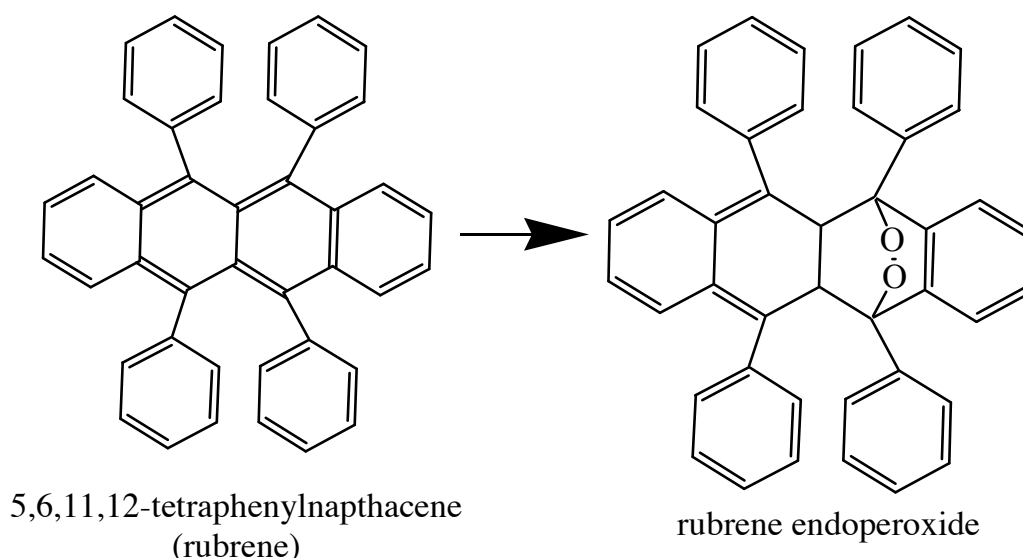


Figure 4.1. The oxidation of the rubrene surface provides a probable silane-bonding site.

The endoperoxide species that forms upon exposure of the rubrene surfaces to atmospheric oxygen and ambient light, which could provide a reactive site for trichlorosilanes, is shown in Figure 4.1. However, infrared transmission of a rubrene crystal does not allow a sufficient infrared beam to reach the detector with acceptable signal intensity. Also, ATR would distort the region of low wavenumber that may coincide with expected SAM bonds to the rubrene. Thin, spun-cast rubrene films on SiO_2 provide sufficient signal for transmission geometry infrared analysis of rubrene surface chemistry with SAMs. Since the rubrene film is not conductive, single crystals are used to correlate the effect of SAMs on surface current. However, spun-cast films on SiO_2 terminated substrates may provide SiO_2 bonding sites for SAM at penetrative film defects. This requires the differentiation of silane bonding with the substrate SiO_2 from

bonding with rubrene. The basis for that distinction begins with reviewing infrared absorption of substrate-bonding peaks concerning alkyl-trichlorosilane hydrolysis and subsequent reactions of alkyl-silanol with SiO_2 substrates. Since to our knowledge the octyltrichlorosilane molecular bonding with SiO_2 substrate has not been thoroughly evaluated with infrared absorption spectroscopy, its substrate bonding modes are predicted from previous studies of similar molecules.

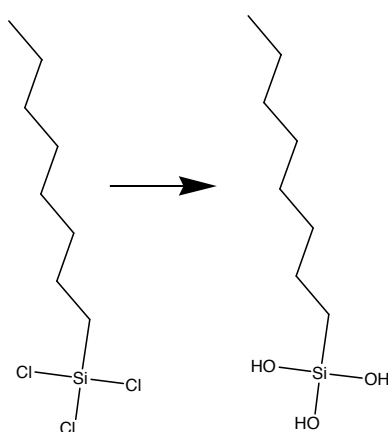


Figure 4.2. Alkyl-trichlorosilane hydrolysis to alkyl-silanol in the presence of water.

Trichlorosilanes undergo hydrolysis in the presence of water on the substrate surface or in solution to trichlorosilanols as shown in figure 4.2. Hydrochloric acid is produced as the chlorine groups are replaced with hydroxyl groups that can then act as bonding sites to SiO_2 or rubrene. Fourier transform infrared spectroscopy (FTIR) studies of alkyltrichlorosilanes and (perfluoroalkyl) trichlorosilanes surface-bonding events on silicon surfaces have shown that water is required for the hydrolysis of the trichlorosilane head group to silanol which bond to the surface and each other (Banga and Yarwood 1995). Surface water would have a peak at 1620 cm^{-1} consumed upon reaction with trichlorosilane; however, it is not often seen due to the additional noise associated with subtracting out ambient water bands in the beam path (Tripp, et al. 1993). The Si-Cl bond

should produce very weak stretching bands at 574 cm^{-1} and 473 cm^{-1} ; however, their intensity is so close to the noise that it was difficult to detect any remaining unhydrolyzed groups (Tripp and Hair 1995). The choice of infrared detector is a tradeoff of infrared spectral range and signal/noise ratio. The increased signal-to-noise ratio of the infrared MCT/A detector is favored over the DTGS detector that is capable of measuring the extended range between $400 - 600\text{ cm}^{-1}$ as well as the reduced experimental time of using the MCT/A.

The expected modes for silane interaction with a thin film on SiO_2 (which must be distinguished from the proposed rubrene bonding at the rubrene endoperoxide group (Si-O-cyclic C)) are: silane bonding with the substrate SiO_2 (Si-O-Si(s)), silane bonding with neighboring silane in a network (Si-O-Si), silane self-polymerization (Si-O-Si), and body/tail modes (C-C, CH_3 , or CH_2 modes). Previous studies of similar silanol interaction with SiO_2 substrates provide a basis for distinguishing these modes.

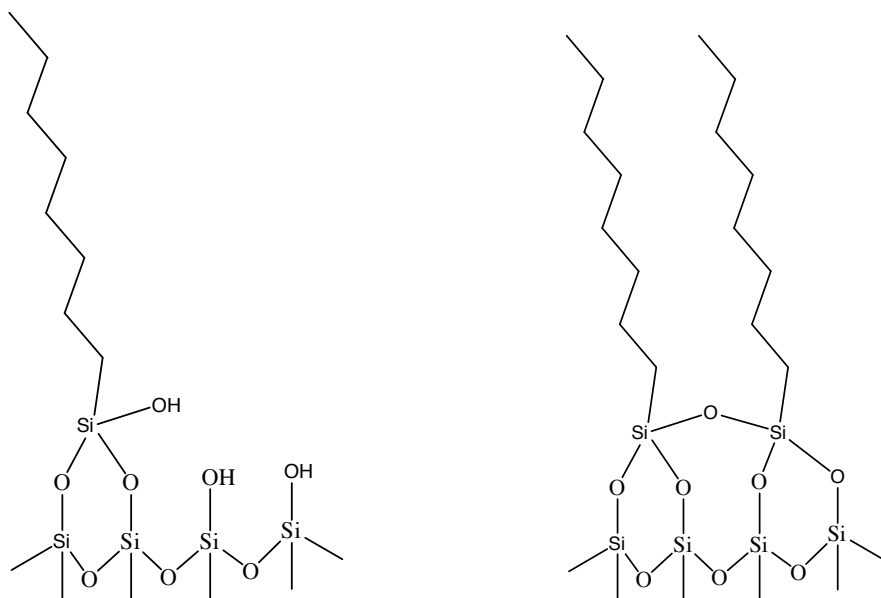


Figure 4.3. Silanol bonding with the substrate SiO_2 (Si-O-Si): and network formation.

Information of the substrate-bonding peak position shown in figure 4.3 for trichlorosilanes varies. This may be due to peak position sensitivity to a different tail group or substrate SiO₂ thickness. The infrared absorption peak for hydrogen-terminated trichlorosilane bonding with a SiO₂ substrate depends on the SiO₂ thickness according to the oxide TO and LO phonon vibrational modes (Li 2007). Hydrogen-terminated trichlorosilane bonding with a 65 Å thermal SiO₂ wafer (with characteristic phonon modes: 1253 cm⁻¹, 1064 cm⁻¹), has shown Si-O-Si(s) at 1256 cm⁻¹, while a thin chemically grown oxide (phonon mode: 1225 cm⁻¹) has a corresponding substrate bonding mode at 1236 cm⁻¹ (Li 2007), Ch. 3, p.31). This was supported by the addition of water to the solution deposition (Li 2007), Ch. 3, p. 36, 42). Additional water caused methyl trichlorosilane polymerization and a scaling of all peaks except the peak attributed to interfacial substrate SiO₂ bonding near 1230 cm⁻¹ with a corresponding TO mode at ~1060 cm⁻¹. This was attributed to H-trichlorosilane thin surface SiO₂ bonding (Li 2007), Ch. 3, p. 36, 42).

Butyl monochlorinated silane was shown by Meng Li to have a substrate SiO₂ bond at 1099 cm⁻¹ as well as a peak at 1261 cm⁻¹, which he attributed to the alkyl chain CH₃ rocking mode (Li 2007), Ch. 3, p.45). As the trichlorosilane carbon chain length increases from 4 to 12 to 18, Meng Li shows that a peak at 1261 cm⁻¹ shifting to lower wavenumber (Li 2007), Ch. 3, p. 13, 45), which may actually be attributed to the surface SiO₂ bond instead of the chosen 1099 cm⁻¹ whose position is maintained. However, this 1100 cm⁻¹ substrate SiO₂ bonding assignment is in closer agreement with a methyltrichlorosilane silica substrate bonding mode assignment made by Tripp and Hair at a broad 1060 cm⁻¹ peak (Tripp and Hair 1995). Therefore, the addition of methyl

groups shifts substrate SiO₂ bonding with lower wavenumbers, which may be between 1100-1060 cm⁻¹.

A negative peak at 975 cm⁻¹ and/or 1230 cm⁻¹ indicates covalent silane bonding with a thin substrate SiO₂ (Li 2007) , Ch. 3, p. 45, (Morrow, et al. 1975). Consumption of surface hydroxyl groups can be followed at 3747 cm⁻¹; however, it is often confounded with ambient moisture and purge contaminant peaks in our lab (Tripp, Veregin and Hair 1993; Tripp and Hair 1995). A broad peak at 921 cm⁻¹ has been observed for propped unreacted silane molecules according to Si-OH stretching (Wen, Maoz, Cohen, Sagiv, Gibaud, Desert and Ocko 2008) and references therein).

The characteristic networking bond (shown in figure 4.3, right) of octadecyltrichlorosilane with a functionalized terminal group shows stretching modes around ~1100 cm⁻¹ ((Wen, Maoz, Cohen, Sagiv, Gibaud, Desert and Ocko 2008) and references therein). Tripp and Hair propose a networking feature at 1007 cm⁻¹ related to a strained methylsilanol network that is not seen in methylmonosilanols compared with methyltrisilanols (Tripp and Hair 1995). In an earlier work, Tripp and Hair observed networking modes at 1100 cm⁻¹, 822 cm⁻¹, and 450 cm⁻¹ for methylsilanol on IR window material (Tripp and Hair 1991). Hydrogen-terminated trichlorosilane networking has been attributed to features at 1060 and 1178 cm⁻¹ (TO,LO) by Meng Li (Li 2007), Ch. 3, p. 42). Octadecyltrichlorosilane investigated by Li showed peaks at 1061/1195 cm⁻¹ and 1108/1150 cm⁻¹ for TO/LO modes of Si-O-Si networking (Li 2007), Ch. 3, p. 52).

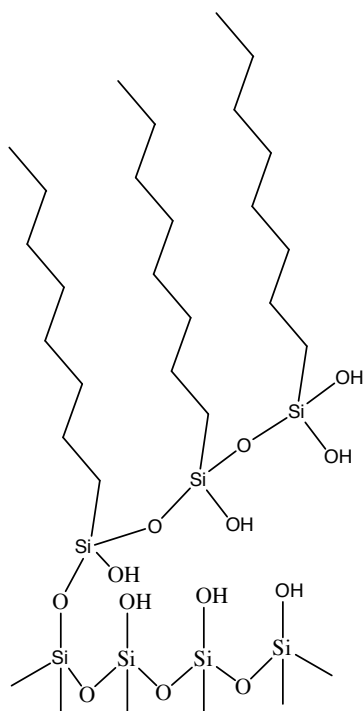


Figure 4.4. Silane self-polymerization (Si-O-Si).

Peaks of polymerized methyltrichlorosilanes shown in figure 4.4 have been explored by adding additional water to reveal the signature of networked silanes at 1023 cm^{-1} , 1063 cm^{-1} , 1115 cm^{-1} , 1178 cm^{-1} with overarching peak shifts from: $1085\text{ (monolayer) cm}^{-1}$ to $1070\text{ (poly) cm}^{-1}$ and $1170\text{ (monolayer) cm}^{-1}$ to $1157\text{ (poly) cm}^{-1}$ (Li 2007), Ch. 3, p. 41). Chains of Si-O groups can be expected to have peaks at 1050 cm^{-1} which broaden to $1100 - 1000\text{ cm}^{-1}$ as the chain length increases, and finally, for long-chain polymers, peaks at 1085 cm^{-1} and 1025 cm^{-1} can be observed ((Socrates 2001), p. 246; (Noll 1963)). Meng Li observed poly-OTS (C_{18}) features at $1095\text{ cm}^{-1}/1180\text{ cm}^{-1}$. Polymeric linear alkyl silanes show bands at 1080 cm^{-1} and 1020 cm^{-1} ((Tripp and Hair 1995): reference 20,21).

Body or tail modes (CH₃ or CH₂ modes):

Alkyl stretching modes can be expected in the 2800 - 3000 cm⁻¹ range. Also, the bending modes for CH₃ occur within 1465 - 1440 cm⁻¹ (asym) and 1390 - 1370 cm⁻¹ (sym, C-CH₃) ((Socrates 2001), p. 52). Si-C modes appear at 600 cm⁻¹ but are too close to the phonon mode of the silicon substrate to be considered reliable. The C-C stretch from the CH₃-C aliphatic tail can be expected at 720 cm⁻¹ (-(CH₂)_{n>3}), 760 - 770 cm⁻¹ (-CH₂CH₃), ((Socrates 2001), references 22, 20). Also, alkanes may show a doublet between 1175 - 1120 cm⁻¹, C-C-C stretching at 1100 - 1040 cm⁻¹, and 900 - 800 cm⁻¹ ((Socrates 2001), p. 54). Methylene groups of the alkyl chain in O(C₁₈)/TS should show bending mode peaks between 1117 - 1230 cm⁻¹ as well as a scissoring mode at 1465 cm⁻¹ (Wen, Maoz, Cohen, Sagiv, Gibaud, Desert and Ocko 2008).

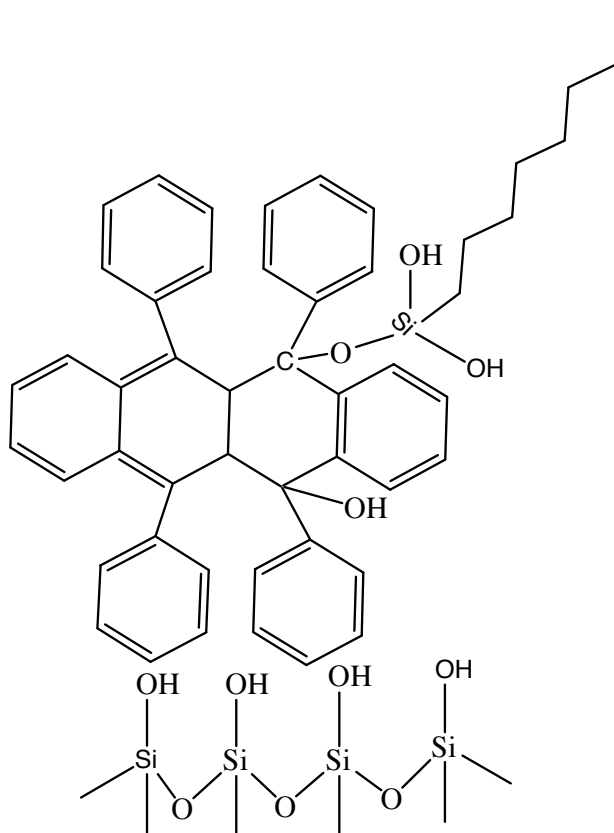


Figure 4.5. Silane bonding with the rubrene endoperoxide group (Si-O-C).

Silane bonding with rubrene is postulated to occur through an endoperoxide site on the rubrene material as shown in figure 4.5. The signature of this interaction, an Si-O-C bond, should be a peak at $\sim 1100\text{ cm}^{-1}$ and may shift slightly lower ($1080 - 1118\text{ cm}^{-1}$) as coverage increases ((Michalak, Rivillon, Chabal, Esteve and Lewis 2006), Michalak, et al. unpublished data). The Si-O-Aromatic peak is expected at $1090 - 1135\text{ cm}^{-1}$ (possibly several strong, sharp bands attributed to Si-O-C stretching) and $920 - 970\text{ cm}^{-1}$ (Si-O-stretching) (Socrates 2001), p. 33, 244). Negative or differential peaks in the regions of the original rubrene film such as those between 1600 cm^{-1} and 1450 cm^{-1} , are normally displaced by 20 cm^{-1} lower wavenumbers when bound to a silicon atom, and often include a peak at 1430 cm^{-1} ((Socrates 2001), p. 245); (Harvey and Nebergall 1962)). In addition, phenyl-silicon bonds have strong peaks at 1100 cm^{-1} that split into two when two phenyl groups attach to the one silicon atom (Socrates 2001), p. 245). Phenyl silicon bands are also present at 1030 cm^{-1} and 1000 cm^{-1} . Overtones are sometimes observed between $2000 - 1660\text{ cm}^{-1}$ (Socrates 2001), p. 245). However, due to the stability of the aromatic resonance and the presumed endoperoxide group in the rubrene structure, a silanol group (Si-OH) is expected to form a Si-O-C with the endoperoxide structure instead of a direct phenyl-silicon bond. Due to the differences in ionic strength, the C-O bond should be less intense than Si-O (Socrates 2001), p. 246). Methoxysilanes are known to have a Si-O-C stretch bond between 1090 cm^{-1} and 1060 cm^{-1} (Wen, Maoz, Cohen, Sagiv, Gibaud, Desert and Ocko 2008).

A unique vacuum gas-exposure cell that allows in-situ and real-time chemical and electrical measurements using infrared and surface current measurements was developed for this study to reveal the chemical bonding site of silanes with rubrene. Using a

vacuum below their vapor pressures, the deposition of the alkyl and perfluorosilanes allows greater control of the amount of water in the system than a solution-phase deposition. Vacuum deposition also insulates the reaction scheme from variations in environmental conditions, such as humidity, which are known to affect film quality. Vapor-phase SAM deposition provides even deposition that permeates any topology associated with surface roughness, and eliminates the use of solvent solutions and washing steps while achieving the same level of surface coverage and molecular ordering as a liquid deposition (Bhushan, Hansford and Lee 2006; Dong, Wang, Ng and Mao 2006). The vapor pressure of OTS is ~ 5 Torr at room temperature (20°C), which necessitates a vacuum level that can be achieved by sorption pumping (~ 5 mTorr). Furthermore, monitoring the current in real time and the infrared signature in situ, under dry nitrogen without exposing the sample to atmospheric conditions, facilitates studying functionalized surfaces while minimizing risk of a confounding secondary reaction or contamination. A custom gas cell integrated into the sample compartment of an infrared spectrometer provided a 5 mTorr vacuum, allowing vapor phase deposition of silanes. Gate valves isolated vapors from KBr windows that separate the gas cell from the spectrometer.

The rubrene bonding with OTS will be explored first by investigating the infrared peaks associated with gas phase OTS exposure to rubrene. Different OTS film exposure methods (bulk liquid deposition, saturated vapor pressure gas exposure, and unsaturated vapor pressure gas exposure) that are assumed to produce different surface coverage were used to differentiate body (scales with thickness) and interfacial chemical bonds (should not scale past surface saturation) between the OTS molecule and rubrene film, with OTS

bonding with the substrate SiO_2 . The basis for this investigation is the assumption that body molecules, such as the alkyl group of the OTS, should scale with the thickness of a film, while interfacial bonds between silane chlorine-converted hydroxyl groups bound to the rubrene or substrate interface should not scale past surface saturation. Bulk liquid deposition should saturate the interface as well as precipitate multilayers of OTS. An unsaturated vapor pressure gas exposure for 15 minutes should not provide sufficient time for a single monolayer of OTS. Therefore, a comparison of surface coverage can be made.

Extended OTS exposures were performed on rubrene and SiO_2 surfaces to distinguish peak assignments. Investigation of the OMS exposures to rubrene, whose single chlorine and two methyl terminal groups do not allow networking bonds to adjacent OMS molecules, should show no networking bonds while allowing rubrene bonds. A comparison of OMS and rubrene absorption spectra with those of OTS and rubrene should reveal the absence of a networking peak in the OMS spectra that is present in the OTS spectra. A comparison of successive OTS exposures determined the correlation between electrical and chemical saturation.

4.3 Materials and Methods

4.3.1 Chemicals

The following silanes were used as received from Gelest: n-Octyltrichlorosilane (OTS) (SIO6713.0), and n-Octyldimethylchlorosilane (OMS) (SIO6711.0). The xylene, isomers plus ethylbenzene solvent, was used as received from Sigma-Aldrich (247642).

4.3.2 Substrates

Silicon (100) wafers (0.68" by 1.46") with 65Å thermally deposited silicon dioxide (SiO₂) were cleaned with a 90°C piranha solution (7:3 sulfuric acid: hydrogen peroxide) for ten minutes. Chemically etching the thick native SiO₂ (65Å thick) and then reoxidizing the surface with a piranha solution was performed to prepare a thin SiO₂ (20Å thick). Samples were cleaned using acetone, methanol, water, and a 90°C piranha solution (7:3 sulfuric acid: hydrogen peroxide) soaking for ten minutes. To make a thin oxide, we continue with a 30-second aqueous 10% HF etch (90mL deionized water, 20 mL 49% hydrofluoric acid), followed by a 45-minute re-oxidation in 90°C piranha solution, blown dry with N₂ gas.

Using a hand press, 200mg KBr powder was pressed into transparent disks. The resulting pellets had the following dimensions: 0.025" thick, and 0.51" diameter.

4.3.3 Rubrene Solution Preparation

Rubrene was spun coat onto silicon wafers using a 0.5% weight solution of rubrene dissolved in xylenes and isomers of ethylbenzene, which are known to evaporate after a few seconds of spinning (Chang, et al. 2004). Weight % is defined as:

$$\frac{\text{weightOfSolute}(g)}{\text{totalSolutionVolume}(mL)} \times 100$$

As a simplification, assuming the material density is ~1g/mL (actual density of xylenes: 0.862 g/mL), the solution for double coating a silicon wafer begins with loading approximately 0.0060g of rubrene into a glass vial pre-cleaned with xylenes. To determine the amount of solvent to add for a 0.5 weight % solution, the following calculation is performed:

$$0.005 = \frac{0.0060 \text{ g}}{X_g}$$

$$X_g = 1.20 \text{ g}$$

Xylene was pipetted into vials to make the total solution mass 1.20 g. Sonication dissolved rubrene crystals to form a bright orange solution. To avoid oxidation, the solution was protected from light with foil and stored under nitrogen for use within one hour.

The rubrene solution is pipetted onto one face of a silicon wafer loaded into a spin coater (Laurell Technologies, WS-400B-6NPP-LITE). Samples were spun at 3000rpm for one minute. Since the infrared beam probes both sides of the sample in the transmission geometry, both sides of a sample need to be coated. Therefore, samples were turned over and the deposition process was repeated on the backside.

4.3.4 Silane Deposition

Rubrene-coated silicon samples were exposed to silane vapors under vacuum. From each SAM liquid shown in table 4.1, 25 g were loaded into separate, vacuumed stainless steel vessels in a nitrogen glove box. A sorption pump was used to reduce the gas cell pressure to 5mTorr. A six-inch exposure line between two valves in front of the filled vessel was also brought down to this pressure. Opening the valve closest to the liquid for 30 seconds allowed SAM vapor (OTS or OMS) to fill the six-inch space within the ¼-inch stainless steel tubing between the valves. Once the volume of vapor was trapped between the two valves, the sorption pump was isolated from the system by closing its dedicated valve. A front valve facing the gas cell was used to allow SAM vapors to backfill for 15 minutes. The SAM vapors were then pumped out for 25 minutes using a sorption pump. To ensure complete removal, the cell was backfilled three times

with nitrogen before returning the system to atmospheric pressure for FTIR scanning. A saturated vapor pressure exposure probably would have given a larger effect in a shorter amount of time. However, large-intensity body peaks may hide peaks of lower intensity attributable to interfacial bonds. Therefore, both dilute and extended exposure times are made to explore peak scaling to this effect.

To explore the effects of water, some surfaces were pre-treated with water before being exposed to SAM vapors. Water exposures were performed by backfilling the gas cell to ~200 mTorr with a small volume of deionized water vapor between two valves separated by two inches of ¼-inch stainless steel tubing.

4.3.5 Measurement of Films and Silanes

Using a Nicolet Magna-IR 760 spectrometer (OMNIC software version 6.2, firmware 4.10), with a signal gain of 1, a 4 cm^{-1} resolution from $4000\text{--}400\text{ cm}^{-1}$, 2 loops of 1000 scans averaged per experimental step, an aperture of 100 (unit-less), and a DTGS detector, FTIR measurements in the transmission geometry were made. For some scans, the MCT/A-enhanced detector was used, with similar settings with the exception of an aperture of 10 and 3 loops averaged with a range of $4000\text{--}650\text{ cm}^{-1}$. Samples were loaded into a custom gas cell with KBr windows sealing the beam path through a stainless steel exposure chamber in the sample compartment. Reference scans were taken under nitrogen purge in order to subtract out the initial film status, substrate, and background from the film after exposure. A reference infrared scan was taken before and after sample exposure under nitrogen. Subtracting the infrared measurements found before exposure from those after the exposure revealed positive peaks, indicating additional bonds were present in the substrate, while negative peaks indicated bonds removed from

the substrate. Data analysis was performed with OMNIC software version 6.1a, firmware 5.12 and Microcal Origin software version 6.0.

Electrical measurements were performed using a Keithley 4200 SCS connected to the gas cell through triaxial-to-BNC adapters that were attached to gold wires that led to two graphite contacts on opposite sides of a rubrene crystal. A constant 5V potential was set between the graphite contacts for all surface current measurements.

4.4 Results and Discussion

4.4.1 Gas cell background

Before discussion of results, some background effects of the gas cell system will be evaluated. A clean, thick SiO₂ sample, which has been loaded into the gas cell and pumped on by the dry and then sorption pump for five minutes, was used to determine if there was any system outgassing.

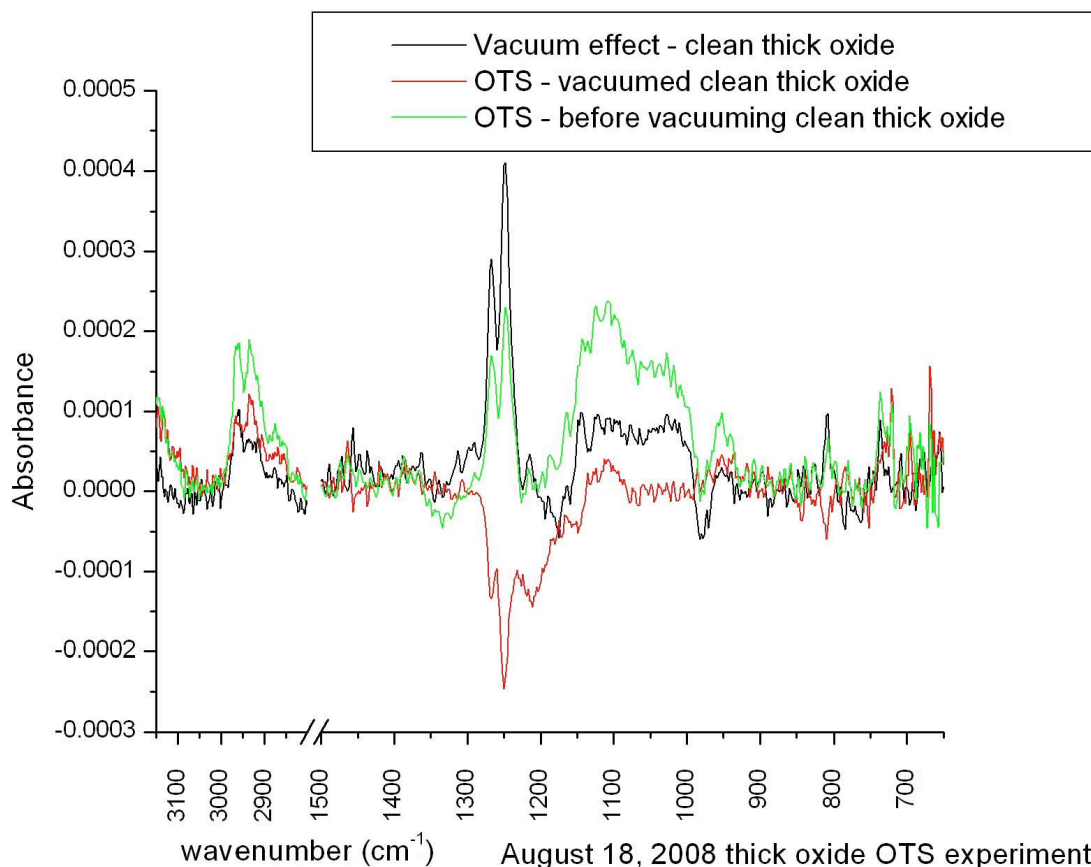


Figure 4.6. Detail of the effect of five minutes of dry pumping followed by sorption vacuuming on the clean thick oxide. Vacuumed oxide - fresh oxide (Black). OTS on oxide - vacuumed oxide (Red). OTS on oxide - fresh oxide (Green).

Active sorption pumping on a clean SiO_2 sample with a thick oxide for five minutes causes a growth of a doublet peak at 1248 cm^{-1} and 1267 cm^{-1} with an intensity of $\sim 4 \times 10^{-4}$ (Figure 4.6). Deposition of OTS causes a partial removal of these peaks along with a peak at 1212 cm^{-1} , with the addition of very broad growth between 1000 cm^{-1} and 1050 cm^{-1} . Therefore, the vacuum may be outgassing and depositing OTS or it could be a contaminant. However, it is unusual that the peak at 1250 cm^{-1} should be removed during the OTS deposition. If the OTS scan is reprocessed with the clean wafer before vacuuming, the green spectrum reproduces the other spectra in Figure 4.14. Therefore, for the sake of reproducibility, OTS spectra on SiO_2 are referenced to the clean substrate

before vacuuming. Also, the intensity of peaks between 1248 and 1267 cm^{-1} should be judged loosely. In the future, applying constant heat to the system or baking the system between each deposition could minimize this outgassing. However, a heated system would also require heating the sample to a temperature near the cell, which could change the reactivity of the surface compared to that of the single crystal. Therefore, we proceeded with a room-temperature system where out-gassing was minimized by baking before switching to new silane materials and regenerating the sorption pump periodically.

The stability of a rubrene thin film under vacuuming was also evaluated in real-time to determine the influence of the gas cell system on a background signal. Using the DTGS detector, four loops of 500 scans (ten minutes each) were recorded and compared (Figure 4.7).

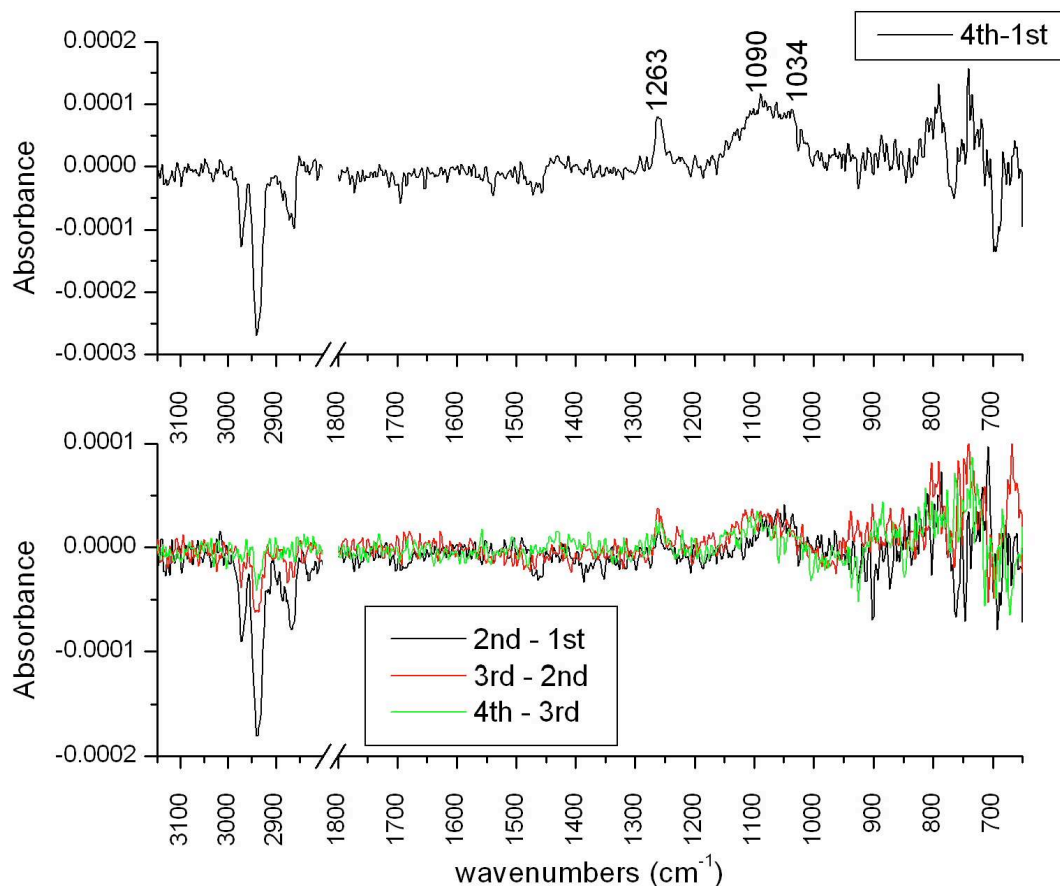


Figure 4.7. Scanning a spun rubrene film with the shutters open to observe changes over ten-minute pumping intervals. The overall 40-minute effect is in the top panel, while the incremental ten-minute changes are in the bottom panel.

Infrared spectra of a pumped rubrene film shows hydrocarbon were slowly removed at high wavenumber, with peak growth near 1263 cm^{-1} (Figure 4.7). Peaks at 1090 cm^{-1} , 1034 cm^{-1} , and 1263 cm^{-1} grew slowly to an intensity of $\sim 1 \times 10^{-4}$ over 40 minutes. This was less than what was shown for the bare SiO_2 reactivity in Figure 4.6. If the features were attributable to OTS outgassing, then the hydrocarbon tail should increase the region between 2800 cm^{-1} and 3000 cm^{-1} unless hydrocarbon removal from the windows (since they are not often pumped on) is greater than the hydrocarbon gain associated with OTS. This may be explained by removal of ethylbenzene solvent from the film. Therefore, over the course of 25 minutes used to remove OTS exposure vapors

from a bare oxide sample, one could expect $\sim 2 \times 10^{-4}$ peak intensity contribution from out gassing, and 5×10^{-5} for a rubrene surface.

A KBr pellet was also used as a substrate to study OTS bonding; this minimized interaction with the substrate in order to differentiate substrate and rubrene bonding peaks. The KBr substrate changes after vacuuming are presented in Figure 4.8.

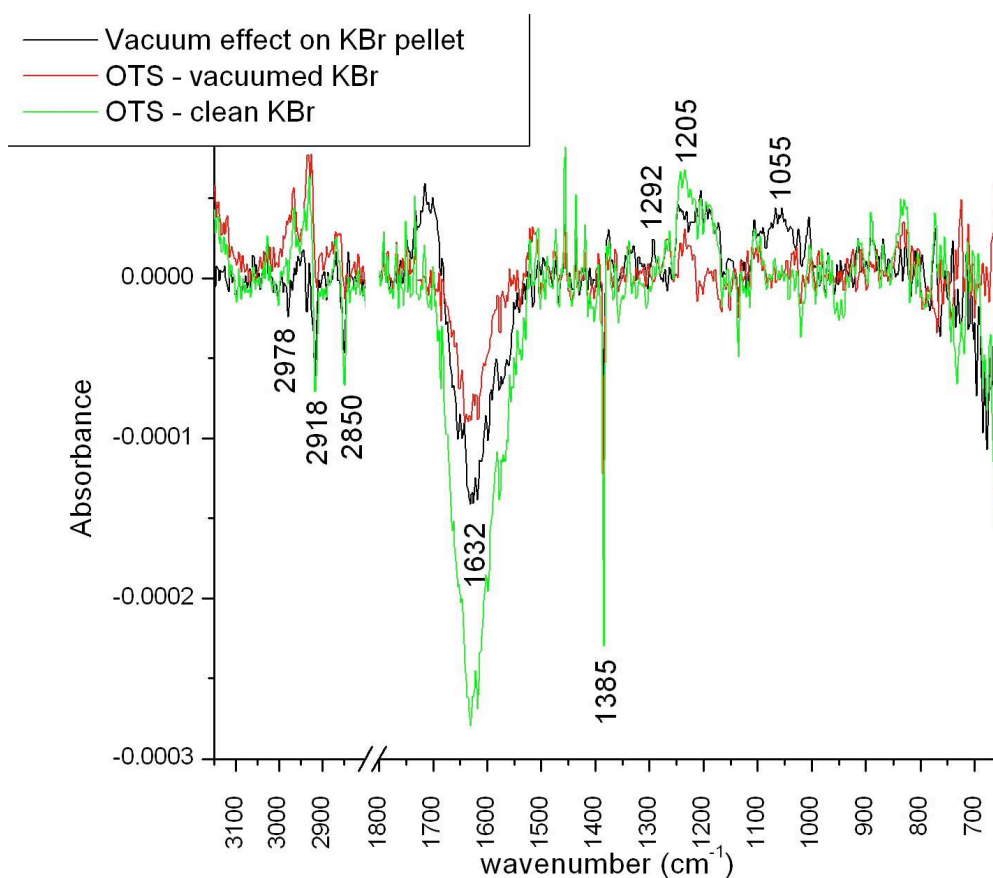


Figure 4.8. A KBr pellet was vacuumed (black) before OTS deposition, which is compared with the pre-vacuumed KBr spectra (green) and vacuumed KBr spectra (red).

Pumping on the KBr pellet removed quite a bit of water above 3100 cm^{-1} (not shown). This may be due to the hygroscopic nature of the pellet. The rest of the spectrum looks different than the pumping effect on SiO_2 and includes the removal of hydrocarbon. The loss of a peak at 1632 cm^{-1} is due to OH bending of physisorbed water

removed by the vacuum. The peak at 1385 cm^{-1} could be attributed to CH_3 bending (NIST, butane). Small peaks increase absorbance intensity between 1200 cm^{-1} and 1000 cm^{-1} on the order of 5×10^{-5} .

4.4.2 OTS deposition validation

Now that we have understood the background effects of the vacuum system on various substrates, we will strive to identify the rubrene-silane bond. First, we must investigate the silane on its own, using the gas cell deposition system on a SiO_2 substrate to identify body and substrate bonding modes so they can be ruled out as rubrene-bonding modes. This test will also validate the ability of the custom gas cell to deposit OTS without contamination. We will then test a less reactive KBr substrate to rule out any substrate-bonding modes.

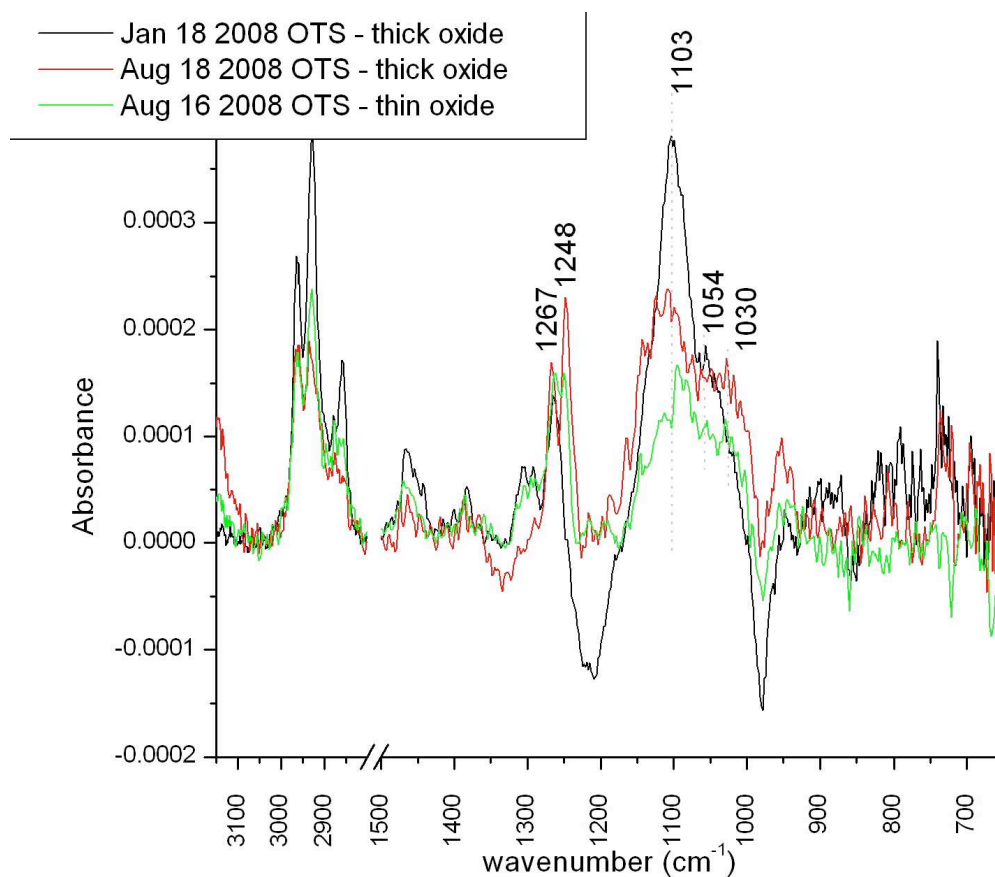


Figure 4.9. Sub-vapor pressure OTS on thick (native) and chemical (re-grown after etching) oxide.

The potential bonding modes for OTS on the substrate SiO_2 include: Si-O-Si(s) , Si-O-Si(n) , and Si-O-Si(p) . The red and black spectra shown in Figure 4.9 depict reproducibility of OTS deposition on thick SiO_2 substrates. The spectra of OTS on thin oxide show peaks at 1261 cm^{-1} , 1095 cm^{-1} , and $1045 - 1030 \text{ cm}^{-1}$. The peaks at 1045 cm^{-1} and 1099 cm^{-1} may represent the TO/LO modes of Si-O-Si (n) . These will be validated later through comparison with a monochlorinated silane. These peaks are in the broad range of one of two assignments proposed in Meng Li's thesis that identified networking of H-TCS at 1060 cm^{-1} and 1178 cm^{-1} as well as by Wen, et al., who referred to the peaks around $\sim 1100 \text{ cm}^{-1}$ as networking ((Li 2007), Ch.3, p. 52); (Wen, Maoz,

Cohen, Sagiv, Gibaud, Desert and Ocko 2008)). The discrepancy with Meng Li's thesis may be related to the increased hydrocarbon chain length in OTS compared with H-TCS.

Surface substrate bonding may be present at 1265 cm^{-1} . The negative peaks at 980 cm^{-1} and 1230 cm^{-1} may indicate the consumption of substrate Si-OH groups (Li 2007; Morrow, Cody and Lee 1975). Tripp and Hair suggest a methyltrichlorosilanol substrate-bonding peak is at 1060 cm^{-1} , which may be evident as a buried shoulder here in the broad peak at 1095 cm^{-1} . We conclude that OTS is bonded with the SiO_2 substrate and that there appears to be more networking than surface bonding.

Extensive polymerization is not evident here due to a lack of prominent peaks at 1157 cm^{-1} and 1070 cm^{-1} (Li 2007). The sharpness of the alkyl stretch peak 2927 cm^{-1} attributable to alkyl stretching modes, which is reduced at normal incidence in the OTS on SiO_2 spectra, shows that alkyl chains are well ordered. There appear to be more CH_2 groups than CH_3 as expected for a clean deposition according to the peak intensities surrounding the 2927 cm^{-1} peak. The peaks in Figure 4.9 (1030 cm^{-1} , 1054 cm^{-1} , 1103 cm^{-1} , 1248 cm^{-1} , and 1257 cm^{-1}) are now ruled out as possible rubrene bonding sites pursued in the next experiments.

4.4.3 OTS-rubrene bonding

To investigate rubrene-silane bonding, OTS material was co-deposited on a rubrene film and a crystal with graphite contacts. An increase in surface current on the rubrene crystal would suggest that an equivalent surface chemistry has taken place on the spun film assuming equilibrium throughout the gas cell. The basis of investigating rubrene-silanol bonding begins with the typical absorption spectrum of a spun rubrene

film on both sides of a silicon wafer like that shown in Figure 4.10. Peak assignments were presented in Chapter 3.

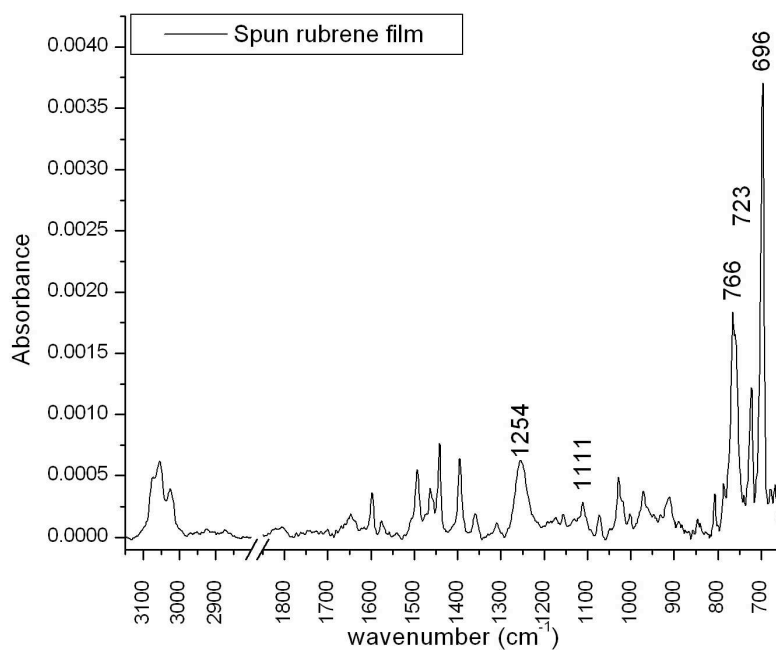


Figure 4.10. Spun rubrene thin film (March 7, 2008) - thick oxide substrate.

A linear current-voltage relationship was used to validate the crystal-graphite contacts. At 5V, the rubrene surface current was $\sim 1 \times 10^{-8}$ Amps. This current was sufficient to monitor subsequent surface current enhancement by self-assembled monolayer depositions, which validate silane exposure to both the single crystal and spun film.

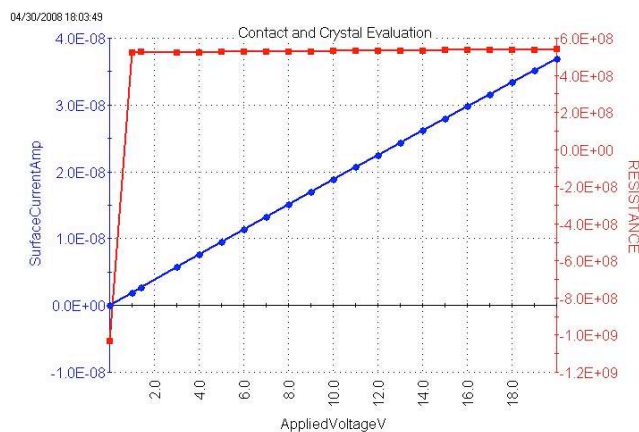
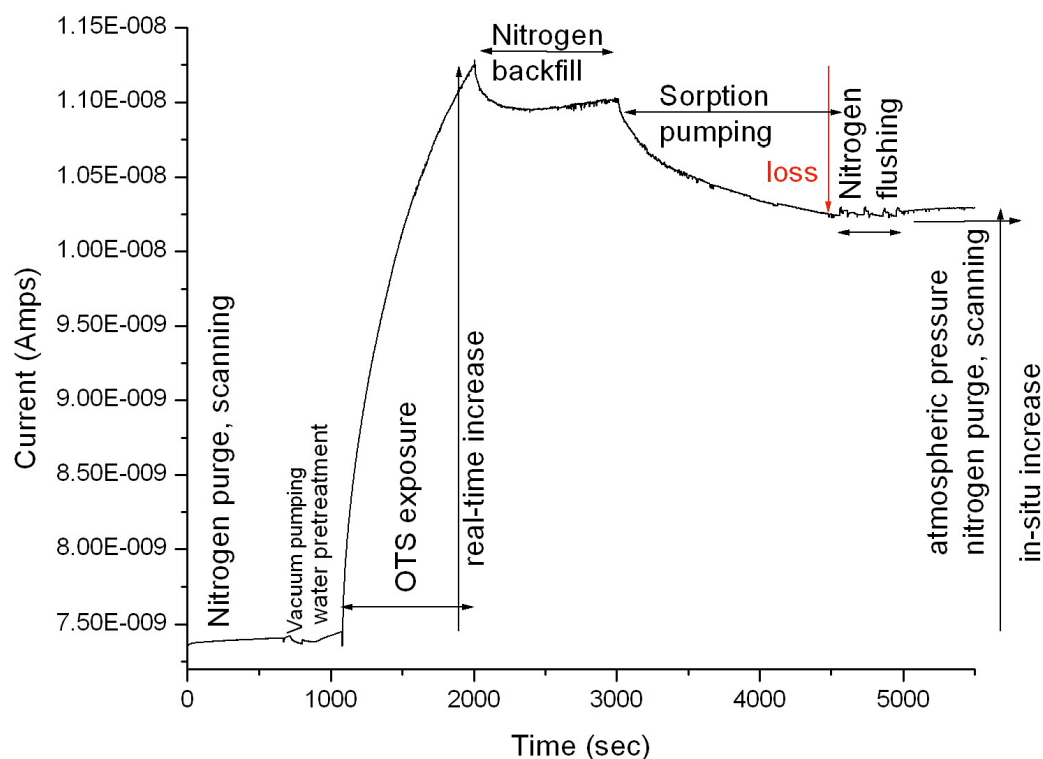


Figure 4.11. Validation of rubrene single-crystal contacts.

Rubrene single crystals showed a characteristic real-time increase in surface current when exposed to OTS vapors as shown in Figure 4.12. This validates the deposition process, and equivalent dosing of spun rubrene films is assumed. To quantify the rubrene crystal surface current enhancement, electrical response was investigated further, using various exposure events. A fixed volume of sub-vapor pressure OTS vapors backfilled the gas cell for 15 minutes; then the vapor was removed by 25 minutes of sorption pumping, followed by flushing the cell three times with nitrogen before returning to atmospheric pressure for infrared scanning.



Feb 9 OTS + water deposition on rubrene

Figure 4.12. The rubrene crystal surface current is increased by sub-saturated vapor pressure water + OTS exposure.

A plateau of surface current enhancement, expected for surface chemistry saturation, was not met during the 15 minutes of OTS deposition as shown in Figure 4.12. Therefore, a saturated monolayer of SAMs was not present during the deposition. Figure 4.12 illustrates that 26% of the enhancement was reversed (shown as loss in red) after 25 minutes of sorption pumping (Table 4.1). Vacuum pumping reduced the coverage further by removing molecules that were not chemisorbed but showed a surface current increase. Therefore, physisorbed molecules can produce a surface current increase. To investigate the peak position of a networking bond, OMS, a monochlorinated silane that can only form one bond to either a neighboring silane (unbound to the surface) or to the surface, is exposed to rubrene. The OMS infrared spectrum is then compared with OTS in Figure

4.14. The rubrene crystal surface current enhancement due to OMS deposition is shown in Figure 4.13.

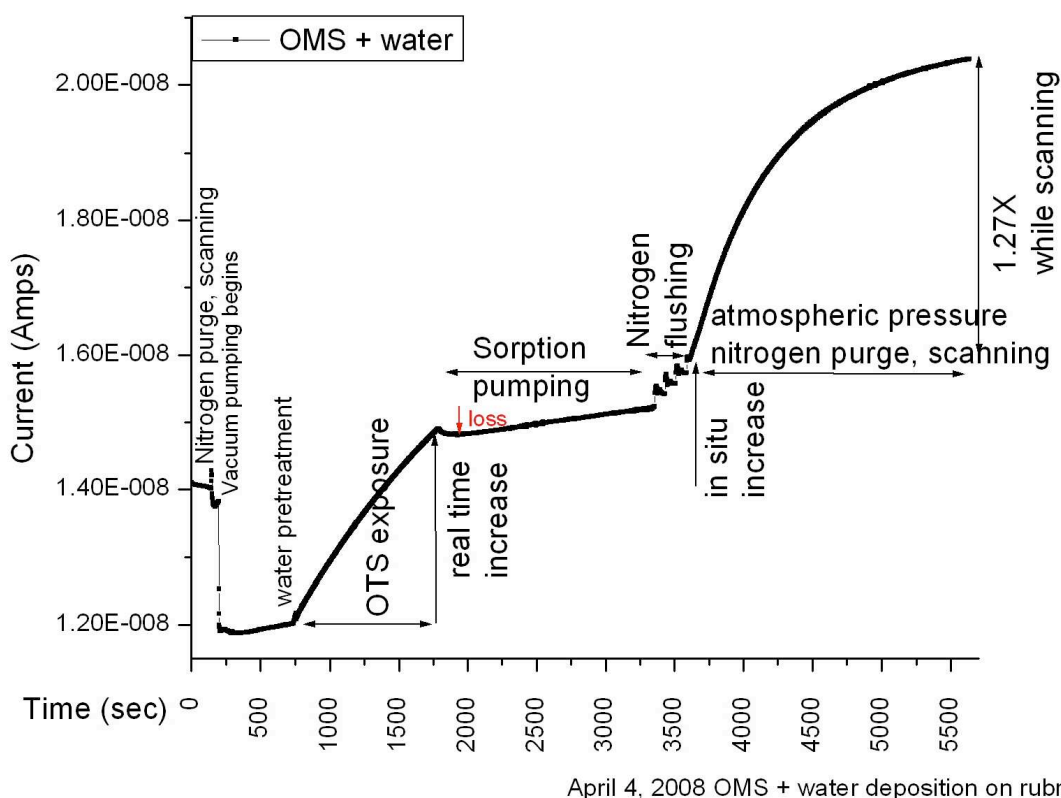


Figure 4.13. The rubrene crystal surface current is increased by sub-saturated vapor pressure water + OMS exposure.

	OTS + water	OMS + water
Real time increase	3.83E-9 Amps	2.82E-9 Amps
In-situ increase	2.95E-9 Amps	1.84E-9 Amps
Enhancement loss	26%	3%

Table 4.1. Rubrene Surface Current Enhancement Quantification from OTS and OMS

Rubrene surface current is increased more by exposure to OTS than OMS in both the real time and in-situ time spans as shown in Table 4.1. A more dramatic difference is seen in the amount of surface current that is lost during sorption pump removal of the vapor. The OTS-treated surface has a much larger reversibility than the OMS-treated

surface; however, the surface current increase was still larger overall. The physisorption of methylsilanol molecules on SiO_2 (silica) increases with increasing numbers of silane hydroxyl groups (1-3); however, surface reactivity decreases with increasing numbers of methylsilanol groups (Tripp and Hair 1995). Therefore, according to our surface current reversibility study, while OMS is less likely to reach the rubrene surface than OTS, it is more likely to chemisorb and sustain its surface current enhancement. The increase in surface current during the scanning after OMS deposition causes a small peak (5×10^{-5} absorption) to grow at 1200 cm^{-1} . Differences in their surface chemistry were therefore explored in Figure 4.14.

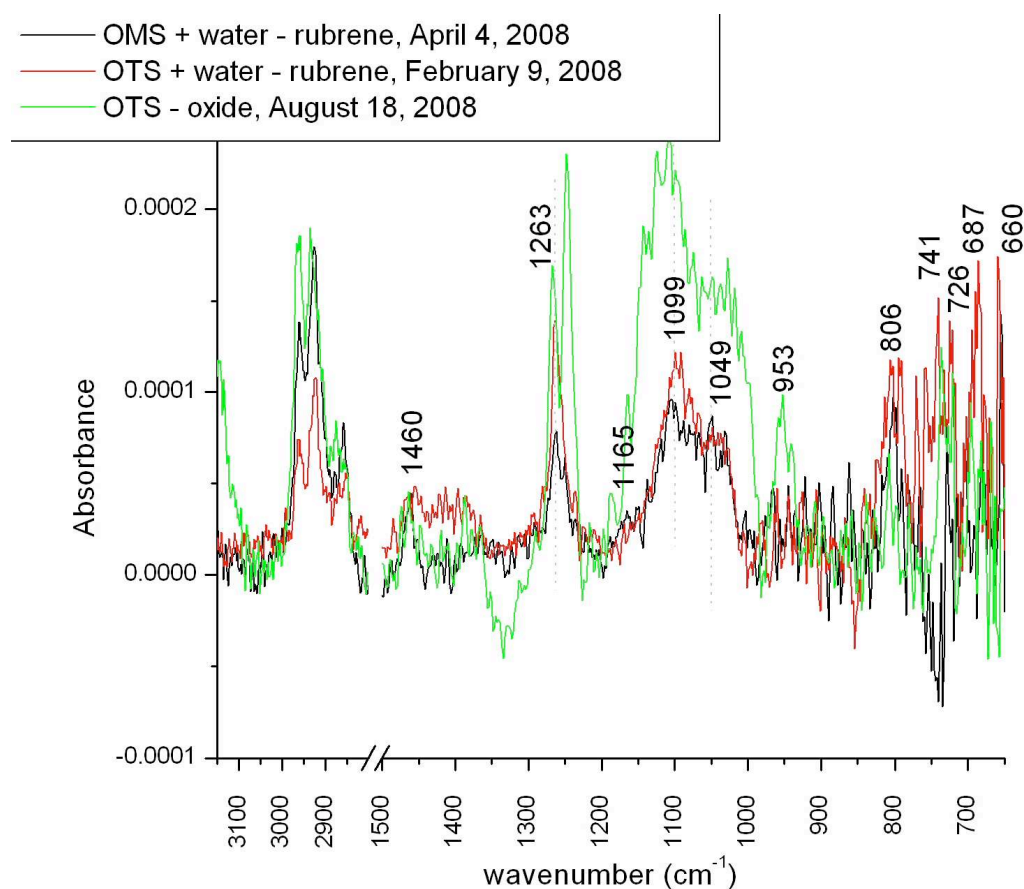


Figure 4.14. The infrared absorption signature of water + OTS and OMS referenced to the spun film of rubrene on SiO_2 . OTS on oxide from Figure 4.9 is shown again for comparison.

Although the OMS molecule should be missing peak(s) associated with networking modes in Figure 4.14, there do not appear to be any substantial differences between the OMS and OTS spectra on rubrene. Therefore, the peaks that were originally attributed to networking at 1045 cm^{-1} and 1099 cm^{-1} have been disproved. This may be explained by a possible OTS contamination in the OMS deposition due to similar peak intensity to that in Figure 4.7. Residual OTS in the vessel, delivery lines, or outgassing from the sorption pump, may have caused a co-deposition with the OMS, owing to insufficient baking time or temperature. However, the 1099 cm^{-1} mode which is slightly shifted to 1104 cm^{-1} as well as the peak at 1263 cm^{-1} decreased in the OMS spectrum, suggesting they may be assigned with reservation to networking. The OMS spectrum minus rubrene shows more hydrocarbon above 2800 cm^{-1} and at 1460 cm^{-1} , which may indicate some hydrocarbon contamination.

In order to distinguish the peaks attributed to silane-rubrene bonding from silane-substrate SiO_2 bonding, the spectra of silane- SiO_2 are also compared in Figure 4.14. First, the spectra on SiO_2 are generally more intense than those on rubrene, as shown in Figure 4.14. The peak at 1265 cm^{-1} is sharper, more intense, and at slightly higher wavenumber for OTS on SiO_2 than on rubrene and less intense than the expected contamination intensity shown in Figure 4.6. Also, a separate polarization study of OTS on rubrene showed that the 1265 cm^{-1} peak was not parallel to the surface since there was some suppression of its peak intensity at normal beam incidence (not shown). Due to its proximity to a peak that increased during rubrene photo-oxidation and outgassing, it is possible that it is also related to rubrene bonding; however, the presence of a similar peak at this position on SiO_2 completely refutes this assignment. Therefore, Figure 4.14 is

inconclusive for rubrene or networking bond assignment. The peaks may be due to bonds the OTS and OMS molecules have in common such as Si-C, unreacted Si-OH, CH₂ or CH₃.

The peak at 806 cm⁻¹ is in the range of out-of-plane aromatic C-H bending, but its presence on the SiO₂ surface refutes this assignment. It must therefore, be attributed to the silane molecule on oxide, and possibly attributed to the tail CH₃ rocking.

When a silane molecule is hydrolyzed by a surface or ambient water molecule, the chlorine molecule is replaced with a hydroxyl group, releasing hydrochloric acid (HCl). The HCl may play a role in breaking open the aromatic groups, similarly to the effect on opening the end of a closed carbon nanotube that can lead to oxidation in the presence of water. Further study of HCl vapor exposure to rubrene is necessary to develop this idea, in addition to reconsidering the gas cell material stability, given HCl's ability to etch metals. Previous study in the literature has shown that saturated fumes of HCl exposed to rubrene crystals under 5V bias in a stainless steel vessel causes an unstable half order of magnitude decrease in surface current (Calhoun, Sanchez, Olaya, Gershenson and Podzorov 2008). However, it was not exposed in conjunction with a silane molecule, which should be more reactive with the surface as a result of possible oxidation formation. In a previous publication, a fluoroalkyl triethoxysilane molecule without chlorines was also shown to cause a persistent increase in rubrene crystal surface current; however, its stability with pumping was not shown (Calhoun, Sanchez, Olaya, Gershenson and Podzorov 2008). This implies that HCl does not play a role in the surface bonding, but does not rule out its ability to enhance rubrene oxidation and rubrene-trichlorosilane bonding.

Since the surface current study of OTS exposure on rubrene did not show saturation, an incomplete monolayer of OTS may have so few rubrene bonds that it was below the detection limit of infrared spectroscopy. It has been reported that a saturated vapor pressure of OTS should take several hours to produce a saturated surface current enhancement (Calhoun, Sanchez, Olaya, Gershenson and Podzorov 2008). Therefore, the results of longer exposures were performed and compared, in Figures 4.15 and 4.16.

01/10/08 ~1.5 hour OTS exposure to rubrene

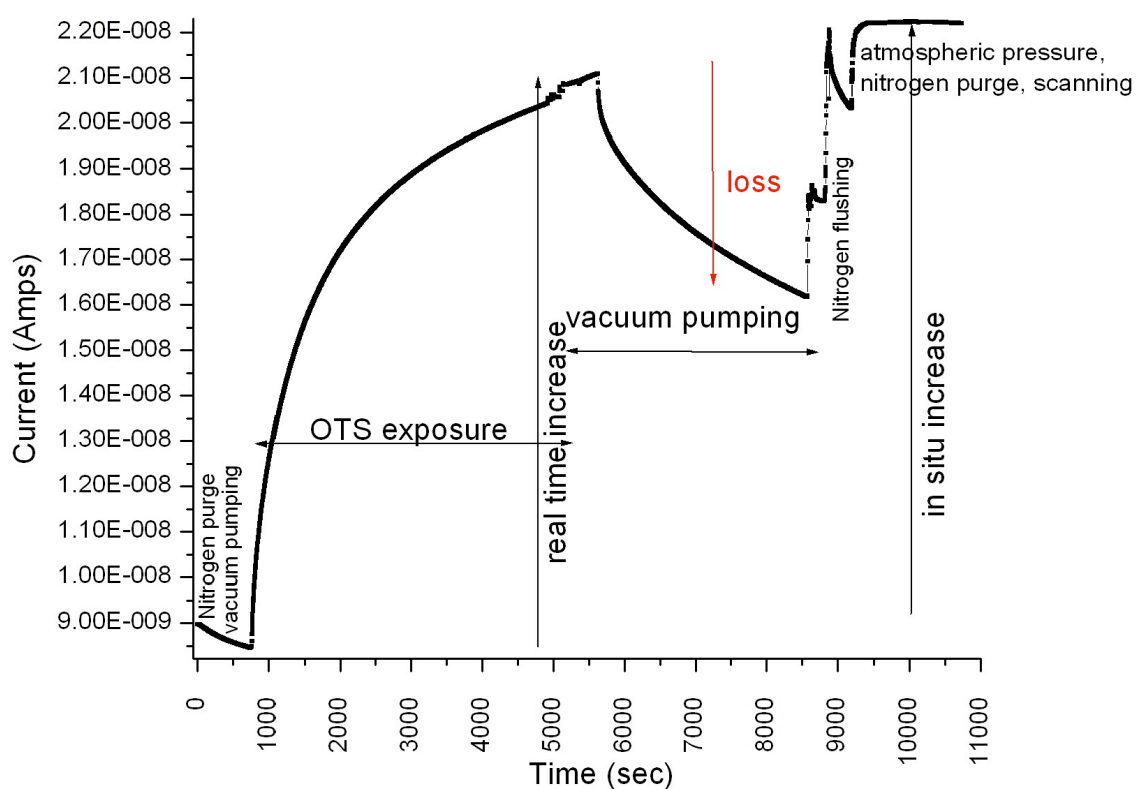


Figure 4.15. The rubrene crystal surface current is increased by sub-saturated vapor pressure OTS exposure for 1.5 hours.

	OTS
Real time increase	1.26E-8 Amps
In-situ increase	1.32E-8 Amps
Enhancement loss	39%

Table 4.2. Quantification of the rubrene surface current enhancement from 1.5 hours OTS exposure

Longer OTS exposure to rubrene was performed to determine whether surface current saturation could be achieved. The increase in surface current did not saturate, even after 1.5 hours of sub-saturated vapor pressure exposure as shown in Figure 4.15. Table 4.2 shows a greater increase in surface current for the extended exposure. This suggests more chemical interaction must have taken place at the rubrene surface, which is investigated in Figure 4.16.

Rubrene Spun Film Exposures

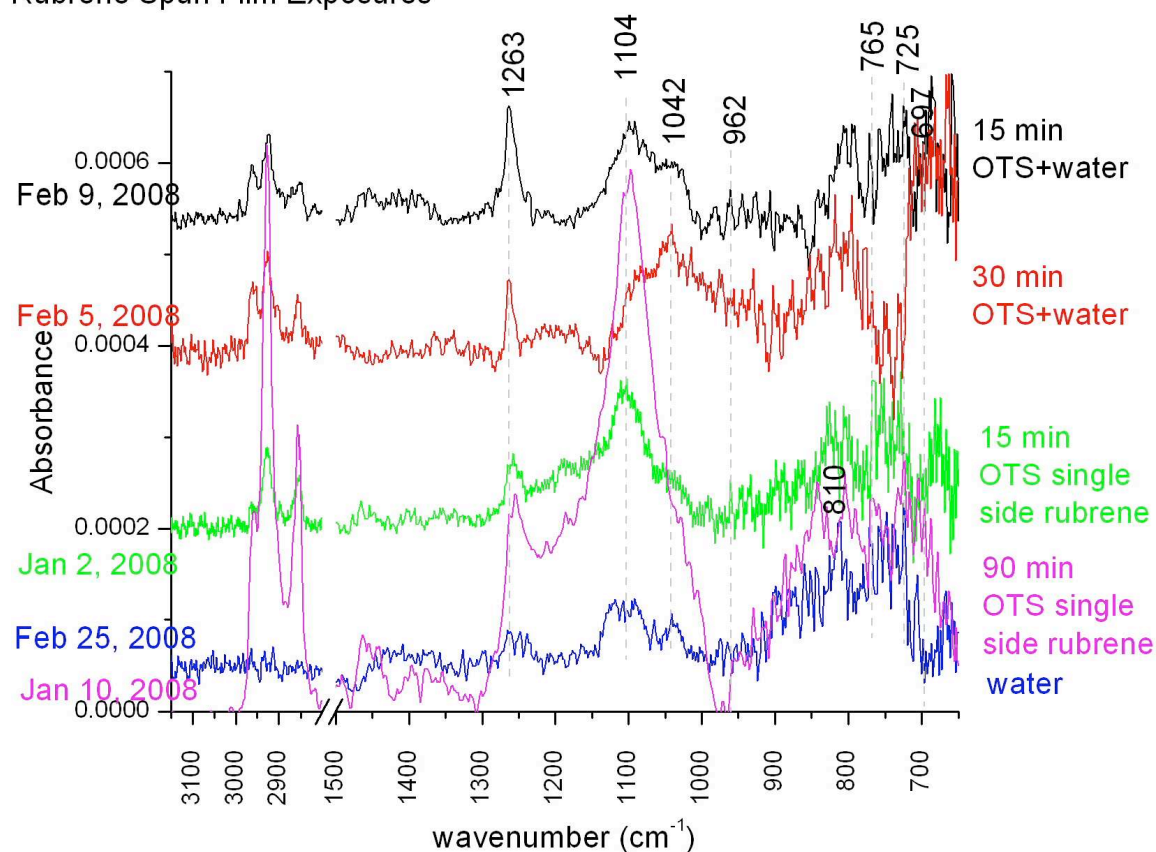


Figure 4.16. Different OTS exposure times referenced to spun rubrene films. The green and pink substrates were coated with spun rubrene on only one side, leaving the other side bare SiO₂. Double-side coating with rubrene (black and red).

Although all of the peaks between 1257 cm⁻¹ and 806 cm⁻¹ have been ruled out from rubrene-silane bonding modes due to their presence in silane-SiO₂ spectra, it is

interesting to observe differences in peak intensity growth with OTS exposure to rubrene and SiO₂ in Figure 4.16. Since the peak at 1042 cm⁻¹ does not seem to scale more with time on a rubrene double-coated sample than single sided perhaps the 1042 cm⁻¹ peak could be a networking phonon mode or could be loosely related to a surface interaction with rubrene while 1104 cm⁻¹ is due to networking.

The single-sided rubrene covered sample presents a bare SiO₂ surface that may explain the growth of a peak at 1104 cm⁻¹ in pink. Figure 4.14 showed that 1104 cm⁻¹ might be due to networking, which may propagate during the additional exposure time. The other possibility is that it originates from an SiO₂-bonding mode, which would be in agreement with Wen et al. (Wen, Maoz, Cohen, Sagiv, Gibaud, Desert and Ocko 2008) and Meng Li (Li 2007) for butyltrichlorosilane on SiO₂. An extended exposure of OMS should be repeated on a blank, clean SiO₂ so that networking and substrate bonding can be distinguished.

Application of OTS liquid directly to a thick SiO₂ sample in the glove box for a few minutes before drying with N₂ produced a bulk casting of OTS that may emulate an extended exposure (Figure 4.17, no vacuum exposure). This shows scaling of the tail body peaks, no scaling of silane-SiO₂ modes.

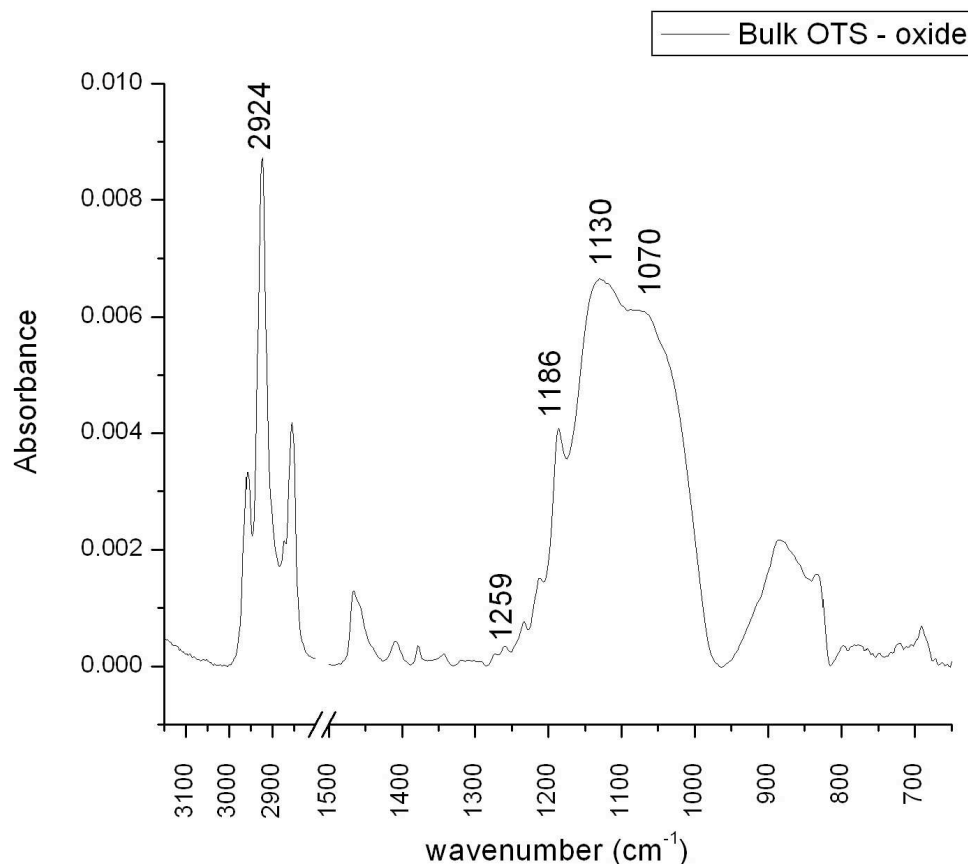


Figure 4.17. Bulk OTS is deposited by soaking a droplet of liquid OTS on a SiO_2 substrate for one minute in a nitrogen glove box. It was blown dry with nitrogen gas in ambient conditions.

Physisorption, polymerization, or networking peaks are assumed to dominate interfacial surface bonding events to the substrate SiO_2 when OTS is cast from a liquid (Figure 4.17) (Tripp, Veregin and Hair 1993). This is in contrast to the gas/solid interface where trisilanol is anticipated to adsorb on the surface with less polymerization (Tripp, Veregin and Hair 1993). A peak at 1259 cm^{-1} does not scale in the bulk deposition, according to peak area (Bulk: $2.4\text{E-}4$, Sub-Sat: $1.09\text{E-}4$), which rules out a body mode origin and supports its assignment to: substrate SiO_2 bonds since networking should have scaled. This agrees with the substrate bond of a similar molecule with no alkyl chain reported by Meng Li on thick oxide at 1256 cm^{-1} (Li 2007). However, since

OTS on bare oxide has peaks at 1267 cm^{-1} and 1248 cm^{-1} (Figure 4.9), it may still be possible that 1259 cm^{-1} originates from a rubrene-silane bond, although it is seen in the bulk OTS spectrum on oxide (Figure 4.17). The peak at 1103 cm^{-1} was also suspected for this same assignment; however, it may have scaled with the large, broad peak at 1130 cm^{-1} indicating a networking origin.

The prominent scaling peaks in the bulk spectrum at 1130 cm^{-1} and 1070 cm^{-1} could be affiliated with bulk physisorbed body modes or networking molecules which corresponds well to the group of self-polymerized silane Si-O-Si peaks reported by Meng Li (Li 2007) with dominant peaks at 1157 cm^{-1} and 1070 cm^{-1} with water added to a trichloro-silane solution deposition. Therefore, we identify bulk-networking phonon modes to 1130 cm^{-1} and 1070 cm^{-1} and thinner film networking to 1103 cm^{-1} .

A peak at 1460 cm^{-1} is attributable to CH_2 scissor mode (NIST, propane, 1462 cm^{-1}), while the peak at 1383 cm^{-1} should be attributed to CH_3 symmetric deformation mode (NIST, propane, 1392 cm^{-1}). The alkyl stretching modes evident between 2800 cm^{-1} and 3000 cm^{-1} show that the OTS liquid is not contaminated with hydrocarbon, which would have added CH_3 peaks.

4.4.4 Surface Coverage Compared With Electrical Enhancement

To explore whether surface current enhancement is limited by coverage or another time-dependent variable such as reorganization of the surface species, a short 30-second exposure of diluted OTS vapor was performed several times in series. This should also reveal any rubrene-silane peaks that may have been too weak to be seen near OTS networking peaks. Dilution of the OTS vapor was performed by backfilling the exposure volume to 200mTorr with N_2 gas, 40X lower than the undiluted condition of

5mTorr. The spun rubrene surface chemistry was evaluated with IRAS in Figure 4.18 with peak areas quantified in Figure 4.19. Rubrene, single-crystal surface current was recorded during each exposure in Figure 4.20.

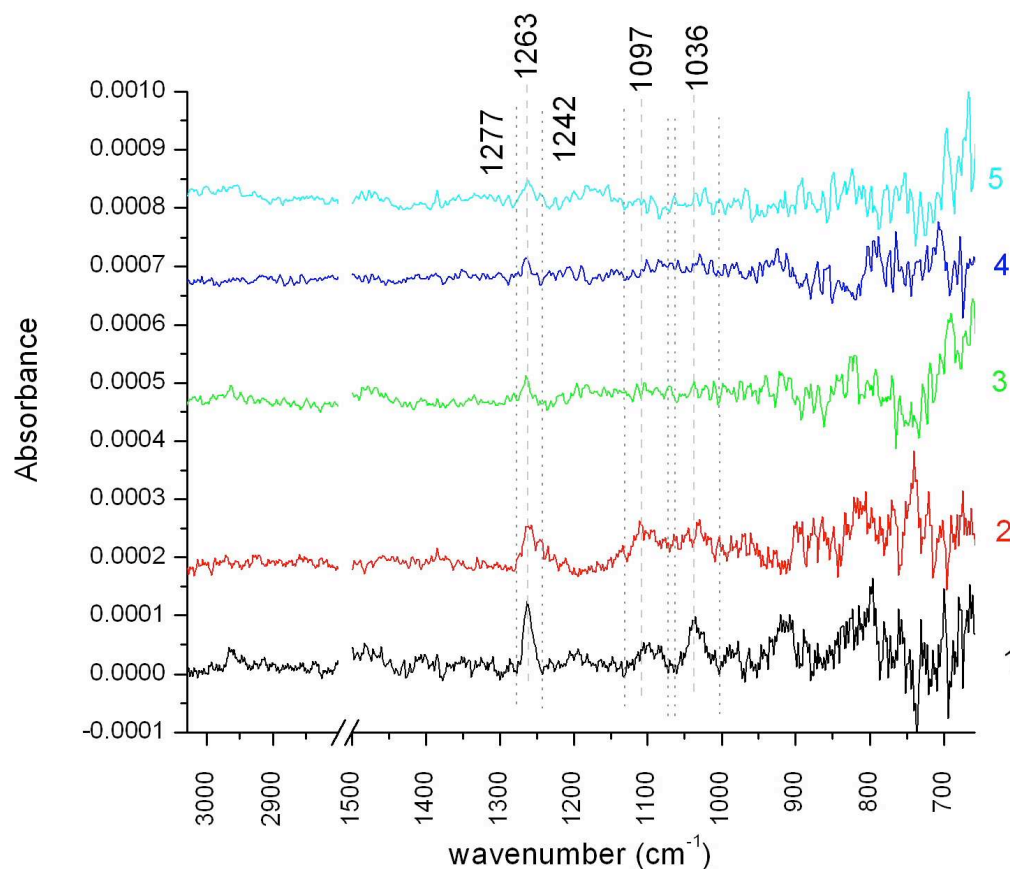


Figure 4.18. Differential scans of water followed by gradual OTS exposure referenced to spun rubrene films. Shifted for clarity. Dotted lines surround the range used in peak area calculation.

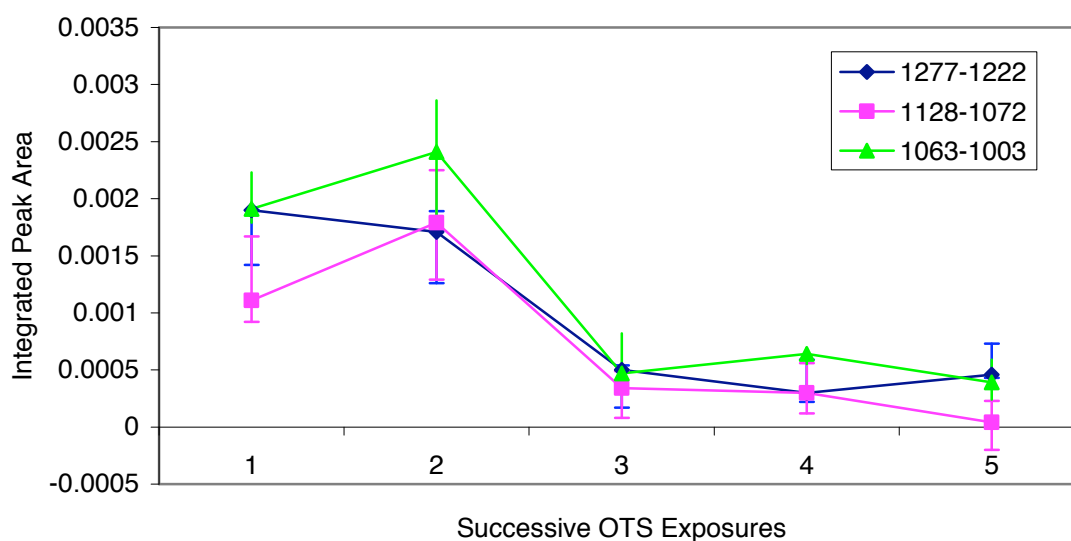


Figure 4.19. Comparison of the peak areas at: 1263 cm^{-1} , 1097 cm^{-1} , and 1036 cm^{-1} after successive OTS exposure to rubrene. Error bars indicate the area range with different baseline assignments.

The most prominent peak resulting from the first exposure was 1263 cm^{-1} , which must therefore be related to some kind of interfacial bond to the substrate SiO_2 or possibly rubrene. This peak does not seem to reach saturation even after five exposures, although a lesser, more consistent amount is added each time after the second exposure as shown in Figure 4.19. The plot of peak area per successive exposures shows peak area beyond the second exposure due to noise.

The peak at 1097 cm^{-1} assigned to networking scales with the peak at 1036 cm^{-1} which may be the other networking phonon mode. The fact that they scale together suggests they may have a common bonding origin. Networking peaks are known to have phonon modes which normally appear as two peaks: LO and TO (Li 2007). They saturate after the second exposure with very little or no additional peaks, with differential comparison of subsequent depositions. This suggests that steric hindrance prevents

further substrate absorption after the second exposure, while the peak at 1263 cm^{-1} is added continually as incomplete networking bonds switch to surface bonding modes.

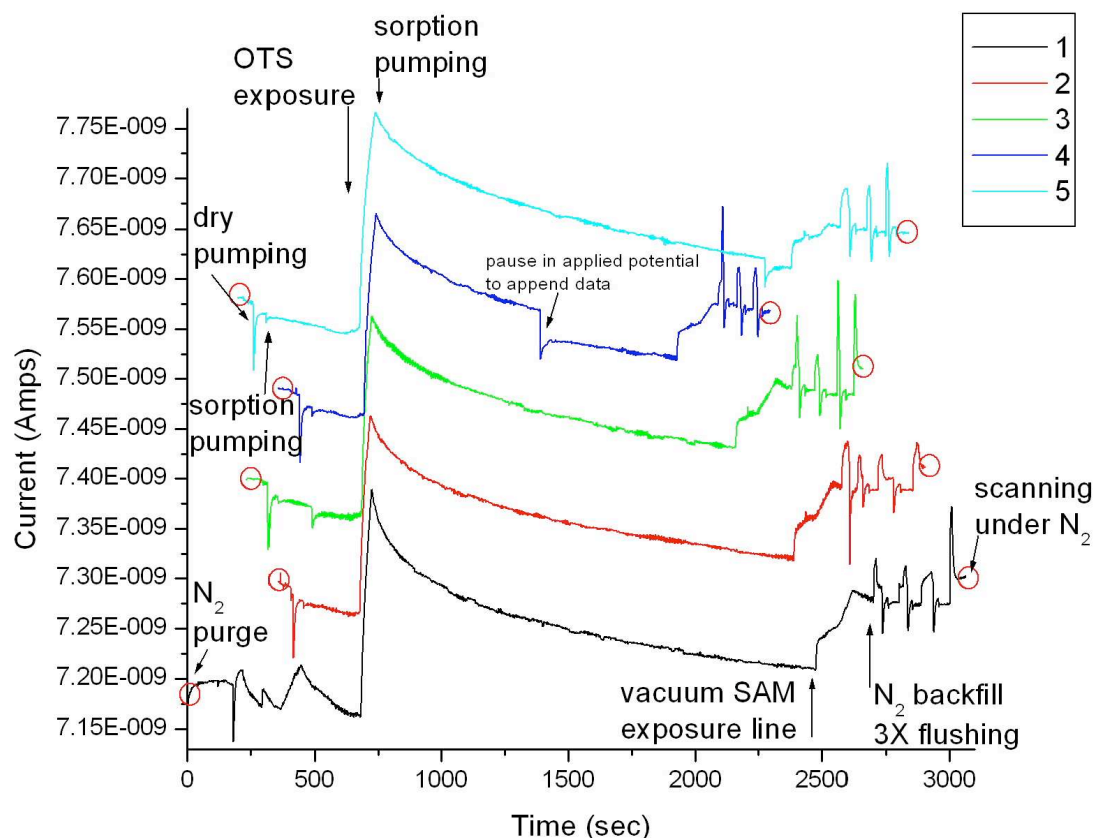


Figure 4.20. Rubrene crystal surface current response to water, followed by diluted OTS exposures. Common exposure events, such as pumping, are labeled once. Small differences in the amount of pumping time account for misalignment of the events. Red circles indicate the current at the beginning of IRAS scanning. The current at those time points were compared for a sustained current enhancement in Figure 4.21. The current during scanning (not shown) was stable. Time course surface current lines were shifted horizontally for clarity. Data collection date: 02/28/08.

OTS exposure	Water (mTorr)	OTS (mTorr)	Comment
1	146	550	30s OTS exposure volume preset to 200mTorr
2	230	384	30s OTS exposure volume preset to 200mTorr
3	306	294	30s OTS exposure volume preset to 200mTorr
4	369	118	30s OTS exposure volume preset to 200mTorr
5	N/A	N/A	30s OTS exposure volume preset to 200mTorr

Table 4.3. Details of the OTS Exposure Conditions

The OTS exposure pressure decreased linearly ($R^2 = 0.99$) with each successive exposure due to a diminishing supply of the liquid as shown in Table 4.3. However, we assumed that the critical number of molecules for surface interaction is in excess, according to reproducibility shown in the appendix. To determine whether chemical saturation followed electrical saturation, we plotted differential peak area and the sustained current increase after the silane exposure (Figure 4.21). Increased surface current in response to subsequent OTS exposures does not saturate after five exposures.

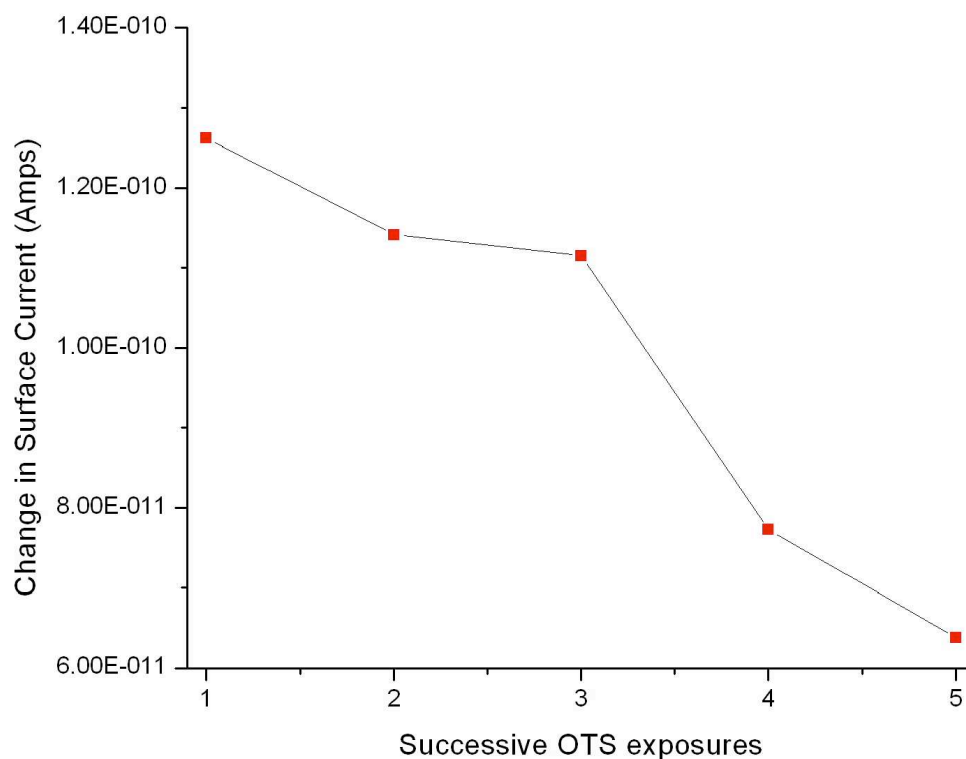


Figure 4.21. The sustained surface current after OTS exposure processing minus the surface current before OTS exposure for successive exposures. Points of comparison before and after FTIR scanning under N_2 purge conditions were indicated by red circles in the current per time plot.

The peak area in Figure 4.19 shows gains after the first two successive exposures, while gains after the third through fifth were small and near the noise level. This is

somewhat similar to the sustained current trend shown in Figure 4.21 where much less is gained after the third exposure. The link between the surface chemistry and current addition is not completely clear since the growing peaks were attributed to substrate oxide bonding and silane networking instead of rubrene bonding.

Performing the experiment on a substrate that is not reactive with the silane can help distinguish between the surface bonding modes and the rubrene bonding modes. One candidate substrate material is KBr. However, since KBr is hygroscopic, there may be terminal hydroxyl groups for surface bonding. To validate that OTS does not react with the KBr pellet substrate an OTS exposure is revisited and interpreted further in Figure 4.21.

Pumping on the KBr pellet removed quite a bit of water above 3100 cm^{-1} (not shown). This may be due to the hygroscopic nature of the pellet and may not have removed surface hydroxyl groups. The rest of the spectrum in Figure 4.22 looks different from the pumping effect on SiO_2 (Figure 4.6) and includes the removal of hydrocarbon. The loss of a peak at 1632 cm^{-1} is due to the removal of adsorbed water bending modes removed with pumping. The negative peaks at 1385 cm^{-1} , 2918 cm^{-1} , 2850 cm^{-1} could be attributed to the removal of CH_3 bending and CH_2 stretching from a possible KBr contaminant (NIST, butane). Peaks at 1055 cm^{-1} and 1205 cm^{-1} are likely related to silane networking observed previously at 1030 cm^{-1} and 1099 cm^{-1} . The peak at 1234 cm^{-1} may be due to KBr bonding since it is near the 1263 cm^{-1} silane- SiO_2 mode.

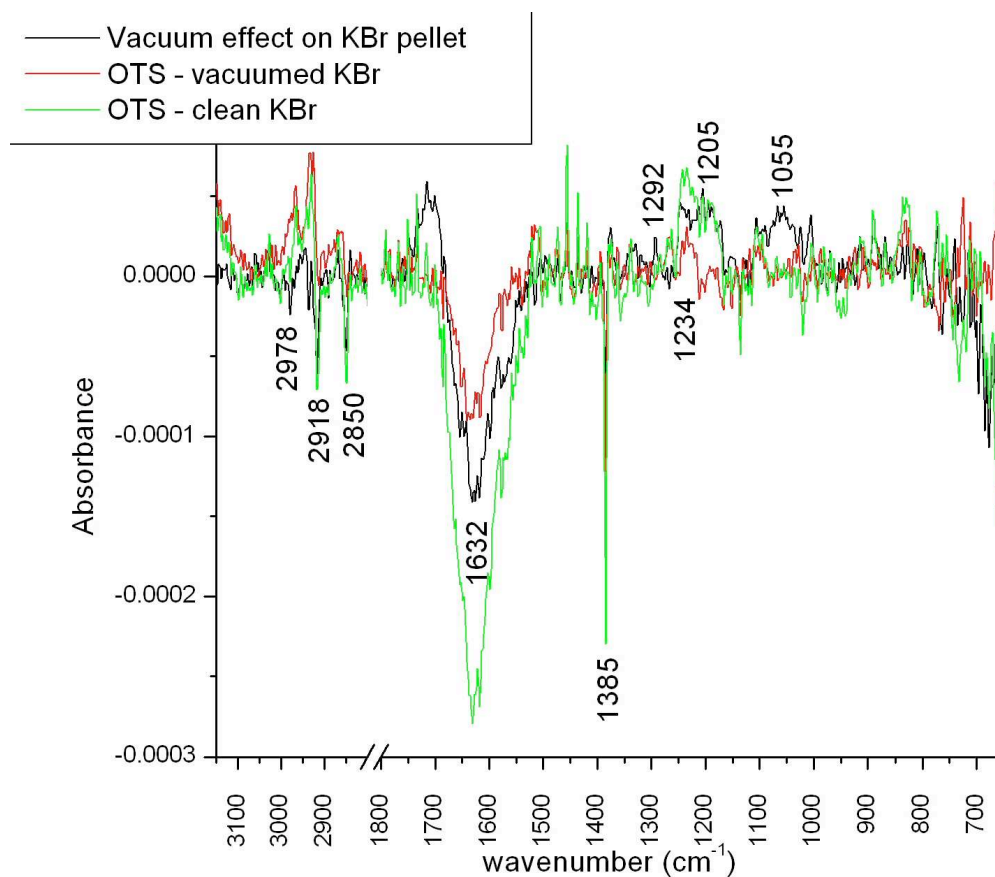


Figure 4.22. A KBr pellet was vacuumed (black) before OTS deposition, which was referenced with prevacuumed KBr spectra (green) and vacuumed KBr spectra (red).

Although we have identified some very low intensity peaks attributed to silane-substrate bonding and networking, we proceed to test the rubrene-silane interaction on KBr. A pellet pressed into a transparent substrate was spun cast on both sides with rubrene and exposed to OTS in the gas cell.

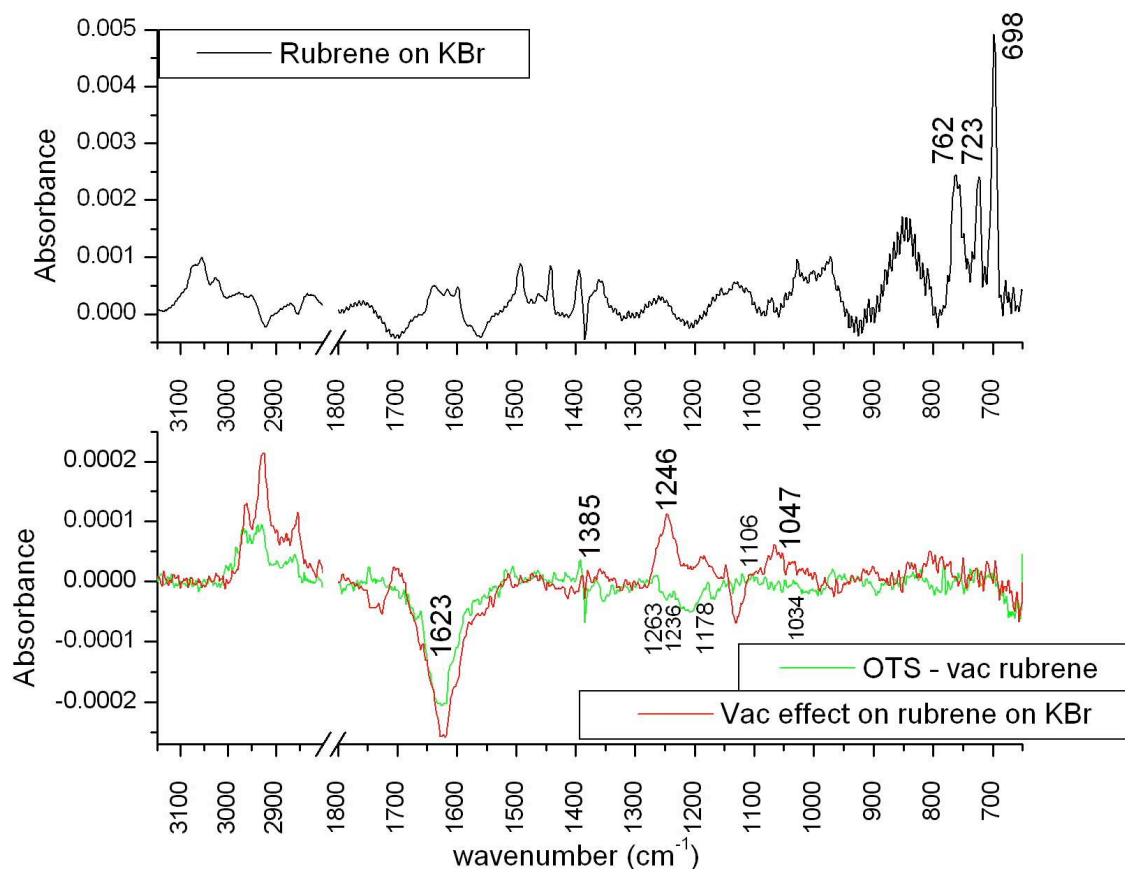


Figure 4.23. The infrared spectra of rubrene cast onto a KBr pellet and then exposed to vacuum and OTS deposition.

Rubrene deposition onto the KBr pellet was validated by the presence of sharp peaks at 698 cm⁻¹, 723 cm⁻¹, and 762 cm⁻¹ (Figure 4.23). The wavy baseline is due to replacement of the KBr pellet after the rubrene deposition in a slightly different angle or position with respect to the KBr windows from the reference scan.

Effects due to vacuuming water and contaminant removal were previously attributed to peaks at 1623 cm⁻¹ and 1385 cm⁻¹. OTS exposure produced similar peaks on rubrene as bare KBr indicating similarly networked silane at 1066 cm⁻¹ but not at 1205 cm⁻¹. Also, a large, broad feature at 1246 cm⁻¹, suggests either substrate (previously 1234 cm⁻¹) or possibly rubrene-silane bonding have occurred.

4.5 Conclusions

The interaction of rubrene with alkyltrichlorosilanes has been investigated using IRAS and a specialized vacuum gas cell. The peak observed at 1099 cm^{-1} was initially attributed to networking because it was shifted and slightly less intense in the OMS spectrum compared to OTS. Bulk cast OTS on oxide revealed the bulk networking phonon modes at 1130 cm^{-1} and 1070 cm^{-1} . A peak at 1263 cm^{-1} did not scale with bulk OTS deposition on oxide and was therefore attributed to silane-SiO₂ bonding. These findings are in agreement with Meng Li's thesis. A limited OTS exposure to rubrene showed the progression of small peaks with successive exposures at 1263 cm^{-1} (silane-SiO₂), as well as less intense broad peaks at 1097 cm^{-1} and 1036 cm^{-1} attributed to networking. OTS on thick oxide SiO₂ (Figure 4.9) refutes assigning 1263 cm^{-1} to a rubrene-silane mode. OTS deposition on KBr pellets indicates silane networking at 1205 cm^{-1} and 1055 cm^{-1} as well as probable substrate bonding through presumed surface hydroxyl groups at 1234 cm^{-1} . However, when rubrene was spun cast onto KBr, a strong broad peak at 1246 cm^{-1} may support a rubrene bonding, but with reservation due to a similar peak seen with OTS on oxide (Figure 4.9).

Surface chemistry attributed to silane-networking (possible with a rubrene crystal) and SiO₂-silane bonding (impossible with a rubrene crystal) observed during successive dilute exposures seems to saturate after the second exposure, while the sustained rubrene crystal surface current increase also diminishes during a third exposure. Therefore, surface chemistry and rubrene surface current enhancement are loosely correlated. Also, no peaks hypothesized for rubrene photo-oxidation (Table 3.4) were attributable.

Therefore, no rubrene-silane peak has been unambiguously identified, however, it has not been ruled out. Silane networking modes have been identified for a thin film at 1099 cm^{-1} and for a bulk film at 1130 cm^{-1} and 1070 cm^{-1} . Silane-SiO₂ bonding may be evident at 1265 cm^{-1} . Silane networking should have similar peak positions for perfluorinated alkyltrichlorosilanes deposited on rubrene, which is discussed next, in Chapter 5. Perfluorinated alkyltrichlorosilanes are known to cause a much larger increase in rubrene surface current, which may be due to more rubrene bonding. Perhaps the large dipole moment in the perfluorinated alkyl chain will increase the number of rubrene bonds and thus produce a stronger infrared signal than that of OTS-rubrene bonding. Comparing oxide and rubrene-coated oxide substrate bonding could identify a rubrene-silane peak.

4.6 References

1. Banga, R.; Yarwood, J., FTIR and AFM Studies of the Kinetics and Self-Assembly of Alkyltrichlorosilanes and (Perfluoroalkyl)trichlorosilanes onto Glass and Silicon. *Langmuir* **1995**, 11, 4393-4399.
2. Banga, R.; Yarwood, J.; Morgan, A. M.; Evans, B.; Kells, J., In-Situ FTIR studies of the kinetics and self assembly of alkyl and perfluoroalkyl trichlorosilanes on silicon. *Thin Solid Films* **1996**, 284-285, 261-266.
3. Bhushan, B.; Hansford, D.; Lee, K. K., Surface modification of silicon and polydimethylsiloxane surfaces with vapor-phase-deposited ultrathin fluorosilane films for biomedical nanodevices. *Journal of Vacuum Science and Technology A* **2006**, 24, (4), 1197-1202.
4. Calhoun, M. F.; Sanchez, J.; Olaya, D.; Gershenson, M. E.; Podzorov, V., Electronic functionalization of the surface of organic semiconductors with self-assembled monolayers. *Nature Materials* **2008**, 7, 84 - 89.
5. Chang, J.-F.; Sun, B.; Breiby, D. W.; Nielsen, M. M.; Sölling, T. I.; Giles, M.; McCulloch, I.; Sirringhaus, H., Enhanced Mobility of Poly(3-hexylthiophene) Transistors by Spin-Coating from High-Boiling-Point Solvents *Chemistry of Materials* **2004**, 16, (23), 4772 -4776.
6. Dong, J.; Wang, A.; Ng, K. Y. S.; Mao, G., Self-assembly of octadecyltrichlorosilane monolayers on silicon-based substrates by chemical vapor deposition. *Thin Solid Films* **2006**, 515, 2116-2122.
7. Geer, R. E.; Stenger, D. A.; Chen, M. S.; Calvert, J. M.; Shashidhar, R.; Jeong, Y. H.; Pershan, P. S., X-ray and Ellipsometric Studies of Self-Assembled Monolayers of Fluorinated Chlorosilanes. *Langmuir* **1994**, 10, (4), 1171 - 1176.
8. Harvey, M. C.; Nebergall, W. H., The Silicon-Phenyl Asymmetrical Stretching Vibration *Applied Spectroscopy* **1962**, 16, (1), 12-14(3).
9. Knieling, T.; Lang, W.; Benecke, W., Gas phase hydrophobisation of MEMS silicon structures with self-assembling monolayers for avoiding in-use sticking. *Sensors and Actuators B* **2007**, 126, 13-17.
10. Kulkarni, S. A.; Vijayamohanan, K. P., Interfacial behavior of alkyltrichlorosilane monolayers on silicon: Control of flat-band potential and surface state distribution using chain length variation. *Surface Science* **2007**, 601, 2983-2993.
11. Li, M. Modification of Silicon By Self-Assembled Monolayer For Application in Nano-Electronics and Biology. Rutgers, The State University of New Jersey, New Brunswick, 2007.
12. Michalak, D. J.; Rivillon, S.; Chabal, Y. J.; Esteve, A.; Lewis, N. S., Infrared Spectroscopic Investigation of the Reaction of Hydrogen-Terminated, (111)-Oriented, Silicon Surfaces with Liquid Methanol. *Journal of Physical Chemistry B* **2006**, 110, (4), 20426-20434.
13. Morrow, B. A.; Cody, I. A.; Lee, L. S. M., Infrared studies of reactions on oxidesurfaces. IV. Structure of chemisorbed ammonia on silica. *Journal of Physical Chemistry* **1975**, 79, (22), 2405-2408.
14. Noll, W., The Silicate Bond from the Standpoint of Electronic Theory. *Angewandte Chemie International Edition in English* **1963**, 2, (2), 73-80.

15. Socrates, G., *Infrared and Raman Characteristic Group Frequencies Tables and Charts*. 3 ed.; John Wiley & Sons Ltd.: West Sussex, England, 2001; p 347.
16. Tripp, C. P.; Hair, M. L., Reaction of chloromethylsilanes with silica: a low-frequency infrared study. *Langmuir* **1991**, 5, (7), 923 - 927.
17. Tripp, C. P.; Veregin, R. P. N.; Hair, M. L., Effect of Fluoroalkyl Substituents on the Reaction of Alkylchlorosilanes with Silica Surfaces. *Langmuir* **1993**, 9, (12), 3518-3522.
18. Tripp, C. P.; Hair, M. L., Reaction of Methylsilanols with Hydrated Silica Surfaces: The Hydrolysis of Trichloro-, Dichloro-, and Monochloromethylsilanes and the Effects of Curing. *Langmuir* **1995**, 11, 149-155.
19. Wasserman, S. R.; Tao, Y. T.; Whitesides, G. M., Structure and reactivity of alkylsiloxane monolayers formed by reaction of alkyltrichlorosilanes on silicon substrates. *Langmuir* **1989**, 5, (4), 1074 - 1087.
20. Wen, K.; Maoz, R.; Cohen, H.; Sagiv, J.; Gibaud, A.; Desert, A.; Ocko, B. M., Postassembly Chemical Modification of a Highly Ordered Organosilane Multilayer: New Insights into the Structure, Bonding, and Dynamics of Self-Assembling Silane Monolayers. *ACS Nano* **2008**, 2, (3), 579-599.

CHAPTER 5: AN IN-SITU INVESTIGATION OF PERFLUORINATED ALKYLTRICHLOROSILANE BONDING WITH RUBRENE

5.1 Abstract

In-situ Infrared Absorption Spectroscopy (IRAS) and real-time electrical measurements are used to study rubrene bonding with tridecafluoro-1,1,2,2,-tetrahydro-octyl trichlorosilane (FTS), which is responsible for rubrene, single-crystal surface current enhancement. The rubrene-silane bond was investigated, using IRAS with rubrene thin films spun-cast on SiO₂ terminated silicon wafers exposed to FTS vapors in a dedicated vacuum cell. Monitoring increased rubrene, single-crystal surface current during the co-deposition validated FTS exposure. An excess FTS exposure was used to distinguish interface bonding from tail body modes that scaled with thickness. To distinguish SiO₂-silane bonding peaks from silane-rubrene bonding peaks, the infrared absorption spectra of FTS on SiO₂ was compared with FTS on SiO₂ blocked by an octadecyltrichlorosilane (O(C₁₈)TS), self-assembled monolayer (SAM). Spectra of mono-chlorinated silane (FMS)-rubrene bonding distinguished the substrate bond from the cross-linking bond peak. Minimal hydroxyl-terminated perfluoro-1-octanol (FOH)-rubrene bonding explained the reversible effect on rubrene surface current.

5.2 Introduction

Perfluorinated, self-assembled monolayers are known to cause a more dramatic increase in rubrene surface current than octyltrichlorosilane molecules (Calhoun, et al. 2008). Therefore, in this chapter we extend our exploration of surface chemistry and surface current to perfluorinated, self-assembled monolayers on rubrene. To do this the gas cell and procedures established in Chapters 2 and 4 are used here.

The proximity of electron-withdrawing groups in a SAM, such as fluorine in FTS deposited from gas phase bonded to rubrene, single-crystals, is thought to be responsible for the dramatic increase in rubrene crystal surface current (Calhoun, et al. 2008). However, validation of rubrene-silane bonding has not been fully explored. A greater understanding of silane bonding events can allow further optimization of their influence on rubrene crystal surface current. Since the reversible polar solvent vapor sensing was only possible with enhanced surface current, studying trichlorosilane bonding with the rubrene crystals could contribute to an understanding of both the surface current enhancement mechanism and subsequent chemisensing applications (Calhoun, et al. 2008).

Although the surface charge accumulation is dominated by the SAM tail dipole, it is not sufficient for sustained current enhancement (Calhoun, et al. 2008). Therefore, covalent bonding through the FTS trichlorosilane group is a hypothesized requirement for surface current enhancement, which has not yet been fully explored (Calhoun, et al. 2008). The silane bonding of FTS with SiO₂ substrates and silica has been determined, using Infrared Absorption Spectroscopy (IRAS) (Banga and Yarwood 1995; Banga, et al. 1996; Dong, et al. 2006; Kulkarni and Vijayamohan 2007; Li 2007; Wen, et al. 2008). Infrared absorption spectroscopy has not yet been applied to extend FTS and OTS studies to understand rubrene bonding with OTS or FTS. IRAS should have sufficient sensitivity for silane-rubrene bonding, since it has revealed submonolayer-bonding events on silicon surfaces that typically support 10^{15} cm^{-2} monolayer⁻¹-absorbing molecules (Michalak, et al. 2006). Previous IRAS studies of perfluorinated molecules aid in distinguishing its

rubrene-bonding modes from substrate-bonding, networking, and self-polymerization modes.

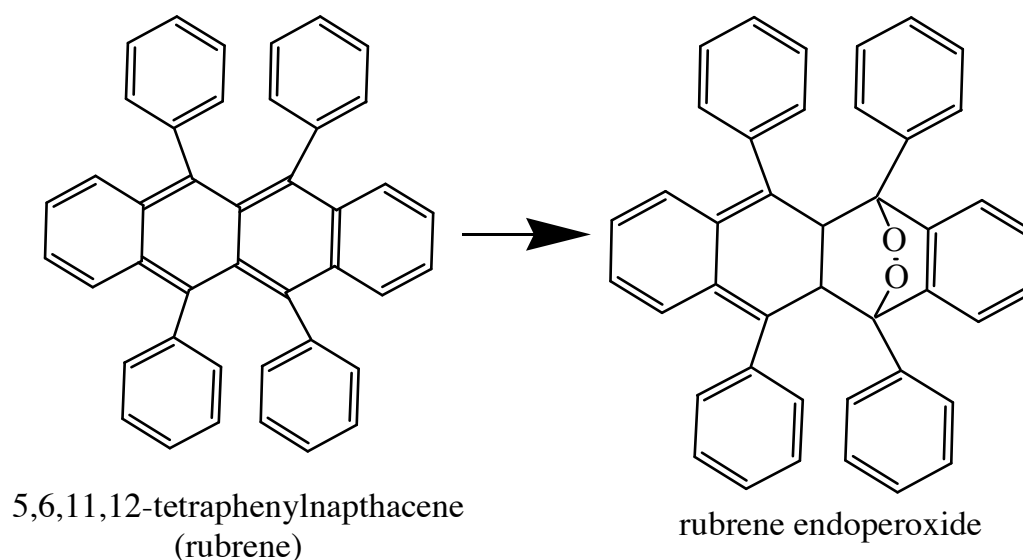


Figure 5.1. The oxidation of rubrene surfaces provides a probable silane-bonding site.

The endoperoxide species that forms upon exposure of rubrene surfaces to atmospheric oxygen and ambient light (Figure 5.1) could provide a reactive site for trichlorosilanes as described in Chapters 3 and 4. The basis for distinguishing substrate-bonding peaks from rubrene-bonding peaks begins with reviewing infrared absorption of substrate-bonding peaks concerning perfluorinated alkyl-trichlorosilane hydrolysis and subsequent reactions of perfluorinated alkyl-silanol with SiO_2 substrates.

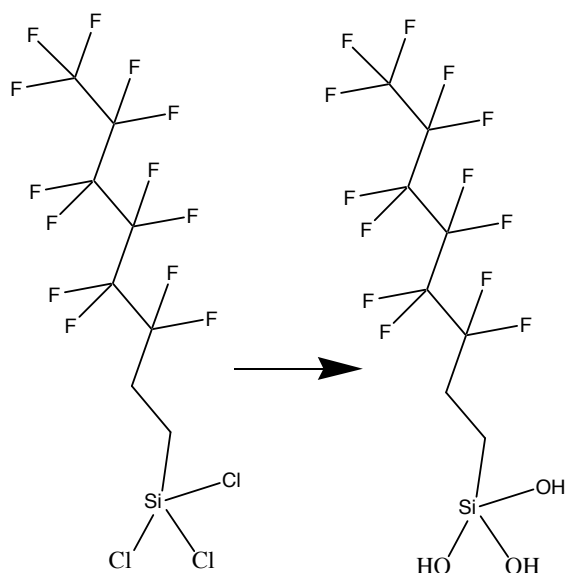


Figure 5.2. Perfluorinated alkyl-trichlorosilane hydrolysis to perfluorinated alkyl-silanol.

Trichlorosilanes undergo hydrolysis in the presence of water on the substrate surface or in solution as shown in Figure 5.2. Hydrochloric acid is produced as the chlorine groups are replaced with hydroxyl groups that can then act as bonding sites to SiO_2 or rubrene. Fourier transform infrared spectroscopy (FTIR) studies of alkyltrichlorosilanes and (perfluoroalkyl) trichlorosilanes surface bonding events on silicon surfaces have shown that water is required for the hydrolysis of the trichlorosilane head group to silanol, which bind to the surface and each other (Banga and Yarwood 1995). Surface water would have a peak at 1620 cm^{-1} , which could be consumed upon reaction with trichlorosilane; however, it was not often seen, due to the water bands adding additional noise to that region (Tripp, et al. 1993). The Si-Cl bond should produce very weak stretching bands at 574 cm^{-1} and 473 cm^{-1} ; however, their intensity is so close to the noise that it is difficult to detect any remaining unhydrolyzed groups (Tripp and Hair 1995). Hydrolysis should cause an increase in a peak at 910 cm^{-1} from Si-OH bending (Tripp, Veregin and Hair 1993).

The expected modes for silane interaction with a thin film on SiO_2 (which must be distinguished from the interesting rubrene bonding at the rubrene endoperoxide group (Si-O-cyclic C)) are as follows: silane bonding with the substrate SiO_2 (Si-O-Si(s)), silane bonding with neighboring silane in a network (Si-O-Si), silane self-polymerization (Si-O-Si), and body/tail modes (C-C, CH_2 , CF_3 , or CF_2 modes). Previous studies of silane interaction with SiO_2 substrates provide a basis for distinguishing these modes.

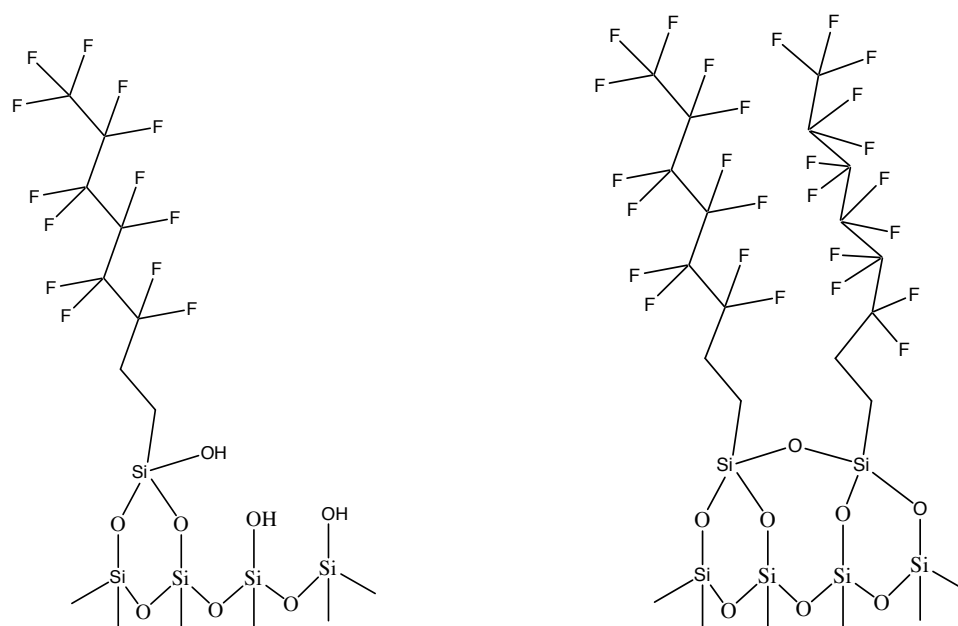


Figure 5.3. Silanol bonding with the substrate SiO_2 (Si-O-Si): and network formation.

Perfluorinated-alkyltrichlorosilane surface bonding shown in Figure 5.3 should be evident at 1060 cm^{-1} , according to $\text{CF}_3\text{CH}_2\text{CH}_2\text{SiCl}_3$ reactions on hydrated silica (Tripp, Veregin and Hair 1993). If trichlorosilane is physisorbed to the surface through hydrogen bonding with hydroxyl groups, the peak at 3747 cm^{-1} should shift to 3350 cm^{-1} (Tripp, Veregin and Hair 1993). Unfortunately, this region ($3747\text{--}3350\text{ cm}^{-1}$) is usually confounded with purge contaminant and broad physisorbed water peaks in our lab.

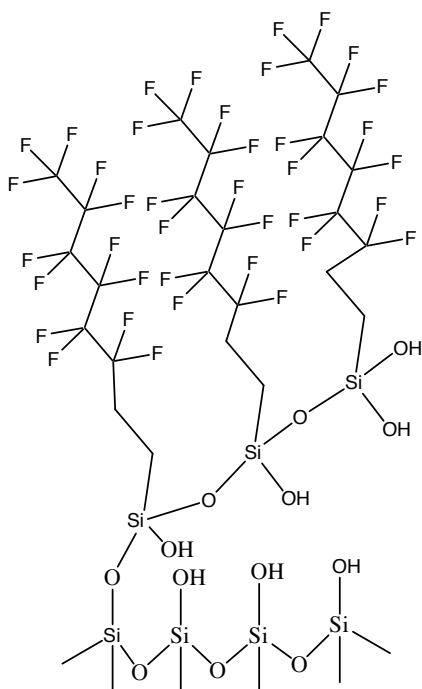


Figure 5.4. Silane self-polymerization (Si-O-Si).

Multilayers as a result of networked Si-O-Si groups from FTS chains shown in Figure 5.4 should be evident at 1016 cm^{-1} , according to $\text{CF}_3\text{CH}_2\text{CH}_2\text{SiCl}_3$ reactions on hydrated silica (Tripp, Veregin and Hair 1993).

Body or tail modes (CH_3 or CH_2 modes):

Alkyl stretching peaks can be expected in the $2800 - 3000\text{ cm}^{-1}$ range. Si-C peaks appear at 600 cm^{-1} , but are too close to the phonon mode of the silicon substrate to be considered reliable. Also, alkanes may show a doublet peak between $1175-1120\text{ cm}^{-1}$, C-C-C stretching at $1100-1040\text{ cm}^{-1}$, and $900-800\text{ cm}^{-1}$ (Socrates 2001, p. 54). C-C and C-F stretching peaks associated with the polyfluorinated molecule (FTS) should be found between $1360 - 1090\text{ cm}^{-1}$ (Socrates 2001, p. 198).

The CF_3CF_2 group has peaks between $1365 - 1325\text{ cm}^{-1}$ and $745-730\text{ cm}^{-1}$ (Socrates 2001, p. 198). Tripp et al. generalizes the $1450 - 700\text{ cm}^{-1}$ region for CF and CH peak assignments (Tripp, Veregin and Hair 1993). $\text{CF}_3(\text{CF}_2)_5\text{CH}_2\text{CH}_2\text{OH}$ has peaks

at 1126 cm^{-1} , 1151 cm^{-1} , 1216 cm^{-1} , and 1251 cm^{-1} that can be assigned to complex mixtures of molecular backbone modes associated with C-F and C-H stretches (Waterland, et al. 2005).

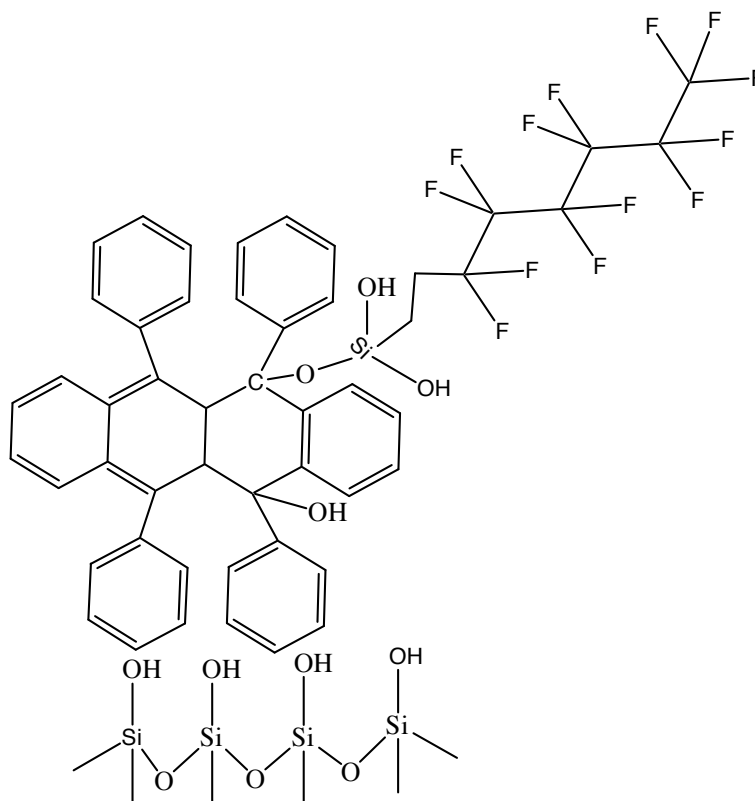


Figure 5.5. Silane bonding with the rubrene endoperoxide group (Si-O-C).

Typically, a Si-O-C peak should be observed at approximately 1100 cm^{-1} , but may shift slightly lower ($1080 - 1118\text{ cm}^{-1}$) as coverage decreases ((Michalak, et al. 2006), Michalak, et al. unpublished data). A Si-O-aromatic peak is expected at $1090 - 1135\text{ cm}^{-1}$ (possibly several strong, sharp bands attributed to Si-O-C stretching) and $920 - 970\text{ cm}^{-1}$ (Si-O-stretch) (Socrates 2001, p. 33, 244). Negative or differential peaks in the regions of the original rubrene film, such as those between $1600 - 1450\text{ cm}^{-1}$ are normally displaced by 20 cm^{-1} lower wavenumbers when bound to a silicon atom and often include a peak at 1430 cm^{-1} ((Socrates 2001, p. 245; (Harvey and Nebergall 1962)). In addition, phenyl-silicon bonds have strong peaks at 1100 cm^{-1} that split into two when two phenyl

groups attach to the one silicon atom (Socrates 2001, p. 245). Phenyl silicon peaks should also be present at 1030 cm^{-1} and 1000 cm^{-1} . Overtones are sometimes observed between $2000 - 1660\text{ cm}^{-1}$ (Socrates 2001, p. 245). However, due to the stability of the aromatic resonance and the presumed endoperoxide group in the rubrene structure, a silanol group (Si-OH) was expected to form a Si-O-C with the endoperoxide structure instead of a direct phenyl-silicon bond. Due to the differences in ionic strength, the C-O bond should be less intense than Si-O (Socrates 2001, p. 246).

A unique vacuum gas-exposure cell that allows in-situ and real-time chemical and electrical measurements using infrared and surface current measurements was developed for this study to reveal the chemical bonding site of silanes with rubrene as discussed in Chapter 4.

Uncertainty as to whether deposited octyltrichlorosilane (OTS) films were complete monolayers inspired switching to FTS. The use of FTS in a separate, dedicated vacuum cell, by our collaborator made it possible to perform extended, saturated vapor pressure depositions overnight without corroding our specialized gas cell. Therefore, a comparison study of FTS bonding with SiO_2 as well as pre-treating the SiO_2 with a self-assembled monolayer of octadecyltrichlorosilane ($\text{O}(\text{C}_{18})\text{TS}$), which blocks SiO_2 bonding sites, was conducted. The FTS deposited on rubrene samples and other surfaces to saturation in a dedicated vacuum cell were compared in order to distinguish FTS-rubrene bonds from SiO_2 or networking bonds. The rubrene bonding with FTS was analyzed by first investigating the infrared peaks associated with FTS exposure to rubrene. Two different FTS film exposure pressures assumed to produce different surface coverage were used to differentiate body (scales with thickness) and interfacial chemical bonds

(they should not scale past surface saturation) between the FTS molecule and rubrene film, with FTS bonding with the substrate SiO_2 . A OC_{18}TS pretreatment which blocks SiO_2 bonding sites was used to rule out silane- SiO_2 interfacial bonding peaks.

Analogous molecules with one (FMS) or no (FOH) terminal chlorine group are used to distinguish silane networking and polymerization from rubrene bonding. A comparison of FMS and rubrene absorption spectra with those of FTS and rubrene should reveal the absence of a networking peak in the FMS spectra that is present in the FTS spectra.

5.3 Materials and Methods

5.3.1 Chemicals

The following silanes were used as received from Gelest: (tridecafluoro-1,1,2,2-tetrahydrooctyl)trichlorosilane (FTS) (SIT8174.0), (tridecafluoro-1,1,2,2-tetrahydrooctyl)dimethyl-chlorosilane (FMS) (SIT8170.0). 1H,1H,2H,2H-Perfluoro-1-octanol (FOH) (370533) was used as received from Sigma-Aldrich. The solvent, xylene, isomers plus ethyl-benzene, (247642) was used as received from Sigma-Aldrich. Rubrene, single-crystals were provided by the Podzorov-Gershenson group. Trichloro(octadecyl)silane ($\text{O}(\text{C}_{18})\text{TS}$) (104817-25G) was used as-received from Sigma-Aldrich and stored in a nitrogen-purged glove box.

5.3.2 Substrates

Silicon (100) wafers (0.68 inch by 1.46 inch) with 65 Å of thermally deposited silicon dioxide (SiO_2) were cleaned with a 90°C piranha solution (7:3 sulfuric acid: hydrogen peroxide) soaking for ten minutes. Chemically etching the thick native SiO_2

(65Å) and then reoxidizing the surface with a piranha solution was performed to prepare a thin SiO₂ (20Å). Samples were cleaned using acetone, methanol, water, and a 90°C piranha solution (7:3 sulfuric acid: hydrogen peroxide) for ten minutes. To make a thin oxide, we then used a 30-second aqueous 10% HF etch (90mL deionized water, 20 mL 49% hydrofluoric acid), followed by a 45 minute re-oxidation in a 90°C piranha solution, which is blown dry with N₂ gas.

5.3.3 Rubrene Solution Preparation

Rubrene was spun coat onto silicon wafers, using a 0.5% weight % solution of rubrene dissolved in xylene (Chang, et al. 2004), described in Chapter 4.

5.3.4 Silane Deposition

Mono-chlorinated (FMS) and hydroxyl terminated (FOH) perfluorinated liquids were exposed to the gas cell for a saturated vapor pressure exposure, while the sorption pump was pumping on the system in order to maintain a vacuum below the materials' vapor pressure. Our collaborator, the Podzorov, Gershenson group at Rutgers University Physics and Astronomy, exposed the trichlorinated perfluoroalkyl silane in a dedicated vacuum cell.

To explore the effects of water on film stability to sorption pumping, some surfaces were pre-treated with water before being exposed to SAM vapors. Water exposures were performed by partially backfilling the gas cell with a volume of de-ionized water vapor between two valves separated by 2 inches of ¼-inch stainless steel tubing.

To block SiO₂ bonding, some SiO₂ samples were pre-treated with a self-assembled monolayer of octadecyltrichlorosilane using 20mL of a 5.0×10^{-3} M solution (Wen, et al. 2008) in anhydrous toluene (Socrates 2001). To make the octadecyltrichlorosilane solution, the molecular formula (C₁₈H₃₇Cl₃Si) was used to calculate the molar mass (387.94 g/mol) where the density is 0.984 g/mL.

Solutions were prepared in a glove box, using test tubes pre-cleaned with a piranha solution (7:3) and rinsed with anhydrous toluene. Octadecyltrichlorosilane (39.4μL) of was added to 20mL anhydrous toluene using a micropipettor. The solution was capped and brought to the hood at 56% relative humidity (46°F dew point, 72°F). New samples were scanned with an infrared spectrometer after they were cleaned, using a 90°C piranha solution (7:3 sulfuric acid: hydrogen peroxide) for ten minutes, followed by a 30-second aqueous 10% HF etch (90mL de-ionized water, 20 mL 49% hydrofluoric acid), followed by a 45-minute re-oxidation in 90°C piranha solution, and finally blown dry with N₂ gas. Samples were re-cleaned with a piranha solution for ten minutes and then immediately immersed in the octadecyltrichlorosilane solution for one hour at room temperature. Samples were then transferred to fresh anhydrous toluene and sonicated for five minutes before being scanned a second time.

5.3.5 Measurement of Films and Silanes

Fourier Transform Infrared Spectroscopy measurements in the transmission geometry were performed, using a Nicolet Magna-IR 760 spectrometer with a MCT/A enhanced detector, as described in Chapter 4. Electrical measurements were performed with a Keithley 4200 SCS, as described in Chapter 4.

5.4 Results and Discussion

5.4.1 FTS Bonding with Rubrene

A co-deposition of FTS on several different surfaces allows us to compare the amount of FTS interaction with each surface. To investigate the bonding of FTS silanes with rubrene, FTS was co-deposited on spun rubrene, bulk rubrene on OTS-blocked SiO_2 , SiO_2 , and OTS-blocked SiO_2 surfaces along with a rubrene crystal. Infrared absorption spectra of FTS on several substrates were collected.

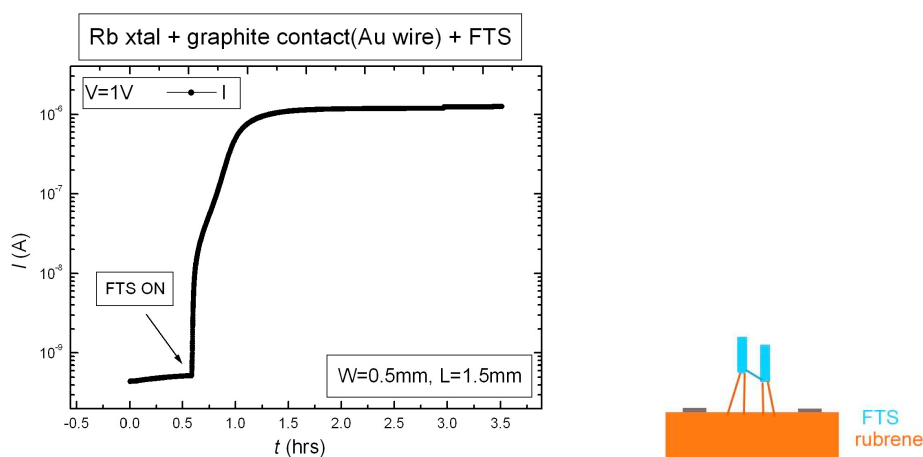


Figure 5.6. Rubrene, single-crystal surface current increase by 3.5 orders of magnitude saturated after two hours of FTS exposure in a dedicated vacuum cell.

The FTS deposited in a dedicated vacuum cell caused rubrene surface current to increase to saturation by ~ 3.5 orders of magnitude over two hours. Since all four silicon wafers were co-deposited with FTS, the rubrene crystal and silicon wafers were assumed covered with a complete FTS monolayer.

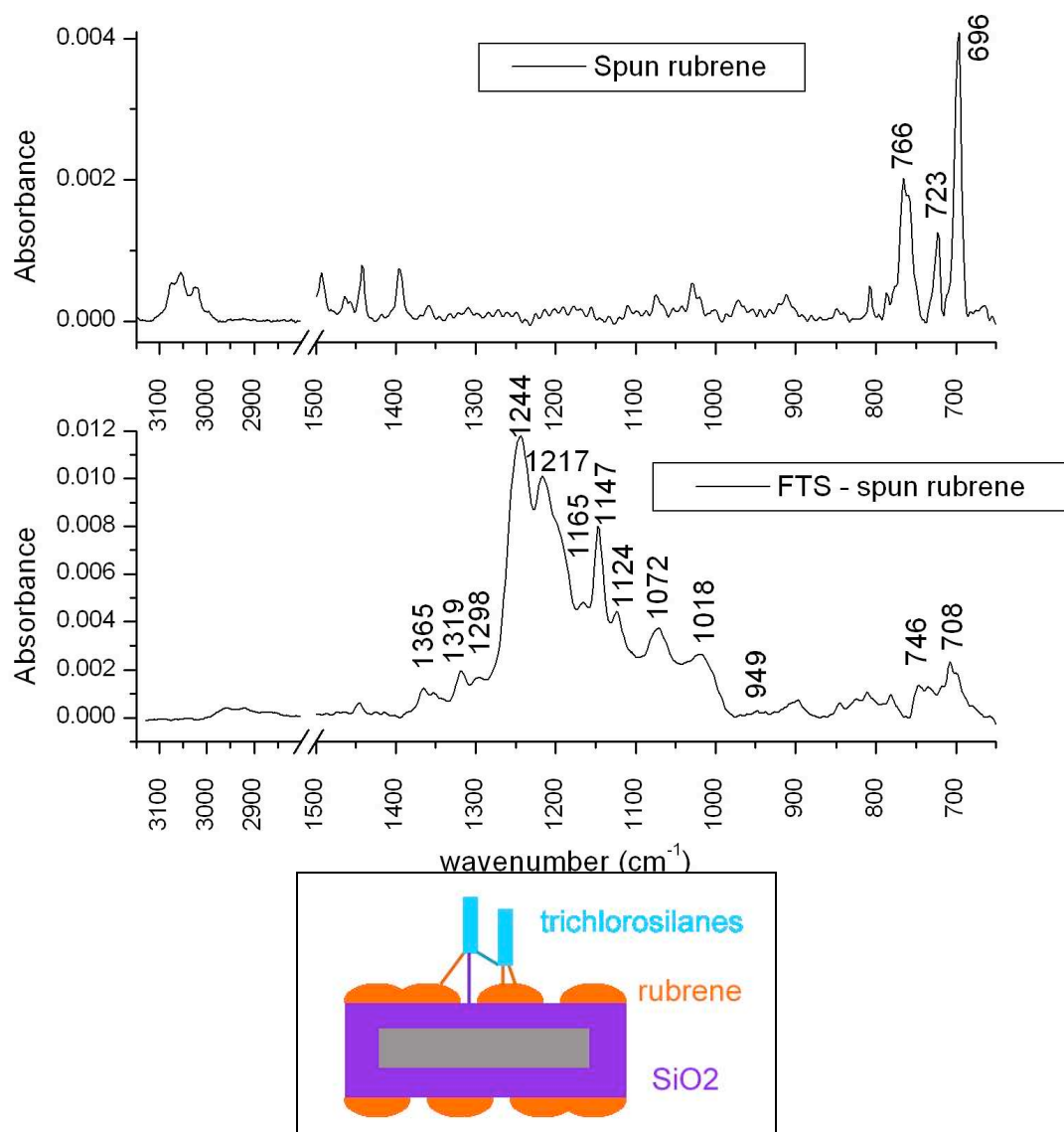


Figure 5.7. Infrared absorption spectra of spun rubrene referenced to a thin SiO₂ and FTS deposition referenced to the spun rubrene film on thin SiO₂ (July 13, 2008).

The recorded spectra of a saturated FTS monolayer referenced to spun rubrene on thin SiO₂ (Figure 5.7) contain several intense tail body peaks, which confirm successful deposition. A doublet peak attributable to C-C-C stretch is observed at 1165 cm⁻¹ and 1147 cm⁻¹. A peak at 897 cm⁻¹ may be attributable to a similar C-C-C stretch origin. Peaks attributable to CF₃CF₂ modes were observed at the following positions: 1365 cm⁻¹, 1319 cm⁻¹, 746 cm⁻¹, and 735 cm⁻¹. Attributable peaks for CF and/or CH were observed

at the following positions: 1217 cm^{-1} and 1244 cm^{-1} . Peaks attributable to Si-O bending were observed at 937 cm^{-1} and 949 cm^{-1} . The prominent peak at 1244 cm^{-1} is assigned to CF stretching or CH bending.

The signature of FTS bonding with rubrene through Si-O-C, where C is part of a cyclic ring, is assigned tentatively to 1124 cm^{-1} . A singly perfluorinated alkyl silane-SiO₂ bond to hydrated silica peak at 1060 cm^{-1} agrees with the peak we observed at 1072 cm^{-1} (Tripp, Veregin and Hair 1993). Also, a singly perfluorinated alkyl silane on hydrated silica showed a peak at 1016 cm^{-1} attributed to polymerized Si-O-Si bonds, which agrees with the peak we observed at 1018 cm^{-1} (Tripp, Veregin and Hair 1993). In order to distinguish substrate SiO₂ bonding from rubrene bonding this spectrum is plotted again with the other co-deposited results in Figure 5.8.

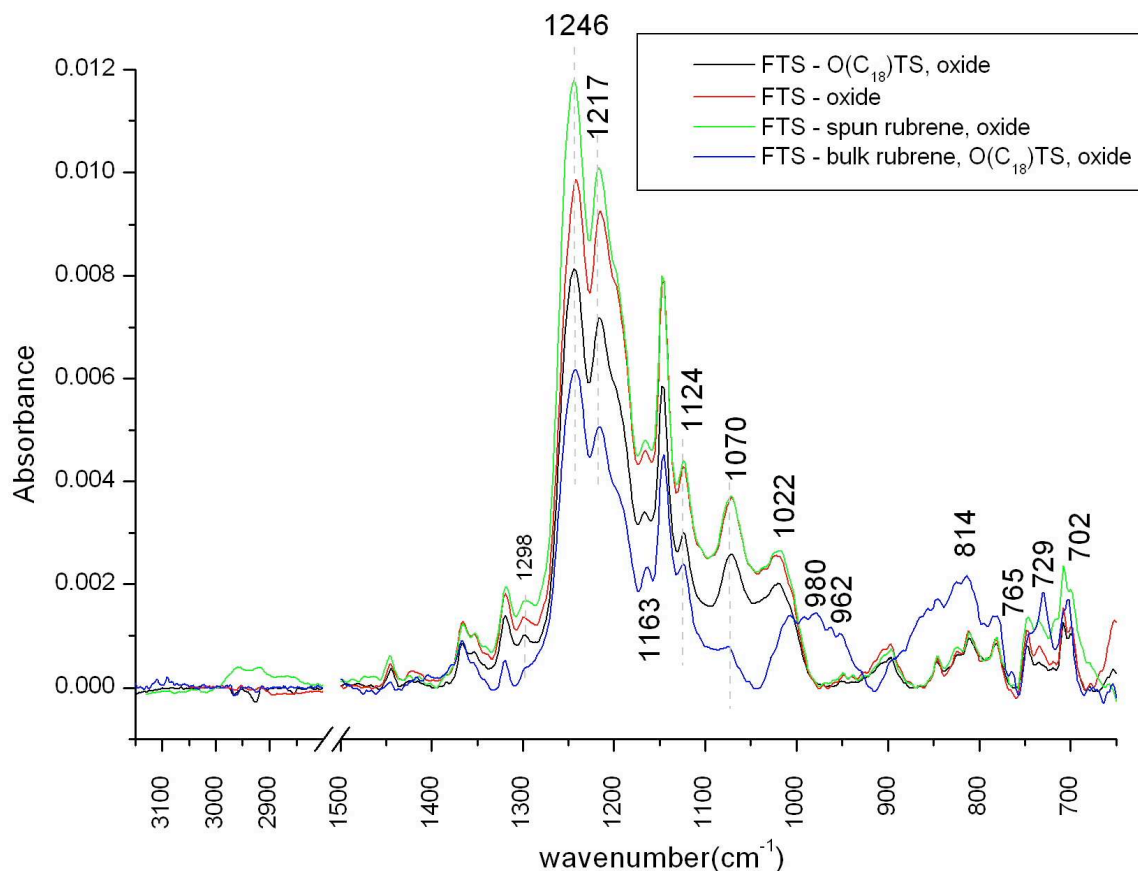
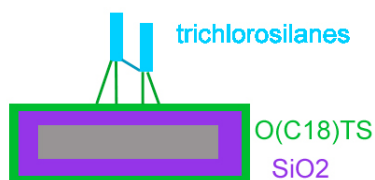


Figure 5.8. Infrared Absorption Spectroscopy summary of four FTS co-depositions referenced to their substrates listed after the legend subtraction sign.

The FTS deposition spectra with their respective substrates subtracted are plotted together on one common scale in Figure 5.8. Since peak intensities are large due to strong dipole moment between carbon and fluorine, they mask any small changes that would be attributable to either substrate SiO_2 or rubrene bonding. However, some scaling is seen. The surface with the highest intensity was FTS on spun rubrene. The surface with the second highest intensity is SiO_2 whose hydroxyl groups might be attractive for FTS bonding. The surface with the third highest intensity is $\text{O}(\text{C}_{18})\text{TS}$ -blocked SiO_2 , while the fourth and least intense peaks are found when FTS is on bulk rubrene on $\text{O}(\text{C}_{18})\text{TS}$ -blocked SiO_2 .

Figure 5.8, The FTS referenced to O(C₁₈)TS on thin SiO₂ (black curve)



The FTS should not be able to bind to any SiO₂ through the O(C₁₈)TS-terminated layer. Assuming O(C₁₈)TS completely prevents FTS from bonding with the SiO₂ surface, any peak that is not found in FTS bonding with O(C₁₈)TS (unlikely) but is present in FTS bonding with SiO₂ (likely) should indicate which peak is attributable to FTS-SiO₂ bonding. The 1072 cm⁻¹ peak was previously assigned to substrate SiO₂ bonding, but is refuted by its presence in the black line spectrum in Figure 5.8, with FTS deposited on O(C₁₈)TS which should not allow substrate SiO₂ bonding. The peak at 1072 cm⁻¹ may instead originate from a CF stretch mode.

Figure 5.8, The FTS referenced to bulk rubrene on O(C₁₈)TS, thin SiO₂ (blue curve)



Rubrene was deposited by bulk casting from a xylene solution in a nitrogen-purged glove box, because the O(C₁₈)TS layer made surfaces so hydrophobic that the solution would not accept a spun casting film with infrared absorption, even after several casts. As the bulk-cast solution dried, rubrene crystals precipitated and formed a large rubrene particle cluster in the center of the wafer. Although rubrene peak intensity was at least as large as that observed in a spun cast film, peaks appear distorted and broader (not shown). The peak at 1124 cm⁻¹ assigned to Si-O-C rubrene-silane bonds had higher

intensity on bulk rubrene with respect to the peak at 1163 cm^{-1} . Therefore, the enlargement of that peak with respect to the tail body bonds nearby suggests additional rubrene bonding, perhaps due to the increased surface area of the precipitated crystals. However, this assignment is made with much reservation because of the presence of the same peak position in the FTS on oxide (red) and FTS on OC₁₈TS blocked oxide (black).

The peak thought to be affiliated with rubrene bonding (1124 cm^{-1}) scaled up with respect to 1163 cm^{-1} in the blue bulk rubrene spectra. New peaks at 980 cm^{-1} and 814 cm^{-1} appeared, perhaps as a result of FTS interaction with bulk rubrene. The 980 cm^{-1} peak could be attributed to an aromatic C-H bend (NIST, benzene, 975 cm^{-1}) that was disturbed in the underlying rubrene layer. The peak at 814 cm^{-1} can be found in deuterated benzene (NIST, benzene-d₆, 814 cm^{-1}) and may be analogous here to the perturbation of aromatic ring hydrogen molecules by the proximity of the electronegative fluorine atoms. However, the use of a single aromatic ring as a comparison for the bonding signature of an extended fused ring structure of rubrene is not direct because of the differences in structure. The exacerbation of the peaks at 980 cm^{-1} and 814 cm^{-1} in the bulk rubrene sample as opposed to the spun samples may be due to the higher concentration of rubrene material in the beam path, with additional in-homogeneity and roughness not seen in the spun rubrene films.

The silane-rubrene bonding peak assignment was supported at 1124 cm^{-1} , while the predicted SiO₂ interaction peak at 1072 cm^{-1} was refuted. A bulk FTS deposition on rubrene would confirm the SiO₂ and body mode assignments, since the body and networking modes should increase with film thickness while the interfacial SiO₂ mode should not.

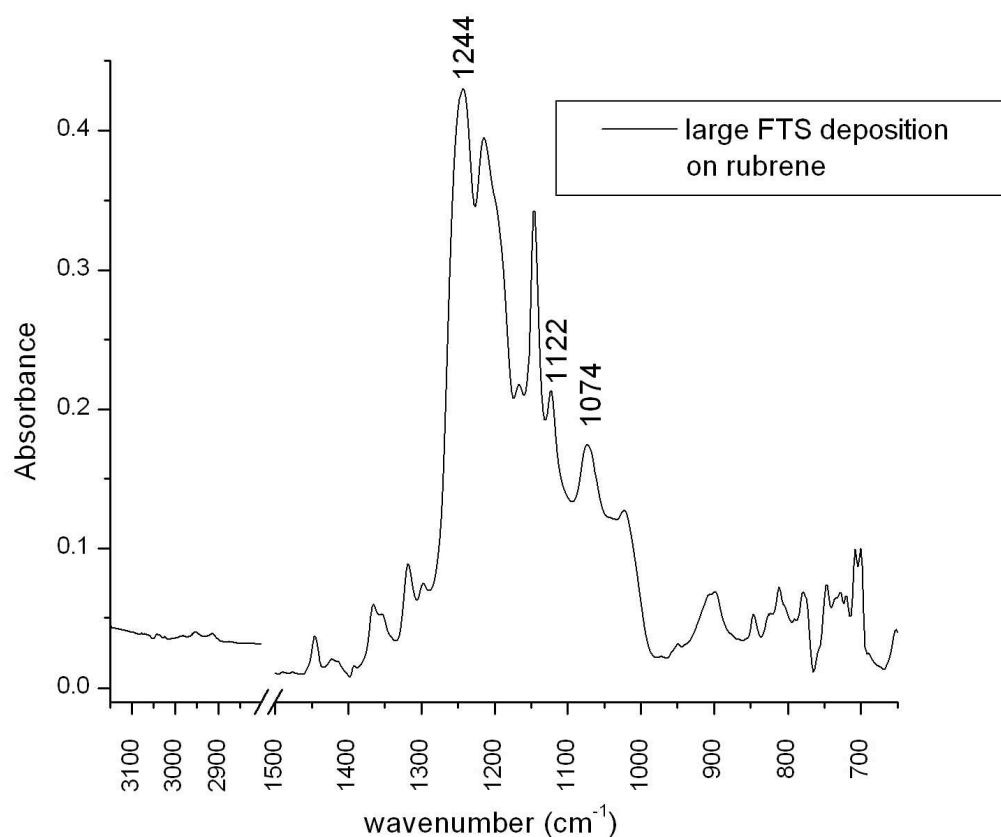


Figure 5.9. Excess FTS deposition on a rubrene-SiO₂ surface.

Figure 5.9 shows the result of excess FTS deposition on rubrene. The peak at 1244 cm⁻¹ was still the largest and confirms its assignment to CF stretching or CH bending. The 1074 cm⁻¹ peak intensity also scaled with excess coverage. The ratio of 1244 cm⁻¹ to 1074 cm⁻¹ peak intensity in the monolayer condition was 3.2, while the excess was 2.5. Thus the peak at 1074 cm⁻¹ grew with respect to 1244 cm⁻¹ as a result of excess coverage. This can be explained by the proximity to other chain body modes that inherently increased and shifted the 1074 cm⁻¹ shoulder peak intensity. This scaling suggests 1074 cm⁻¹ might be related to networking instead of to a substrate SiO₂ bond. Therefore the 1074 cm⁻¹ and 1018 cm⁻¹ peaks make up the TO/LO silane networking or polymerization phonon mode pair. It may be that 1074 cm⁻¹ is related to networking and

1018 cm^{-1} is related to polymerization based on the prior assignment of 1018 cm^{-1} .

Therefore, depositing FTS directly on SiO_2 where there is no rubrene or carbon for silane bonding would confirm peak assignments to SiO_2 bonding: 1072 cm^{-1} if the peak position shifted with different SiO_2 thicknesses. The SiO_2 bond should shift to higher wavenumber on thick SiO_2 , according to previous studies on methyl trichlorosilane; the peak shift should be similar to that of OTS Si-O-Si(s) on thermally deposited thick SiO_2 at 1256 cm^{-1} and on thin, chemically grown SiO_2 at 1236 cm^{-1} (Li 2007). Therefore, since FTS on thin, chemically grown SiO_2 is suspected to have a peak at 1074 cm^{-1} , it should shift to $\sim 1094 \text{ cm}^{-1}$ on thick SiO_2 .

No peaks showed a shift in position with different SiO_2 thickness; however, the peak at 1167 cm^{-1} , previously attributed to the C-C-C tail body stretch, seems disproportionately suppressed on the thick SiO_2 (Figure 5.10). The expected peak shift associated with Si-O-Si(s) on different SiO_2 thicknesses was not observed and may be explained by the large dipole moment of fluorine preventing substrate SiO_2 phonon resonance. Substrate bonding is confirmed by the negative 962 cm^{-1} peak in the thick SiO_2 spectra attributed to removal of Si-OH surface bonds but did not reveal any substrate bonding peaks identified by shifting. The presence of a peak at 1124 cm^{-1} here in the spectra for FTS on SiO_2 further refutes its assignment to the Si-O-C rubrene-silane bond.

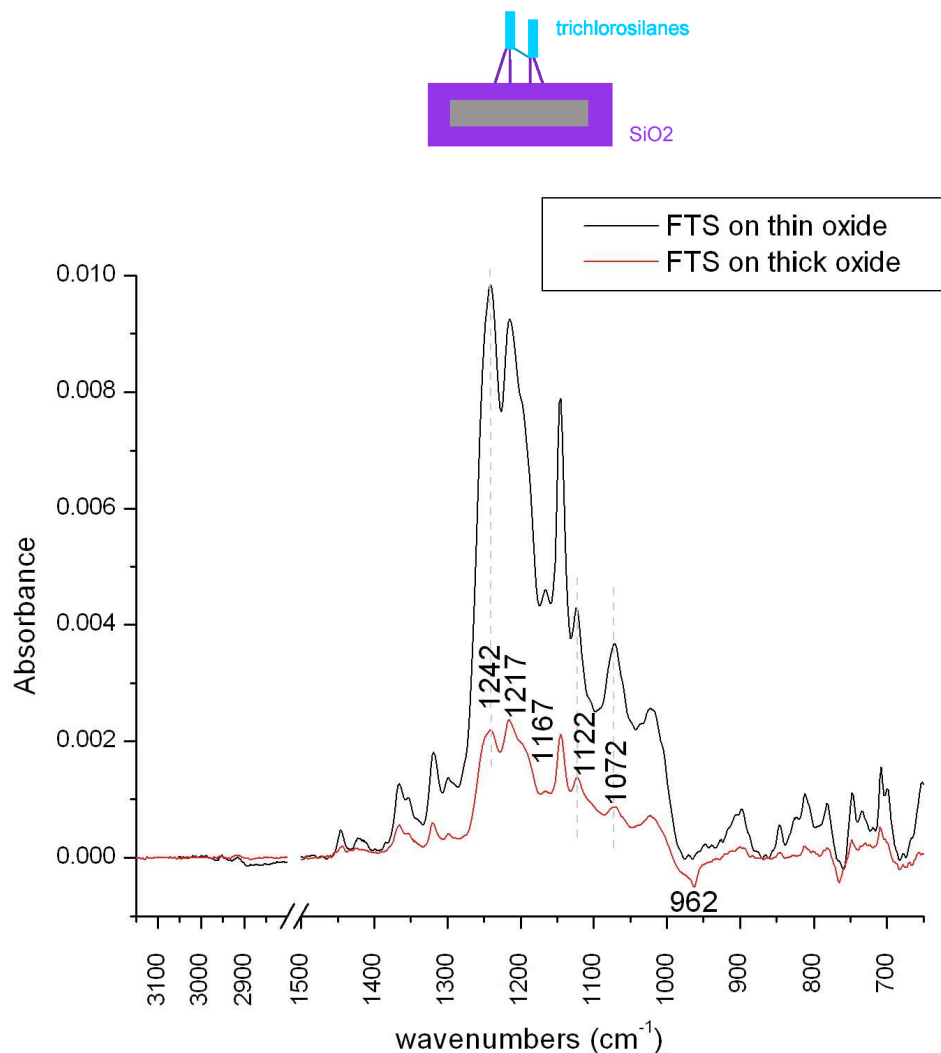


Figure 5.10. Separate FTS depositions on thin chemical SiO₂ and thick chemical SiO₂. The thick SiO₂ FTS deposition showed incomplete rubrene surface current enhancement (not shown).¹

A scaling experiment where FTS coverage is decreased in order to minimize the strong body peaks in an effort to distinguish the low-intensity substrate and rubrene-bonding peaks would help to de-convolute the bonding events. Also, a comparative deposition on KBr pellets should potentially remove substrate SiO₂ bond peaks and bring greater clarity for a rubrene-bonding assignment. Less corrosive derivatives of the FTS molecule with one chlorine group (FMS) were compared with a molecule having a

¹ The thick-SiO₂ reference was substituted with a similarly prepared sample.

hydroxyl group (FOH) instead of chlorine using the gas cell for saturated vapor pressure exposures. The FMS was investigated to determine the position of networking peaks that should be present in FTS but missing in FMS spectra. The surface current enhancement from FMS exposure was used to validate the exposure procedure shown in Figure 5.11.

5.4.2 FMS Bonding with Rubrene

The silane network bond Si-O-Si between two surface-bound silanes Si-O-Si(s) has not been identified. This might be found by studying the FMS molecule, whose single chlorine-bonding group cannot network with neighboring silanes while also bonding with either SiO₂ or rubrene. To further study rubrene-silane bonding, molecules with different anchor groups, such as hydroxyl and mono-chlorinated silane, were deposited on rubrene spun on thermal SiO₂. The FMS contains one silane chlorine anchor group, which will not allow stabilizing cross-linking of molecules bonded to rubrene or SiO₂.

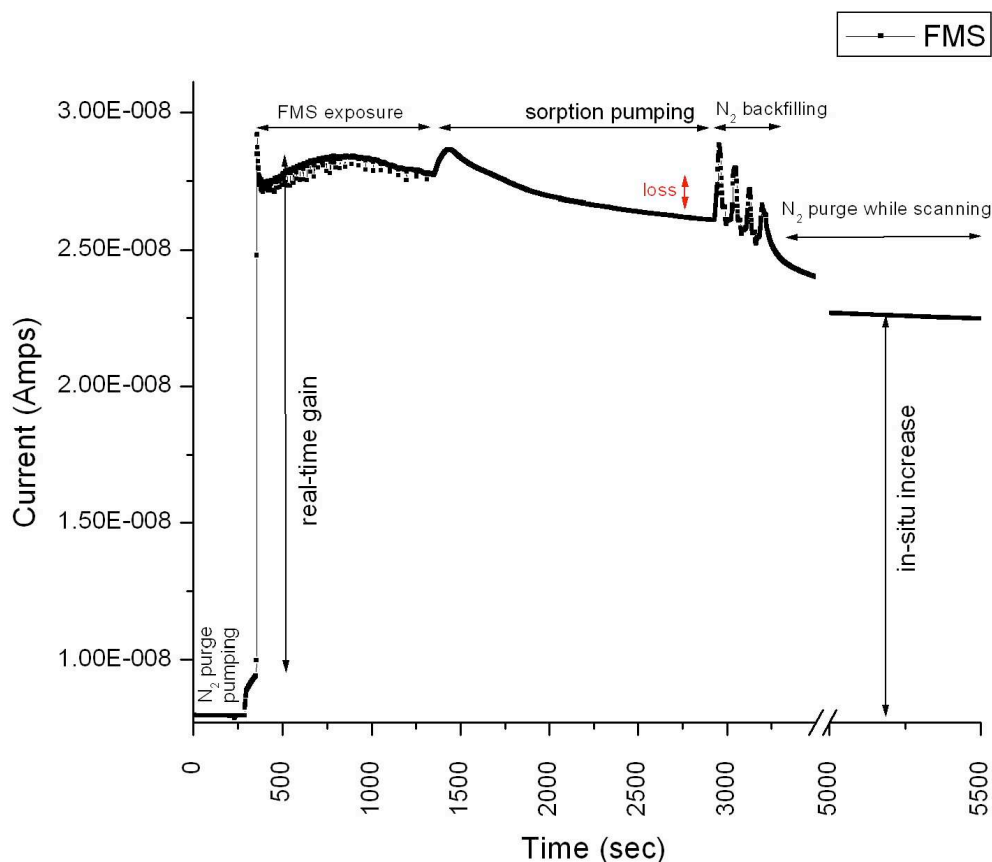


Figure 5.11. Rubrene-crystal-surface current increased as a result of saturated vapor pressure FMS exposure.

	FMS
Real time increase	1.89×10^{-8} Amps
In-situ increase	1.47×10^{-8} Amps
Enhancement loss	9%

Table 5.1. Rubrene Surface Current Enhancement Quantification From FMS Exposure

The FMS readily condensed on the gas cell and system surfaces; system pressure decreased after exposure whenever the sorption pump was not actively pumping the system. Therefore the system was actively pumped during the exposure to the liquid source. In order to remove unreacted FMS vapors, the system was pumped for 25 minutes while the source was isolated. Very little reversal of the initial current enhancement (9%) occurred with sorption pumping as shown in Table 5.1. This agrees

with the previous OMS results and matches the literature (Tripp and Hair 1995), which described monochlorinated silanes more readily bonding with SiO_2 than trichlorinated silanes; however, a comparison to FTS pumping stability was not made. Also, the fluorine groups may make the FMS more reactive to rubrene and SiO_2 surfaces than OTS in dry, room temperature surface conditions (Tripp, Veregin and Hair 1993).

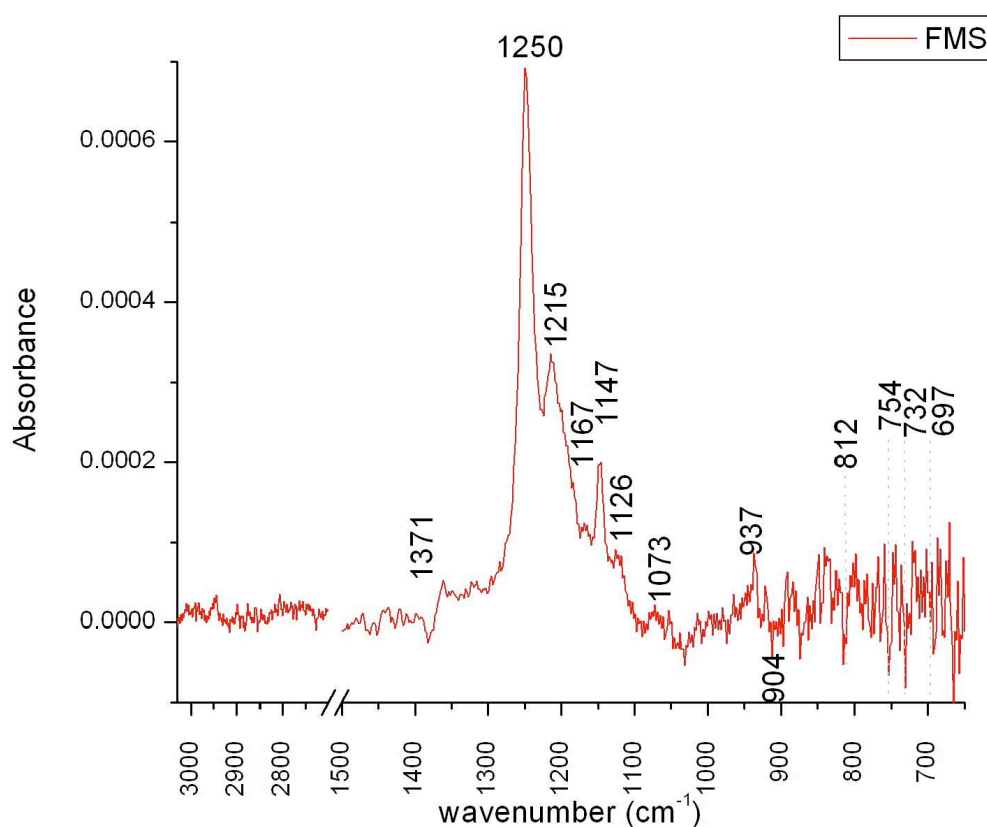


Figure 5.12. The infrared absorption signature of FMS referenced to the spun film of rubrene on thick SiO_2 (65Å) prior to the exposure.

The intensity of the FMS on rubrene- SiO_2 peaks was less than that for FTS on rubrene- SiO_2 as a result of depositing FMS for a shorter time in our gas cell (Figure 5.12) that was done in our collaborator's dedicated system. Therefore, peak intensity cannot be directly compared; however, peak positions that have shifted can be compared. The peak

assigned to one of many CF or CH tail body modes at 1246 cm^{-1} shifted to 1250 cm^{-1} . Another tail body peak at 1165 cm^{-1} shifted to 1173 cm^{-1} . The unassigned peak at 1126 cm^{-1} shifted to 1124 cm^{-1} . The origin of shifting may be due to a difference in the disorder of the two systems. Since both the FTS and FMS surface current measurements showed a plateau of current enhancement, it can be predicted that a monolayer of coverage occurred in both experiments. However, the FMS exposure was conducted for a much shorter time than FTS exposure.

The networking peak at 1072 cm^{-1} appears much smaller in the FMS spectra than FTS, which confirms its networking assignment. The 1018 cm^{-1} peak is also very small, as expected since polymerization is not possible. This supports its assignment to silane polymerization but it does not rule out an assignment to a networking mode (Tripp, Veregin and Hair 1993).

5.4.3 FOH Bonding with Rubrene

While FOH has a terminal hydroxyl group it does not have the necessary chlorine groups to bind to the SiO_2 . Its affiliation toward the rubrene surface could only be through hydrogen bonding. Therefore, we expect a strong reversal of the surface current enhancement (Figure 5.13) and very small chemisorption infrared peaks (Figure 5.14).

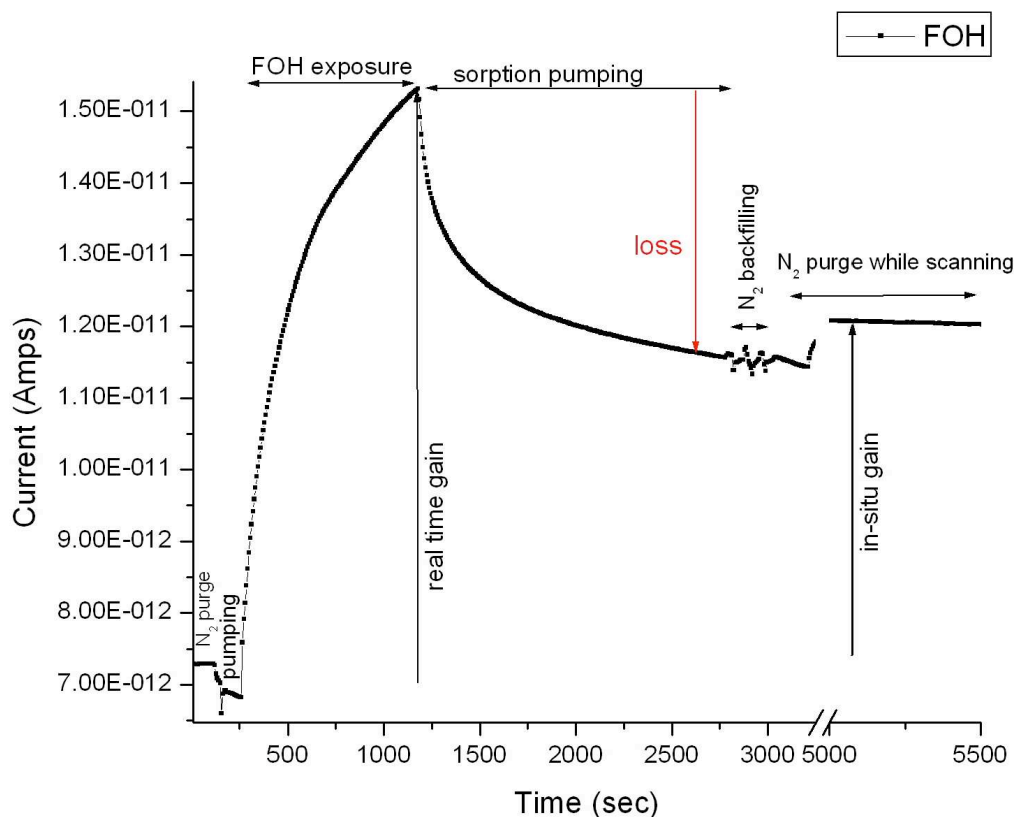


Figure 5.13. Real-time rubrene crystal surface current enhancement during FOH exposure.

	FOH
Real time increase	8.52×10^{-12} Amps
In-situ increase	4.79×10^{-12} Amps
Enhancement loss	44%

Table 5.2. Rubrene Surface Current Enhancement Quantification from FOH Exposure

The surface current enhancement of the rubrene crystal surface current by the FOH molecule shown in Figure 5.13 is not stable to sorption pumping, as evident by the 44% loss shown in table 5.2. The low initial surface current was likely due to a wide spacing of the graphite contacts on the rubrene crystal. It is interesting to note that since there are no groups suitable for bonding FOH to rubrene, physisorption and hydrogen bonding are sufficient for a small increase in surface current that is unstable to sorption

pumping. This was expected, according to the reported increase and total removal from using FOH on rubrene (Calhoun, et al. 2008). Therefore, a low surface chemistry signature was expected as shown in Figure 5.14.

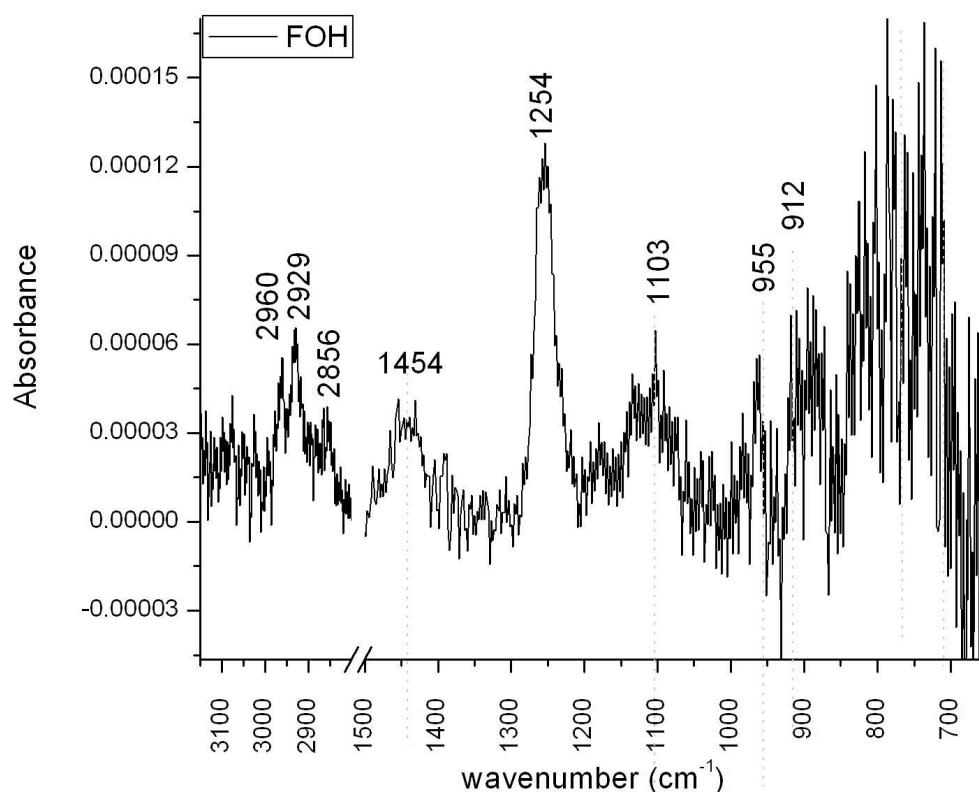


Figure 5.14. The infrared absorption signature of FOH referenced to the spun film of rubrene on thick SiO₂ (65Å) wafers prior to the exposure.

The peak intensity of the FOH spectrum is about six times smaller than that of the FMS spectrum. The surface-current enhancement from FMS bonding is much more than six times larger than the FOH effect. Therefore, a direct relationship between surface-current enhancement and the intensity of surface-chemistry peaks cannot be made.

Other than the peak at 1254 cm⁻¹, the FOH spectra is missing many peaks reported for CF₃(CF₂)₅CH₂CH₂OH (1126 cm⁻¹, 1151 cm⁻¹, 1216 cm⁻¹, and 1251 cm⁻¹) that

can be assigned to complex mixtures of molecular backbone modes associated with C-F and C-H stretches (Waterland, et al. 2005). The peak at 1256 cm^{-1} could be assigned to a methylene twist (Waterland, et al. 2005). Peak absorbance was also very low, indicating that its vapor pressure ($<\sim 200\text{mTorr}$) may have been below the vacuum level in the cell (5mTorr) or insufficient material remained in the vessel (Waterland, et al. 2005). Other researchers have used dosages with this vapor by flowing air diluents over a solid sample (Waterland, et al. 2005). However, similar molecules such as FMS and FTS, that presumably should have a similar vapor pressure were successfully deposited, using the same method. Given our experimental capability to measure surface current in real time, the complementary electrical data confirm that the deposition occurred. The electrical data also reveal that the deposition is highly reversible. Since the FOH does not contain any bonding groups it is not surprising that very little chemical bonding occurred and also confirms the reversible effect noted by Calhoun (Calhoun, et al. 2008). Other broad peaks at 1454 cm^{-1} , 2856 cm^{-1} , 2929 cm^{-1} , and 2960 cm^{-1} indicate tail body modes.

5.5 Conclusions

In summary, the infrared absorption of FTS was analyzed with several different substrates to distinguish tail body peaks from silane-rubrene bonding, silane polymerization, and silane networking. Strong FTS body modes were identified at 735 cm^{-1} , 746 cm^{-1} , 1147 cm^{-1} doublet, 1165 cm^{-1} , 1217 cm^{-1} , 1244 cm^{-1} , 1319 cm^{-1} , 1365 cm^{-1} , and possibly 937 cm^{-1} and 949 cm^{-1} from an initial FTS deposition on a spun rubrene film. Bulk rubrene deposition showed the scaling of a peak near 1124 cm^{-1} , which may originate from a rubrene-silane bond, but the presence of this peak on SiO_2 refuted this assignment. The presence of a peak at 1124 cm^{-1} on SiO_2 and $\text{O}(\text{C}_{18})\text{TS}$

reveals that further de-convolution and experiments to distinguish tail body peaks for validation of rubrene-silane peak are required. The FTS deposition on bulk rubrene upon blocked SiO₂ also revealed peaks that show rubrene aromatic (benzene) hydrogens are perturbed by the electronegative fluorine in the tail body. A silane-rubrene peak was not visible; however, the broad peaks for silane-bulk rubrene suggest a weaker interaction, strong enough to withstand the sorption pumping, and are responsible for the sustained increase in rubrene surface current. Although we have not identified a rubrene-silane bond, again, we have not ruled out its presence.

Silane networking was observed at 1072 cm⁻¹ and possibly 1018 cm⁻¹ (polymerization) due to their absence from the FMS on rubrene spectrum. The FOH molecule produces a rubrene surface current enhancement that is not stable against sorption pumping. However, a few small features remain on the surface that may be the result of limited contamination.

Now that the surface current of rubrene has been enhanced with FTS pretreatment, we can now move to investigate the acetone sensing ability of the surface. This will be explored in Chapter 6 using the solvent exposure procedures described in Chapter 2. The sensing ability of rubrene pretreated films and crystals will be compared with sublimated organic semiconductor films and organic transistor devices with similar current in Chapter 6. We predict the strong dipole of FTS will attract polar solvents to the rubrene surface and facilitate a stronger sensing response than pentacene and C6 transistors in Chapter 6.

5.6 References

1. Banga, R.; Yarwood, J., FTIR and AFM Studies of the Kinetics and Self-Assembly of Alkyltrichlorosilanes and (Perfluoroalkyl)trichlorosilanes onto Glass and Silicon. *Langmuir* 1995, 11, 4393-4399.
2. Banga, R.; Yarwood, J.; Morgan, A. M.; Evans, B.; Kells, J., In-Situ FTIR studies of the kinetics and self assembly of alkyl and perfluoroalkyl trichlorosilanes on silicon. *Thin Solid Films* 1996, 284-285, 261-266.
3. Calhoun, M. F.; Sanchez, J.; Olaya, D.; Gershenson, M. E.; Podzorov, V., Electronic functionalization of the surface of organic semiconductors with self-assembled monolayers. *Nature Materials* 2008, 7, 84 - 89.
4. Chang, J.-F.; Sun, B.; Breiby, D. W.; Nielsen, M. M.; Sölling, T. I.; Giles, M.; McCulloch, I.; Sirringhaus, H., Enhanced Mobility of Poly(3-hexylthiophene) Transistors by Spin-Coating from High-Boiling-Point Solvents *Chemistry of Materials* 2004, 16, (23), 4772 -4776.
5. Dong, J.; Wang, A.; Ng, K. Y. S.; Mao, G., Self-assembly of octadecyltrichlorosilane monolayers on silicon-based substrates by chemical vapor deposition. *Thin Solid Films* 2006, 515, 2116-2122.
6. Harvey, M. C.; Nebergall, W. H., The Silicon-Phenyl Asymmetrical Stretching Vibration *Applied Spectroscopy* 1962, 16, (1), 12-14(3).
7. Kulkarni, S. A.; Vijayamohan, K. P., Interfacial behavior of alkyltrichlorosilane monolayers on silicon: Control of flat-band potential and surface state distribution using chain length variation. *Surface Science* 2007, 601, 2983-2993.
8. Li, M. Modification of Silicon By Self-Assembled Monolayer For Application in Nano-Electronics and Biology. Rutgers, The State University of New Jersey, New Brunswick, 2007.
9. Michalak, D. J.; Rivillon, S.; Chabal, Y. J.; Esteve, A.; Lewis, N. S., Infrared Spectroscopic Investigation of the Reaction of Hydrogen-Terminated, (111)-Oriented, Silicon Surfaces with Liquid Methanol. *Journal of Physical Chemistry B* 2006, 110, (4), 20426-20434.
10. Socrates, G., *Infrared and Raman Characteristic Group Frequencies Tables and Charts*. 3 ed.; John Wiley & Sons Ltd.: West Sussex, England, 2001; p 347.
11. Tripp, C. P.; Veregin, R. P. N.; Hair, M. L., Effect of Fluoroalkyl Substituents on the Reaction of Alkylchlorosilanes with Silica Surfaces. *Langmuir* 1993, 9, (12), 3518-3522.
12. Tripp, C. P.; Hair, M. L., Reaction of Methylsilanols with Hydrated Silica Surfaces: The Hydrolysis of Trichloro-, Dichloro-, and Monochloromethylsilanes and the Effects of Curing. *Langmuir* 1995, 11, 149-155.
13. Waterland, R. L.; Hurley, M. D.; Misner, J. A.; Wallington, T. J.; Melo, S. M. L.; Strong, K.; Dumoulin, R.; Castera, L.; Stock, N. L.; Mabury, S. A., Gas Phase UV and IR absorption spectra of CF₃CH₂CH₂OH and F(CF₂CF₂)_xCH₂CH₂OH (x=2,3,4). *Journal of Fluorine Chemistry* 2005, 126, 1288-1296.
14. Wen, K.; Maoz, R.; Cohen, H.; Sagiv, J.; Gibaud, A.; Desert, A.; Ocko, B. M., Postassembly Chemical Modification of a Highly Ordered Organosilane Multilayer: New Insights into the Structure, Bonding, and Dynamics of Self-Assembling Silane Monolayers. *ACS Nano* 2008, 2, (3), 579-599.

CHAPTER 6: INVESTIGATING ORGANIC SEMICONDUCTOR KETONE AND ALCOHOL GAS SENSING

6.1 Abstract

Organic transistors, constructed using sublimated C6 and pentacene thin films with evaporated gold contacts, were studied, using infrared absorption spectroscopy (IRAS) and electrical measurements on the same substrate. Rubrene spun films were also investigated with IRAS while surface current was evaluated with a separate rubrene single crystal (pretreated with a perfluorinated alkyl silane self-assembled monolayer (SAM)). Exposure of acetone vapors to pentacene, C6, and rubrene surfaces suppressed device current, an effect that was found to be only partially reversible. Only one material exposure could be performed on each sample, due to changes in the surface current response observed with a rubrene single crystal with different series ordering. The thickest pentacene thin film (1500 Å) produced the highest infrared absorption response to saturated acetone vapors with intense differential peaks. The differential peaks were reproduced by a surface cooling effect. However, the degree of surface cooling predicted does not fully account for the magnitude of the transistor drain-source current suppression. The surface current of rubrene crystals pretreated with a sub-monolayer perfluorinated SAM layer was reduced by saturated acetone exposure due to a disruption or removal of the spun rubrene film. Surface current reduction saturation was not observed if SAM coverage was allowed to saturate where IRAS suggests FTS removal from the spun rubrene film. Successive acetone exposure to saturated FTS-covered rubrene was more reversible (63 - 75%) and had larger response (1.8×10^{-6} - 1.5×10^{-6} amps) than sub-monolayer FTS coverage. This is greater than the response of pentacene (1.0 - 1.6×10^{-6} amps) and C6 ($\sim 2.9 \times 10^{-7}$ amps). Therefore, the best sensing material

tested was a rubrene single crystal with graphite contacts coated with a saturated FTS layer.

6.2 Introduction

The projected low cost of organic transistors due to large-area processing makes such devices attractive for disposable chemical sensors. Exhaled volatile organic compounds such as ethanol and ketones could be used as markers for non-invasive diagnostic monitoring of blood alcohol level and ketoacidosis, respectively. Several organic semiconducting materials have been used as organic transistor chemisensors; however, an understanding of the sensing mechanism that differentiates their selectivity has not been established. Characteristics of candidate materials for organic transistor chemisensors include the following: measurable current (micro-amps), selectivity, reversibility, and reusability.

Organic field-effect transistors are often constructed from sublimated or spun cast pentacene thin films, because pentacene is considered a robust material that produces sufficient field-effect mobility (Gundlach, et al. 1997). Therefore, we validate pentacene transistor performance before perturbing and monitoring the response to acetone and ethanol vapors. Surface chemistry was evaluated for saturated and unsaturated vapor pressure exposures. Successive exposures were performed to reveal whether the surface chemistry is consistent for successive exposures.

Rubrene has also been demonstrated to be a very high mobility organic semiconductor material (Podzorov, et al. 2003). Recently, the enhancement of rubrene surface current with SAMs or alkyl and perfluoralkyl trichlorosilanes made possible the demonstration of surface current response to acetone vapors (Calhoun, et al. 2008).

Solvent sensing through the suppression of organic thin-film, field-effect transistor drain-source current has been demonstrated to have variable selectivity. Reversible polar solvent vapor sensing was demonstrated by silane-enhanced rubrene surface current perturbation (Calhoun, Sanchez, Olaya, Gershenson and Podzorov 2008). Polar solvents caused a decrease in rubrene crystal surface current while non-polar solvents produced a weak increase in surface current (Calhoun, Sanchez, Olaya, Gershenson and Podzorov 2008).

Rubrene chemisensing is not fully understood and offers an opportunity to study the surface chemistry (Calhoun, Sanchez, Olaya, Gershenson and Podzorov 2008). The unknown mechanism of the reversible and non-specific interaction of gases with organic transistors (indicated by drain-source current suppression) has prevented the development of selective gas sensors based on organic electronics. Therefore, a similar in-situ infrared analysis of analyte vapor interaction with rubrene spun-cast thin films will be used to study the factors influencing surface interaction of alcohol vapors.

A family of bithiophene, phenol-linked aromatic molecules with alkoxy tails, including the same material we study, 5,5'-bis-4-(6-hydroxyhexyloxy)-phenyl-2,2'-bithiophene (C6), was shown to be a chemisensor for phosphonate functional groups (Huang, et al. 2007; Huang, et al. 2008). We performed an in-situ infrared analysis of C6 and compare the sensing interaction according to infrared absorption analysis of this material to that of pentacene and rubrene.

Infrared absorption spectroscopy can provide information about intermolecular material interactions that we postulate will occur with organic thin-film sensing. Interactions with the electron distribution of an aromatic molecule include pi-bonds and

free electron pairs that could participate in hydrogen bonding with solvents (Kiselev and Lygin 1975), p. 5). Although the interacting molecules remain intact, their interaction can affect the spectra of both molecules.

Generally, the wavenumber of a molecular peak is due to the masses of atoms and the force constant of their bonds. The wavenumber can also be affected by external influences, such as a surrounding solvent (Conley 1972). Polar solvents, such as acetone and ethanol, could cause the peaks of materials they interact with to shift to lower wavenumbers with increasing solvent polarity (Conley 1972), p. 85). Likewise, solvent peaks could shift with hydrogen bonding. In alcohols, a hydroxyl group that is not hydrogen bonding has a peak at 3640 cm^{-1} (primary alcohols) that is shifted to $3500 - 3600\text{ cm}^{-1}$, an electron-rich group with weak hydrogen bonding (Conley 1972), p. 129, 131). Alcohol out-of-plane bending (near 650 cm^{-1}) shifts to higher wavenumbers with increased hydrogen bonding (Conley 1972), p. 136). Hydrogen bonding with an acetone molecule should cause both the acetone C=O peak to shift to lower wavenumber as well as the peaks of the species it was hydrogen bonding with (Zhang, et al. 2005). Acetone dimer hydrogen bonding may also be apparent at 920 cm^{-1} (Conley 1972), p. 154).

We investigated the molecular modes of structures similar to organic sensor aromatic molecules, and postulated that molecules adsorbed into the film with close proximity to the surface material have a similar substitution effect on wavenumber position shifting. Aromatic out-of-plane bending (below 900 cm^{-1}) is normally more intense than in-plane bending ($1275 - 960\text{ cm}^{-1}$) and is used to determine the number of ring substituents (Conley 1972), p. 112). Out-of-plane bending peaks shift to higher wavenumbers with the substitution of an electron-attracting groups such as N (Conley

1972), p. 113). When a double bond to oxygen is inserted into an aromatic ring (cyclohexanone), the intensity of the double bond vibration increases and shifts to a lower wavenumber (Conley 1972), p. 156). As the number of adjacent hydrogens around the aromatic ring decreases from five (the maximum for benzene) due to substitutions, their frequency increases from $730 - 770 \text{ cm}^{-1}$ to as high as $860\text{-}900 \text{ cm}^{-1}$ (Conley 1972), p. 117).

The intensity of an IRAS peak is in part related to the dipole moment of the molecule with respect to the position of its vibrating structure as well as the bond environment (Kiselev and Lygin 1975), p. 40, 42). Thus, C-H bonds are less intense than C-O bonds (Conley 1972), p. 138) due to the smaller dipole moment despite their similar masses. The delocalized electrons of aromatic molecules give rise to polarized electron orbitals, especially those in electrostatic crystal structures, whose charge can be redistributed by an adsorbent, and thus affect their peak intensity (Kiselev and Lygin 1975), p. 42).

Saturated and sub-saturated vapor pressure responses of organic thin films were studied in order to see small changes in surface chemistry preceding the response at saturation. Lower exposures also provide information regarding the sensor's ability to detect lesser quantities; however, the sensor detection limit is not addressed here. The infrared signature of successive surface exposures was used to test for reversibility and reusability. The saturation response is presented as differential spectra where the spectra represent the incremental as opposed to cumulative changes in the film. We investigated the interaction of these materials with acetone and ethanol vapors. Acetone is studied

more extensively due to the unique signature of the C=O double bond in infrared absorption of acetone thin films.

A unique gas exposure chamber was developed to allow for chemical analysis of alcohol interaction with organic thin films as well as simultaneous measurement of the current response. Unfortunately, difficulties encountered with connecting gold wires to evaporated gold pads, using silver paint, may undermine the chemisensing response due to the solubility of the silver paint in the exposure solvents.

6.3 Materials and Methods

6.3.1 Chemicals

SPI Flash Dry Silver Paint (04998-AB) was used to connect gold wires to evaporated gold pads. Pentacene was used as received from Sigma-Aldrich. The Podzorov-Gershenson group provided rubrene single crystals with painted graphite contacts. (Trideca-fluoro-1,1,2,2-tetrahydrooctyl)trichlorosilane (FTS) (SIT8174.0), and n-Octyltrichlorosilane (OTS) (SIO6713.0) were used as received from Gelest. Xylene (isomers plus ethyl-benzene) was used as received from Sigma-Aldrich (247642). 5,5'-bis-4-(6-hydroxyhexyloxy)-phenyl-2,2'-bithiophene (HOC6PTTPC6OH) was synthesized according to our previous publication (Stokes, et al. 2007).

6.3.2 Substrates

Double-sided polished, moderately doped, silicon (111) wafers (0.75" x 1.46") with 1218Å of thermally deposited silicon dioxide (SiO₂) were cleaned with acetone, methanol, water, and a 90°C piranha solution (7:3 sulfuric acid:hydrogen peroxide) soak

for ten minutes before being used for pentacene and C6 substrates. The same cleaning procedure was performed for rubrene substrates (Si[100] 65Å SiO₂).

6.3.3 Thin-Film Deposition

Thin organic films, which were not easily dissolved in solvents such as pentacene and C6, were sublimated onto SiO₂ using a vacuum bell jar system. Rubrene, which can be dissolved in xylene, was spun coat onto SiO₂.

6.3.3.1 Organic Thin-Film Sublimation

The deposition of pentacene and C6 by vacuum sublimation require slightly different conditions for optimal field effect mobility transistors. These parameters are discussed below.

6.3.3.1.1 Pentacene

Using a bell-jar sublimator with a vacuum of at least 5×10^{-6} Torr, a crucible filled with pentacene powder was slowly warmed through resistive heating. For slow pentacene preheating, an external power supply was set to 30 AC amps for the first 13 minutes, then 45 AC amps for the next ten minutes, and then 55 AC amps for 15 minutes before a consistent slow deposition rate of 0.1-0.3 Å/s was achieved. The current was adjusted to maintain a ~317°C crucible temperature. Film thickness and deposition rate were monitored, using a quartz crystal microbalance (QCM). The density and z-ratio used for organic films were 1.740 g/cm³ and 1.610 (unit-less)¹, respectively. During depositions, the substrate temperature increased from room temperature to at most 40° C. 800Å, 400Å, and 1500 Å-thick pentacene films were sublimated on both sides of silicon

¹ Film thicknesses were validated with Rutherford Backscattering (RBS).

wafers. Kapton tape blocked a pre-carved gate contact. 250Å-thick gold contacts were deposited through a molybdenum mask near the top edge of the sample by gold pellet evaporation.

6.3.3.1.2 C6

500Å of C6 was sublimated on both sides of a silicon wafer, using the same vacuum and preheating procedure as for pentacene. The sublimation temperature of C6 was $\sim 374^{\circ}\text{C}$ at 60AC amps for a high rate of deposition ($\sim 1.0 \text{ Å/s}$). Gold contacts were deposited as previously described. An example device with gold contacts above the beam path is shown below in Figure 6.1.

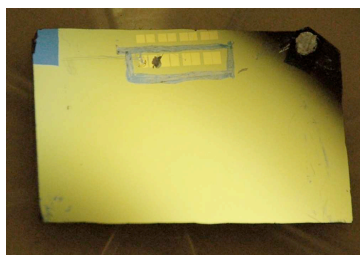


Figure 6.1. An organic field effect transistor device above the infrared beam-probed region. The dark shadows on the corners are photographic anomalies.

6.3.3.2 Sublimated Thin-Film testing

An infrared scan of each film was performed before the exposure. The clean substrate spectrum was subtracted to remove the background as described in Chapter 1. The transistor performance of each sublimated film was tested, using a Keithley 4200-SCS. Transistor performance of pentacene and C6 films were first evaluated by performing an I-V scan with use of the program shown in Figure 6.2a. To increase the number of data points for the field-effect mobility calculation, the drain-source current was measured at constant drain-source bias with a gate voltage sweep, using the program shown in Figure 6.2b.

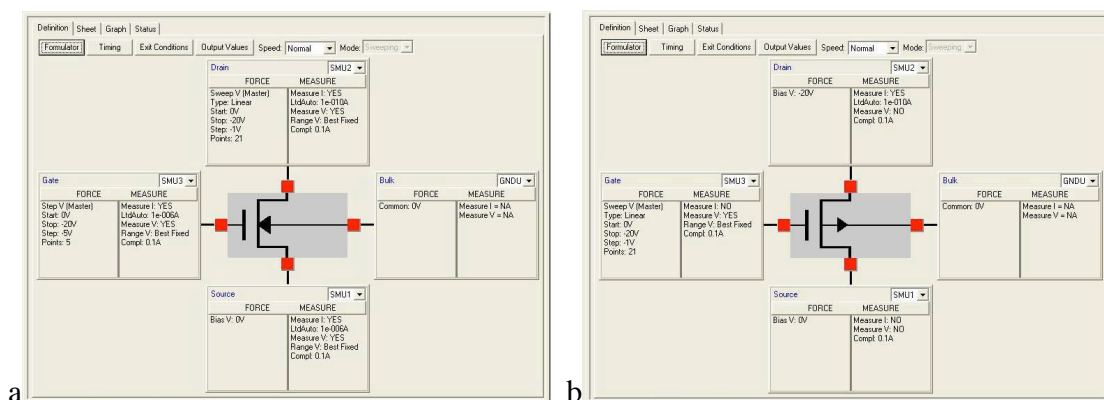


Figure 6.2. Keithley 4200-SCS programs for a: Ids-Vds transistor test; and b: Vg-Ids device test. The Ids-Vds program sweeps the drain source potential from 0 to -20 in -5V steps and then increments to the next gate voltage (in -5V increments) before sweeping the drain source potential again. The Vg-Ids program holds the drain source potential constant while sweeping the gate voltage.

To study how exposure vapors affect sublimated films, surface current was recorded over time, using the test program shown in Figure 6.3. Pentacene films were tested with -20V applied to the gate, and drain and the source at ground. The C6 film was tested with -50V applied to the gate and drain and the source at ground.

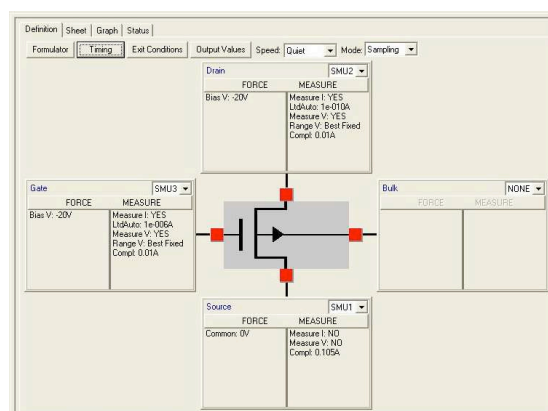


Figure 6.3. A Keithley 4200-SCS program for monitoring changes in drain-source current over time. Gate and drain voltages are held constant.

6.3.3.3 Spin Coating Rubrene Films

Rubrene was spun cast onto both sides of silicon wafers, using a 0.5% weight % solution of rubrene dissolved in xylene (Chang, et al. 2004) as described in Chapter 4.

6.3.4 Rubrene Crystal Preparation

Graphite contacts ($\sim 0.5\text{mm}$ -wide) spaced $\sim 1.5\text{mm}$ apart were painted on rubrene single crystals and attached to BNC feedthroughs with gold wires. Validation of the contacts' I-V linearity was performed with a Keithley 4200-SCS program. Figure 6.4a shows the test configuration where current is recorded while potential is swept from 0V to 20V. Applying 5V across the gold contacts, using the program shown in Figure 6.4b, tested current over time.

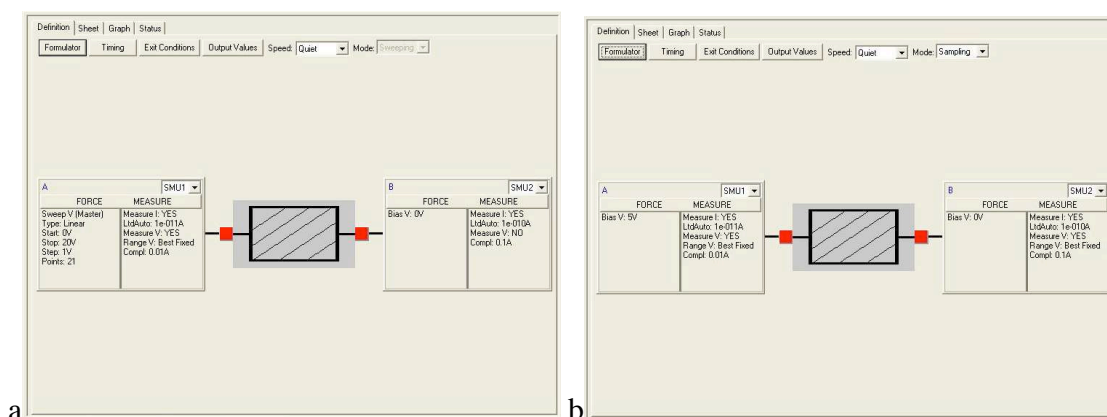


Figure 6.4. Keithley 4200-SCS test programs for evaluating: rubrene single-crystal contacts (a) and enhanced surface current over time (b).

6.4 Results and Discussion

The viability of testing a single rubrene sample sensing response with several analytes in succession is evaluated using IRAS and surface current measurements. This provided the basis for the solvent testing procedure of three organic semiconductor materials; pentacene, rubrene, and C6. The results of pentacene, rubrene, and C6 response to acetone vapors are presented below. Only the C6 material was tested with ethanol in comparison to acetone.

6.4.1 Investigating Rubrene Sensing Reversibility

To establish whether rubrene films can be exposed to successive solvent vapors and to test whether rubrene responds without a SAM-enhanced layer, sub-saturated vapor pressure solvents were exposed to rubrene spun films and single crystals. Since sensing interactions are expected to be reversible (using either N₂ or mechanical pumping for gas delivery and removal) (Calhoun, Sanchez, Olaya, Gershenson and Podzorov 2008), several solvents were exposed to the rubrene films in series. The surface current of a rubrene single crystal and the infrared surface chemistry of a rubrene spun film are presented. A current-voltage test was used to validate the presence of good rubrene crystal graphite contacts (not shown).

A non-polar solvent, such as pentane, should have a small positive effect on surface current, while polar solvents, such as acetone and ethanol, should decrease surface current (Calhoun, Sanchez, Olaya, Gershenson and Podzorov 2008). To validate that our system produced similar effects, we compared the surface current of rubrene single crystals during exposures to sub-vapor pressure acetone, methanol, and pentane (Figure 6.5). A sub-vapor pressure exposure, which should give a less intense response than saturated vapor pressure (Calhoun, Sanchez, Olaya, Gershenson and Podzorov 2008), was initially chosen to control the exposure volume and avoid gas phase solvent domination in the real-time infrared absorption spectra.

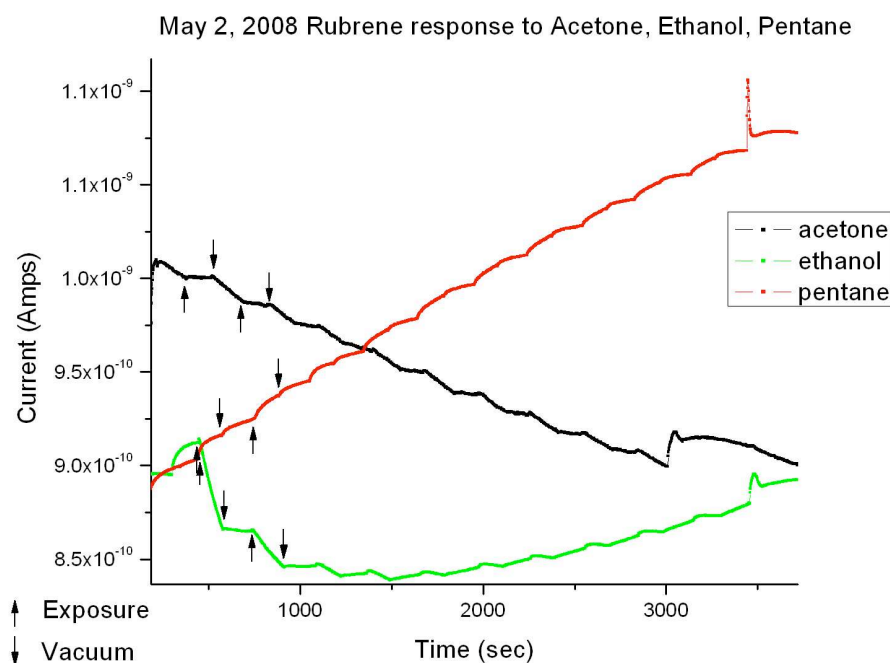


Figure 6.5. Rubrene crystal surface-current perturbation from a series of sub-saturated vapor pressure exposures to acetone, ethanol, and pentane. First few of ten solvent exposures (upward arrows). First few of ten sorption pumping (downward arrows). Final surface current jump at the end indicates a return to atmospheric pressure. (May 2, 2008)

Rubrene crystal surface current decreased slightly upon exposure to acetone and was reduced further by sorption pumping (Figure 6.5 and Table 6.1). The second solvent exposed to the same rubrene crystal, ethanol, produced a more dramatic decrease in surface current. This response saturated after the first two exposures. Ethanol removal by sorption pumping produced no change. The third solvent exposed to the same rubrene crystal, pentane, increased the surface current. This effect was continued with sorption pumping. The small changes to surface current agree with the direction of the expected response of a rubrene single crystal, coated with a perfluorinated alkyltrichlorosilane layer, to polar and non-polar solvents (Calhoun, Sanchez, Olaya, Gershenson and Podzorov 2008). Therefore, rubrene without silane pre-treatment responded with a small sensing effect to solvent exposure.

Solvent	Exposure Effect	Vacuumping Effect
Acetone	Small decrease	Decrease
Ethanol	Decrease	No change
Pentane	Increase	Increase

Table 6.1. The Effect of Various Solvents and Vacuum on Rubrene Surface Current

The surface current after the first solvent exposure (acetone) approximates the starting surface current before the second solvent exposure (ethanol). Also, since sorption pumping did not reverse the response to solvents, this suggests that solvent vapor interactions are not reversible. We next investigated the surface chemistry of spun rubrene films after solvent exposure. The infrared absorption of the native rubrene spun film before exposure is shown in Figure 6.6. This spectrum will be used to subtract the background from the solvent exposure spectra.

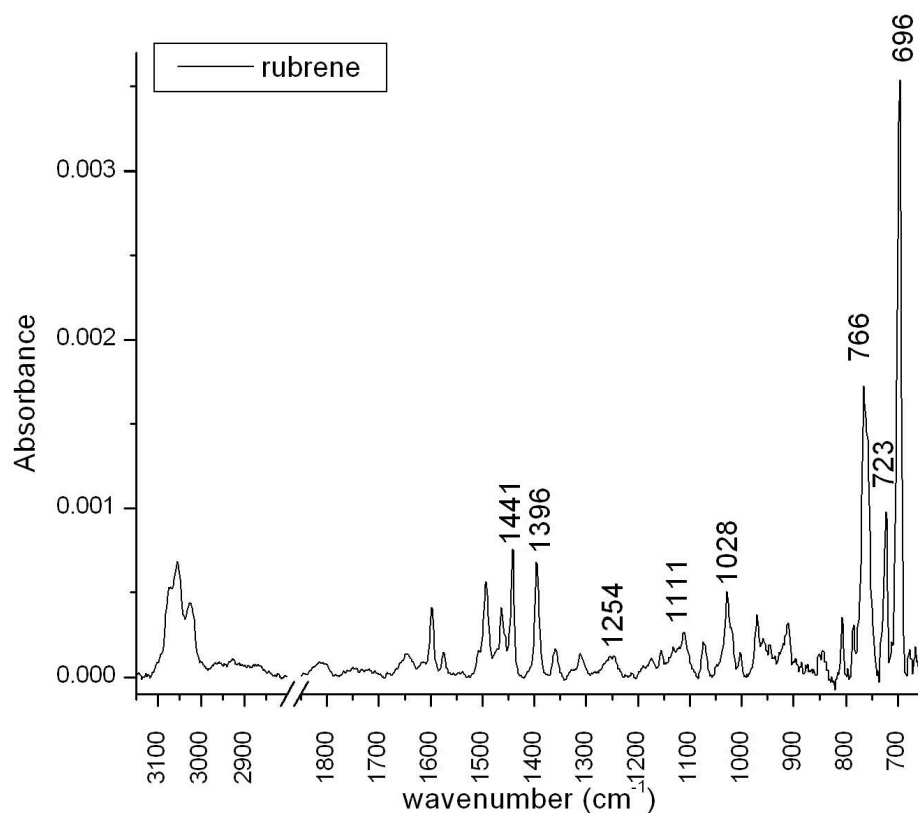


Figure 6.6. Spun rubrene film absorption spectrum. (May 2, 2008)

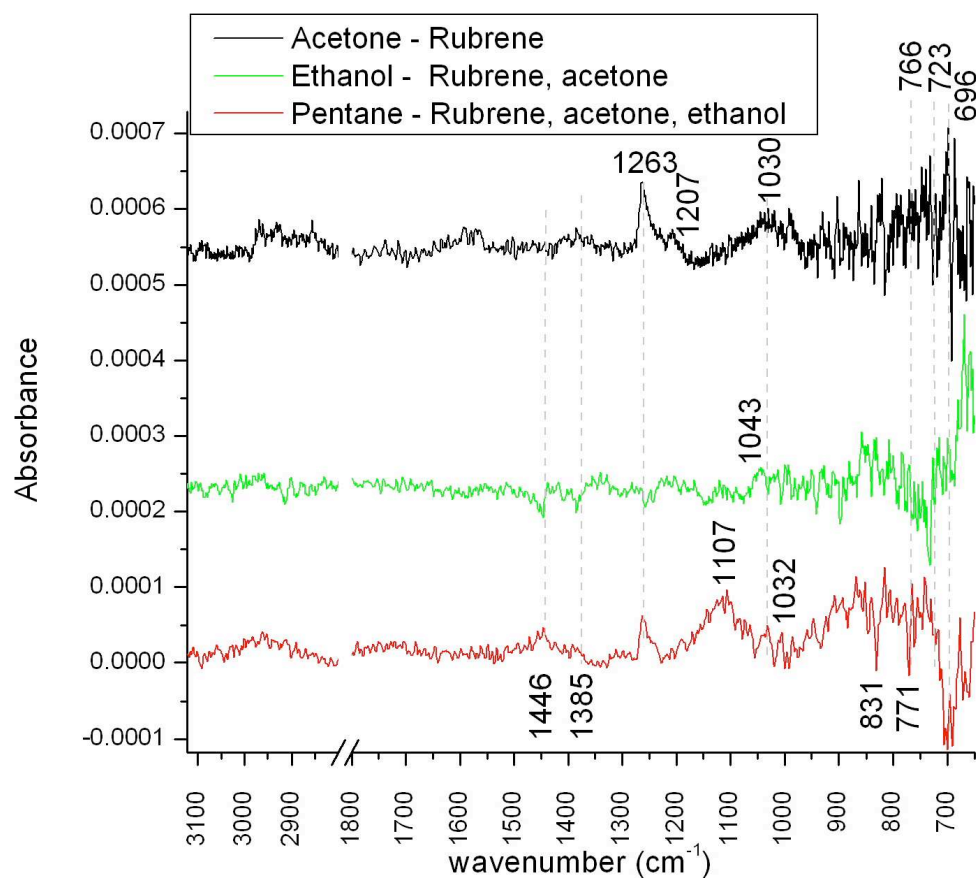


Figure 6.7. Differential infrared absorption spectra of rubrene without SAM after a series of sub-saturated vapor pressure exposures to acetone, ethanol, and pentane. (May 2, 2008)

Real-time spectra (averaged over ten exposures) showed a dominance of the solvent gas phase that prevented analysis of surface-bonded peaks (not shown).

Therefore, we present in-situ spectra taken before and after solvent exposure. The differential spectra in Figure 6.7 depict the effect of acetone exposure (black), the changes that occurred to the acetone exposed sample as a result of ethanol exposure (green), and the changes to the acetone- and ethanol-exposed sample as a result of pentane exposure (red).

A sharp peak at 1263 cm^{-1} and a broad peak at 1030 cm^{-1} appeared in both acetone and pentane exposure spectra. These are near rubrene spectral features at

1254 cm^{-1} and 1030 cm^{-1} , respectively. Therefore, since these peaks are in the in-plane aromatic C-H bending range, the proximity of the solvents must have changed the delocalized electron distribution to favor in-plane bending modes. Negative features at 831 cm^{-1} and 771 cm^{-1} in the pentane spectra (Figure 6.7), as well as negative features in the ethanol spectra at 1446 cm^{-1} , 1385 cm^{-1} , and possibly 1257 cm^{-1} are also near peaks shown in the original rubrene spun film, and further support a shift from out-of-plane C-H bending modes (below 900 cm^{-1}) toward in-plane bending modes (Figure 6.6). Finally, the peak at 831 cm^{-1} is one that had been affiliated with rubrene endoperoxide formation (Table 3.4). The peak at 831 cm^{-1} was attributed to C-O bending or simply out-of-plane bending (Table 3.4). The corresponding C-O stretch mode at 1245 cm^{-1} or 1260 cm^{-1} , however, does not scale in the same direction, since there is a positive peak at 1263 cm^{-1} (Figure 6.7). The peak at 1263 cm^{-1} was assigned to silane-SiO₂ (Chapter 4) due to its presence in silane-on-oxide spectra.

Since acetone vapors were delivered to the gas cell through the same tubing as OTS, the 1263 cm^{-1} peak may be the result of OTS contamination. The most dramatic increase in surface current in this set is produced by pentane, whose infrared signature includes the 1107 cm^{-1} attributed to OTS networking. Since pentane is a non-polar solvent, it may more readily dissolve and carry the hydrophobic OTS residue than polar solvents such as acetone or ethanol. To reduce potential contamination, the solvent line was repositioned to a dedicated port directed at the sample for later saturated vapor pressure experiments. Also, as a result of this order comparison, we discontinue the study of non-polar solvents, such as pentane, to avoid contamination.

Reversibility suggests the same response should occur when the solvents were exposed in a different order. When testing for reversibility, acetone was not exposed before ethanol and pentane.

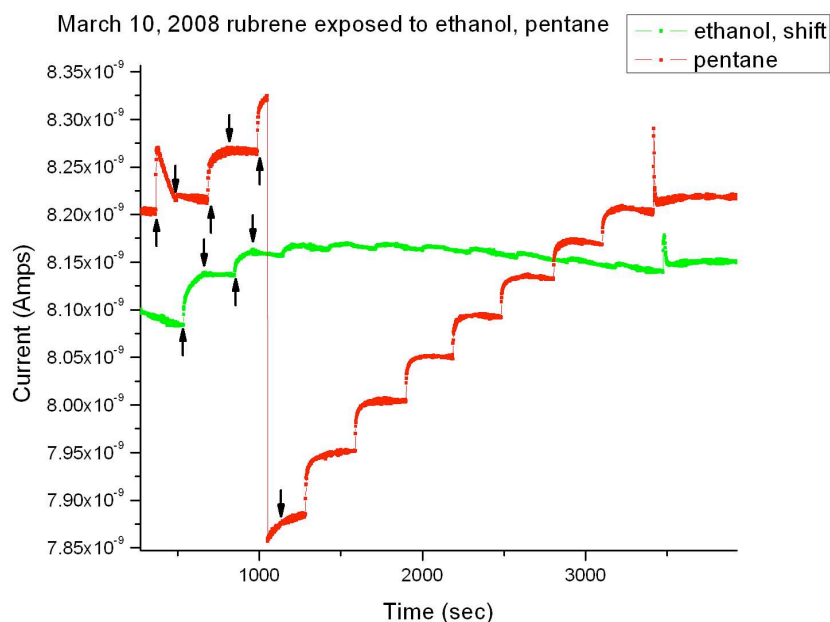


Figure 6.8. Rubrene crystal surface current in response to a series of sub-saturated ethanol and pentane vapor pressure exposures. First few of ten solvent exposures (upward arrows). First few of ten sorption-pumping periods (downward arrows). The final jump in surface current occurred when bringing the cell up to atmospheric pressure. (March 10, 2008)

Exposing ethanol to a fresh rubrene crystal produced a diminishing increase in surface current (Figure 6.8). This is in contrast with decreasing surface current in response to ethanol exposures that were preceded by an acetone exposure (Figure 6.5). Therefore, acetone may change the rubrene surface chemistry to influence the ethanol effect we next investigated with Fourier transform infrared spectroscopy (FTIR) (Figure 6.9). The surface current response to pentane (Figure 6.8) shows a saturating, incremental increase that is about twice as large as that in Figure 6.5. Sorption pumping

had no effect on the surface current enhancement. This suggests surface chemistry is not reversible and that a sample should only be exposed to one vapor material.

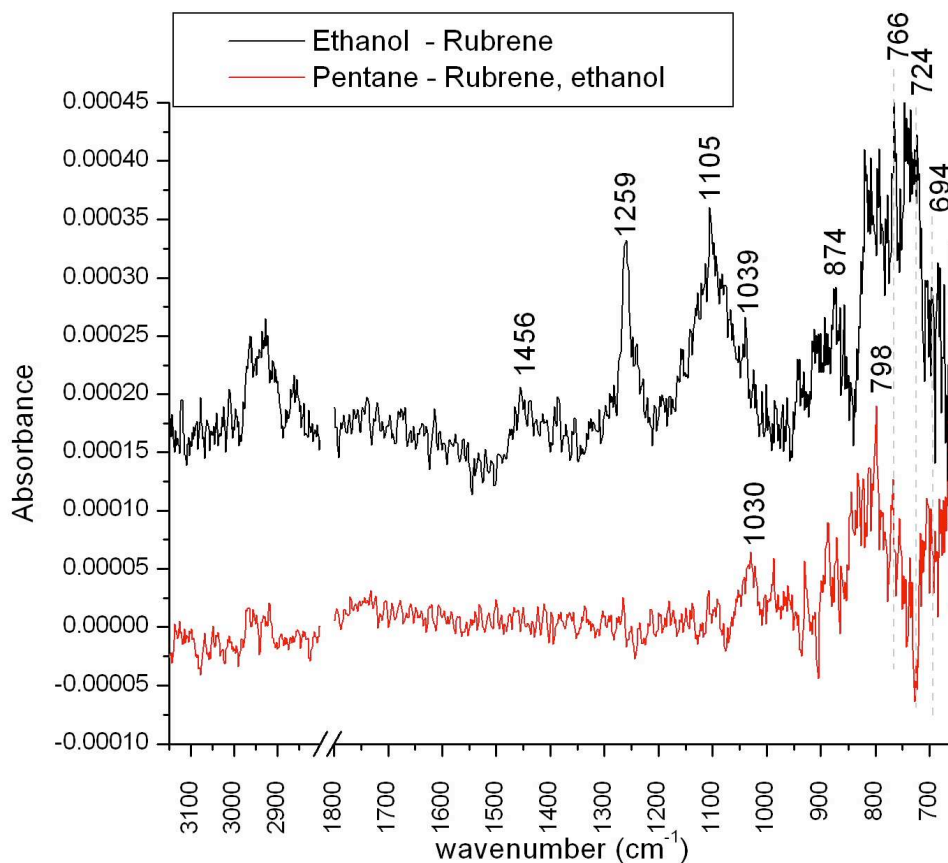


Figure 6.9. Series of rubrene (no SAM) sub-saturated vapor pressure exposure to ethanol, and pentane. (March 10, 2008)

The infrared absorption spectra of ethanol and pentane on rubrene are very different than when preceded by acetone (Figure 6.7, 6.9). The spectrum produced after exposing the rubrene spun film to ethanol (Figure 6.9) shows several positive peaks at 874 cm⁻¹, 1105 cm⁻¹ (OTS), 1259 cm⁻¹ (OTS), and 1456 cm⁻¹ (ethanol CH bend). The broad positive peak at 874 cm⁻¹ may be due to decreasing the number of adjacent hydrogens in the aromatic ring structure, although it is unlikely to have displaced four of five adjacent hydrogens, and the peak breadth does not include 770 - 860 cm⁻¹. This

assignment is therefore unlikely. Also, since the peak is not seen with OTS on rubrene, the assignment remains undefined. Previously, when ethanol was preceded by acetone, there were only negative peaks (Figure 6.6). The second solvent (pentane) also showed different features at 798 cm^{-1} and 1030 cm^{-1} . Since the order of solvent vapor exposure influenced both the electrical and chemical response of rubrene crystal and thin-film surfaces, respectively, rubrene sensing may not be reversible and subsequent samples should not be reused for a series of solvent tests. This suggests that the surface chemistry and electrical response are linked. Further experiments should use only one sample per solvent.

Saturated vapor-pressure solvent exposures were conducted by isolating the sorption pump and backfilling the gas cell through a dedicated port (separate from the OTS delivery line) directed at the sample. The liquid solvent source was exposed to the system for ten minutes. After isolating the solvent source, solvent vapors were removed by 25-minute sorption pumping, followed by backfilling with N_2 three times before returning the cell to atmospheric pressure for scanning.

6.4.2 Pentacene

The infrared absorption spectra of three sublimated pentacene films with different thicknesses are shown in Figure 6.10.

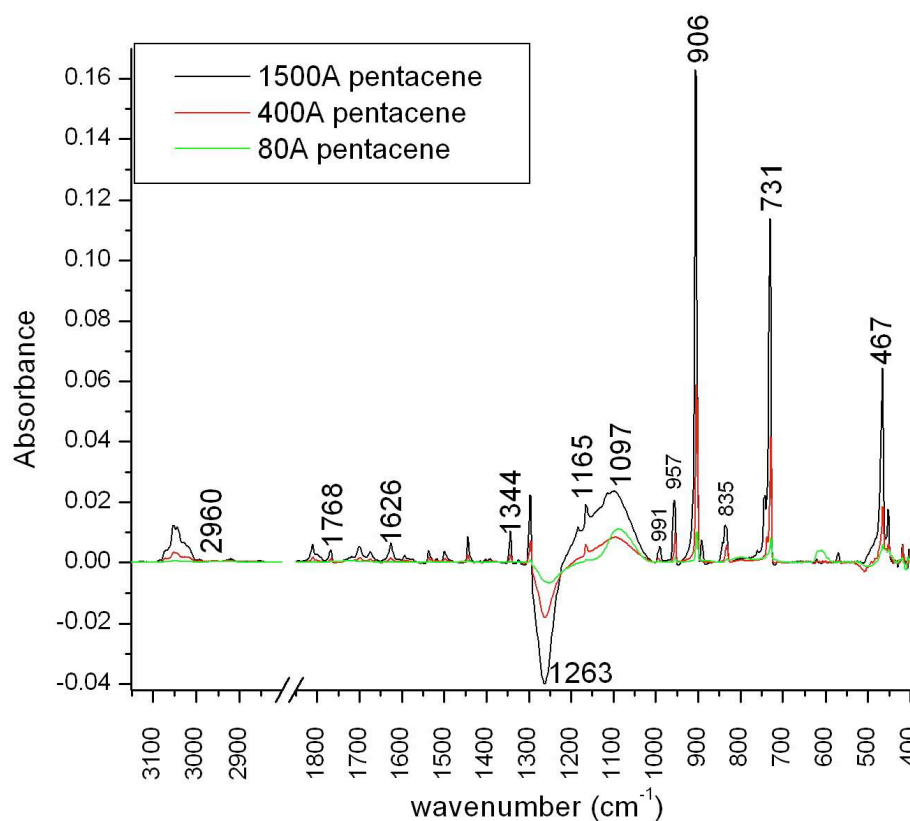


Figure 6.10. Infrared absorption spectra of three double-coated pentacene film thicknesses referenced to their clean substrates. (July 2-8, 2008)

Pentacene film peaks (Figure 6.10) match the expected aromatic features shown in Chapter 3. As expected, peak intensity increases with increased pentacene film thickness. The negative peak at 1263 cm^{-1} may be due to a difference in the angle of incidence between the reference and experimental scans. However, since this behavior is consistent as film thickness is increased, it may be that the film thickness induces a change in the infrared probe of the surface, perhaps due to a change in the material index of refraction or dielectric screening. Dielectric screening by the polarizable insulating oxide may occur when the external field of the de-localized electron cloud of the aromatic molecules attenuates its dipole moment and thus its intensity (Tolstoy, et al. 2003), p. 183).

Field-effect transistor performance was verified by generating a gate-amplified drain-source current I-V curve (Appendix: A5, A7, and A8). The resulting field-effect mobility was calculated, using a secondary I-V_g sweep (Appendix: A5, A7, and A8) and is summarized in Table 6.2. Reasonable field-effect mobility with micro-amp, drain-source current demonstrated sufficient current for chemisensing (Bouvet 2006; Huang, Sun and Katz 2008).

Pentacene Thickness (Å)	Field-effect Mobility (cm ² /Vs)
1500	0.0738
400	0.123
80	0.0931

Table 6.2. Field-Effect Mobility for Each Pentacene Film Thickness with Device Dimensions: Width: 1638 μm, Length: 198 μm.

First, we investigated in-situ surface chemistry change resulting from saturated, vapor-pressure acetone exposure (Figure 6.11). Then, we illustrated the real-time surface current responses collected during each exposure (Figure 6.14).

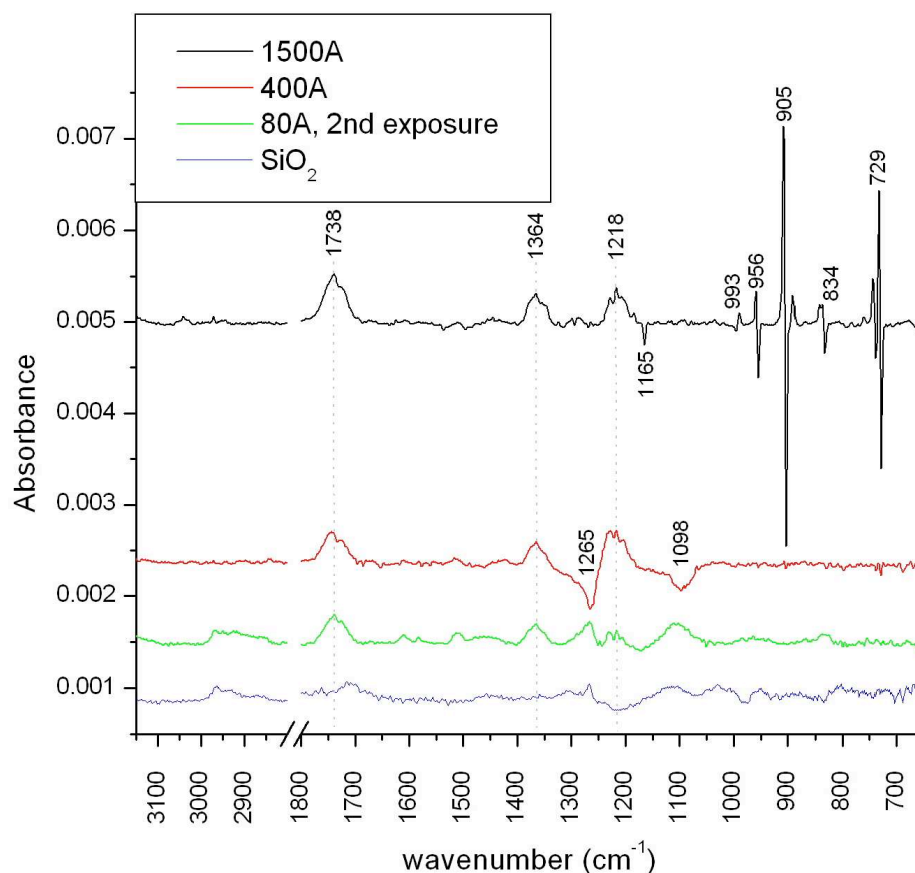


Figure 6.11. Saturated vapor pressure acetone exposures to different pentacene film thicknesses. The 80 Å sample is shown with the second exposure due to a dominance of gas phase peaks in the first. A control surface (blue) was exposed to sub-saturated vapor pressure acetone.

Thickness	cm ⁻¹	peak-to-peak Intensity		O/A ²
		Original	Acetone	
80 Å	903	0.0103	0	-
400 Å	904	0.05877	8.2204E-5	715
1500 Å	906	0.16296	0.004593	35

Thickness	cm ⁻¹	peak-to-peak Intensity		O/A
		Original	Acetone	
80 Å	729	0.00813	0	-
400 Å	729	0.04163	1.4548E-4	286
1500 Å	731	0.114	0.003038	38

Table 6.3. Peak-to-Peak Intensity Changes as a Result of Acetone Exposures

² O/A = Original/Acetone

Several peaks in Figure 6.11 are affiliated with acetone modes: 1218 cm^{-1} (C-C stretching), 1365 cm^{-1} (CH_3 bending), and 1740 cm^{-1} (C=O stretching) (NIST, acetone: 1216 cm^{-1} , 1364 cm^{-1} , 1731 cm^{-1}). The presence of a nearly equal amount of acetone peak intensity across the film thicknesses indicates acetone was physisorbed and did not react with the pentacene film. The acetone exposure control spectrum, 65 \AA silicon dioxide on Si(100), indicates that the peak at 1265 cm^{-1} may be due to contamination and that relatively little interaction occurred between acetone and SiO_2 .

Pentacene films (1500 \AA) showed the largest surface chemistry changes in response to saturated acetone vapor exposures (Figure 6.11). There may be a critical mass or infrared absorption that the thickest film achieves for an evident bulk film interaction with acetone. Differential peaks, which increase in intensity from the left to right, were observed at 729 cm^{-1} , 834 cm^{-1} , 905 cm^{-1} , and 956 cm^{-1} . These indicate the original pentacene film out-of-plane bending peaks shifted to higher wavenumbers, which require more energy for vibration. This shift direction is opposite of that expected with polar solvent hydrogen bonding. The shift may be due to the proximity of acetone molecules physically intercalated into the film, restricting or straining out-of-plane bending. Also, acetone surface cooling may impede bending, explaining the shift. The peak-to-peak intensity of the differential peaks at 729 cm^{-1} and 905 cm^{-1} represent a very small shift, between 1% and 3% of the peak-to-peak intensity of the original film peaks, as shown in Table 6.3. A weaker peak at 993 cm^{-1} shifted toward lower wavenumbers, which suggests solvent hydrogen bonding. A unique negative peak at 1165 cm^{-1} , which occurred in the pentacene film, may indicate a decreased in-plane bending dipole moment as a result of a redistribution of the delocalized aromatic electrons. An I-V sweep after

acetone exposure revealed the field-effect mobility of the 1500 Å pentacene film decreased by 19% to 0.060 V/cm²s (Appendix: A6). This suggests a disruption of the delocalized electron cloud overlap between adjacent pentacene molecules, particularly the out-of plane bending dipole, due to acetone exposure.

Thicker films may consume more surface energy in order to produce equal decreases in surface temperature. If the same effect were indeed occurring on both film thicknesses and if the effect were linear with respect to film thickness, then normalizing the peak shift peak-to-peak intensity of the 1500 Å pentacene film by 3.75 would allow us to compare the film changes directly. However, the peak-to-peak intensity of the normalized 1500 Å pentacene film is 0.0012, while the 400 Å pentacene film is still much smaller at 8.2204×10^{-5} . Therefore, there may be a non-linear thickness to temperature relationship, or a different mechanism accounting for possible differences in film morphology. Further characterization of the differences in film topology, using atomic force microscopy (AFM) might reveal whether grain size or surface roughness also contribute to variations in peak intensity. The substrate and its oxide should act as a heat source for the cooled films, eventually returning films to room temperature.

The 400 Å pentacene film had very small negative features that may be in the same position and direction as some of the differential peaks of the 1500 Å pentacene film. A small, differential peak also occurs at 908 cm⁻¹. However, larger losses uniquely occur at 1098 cm⁻¹ and 1265 cm⁻¹. The peak at 1098 cm⁻¹ may be due to a C-O asymmetric stretch (NIST, dimethyl ether, 1102 cm⁻¹). The negative peak at 1265 cm⁻¹ will be disregarded for the moment, since it has been affiliated with substrate interaction with possible contamination. Or, as shown in Figure 6.10, an effect due to

dielectric screening increased with pentacene film thickness. The negative peak at 1098 cm^{-1} is unique among the spectra (Figure 6.11), suggesting there is a different type of reaction occurring with this film. The negative peak at 1098 cm^{-1} could be related to a decrease in the dipole moment of in-plane bending modes due to acetone exposure. It was not possible to assess the change in field-effect mobility with 80 Å and 400 Å pentacene films, since acetone weakened the silver paint connections.

Other than peaks attributed to acetone, the 80 Å pentacene film showed weak, broad, positive peaks at 839 cm^{-1} , 1103 cm^{-1} , and 1510 cm^{-1} . Positive peaks at both 839 cm^{-1} and 1103 cm^{-1} suggest an increase in both the in-plane and out-of-plane pentacene dipole moments.

To determine whether chemical bonding occurred between acetone and pentacene thin films, which should be stable to an inert nitrogen purge, we investigated 400 Å and 1500 Å film stability (Figure 6.12).

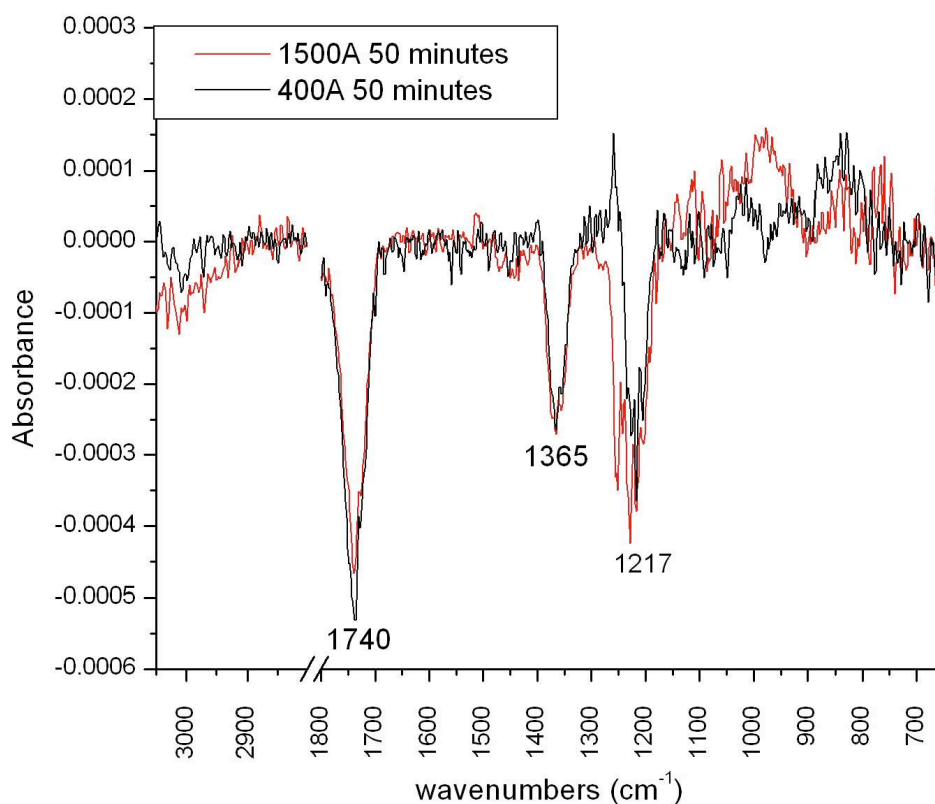


Figure 6.12. Differential stability of 400 Å and 1500 Å pentacene films exposed to 1x acetone after 50 minutes of N₂ purge and, finally, an overnight N₂ purge. Black and red spectra were referenced to the first of five scanning loops and represent the differential change over 50 minutes.

Physisorbed acetone in the 1500 Å and 400 Å pentacene thin-film is removed during the first 50 minutes after acetone exposure (Figure 6.12). This is evident by the negative acetone peaks at 1365 cm⁻¹ and 1740 cm⁻¹. Therefore, the pentacene film is stable over 50 minutes under N₂.

To investigate reusability, successive exposures of saturated vapor pressure acetone were performed on pentacene thin films. Re-use of the 1500 Å pentacene film after acetone exposure (black) and an overnight N₂ purge delay (red) are shown in Figure 6.13. The second exposure caused a differential infrared peak-to-peak intensity at 908 cm⁻¹ that was 66% less intense than the first-exposure, peak-to-peak intensity. A

differential spectrum of the third exposure caused an 82% drop in peak-to-peak intensity compared with the first exposure with consistent acetone exposure features.

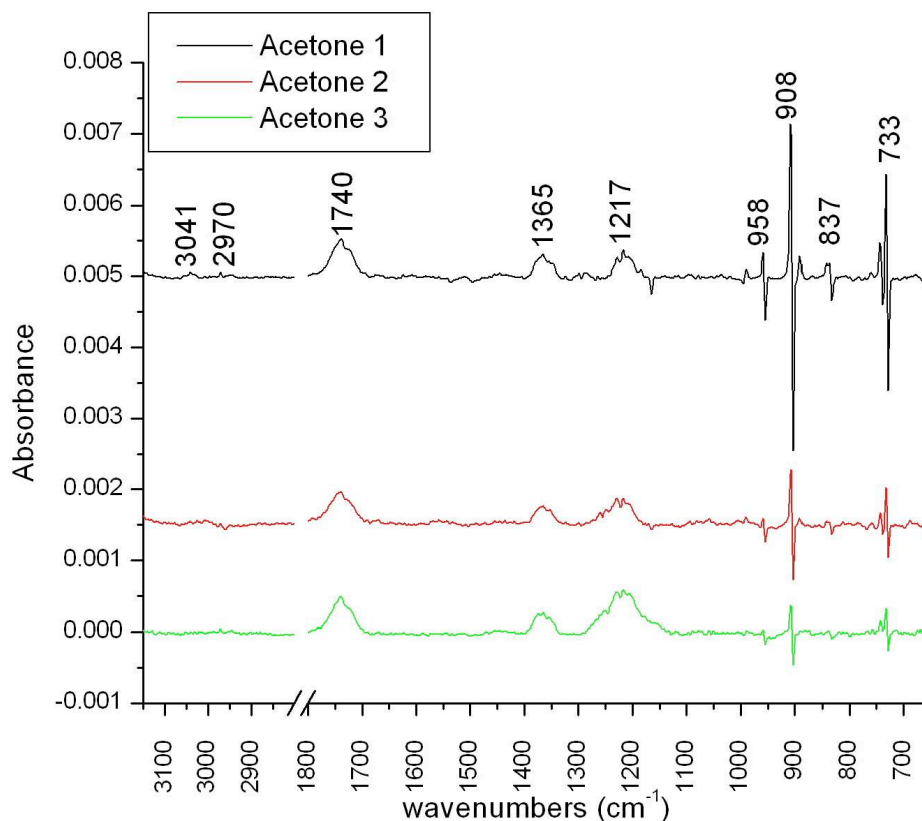


Figure 6.13. Differential infrared absorption spectra of 1500 Å pentacene film exposed to saturated-vapor-pressure acetone to test reusability. (July 2, 2008)

The response of the 1500 Å pentacene field effect transistor drain-source current is shown in Figure 6.14. We observe a slight decrease in drain-source current over time that is likely due to the bias stress effect, commonly observed in organic transistors (Dodabalapur 2006). Since current was not recorded during scanning at atmospheric pressure, a direct comparison to the peak intensity cannot be made. However, a qualitative drain-source current sensing effect is shown and summarized in Table 6.4. Since gold wires often detached before the vapor could be removed, the final current used for Table 6.4 was the last measurement recorded.

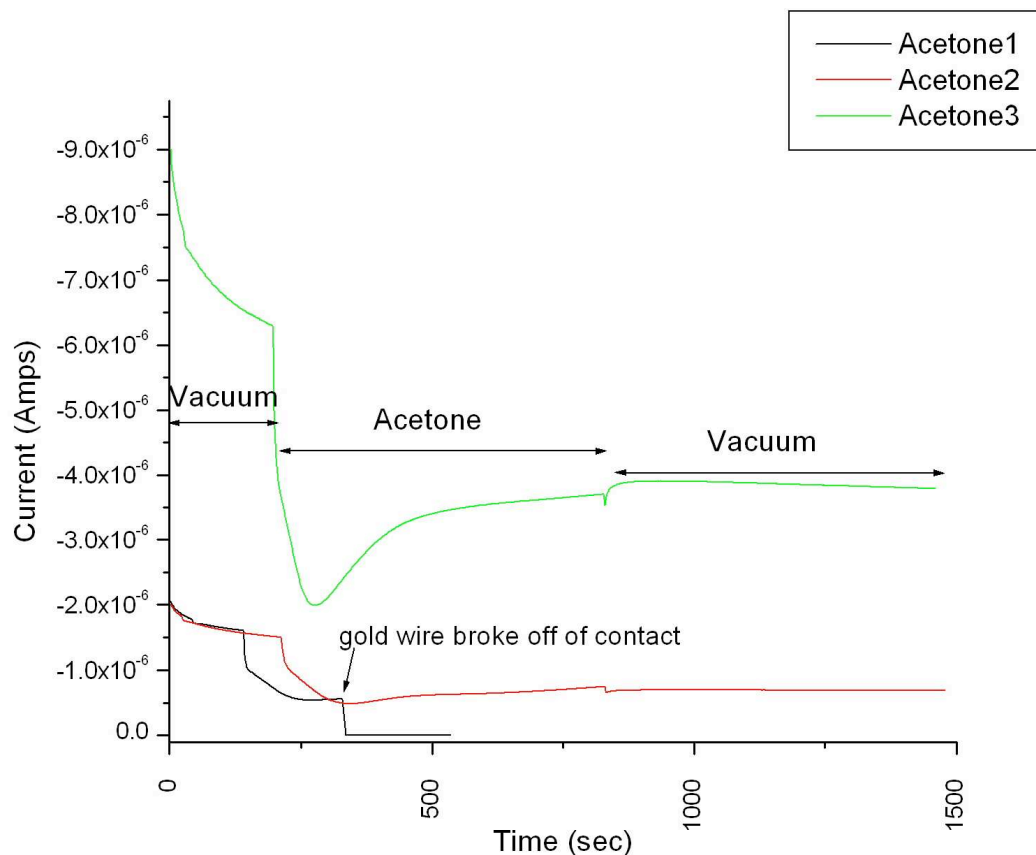


Figure 6.14. Drain source current during acetone exposures to 1500Å pentacene. -20V was applied to the drain and gate for exposures 1 and 2, while -50V was used for exposure 3. (July 2, 2008)

The largest change in surface current seems to occur near the beginning of the exposure, suggesting rapid surface cooling³. A separate experiment tracking the surface temperature during an acetone exposure showed no change in surface temperature, except a decrease by up to 2°C during dry pumping. The immediate dip in surface current upon vacuuming may represent the cooling effect of acetone removal. Vacuuming does not seem to decrease the surface current dramatically because temperature is slow to change

³ Depending on the conduction mechanism, surface cooling may have a different effect on organic transistor current. If the charge carrier transport is dominated by phonon scattering, decreasing surface temperature should increase surface current. If the carrier transport is dominated by hopping, then the reduced system energy with cooling should decrease the current. Therefore, our result supports the hopping mechanism if the surface is indeed cooled.

under moderate vacuum. The third exposure (green) is dramatically different than the first two (black and red). Since the IRAS spectrum in Figure 6.13 showed decreased surface chemistry response to the third exposure, this suggests that the surface chemistry and electrical measurements are decoupled. Indeed, perhaps the sensing origin is only related to surface temperature changes. However, this may be due to the solubility of the silver paint used to make the gold wire connections to gold pads. Repeated experiments using an adhesive, which was not soluble in acetone such as conductive epoxy, would better study this relationship.

Acetone condenses on the sample surface upon exposure. When the condensate evaporates upon sorption pumping below its vapor pressure, the heat of vaporization represents the energy consumed. Acetone evaporation cools a surface by consuming its heat of vaporization energy, 30.45 kJ/mol⁴. The shape of the potential energy well is defined by several polymeric terms including a cubic term that accounts for thermal expansion (Elliott 1969). Cooling a sample leads to a blue shift of peaks, including the oxide phonon modes (Chabal 2008). A blue shift to higher energy means a shift to higher wavenumber. Removing energy (cooling) the pentacene film shifts its modes to higher wavenumbers (higher energy). To test the hypothesis of acetone surface cooling, we cooled the 1500 Å pentacene film with liquid nitrogen through the sample holder power feedthroughs while scanning the film with IRAS (Figure 6.15).

⁴ For reference, the heat of vaporization for water and ethanol are 40.65 kJ/mol and 38.5 kJ/mol, respectively.

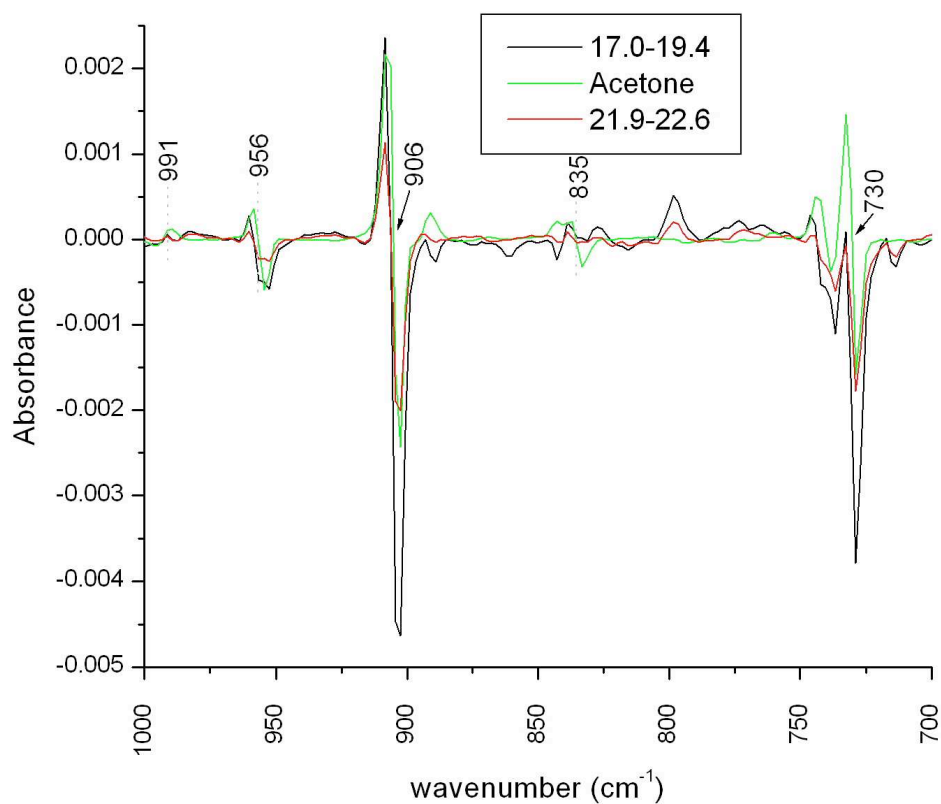


Figure 6.15. Surface cooling compared with acetone's effect on 1500 Å pentacene film.

Acetone has the same effect as cooling the pentacene film under N₂ purge by ~3.25°C - ~7.3 °C. This accounts for all of the spectrum changes upon acetone exposure except for the physisorbed acetone peaks. We now investigate whether the transistor current is similarly accounted for by cooling during acetone exposure (Figure 6.16).

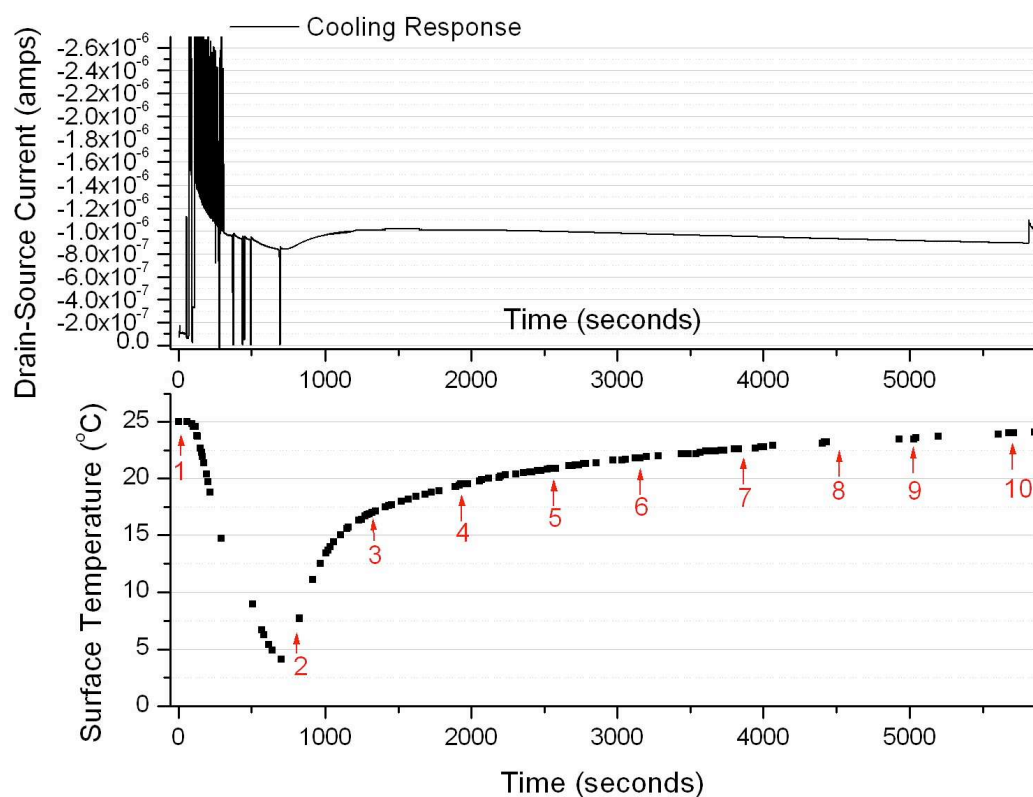


Figure 6.16. 1500 Å pentacene organic, thin-film transistor current during N_2 surface cooling plotted with surface temperature.

The surface current of a 1500 Å pentacene thin film transistor decreases by $\sim 0.8 \times 10^{-6}$ amps while the surface temperature decreases from room temperature (25°C) to 4°C . The noise in the current data was due to a poor external connection which when reattached at the 15°C the noise was reduced. This drop in current is approximately that which occurs during the first two acetone exposures to the same film. However, the IRAS spectra indicate a match with the surface temperature of $17 - 22^{\circ}\text{C}$, which produced an even smaller current change $\sim 0.5 \times 10^{-6}$ amps. Therefore, surface current and surface temperature may not exactly scale with each other to account for the acetone affect.

The surface temperature change theory for subsequent acetone exposures seems to have less effect. The second acetone exposure was performed the next day, so the sample should have had sufficient time to equilibrate to room temperature. Therefore, the temperature change effect seems somewhat inconsistent, since it should be repeatable with the same peak area of adsorbed acetone in the spectra as shown in Figure 6.13. To explore the effect of film thickness on the acetone response, we explore the reusability of a 400 Å pentacene film in Figure 6.17.

400Å pentacene saturated vapor pressure acetone exposures

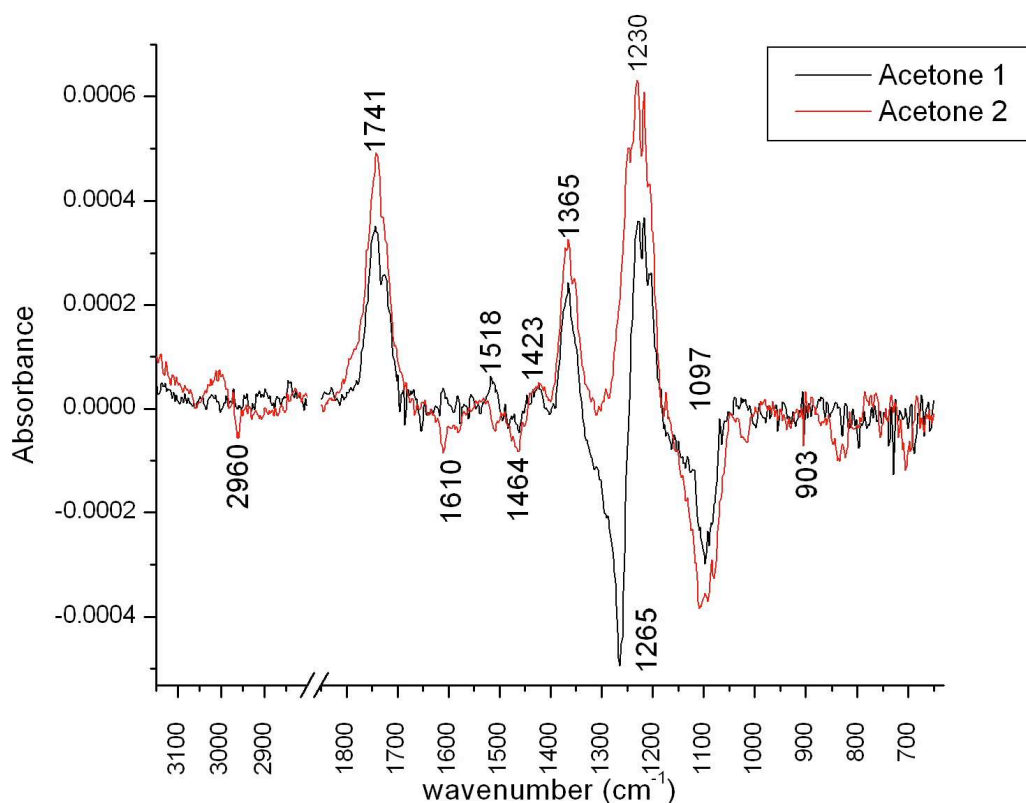


Figure 6.17. Differential infrared absorption spectra of a 400Å pentacene film twice exposed to acetone. (July 7, 2008)

Reuse of the 400Å pentacene film after acetone exposure and purging with N₂ overnight produced small, negative features at 706 cm⁻¹, 839 cm⁻¹, 1014 cm⁻¹, 1464 cm⁻¹, and 1610 cm⁻¹ (Figure 6.17). The differential peak at 903 cm⁻¹ occurred again with

nearly the same intensity. The peak at 1098 cm^{-1} was also repeated with even stronger negative intensity. Therefore, other than additional negative peaks, the changes affiliated with pentacene interaction at 908 cm^{-1} and 1098 cm^{-1} seem consistent and, therefore, perhaps reusable.

The negative peak at 1265 cm^{-1} was missing from the second exposure spectrum, which further removes it from any affiliation with acetone or pentacene interaction, and supports its assignment to an oxide phonon mode due to small changes in the sample angle. This made the adjacent peak at 1230 cm^{-1} more defined. The peak at 1217 cm^{-1} from Figure 6.11 was assigned to C-C acetone stretching. The peak at 1230 cm^{-1} could not be assigned to OH bending (NIST, formic acid, 1229 cm^{-1}), because the corresponding OH stretching mode was not present at 3570 cm^{-1} .

Evaporated gold electrical contacts positioned above the beam path (shown in Figure 6.1) were connected to BNC feedthroughs, using silver paint in order to explore how the electrical response during the previous acetone exposures varies with film thickness and successive exposures. Since the silver paint is soluble in acetone, degradation of the contacts limited interpreting the drain-source current response to acetone vapors. Alternative adhesive materials were investigated, such as graphite paste, silver paste in amyl acetate, and conductive epoxy. However, they were difficult to control on the small, several-mm-sized gold pads. The faster drying time of the silver paint, as well as its amenable viscosity and wetting properties made it the best option available. Now that contacts have been applied, the surface current of the 400 Å pentacene film will be evaluated (Figure 6.18).

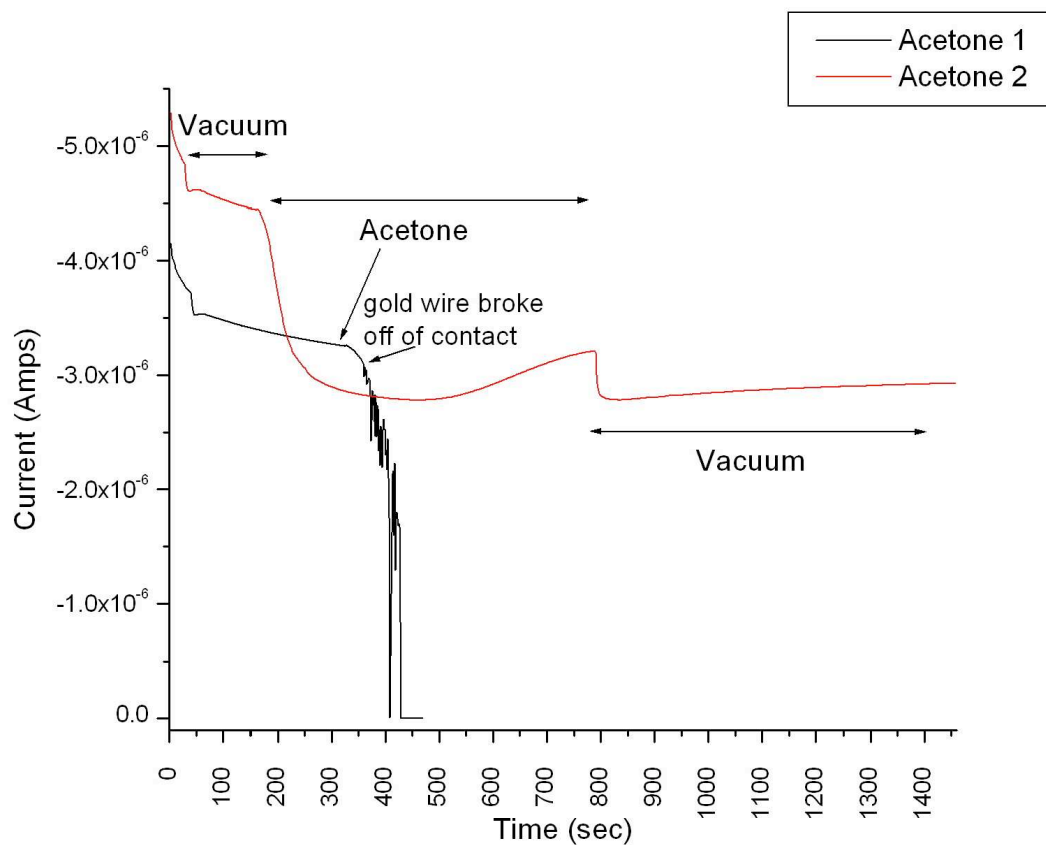


Figure 6.18. Drain source current response of 400 Å pentacene transistor to saturated-vapor-pressure acetone exposure. (July 7, 2008)

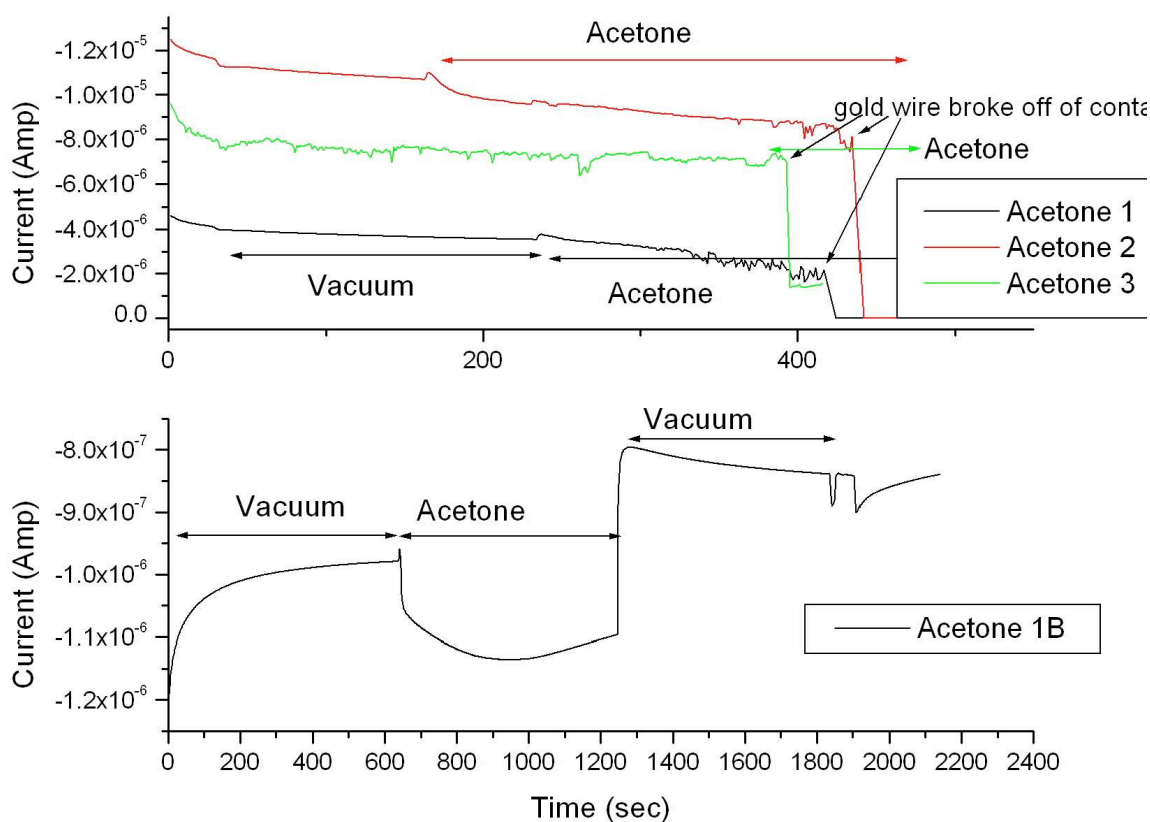


Figure 6.19. Drain source current of 80 Å pentacene transistor response to saturated-vapor-pressure acetone exposure. Result of re-trying sensing with a fourth acetone exposure on a smaller-dimension device after having difficulty attaching gold wires to the other pad (lower graph). (July 8, 2008)

The affect on 80 Å pentacene thin-film transistor current is included to show that it was responsive (Figure 6.19). The fourth exposure current measurement was performed on a different channel dimension, due to damage accrued from wire reattachment. Therefore, this measurement is not directly comparable with the other film responses. The IRAS is not presented for the successive film exposures due to the difficulty involved with electrical measurements.

	1500 Å	400 Å	80 Å
1	1.044E-6	-	1.5903E-6
2	7.536E-7	1.2287E-6	-
3	2.5976E-6	-	2.2445E-6
1B			1.3755E-7

Table 6.4. The difference of the beginning and ending pentacene transistor drain-source current during saturated-vapor pressure acetone exposures. 1B indicates the performance of a device with different channel dimensions tested for the first time after difficulty with the first three measurements on the standard gold pad size.

The change in source-drain current with acetone exposure seems fairly consistent (Table 6.4). This supports a disconnection between the surface chemistry presented in Figures 6.11, 6.13, 6.17. However, if film cooling was the true explanation, a thinner film should have less thermal mass and thus recover its temperature sooner. Since the conduction interface is closest to the oxide heat source and a possible temperature gradient in the film thickness, the conduction may have been consistently less susceptible to temperature fluctuation with different film thicknesses.

Silver paint proved to be a problematic method for attaching gold wires to the gold contacts since several times during the saturated acetone exposure a wire detached from the gold pad (Figure 6.18 -6.19). However, quantitative comparison of the drain-source current response to acetone can be made using Table 6.4. A suppression of drain-source current was consistent upon exposure to acetone. Generally, the magnitude of change was about 10^{-6} amps. Cooling the surface with liquid N_2 supports the interpretation that acetone cools the surface.

Although the surface chemistry effect of acetone on a thick pentacene film was the most intense, the differences in the surface current response are not as dramatic. Since the wire broke off several times and sometimes contributed substantial noise to the data (Figure 6.18 -6.19), the results are difficult to compare. This especially applies to

the 80 Å pentacene film whose most successful wire contact to a smaller device occurred during the fourth exposure and showed the smallest response.

There does not seem to be a decline in the surface current response in the three successive exposures to the 1500 Å pentacene film. This suggests that the negative charge on the acetone's oxygen may draw hole carriers toward the surface and away from the oxide-organic interface, decreasing the accumulation of charge carriers and decreasing the organic transistor drain-source current. This effect seems to be consistent for several exposures.

Since we have shown that the acetone effect on the surface chemistry is partially reversible, we know that the pentacene-acetone interaction is due at least in part to physisorption. It is possible the relaxation of the surface chemistry under nitrogen purge is more dependent on time than on the removal of acetone, since acetone signatures are removed after 50 minutes of N₂ purging. The preceding 25 minutes of sorption pumping with N₂ flushing should be more effective at acetone removal.

6.4.3 Rubrene

Since we know from the previous chapter that perfluorinated-alkyltrichloro silane (FTS) exposure to rubrene produces ~3.5 orders of magnitude increase in the rubrene surface current, we compare its effect on acetone sensing with use of sub-monolayer and saturated-monolayer rubrene coverage. Previous studies suggest the solvents intercalate into the film and create both film and induced potential disorder (Calhoun, Sanchez, Olaya, Gershenson and Podzorov 2008). We hypothesize physisorbed acetone and broadened peaks will be evident in IRAS of exposed films.

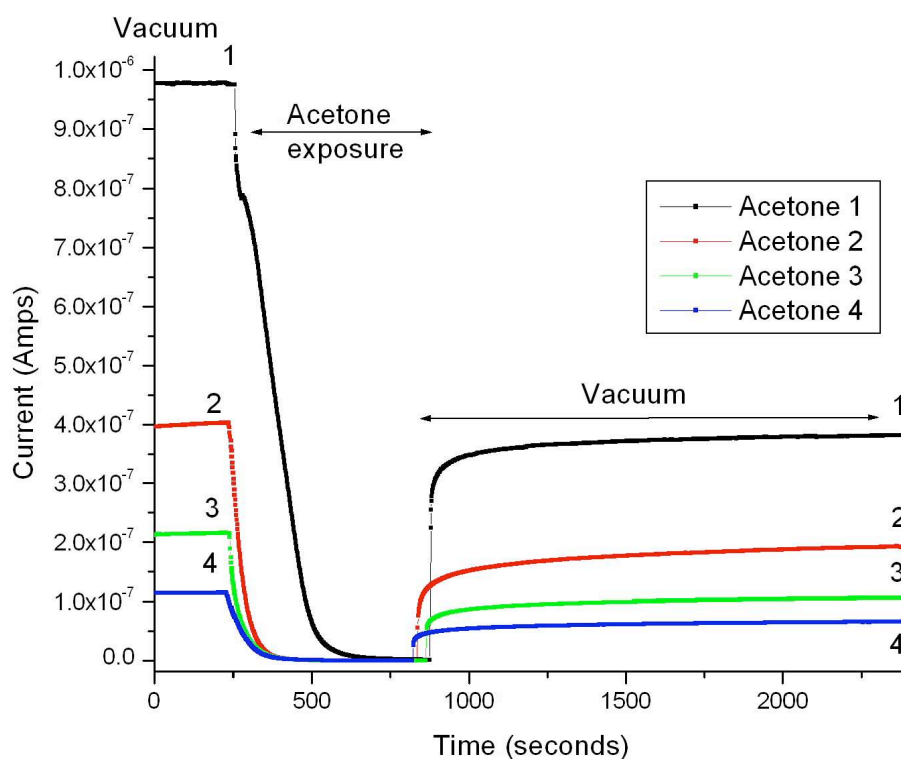


Figure 6.20. Surface current for rubrene coated with sub-monolayer FTS in response to a series of saturated acetone vapor exposures. (June 7, 2008)

According to rubrene single-crystal surface current measurements recorded while depositing FTS (not shown), incomplete FTS monolayer coverage was expected for the lines shown in Table 6.5, and Figure 6.20. The decrease in rubrene single-crystal surface current as a result of acetone exposure to FTS-coated rubrene crystals is much larger and shows saturation compared with the surface without FTS pre-treatment (Figure 6.4). The saturation may be due to acetone physisorption, which might disorder the surface conduction layer. Upon vacuuming, the physisorbed acetone was removed and may allow the rubrene molecules to incompletely return to their previous conductive orientation. The incomplete recovery is likely due to permanent film damage due to the

acetone. Rubrene surface current reversibility after the acetone response is quantified in

Table 6.5.

Exposure	Start ⁵	Saturate ⁶	Recover ⁷	Response ⁸	Reversible ⁹
1	9.76E-07	1.85E-09	3.81E-07	9.74E-07	39%
2	4.02E-07	7.52E-10	1.92E-07	4.02E-07	48%
3	2.15E-07	4.83E-10	1.06E-07	2.15E-07	49%
4	1.15E-07	3.37E-10	6.60E-08	1.14E-07	57%

Table 6.5. Sub-monolayer FTS-Coated Rubrene Surface Current Response and Reversibility When Exposed to Acetone.

Sub-monolayer, FTS-coated rubrene surface current recovers more with successive exposures; however, the magnitude of the response is decreased. A separate rubrene crystal, with saturated FTS coverage, was used to repeat the acetone exposure experiment to determine the influence of complete FTS coverage on sensing.

A saturated coverage of FTS on a rubrene crystal caused the starting surface current to be approximately 4.75X larger than the unsaturated crystal. Acetone does not saturate the surface current, given the same exposure conditions (Figure 6.21). This may be due to the larger surface current, which may cause saturation to take more time. The acetone response is larger and more reversible, comparing Tables 6.5 and 6.6. Therefore, for a larger and more reversible acetone response, which is favored for sensors, a rubrene crystal with saturated FTS coverage is advantageous.

⁵ The start point is at the beginning of the acetone exposure.

⁶ The saturate point is at the plateau during acetone exposure.

⁷ The recover point is at the end of the vacuuming.

⁸ The response is the difference between the current at the start and saturate points.

⁹ Reversible denotes the percentage of the response recovered after vacuuming ($100 \times \text{Recover} / \text{Response}$).

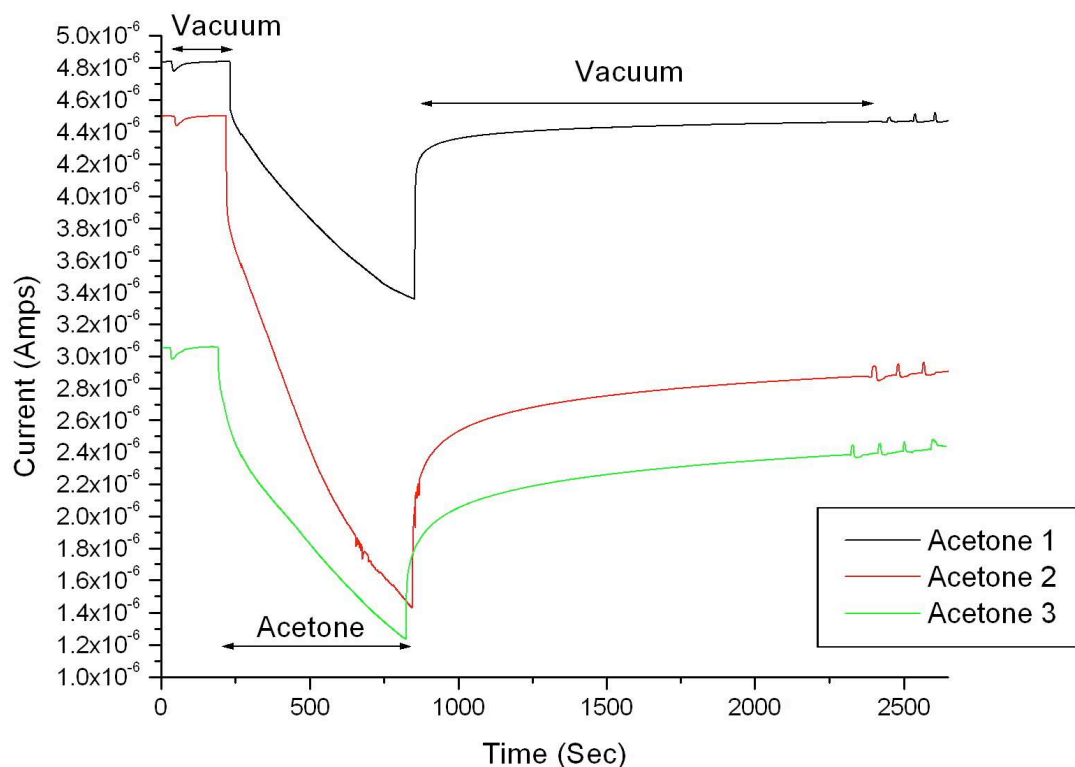


Figure 6.21. Surface current of saturated-monolayer, FTS-coated rubrene in response to a series of saturated acetone vapor exposures

Exposure	Start	Saturate	Recover		Response	Reversible
1	4.838E-6	3.357E-6	4.461E-6		1.481E-6	75%
2	4.497E-6	1.431E-6	2.870E-6		3.066E-6	47%
3	3.057E-6	1.236E-6	2.381E-6		1.821E-6	63%

Table 6.6. Saturated-Monolayer FTS-Coated Rubrene Surface Current Response Reversibility upon Acetone Exposure

To determine if the surface chemistry supports our removal interpretations, the infrared spectrum of sub-monolayer, FTS-covered rubrene surfaces that were exposed to acetone several times were recorded under N_2 (Figure 6.22).

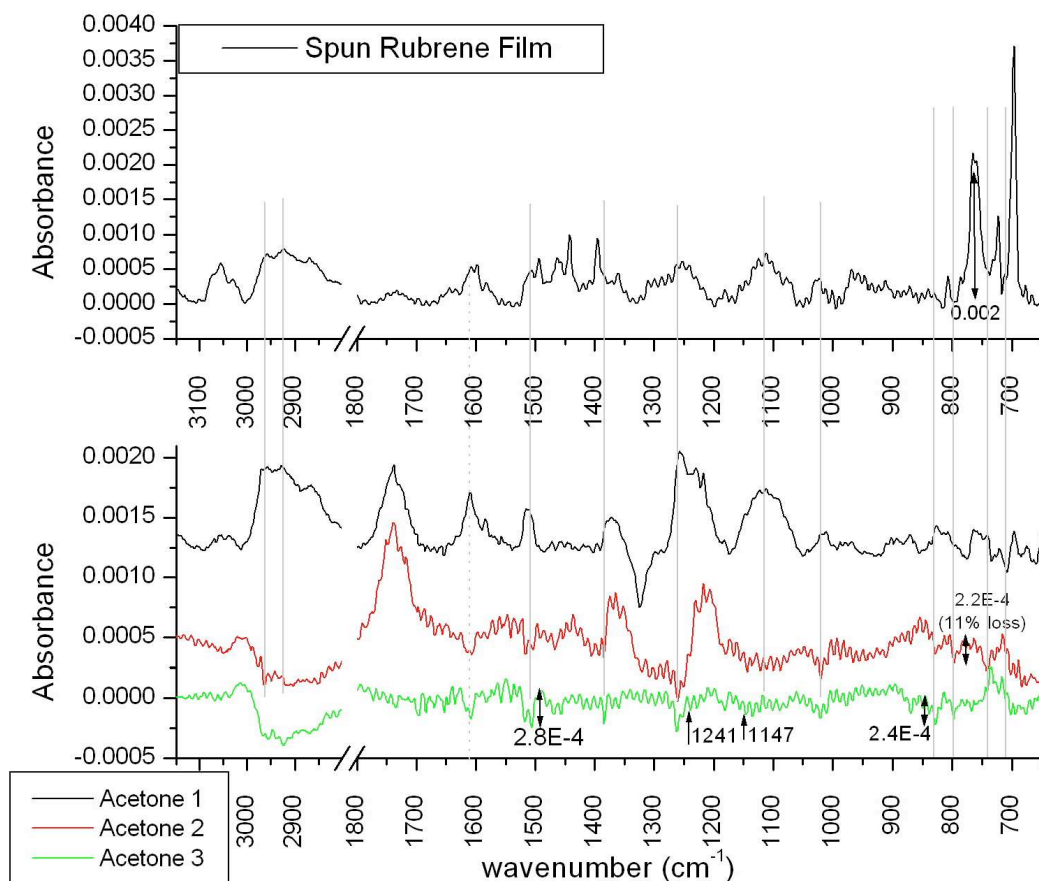


Figure 6.22. Rubrene coated with sub-monolayer FTS surface chemistry in response to a series of saturated acetone vapor exposures on FTS/rubrene/SiO₂. (June 7, 2008)

The peaks in Figure 6.20 at 1217 cm⁻¹, 1371 cm⁻¹, and 1738 cm⁻¹ are affiliated with acetone's C-C stretching, CH₃ bending, and C=O stretch mode (NIST, acetone) and do not line up with major peaks in the rubrene or FTS spectra (Figure 6.22).

Hydrocarbon stretching, observed near 2900 cm⁻¹ with greater intensity than expected from acetone, seems to be added in the first exposure and then removed in successive exposures. The corresponding bending modes for hydrocarbon contamination expected at 1450 cm⁻¹ may explain the peak at 1510 cm⁻¹ as well as a twist mode at 1111 cm⁻¹.

These contamination features seem to be removed in subsequent exposures.

Peaks at 1019 cm⁻¹, 1257 cm⁻¹, and 1610 cm⁻¹ are positive and broadened in the first-exposure spectrum but are negative in the second- and third-exposure spectra.

Broadened peaks after the first exposure suggest film disorder due to the physisorbed acetone. The peaks at 1257 cm^{-1} and 1610 cm^{-1} are near rubrene film features (1254 cm^{-1} and 1599 cm^{-1}) and may indicate a corresponding film perturbation. However, the 1257 cm^{-1} peak was previously assigned to oxide phonon-mode polarization due to slight changes in the sample-holder position. The negative peaks at 1019 cm^{-1} and 1324 cm^{-1} are close to an aromatic CH bend and aromatic ring deformation (NIST, benzene, 1010 cm^{-1} and 1326 cm^{-1}), indicating a possible assignment to aromatic perturbation or bonding.

After the second exposure most spectral peaks are negative, which indicates removal of rubrene material since no chemical reaction is expected. Rubrene is soluble in acetone. While the rubrene single crystal molecules are tightly bound to their solid state, the amorphous nature of the spun rubrene film may make them susceptible to acetone-induced removal. At lower wavenumber, a series of four negative peaks emulates the shifted positions of four positive peaks. Comparing the peak area of the negative peak with the originating peak, we calculate that the negative peak is 10% of the positive peak area. This suggests, but does not prove that 10% of the rubrene film is removed by the second acetone exposure. We now explore a rubrene spun film that is fully protected by a saturated FTS monolayer.

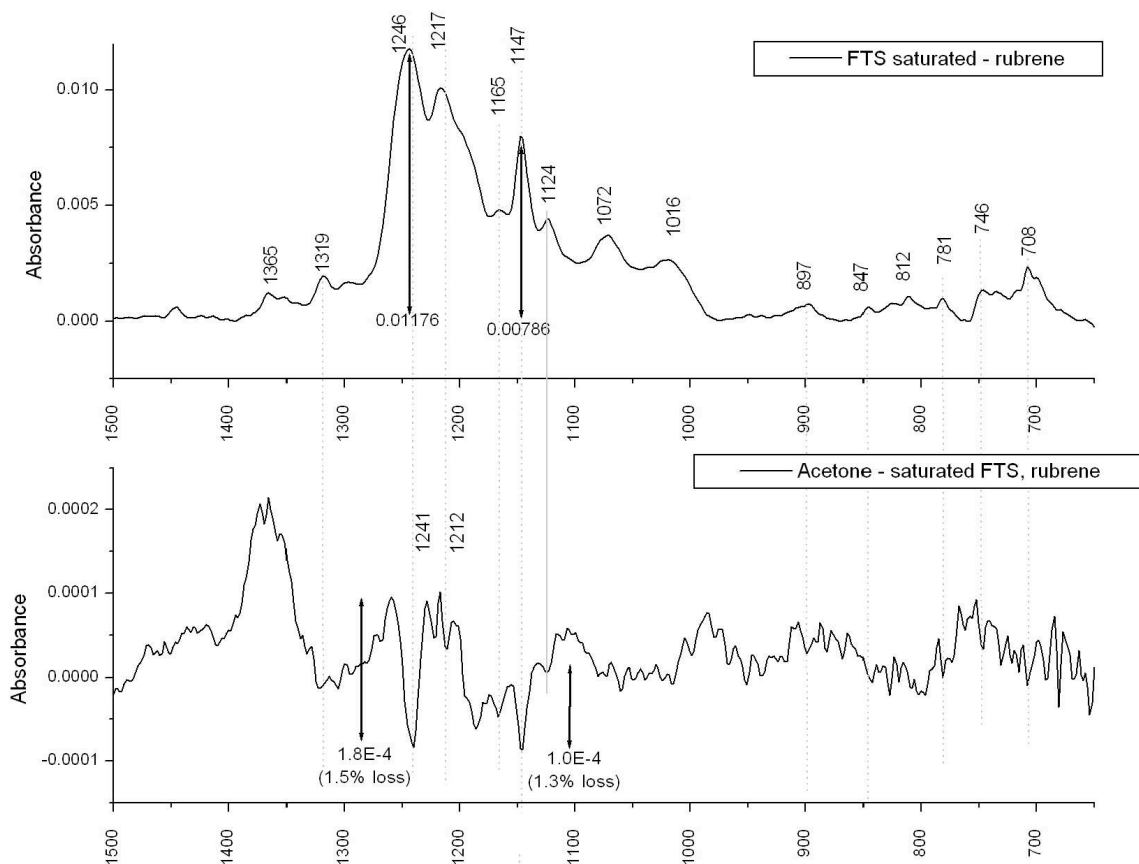


Figure 6.23. Acetone removal of saturated, FTS-covered from rubrene on SiO_2 .

Acetone interaction with the saturated FTS-covered sample suggests either FTS dipole perturbation or removal by acetone (Figure 6.23). The negative peak intensity at 1241 cm^{-1} represents $\sim 1.5\%$ of the peak intensity of the originating FTS peak at 1246 cm^{-1} . Also, the triplet peak centered at 1147 cm^{-1} is shown as negative peaks at about 1.3% of the originating intensity. Although less FTS is removed from a saturated FTS covered rubrene surface, as predicted by negative peak intensity, the effect of FTS removal on surface current is larger than that of rubrene removal. FTS removal has a stronger effect on surface current enhancement than rubrene removal.

6.4.4 C6

The hexyloxy tail of the C6 molecule may be advantageous for polar acetone and/or ethanol molecule sensing. The field-effect mobility of the 500Å C6 film shown in Figure 6.23 was $0.00139 \text{ V/cm}^2\text{s}$ for a device with the following dimensions: width = $1638 \text{ }\mu\text{m}$ and length = $198 \text{ }\mu\text{m}$. The drain-source current was on the order of 10^{-7} amps, which was sufficient for sensing. Therefore, we investigated the surface chemistry and sensing capabilities of a 500 Å C6 film (Figure 6.24).

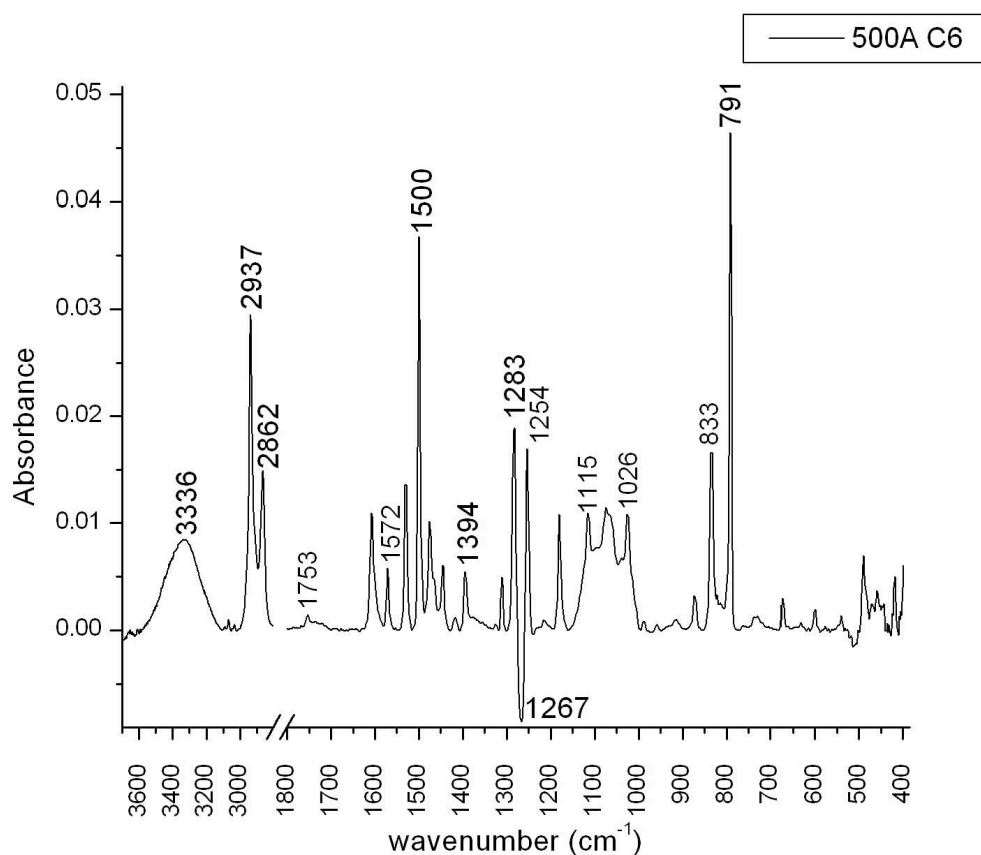


Figure 6.24. Infrared absorption spectra of a 500Å C6 film. (July 9, 2008)

Ethanol was first exposed to the C6 film as ten short sub-vapor pressure doses. Infrared scanning was performed before and after the exposures under N_2 purge due to the dominance of the gas phase in the real-time spectra.

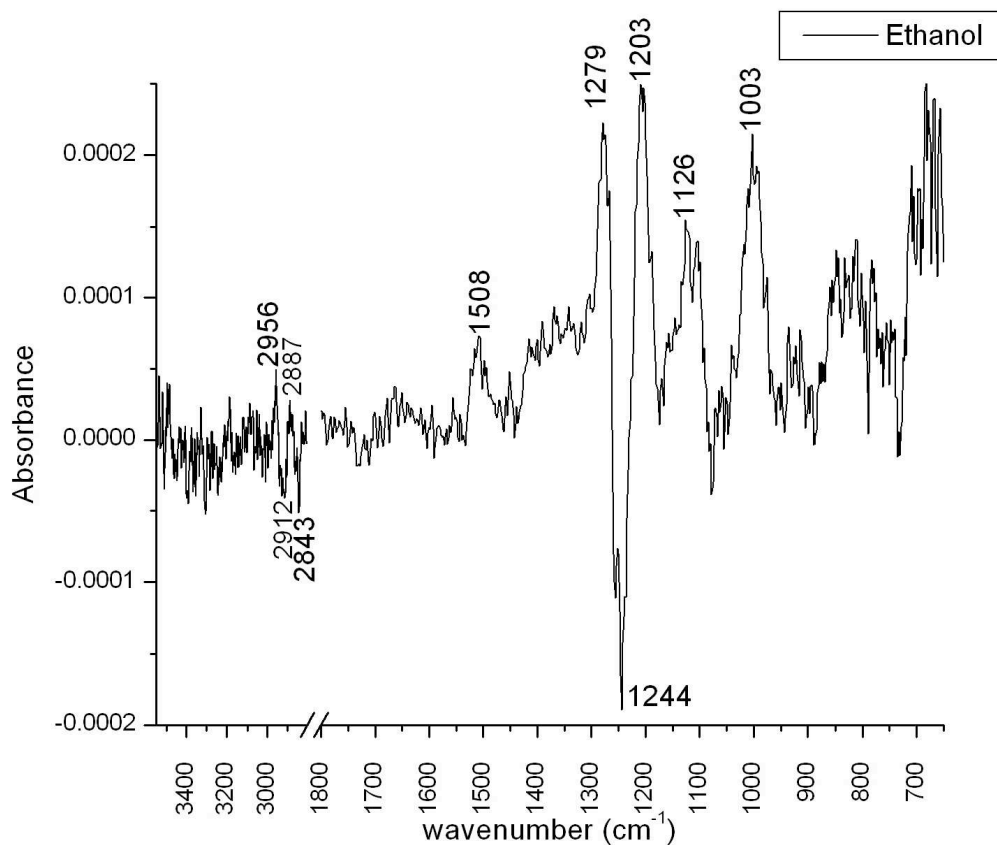


Figure 6.25. Sub-vapor pressure exposure of ethanol to a 500Å C6 film referenced to the C6 film on thick SiO₂. (March 12, 2008)

Ethanol interaction with a 500Å C6 film (Figure 6.25) produces positive peaks at 1003 cm⁻¹, 1126 cm⁻¹, 1203 cm⁻¹, 1279 cm⁻¹, and 1508 cm⁻¹ that may correlate to the following peaks in the original C6 film: 1026 cm⁻¹, 1115 cm⁻¹, 1215 cm⁻¹, 1283 cm⁻¹, and 1500 cm⁻¹. The increase in C6 film intensity suggests that the dipole moment of these peak origins has been increased. A negative peak at 1244 cm⁻¹ may be related to a strong peak at 1254 cm⁻¹ in the original film spectrum or a slight change in the sample angle of incidence causing a change in the oxide phonon mode infrared absorption. It could also be the result of peaks at 1254 cm⁻¹ and 1283 cm⁻¹ shifting to differential peaks. The negative peaks at 2843 cm⁻¹ and 2912 cm⁻¹ can be affiliated with symmetric and asymmetric CH₂ stretching modes, which do not quite match with the original film peaks.

Therefore, these negative peaks may originate from the exposed ethanol that produced additional positive peaks at 2887 cm^{-1} and 2956 cm^{-1} , indicating CH_3 symmetric and asymmetric stretching modes are also present as expected with the ethanol molecule. Overall, ethanol seems to have increased the intensity of some of the original C6 film modes, which may be due to a decrease in material dipole moments. While it was difficult to interpret the baseline, after purging five minutes, checking feature stability revealed a loss at 1200 cm^{-1} and 1270 cm^{-1} and a gain at 1244 cm^{-1} on the order of 3×10^{-4} . There was also a loss at 1003 cm^{-1} of 2×10^{-4} , but a sustained feature at 1508 cm^{-1} had only a small loss of 1×10^{-5} . This indicates that the ethanol interaction with C6 may be less transient under N_2 . For comparison of a different functional group analyte, acetone is exposed to a separate C6 film (Figure 6.26).

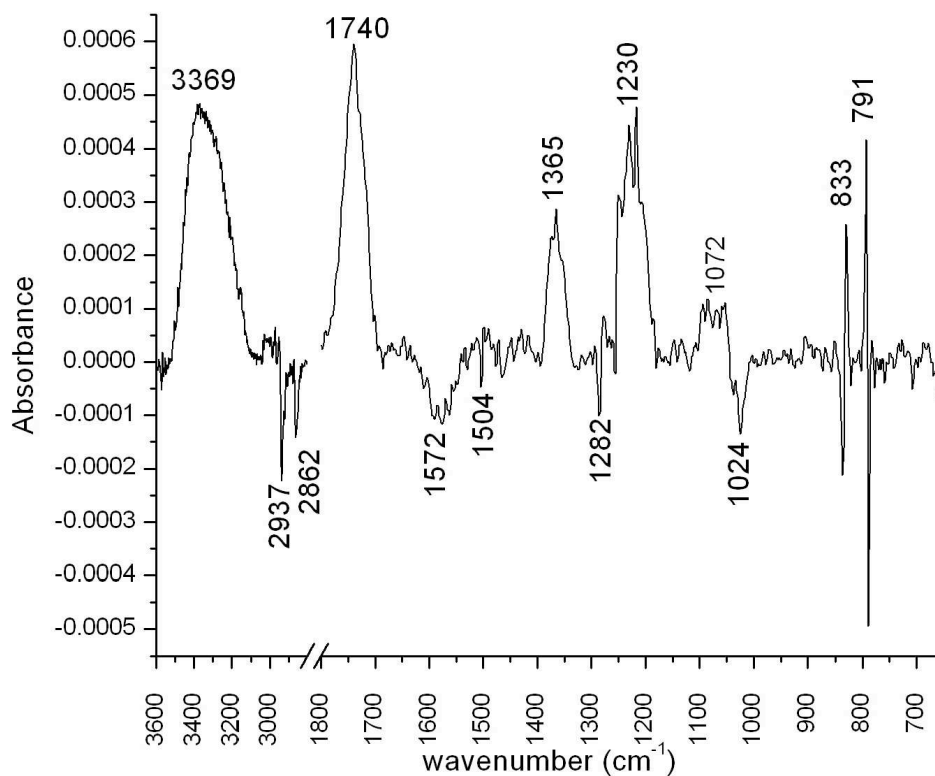


Figure 6.26. Differential infrared absorption spectra of a 500Å C6 film exposed to acetone. (July 9, 2008)

Saturated vapor pressure acetone exposures to the C6 film shown in Figure 6.26 indicate a consistent amount of physisorbed acetone at 1365 cm^{-1} , 1740 cm^{-1} , and possibly 1230 cm^{-1} compared with the other film materials. Three types of changes to the original film peaks are observed: negative peaks, peaks shifting to higher wavenumbers, and peaks shifting to lower wavenumbers. Several negative peaks at 1024 cm^{-1} , 1282 cm^{-1} , 1504 cm^{-1} , 1572 cm^{-1} , 2862 cm^{-1} , and 2937 cm^{-1} are in the exact same position as peaks in the original C6 film (1025 cm^{-1} , 1283 cm^{-1} , 1500 cm^{-1} , 1572 cm^{-1} , 2862 cm^{-1} , and 2937 cm^{-1}). This may indicate a loss of dipole moment according to acetone physisorption. The most negative peak at 1024 cm^{-1} may be due to a decrease of aromatic in-plane bending. The differential peaks at 833 cm^{-1} and 1282 cm^{-1} indicate the

originating film peak shifted to a lower wavenumber as a result of possible hydrogen bonding with acetone. The peak at 791 cm^{-1} , which originated from an out-of-plane bending mode, indicates a peak shifting to a higher wavenumber and suggests a disruption of the number of adjacent aromatic hydrogen atoms. The peak at 3336 cm^{-1} in the original spectrum shifted to 3369 cm^{-1} , which may refute hydrogen bonding between the terminal OH group and acetone since if such bonding took place this peak would have shifted to a lower wavenumber. Therefore, the exact sensing mechanism of C6 is unclear; however, the response to acetone is more dramatic, according to IRAS, than ethanol. This was unexpected due to the terminal group's similarity to ethanol.

Analysis of the stability of the spectrum over 30 minutes reveals decreasing intensity of acetone peaks at 1216 cm^{-1} , 1366 cm^{-1} , and 1738 cm^{-1} by at most 4×10^{-4} . Therefore, acetone must have physisorbed to the C6 film since it was removed from the film over time. No other spectral changes were seen. The C6 film changes were sustained for at least 30 minutes. The transistor current response to acetone is shown next in Figure 6.27.

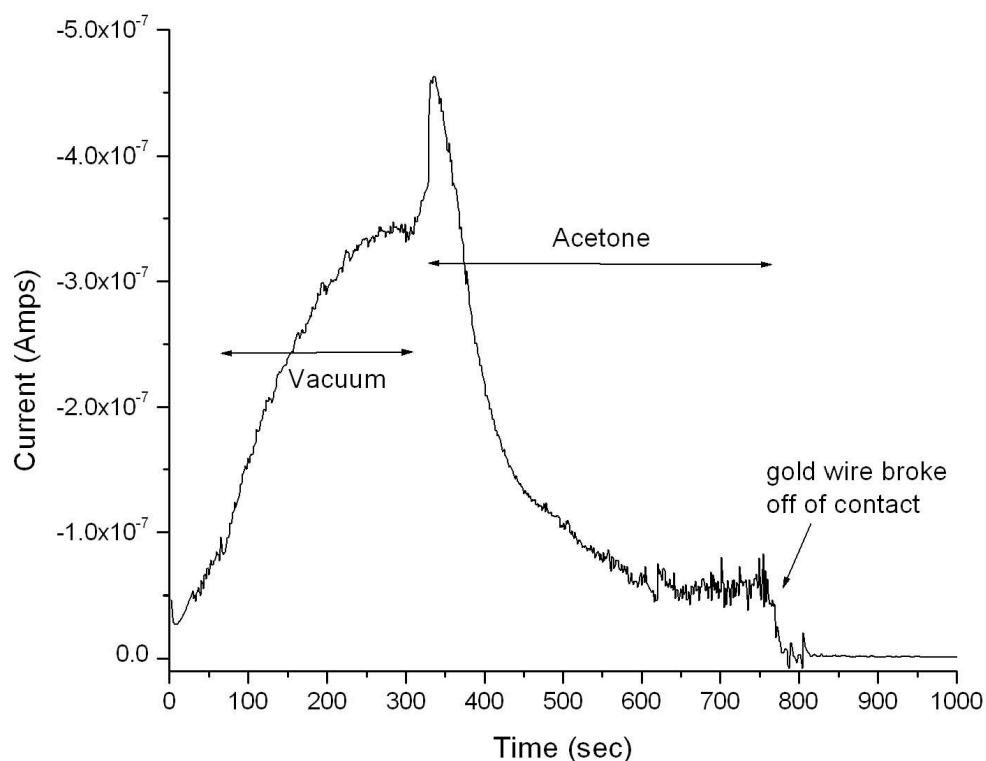


Figure 6.27. Drain-source current response of 500Å C6 to saturated-vapor-pressure acetone exposure using -50V.

The drain-source current, under a -50V potential applied to the drain and gate, decreased by 2.9×10^{-7} amp, when the film was exposed to acetone.

6.5 Conclusions

A method for studying the effects of acetone, ethanol and pentane vapor exposures to organic semiconductor films, using IRAS and surface current, was established. The surface chemistry and the direction of rubrene surface current in response to ethanol exposure were different when preceded by acetone. Although initial results may have been confounded by OTS contamination, this was resolved in later exposures by adding a dedicated exposure line. Because vapor response was not

reversible, we conclude it is best to switch samples between solvent exposures. Sub-vapor pressure acetone and pentane exposures to rubrene crystals caused an increase in in-plane bending peaks and a decrease in out-of-plane bending.

The thickest pentacene thin film (1500 Å) produced the highest peak-to-peak intensity of differential peaks in response to saturated acetone vapors. This suggests the acetone interaction must occur in the bulk of the film as opposed to the top 80 - 400 Å, or else a critical thickness was not achieved for IRAS detection. Pentacene film peaks at 729 cm^{-1} , 834 cm^{-1} , 905 cm^{-1} , and 956 cm^{-1} produced differential peaks after acetone exposures that slightly shifted these out-of-plane aromatic CH bending modes to higher wavenumbers. Acetone has the same effect on the IRAS as cooling the pentacene film under N_2 purge by $\sim 3.25^\circ\text{C}$ - $\sim 7.3^\circ\text{C}$. This accounts for all of the spectrum changes upon acetone exposure except for the physisorbed acetone peaks. However, the reduction in surface current due to liquid N_2 cooling does not fully account for acetone's reduction of transistor current. Alternatively, the shift may also be due to steric hindrance as opposed to the much smaller signature of solvent hydrogen bonding at 993 cm^{-1} , shifting in-plane bending modes to lower wavenumbers.

A loss of in-plane bending at 1165 cm^{-1} further supports the hypothesis that these changes may have caused the 19% decrease in the organic transistor field-effect mobility. It is interesting to note that acetone penetration occurred in the bulk of the film, since bulk penetration is more likely to affect the field-effect mobility than a surface-restricted effect due to the carrier accumulation at the buried oxide interface. The 1500 Å pentacene film had the lowest field-effect mobility compared with the thinner films. This implies the 1500 Å pentacene film has a greater surface area due to smaller grain size or

increased roughness, which could be validated by AFM surface topology analysis. After exposing a 1500 Å pentacene film to acetone and purging the sample chamber overnight under N₂, pentacene features decreased by 13%. The pentacene peaks, while reduced, indicated the molecule remained intact. This reversal supports a physisorption sensing mechanism.

Saturated FTS-covered rubrene surfaces showed negative peaks attributed to FTS stretching modes, when exposed to saturated acetone vapors. This suggests acetone decreased the dipole moment of the FTS molecule, which could then decrease its surface-current-enhancing effect, offering an origin to the sensing mechanism. However, electron spin resonance (ESR) measurements previously suggest that solvent exposure does not alter the dipole moment of the SAM layer upon rubrene (Calhoun, Sanchez, Olaya, Gershenson and Podzorov 2008). Our data showing out-of-plane aromatic C-H bending perturbation supports acetone intercalation into the film. The anticipated disorder did not cause peak broadening because the negative peaks we found suggest the acetone effect may also be due to FTS film removal. Intercalation would likely occur during acetone removal of FTS or rubrene in the saturated and unsaturated FTS coverage on rubrene-spun surfaces, respectively. Rubrene is soluble in acetone, which supports the ability of acetone to lightly etch the amorphous rubrene film. While there is reason to believe the strongly bound rubrene molecules in a crystal would not delaminate as we predict for the amorphous rubrene spun film, we are not able to check this experimentally.

Successive acetone exposure to saturated FTS-covered rubrene was more reversible (63 - 75%) and had larger response (1.5×10^{-6} - 1.8×10^{-6} amps) than sub-

monolayer FTS coverage. The IRAS spectra of sub-monolayer FTS rubrene coverage showed unprotected rubrene film degradation and then removal, which suggests that its reduced sensing response was due to a disruption of the rubrene film. The saturated FTS film protects the rubrene film and only modulates the number of charge carriers at the rubrene surface. Rubrene response is greater than with pentacene ($1.0 - 1.6 \times 10^{-6}$ amps) and C6 ($\sim 2.9 \times 10^{-7}$ amps). Therefore, the best sensing material tested was a rubrene single crystal pretreated with saturated FTS coverage.

The sensing mechanism of the C6 molecule is ambiguous at this time. Acetone is removed from the C6 film over 30 minutes of N_2 purge without reversing the other spectral changes that occurred upon exposure. There was conflicting spectral evidence of solvent hydrogen bonding supported by out-of-plane aromatic bending modes at 791 cm^{-1} and 833 cm^{-1} , while the peak attributed to the terminal hydroxyl group at 3369 cm^{-1} shifted in the opposite direction. Very little surface chemistry change was observed in response to ethanol vapors, despite the specialized hexanol film termination.

6.6 References

1. Bouvet, M., Phthalocyanine-based field-effect transistors as gas sensors. *Analytical Bioanalytical Chemistry* **2006**, 384, 366-373.
2. Calhoun, M. F.; Sanchez, J.; Olaya, D.; Gershenson, M. E.; Podzorov, V., Electronic functionalization of the surface of organic semiconductors with self-assembled monolayers. *Nature Materials* **2008**, 7, 84 - 89.
3. Chabal, Y., In 2008.
4. Chang, J.-F.; Sun, B.; Breiby, D. W.; Nielsen, M. M.; Sölling, T. I.; Giles, M.; McCulloch, I.; Sirringhaus, H., Enhanced Mobility of Poly(3-hexylthiophene) Transistors by Spin-Coating from High-Boiling-Point Solvents *Chemistry of Materials* **2004**, 16, (23), 4772 -4776.
5. Conley, R. T., *Infrared Spectroscopy*. 2 ed.; Allyn and Bacon, Inc.: Boston, 1972; p 355.
6. Dodabalapur, A., Organic and polymer transistors for electronics *Materials Today* **2006**, 9, (4), 24-30.
7. Elliott, R. J., General Introduction. *Discussions of the Faraday Society* **1969**, 48, 7-14.
8. Gundlach, D. J.; Lin, Y. Y.; Jackson, T. N.; Nelson, S. F.; Schlom, D. G., Pentacene Organic Thin-Film Transistors—Molecular Ordering and Mobility. *IEEE Electron Device Letters* **1997**, 18, (3), 87-89.
9. Huang, J.; Miragliotta, J.; Becknell, A.; Katz, H. E., Hydroxy-Terminated Organic Semiconductor-Based Field-Effect Transistors for Phosphonate Vapor Detection. *Journal of the American Chemical Society* **2007**, (129), 9366-9376.
10. Huang, J.; Sun, J.; Katz, H. E., Monolayer-Dimensional 5,5'-Bis(4-hexylphenyl)-2,2'-bithiophene Transistors and Chemically Responsive Heterostructures. *Advanced Materials* **2008**, 20, 2567-2572.
11. Kiselev, A. V.; Lygin, V. I., *Infrared Spectra of Surface Compounds*. Halsted Press of John Wiley & Sons, Inc.: New York, 1975; p 384.
12. Podzorov, V.; Sysoev, S. E.; Loginova, E.; Pudalov, V. M.; Gershenson, M. E., Single-crystal organic field effect transistors with the hole mobility $\sim 8 \text{ cm}^2/\text{V s}$. *Applied Physics Letters* **2003**, 83, 3504.
13. Stokes, M. A.; Kortan, R.; Amy, S. R.; Katz, H. E.; Chabal, Y. J.; Kloc, C.; Siegrist, T., Molecular Ordering in Bis(phenylenyl)bithiophenes. *Journal of Materials Chemistry* **2007**, 17, 3427-3432.
14. Tolstoy, V. P.; Chernyshova, I. V.; Skryshevsky, V. A., *Handbook of Infrared Spectroscopy of Ultrathin Films*. John Wiley & Sons, Inc.: Hoboken, NJ, 2003; p 710.
15. Zhang, J.; Sato, H.; Tsuji, H.; Noda, I.; Ozaki, Y., Infrared Spectroscopic Study of $\text{CH}_3 \text{O}=\text{C}$ Interaction during Poly(L-lactide)/Poly(D-lactide) Stereocomplex Formation. *Macromolecules* **2005**, 38, 1822-1828.

CHAPTER 7: CONCLUSION

Directed selection (molecular recognition of the semiconductor functional group by the desired analyte) and optimization of organic semiconductors would be possible, if there were a system for characterizing the surface chemistry of demonstrated chemical sensors. By understanding the sensing mechanism, future research can focus on the most influential variables that affect organic semiconductor design. Possible variables include grain or boundary size, terminal functional groups or material selection, and film thickness. We developed deposition and custom-designed exposure systems and used these to study the surface chemistry response of pre-treated rubrene, several pentacene film thicknesses, and C6 to acetone and ethanol vapors.

We postulated that the endoperoxide group on the rubrene surface was a potential bonding site for surface-current-enhancing silanes. We found evidence of endoperoxide formation on rubrene surfaces exposed to oxygen and white light over the course of five hours. However, these bonds did not appear changed upon exposure to trichlorosilanes, acetone, or ethanol. No rubrene-silane peak has been unambiguously identified. The SiO_2 substrate used to support a spun rubrene film provided bonding sites for trichlorosilane self assembled monolayer (SAM) materials. Future investigation of the rubrene-silane bonding should be conducted on a more inert substrate. KBr pellets were investigated for this purpose, but their surface hydroxyl groups seem to have provided a substrate-bonding site.

Similar spectra for octyltrichlorosilane (OTS) on SiO_2 and spun rubrene films provided evidence of OTS- SiO_2 bonding and silane networking. Surface chemistry attributed to silane networking (possible with a rubrene crystal) and SiO_2 -silane bonding

(impossible with a rubrene crystal) observed during successive dilute exposures seems to saturate after the second exposure, while the sustained rubrene crystal surface current increase diminishes during a third exposure. Surface chemistry and rubrene surface current enhancement are loosely correlated.

Perfluorinated alkyltrichlorosilane (FTS)-rubrene pretreatment showed dominant peaks due to the strong C-F dipole moment. Therefore, differences between blocked oxide, oxide, and rubrene surfaces were difficult to distinguish. Although we do not unambiguously assign a rubrene-silane bond peak, we have not ruled out its presence. We identify FTS networking and possibly FTS-SiO₂ bonding. The FTS pretreatment produced a larger surface current enhancement of the rubrene surface than OTS pretreatment.

Saturated FTS-rubrene coverage is important for sensing acetone, because it protects rubrene from solvent interaction. The rubrene-solvent interaction is less reversible and saturates, perhaps due to film disruption (rubrene is soluble in acetone). The saturated, FTS-covered rubrene surface can modulate the charge-carrier density in the rubrene thin film more reversibly and with larger effect than the other materials described in this thesis, perhaps because it protects the conductive rubrene film. The dipole moment seems to be modulated by acetone, which decreases the presence of charge carriers at the rubrene surface. The IRAS data shows that FTS may also be removed from the saturated-coverage rubrene surface. In addition, rubrene seems to be removed by acetone when FTS does not completely cover the amorphous spun film according to IRAS data. While there is reason to believe the strongly bound rubrene molecules in a crystal would not delaminate as we predict for the amorphous rubrene

spun film, we are not able to check this experimentally. Generally, if the organic layer is soluble in the sensed analyte, then the organic layer should be protected by a saturated self-assembled monolayer, such as FTS.

Further development of rubrene-protective layers with large dipole moments could be designed to modulate the rubrene surface current for sensing. The use of a SAM layer from the vapor phase to protect and enhance the surface current and the sensing ability of soluble organic semiconductors suggests that future organic semiconductor development does not need specific functional group development as much as molecules with large field-effect mobility. Functional group development should be focused on the terminal groups of SAM molecules, which can be easily applied to organic transistors and rubrene surfaces in a vacuum gas cell. Vacuum-vapor deposition has the advantage of coating large-area sensors. Liquid deposition of SAM may be a problematic way to functionalize organic transistor sensors due to the risk of semiconductor film liftoff or solvent degradation.

Future evaluation of the FTS-rubrene bonding site may be improved by using a molecule similar to FTS but with only one CF_3 terminal group. This should make it easier to distinguish rubrene-FTS bonding from the body modes in the infrared absorption spectroscopy (IRAS) spectra. Also, the replacement of trichlorosilane with a more reactive phosphonate termination may promote rubrene bonding (Silverman, et al. 2005). Phosphonated SAMs might reduce the time required for saturated surface coverage and provide a stable rubrene bond. The increased bonding would increase the signal for IRAS detection of the rubrene-silane bond.

The thickest pentacene thin-film tested (1500 Å) produced higher peak-to-peak intensity of differential peaks in response to saturated acetone vapors than other film thicknesses. Film delamination was not observed in pentacene IRAS spectra perhaps due to acetone insolubility as well as film-stabilizing van der Waals forces from overlapping pi-bonds. The surface chemistry response included the perturbation of out-of-plane bending modes and adsorbed acetone. While repeated exposures revealed a dramatically decreased surface chemistry response, transistor drain-source current did not change dramatically. This further supports decoupled surface chemistry and current sensing response. However, the instability of the gold wire attachment to the gold pads by quick-dry silver paint may undermine the surface chemistry/current sensing relationship. Shifts in the IRAS spectra and decreased surface current might be the result of surface temperature variation. Additional film thicknesses should be explored to further detail the relationship of pentacene film thickness with sensing response. Furthermore, the film morphology for each of the film thicknesses was presumed similar in this thesis because they were deposited at the same slow rate. However, AFM or other topographical technique should be used to characterize each film to rule out a morphological variation among films with different thicknesses.

Acetone has the same effect on the IRAS as cooling the pentacene film under N₂ purge by ~3.25°C - ~7.3°C. This accounts for all of the spectrum changes upon acetone exposure except for the physisorbed acetone peaks. However, the reduction in surface current due to liquid N₂ cooling does not fully account for acetone's reduction of transistor current. Reversibility of the sensing effect could be limited by: desorbed acetone, film reorganization, or re-deposition of the removed film.

Very little surface chemistry change was observed in response to ethanol vapors, despite the specialized hexanol film termination of C6 transistor films. The material does respond to acetone with a similar amount of acetone physisorption. There was conflicting spectral evidence of solvent hydrogen bonding supported by shifting of out-of-plane aromatic bending modes, with the peak attributed to the terminal hydroxyl group shifting in the opposite direction.

Organic semiconductors exposed to solvent vapors show film perturbation that may disrupt the pi-bond overlap of neighboring conjugated rings. This was evident in the perturbation of the aromatic in-plane and out-of-plane modes. For the hexyloxy-terminated film, C6, the alkyl chain modes were also suppressed in the presence of acetone. The sensing mechanism of these films seems to be a disruption of charge distribution and dipole moments at the film surface. It is partially reversible due to our observation of acetone removal over 20 - 50 minutes as well as film changes overnight.

Since the surface chemistry seems decoupled from the transistor current response, exploration of the infrared and surface current response to film temperature changes should be carried out. This may dictate future sensor design to include considerations for heat transfer and analyte heat of vaporization. Also, the contact connection to a gold wire needs to be more resistant to solvent degradation than silver paint. Conductive epoxy may be a good option. However, proper viscosity for handling, fast drying time, low outgassing, hard connection with little effect on the organic semiconductor material are desired qualities.

Studying the film topology could add to the study of sublimated organic semiconductor sensing. If it were possible to achieve infrared spectral mapping of a

surface grain, it would be intriguing to see if any sensing anisotropy occurred near the grain boundary. Further comparison of grain boundary size and the van der Waals radius of sensed solvents could help evaluate the best thin-film preparation conditions to make customized grain sizes. Varying the deposition rate or the substrate temperature could be used to customize grain size.

One of the most important contributions of this thesis was the creation of a system for in real-time or in-situ testing of thin films, including transistor devices that revealed the susceptibility of organic chemisensors to analyte degradation. We have shown that a saturated layer of FTS on rubrene allows more stable, reversible acetone sensing, while allowing some FTS removal. The small, 1.5% FTS removal may be the result of multilayered physisorbed FTS which is less tightly bound than the surface monolayer. If FTS does not completely cover the rubrene, the conduction layer rubrene is degraded resulting in a less reversible, saturated sensor response and some rubrene removal.

The gas cell has allowed us to uniquely study the surface chemistry changes of pentacene thin films after acetone exposure. The only similar study of 1,4,5,8-Napthalene-tetracarboxylic-dianhydride (NTCDA) was unable to find a change in a nujoll mull and KBr pellet as a result of water vapor exposure (Torsi, et al. 2001). Our ability to mount silicon wafers with sublimated organic thin film coatings allows us to probe both the surface chemistry and surface current on the same sample for a more direct analysis of the sensing surface.

The limitation of this gas cell system is our inability to study the surface chemistry in real time due to the prominent infrared absorption of gas phase acetone over surface interactions. Reduction in the amount of acetone exposed to the rubrene film in

order to alleviate this will result in a linearly reduced sensor response. Therefore, there is a tradeoff of sensor response and reduced infrared absorption of gas phase analyte for the study of real-time sensor surface chemistry. In the future, a reflection geometry sample mounting could be designed (Hierlemann, et al. 1999). This would prevent probing of both sides of the wafer and allow us to reduce material consumption by coating only one side. However, a reflective gold film must be evaporated either on the front or under the film of interest. Since the morphology of polycrystalline thin films is known to differ on gold versus SiO₂ surfaces, gold evaporation on the backside of the silicon wafer is preferred. Also, currently the transmission geometry, which probes both sides of the organic coated sample, provides an increased signal due to the double coating compared to the single reflection mode.

The gas cell could be used in the future to study the interaction of solvents with different polarity or different semiconductor molecules in order to further understand organic transistor sensing mechanisms. Also, the effect of transistor device cycling, aging, or annealing on thin films could be studied. The efficiency of organic semiconductor protecting or sealing layers, such as FTS, could also be evaluated. Other chemisensor or biosensor recognition events for both organic and inorganic platforms could be evaluated in the gas cell system if the analyte were delivered as a vapor. Vapor deposition is favored in this system for surface sensing because aqueous deposition would likely result in sublimated organic film liftoff.

This gas cell system complements the existing approach traditionally used to characterize inorganic gas sensor materials using FTIR, electrical, and temperature measurements (Chiorino, et al. 1999a). In addition to surface chemistry and electrical

response, the morphology of inorganic sensor powder and thick films are evaluated with XRD, SEM, TEM, volumetric measurements to study the role of additional molybdenum in sensing (Chiorino, et al. 1999b). We also study the powder form of our organic semiconductor C6 with XRD since it had not been previously explored and found a common herringbone molecular organization pattern. SEM and TEM studies of the organic film morphology in the future would complement the information gained from the gas cell. Due to the reversible nature of organic semiconductor-analyte interaction, real-time or in-situ surface chemistry studies possible with our system allow us to avoid exposure to environmental light and humidity during transport to other characterization techniques.

7.1 References

1. Chiorino, A.; Ghiotti, G.; Prinetto, F.; Carotta, M. C.; Gallana, M.; Martinelli, G., Characterization of materials for gas sensors. Surface chemistry of SnO₂ and MoO_x-SnO₂ nano-sized powders and electrical responses of the related thick films *Sensors and Actuators B: Chemical* **1999a**, 59, (2), 203-209.
2. Chiorino, A.; Ghiotti, G.; Prinetto, F.; Carotta, M. C.; Gnani, D.; Martinelli, G., Preparation and characterization of SnO and MoO –SnO nanosized 2 x 2 powders for thick film gas sensors. *Sensors and Actuators B* **1999b**, 58, (338–349).
3. Hierlemann, A.; Ricco, A. J.; Karl Bodenhöfer; Göpel, W., Effective Use of Molecular Recognition in Gas Sensing: Results from Acoustic Wave and in Situ FT-IR Measurements. *Analytical Chemistry* **1999**, 71, (15), 3022 - 3035.
4. Silverman, B. M.; Wiegand, K. A.; Schwartz, J., Comparative Properties of Siloxane vs Phosphonate Monolayers on A Key Titanium Alloy. *Langmuir* **2005**, 21, (1), 225 - 228.
5. Torsi, L.; Dodabalapur, A.; Cioffi, N.; Sabbatini, L.; Zamboni, P. G., NTCDA organic thin-film-transistor as humidity sensor: weaknesses and strengths. *Sensors and Actuators B* **2001**, 77, 7-11.

CHAPTER 8: APPENDIX

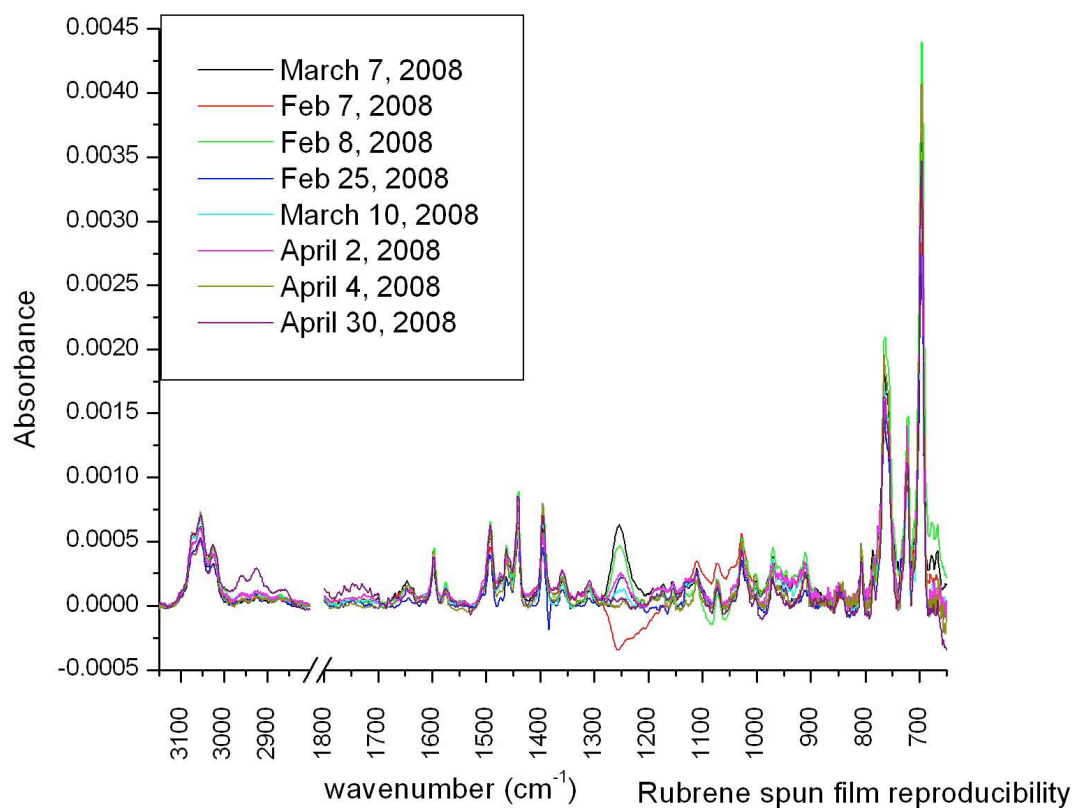


Figure A1. Reproducible infrared absorption spectroscopy of rubrene-spun films referenced to a thick oxide.

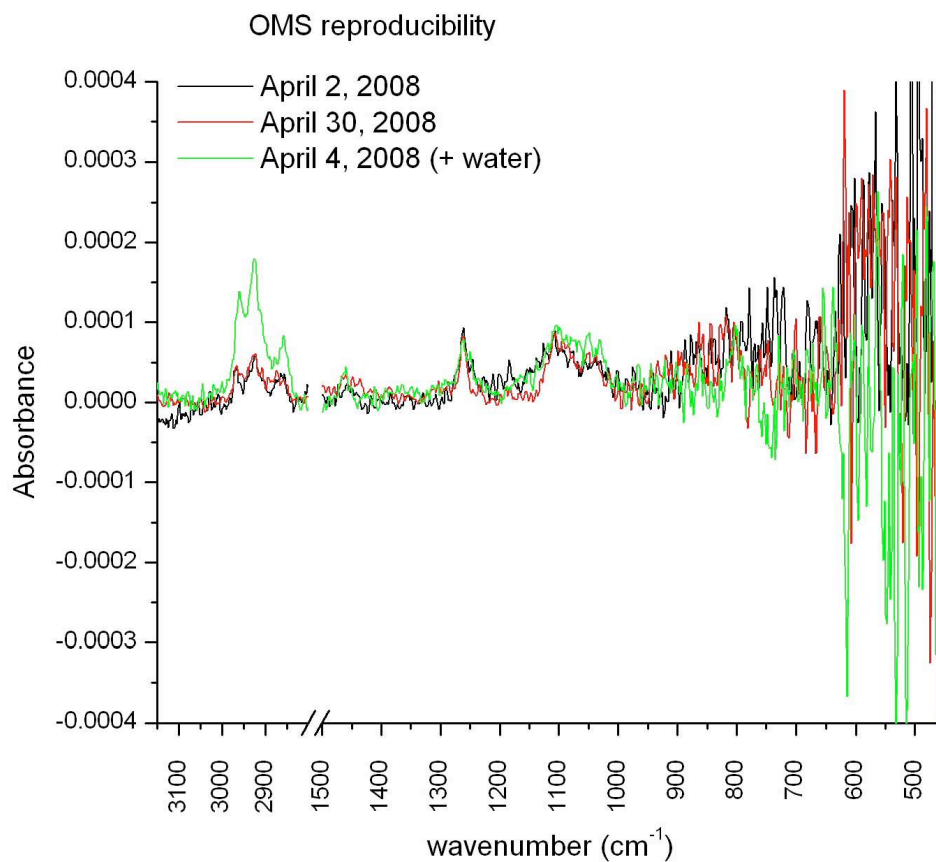


Figure A2. Reproducible infrared absorption spectroscopy of OMS referenced to rubrene on thick oxide substrates.

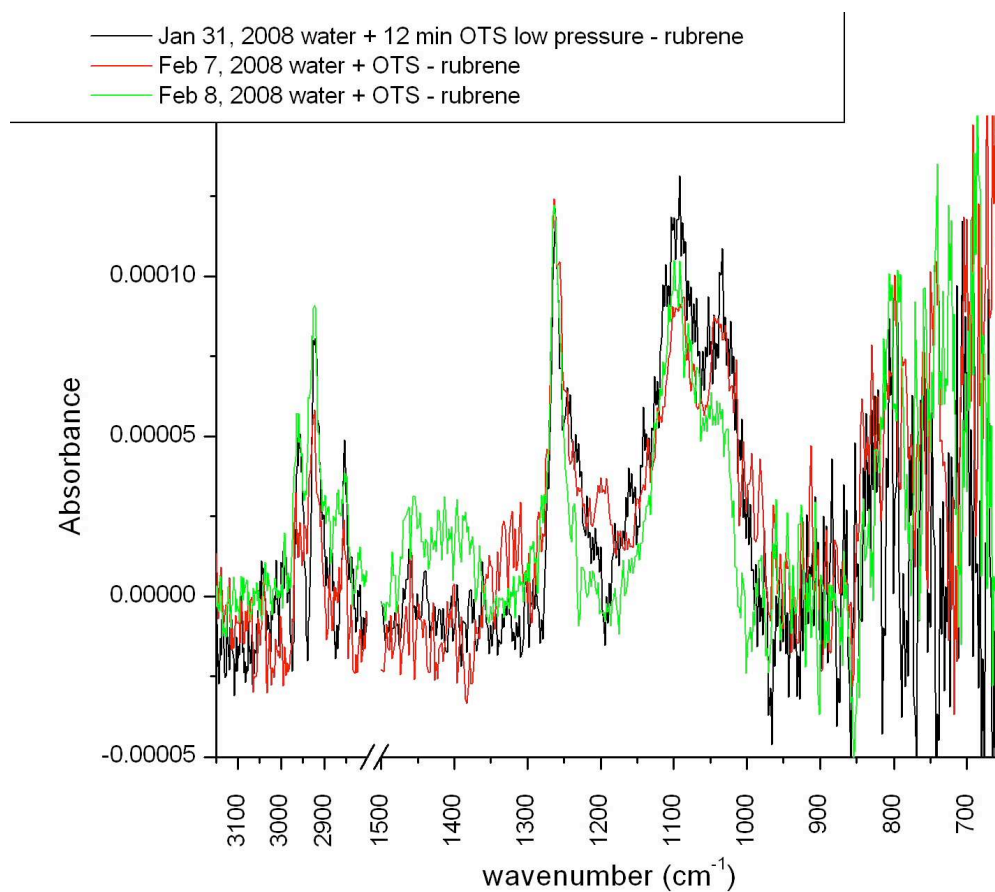


Figure A3. Reproducible infrared absorption spectroscopy of water, OTS deposition referenced to double-coated rubrene on thick SiO_2 substrates.

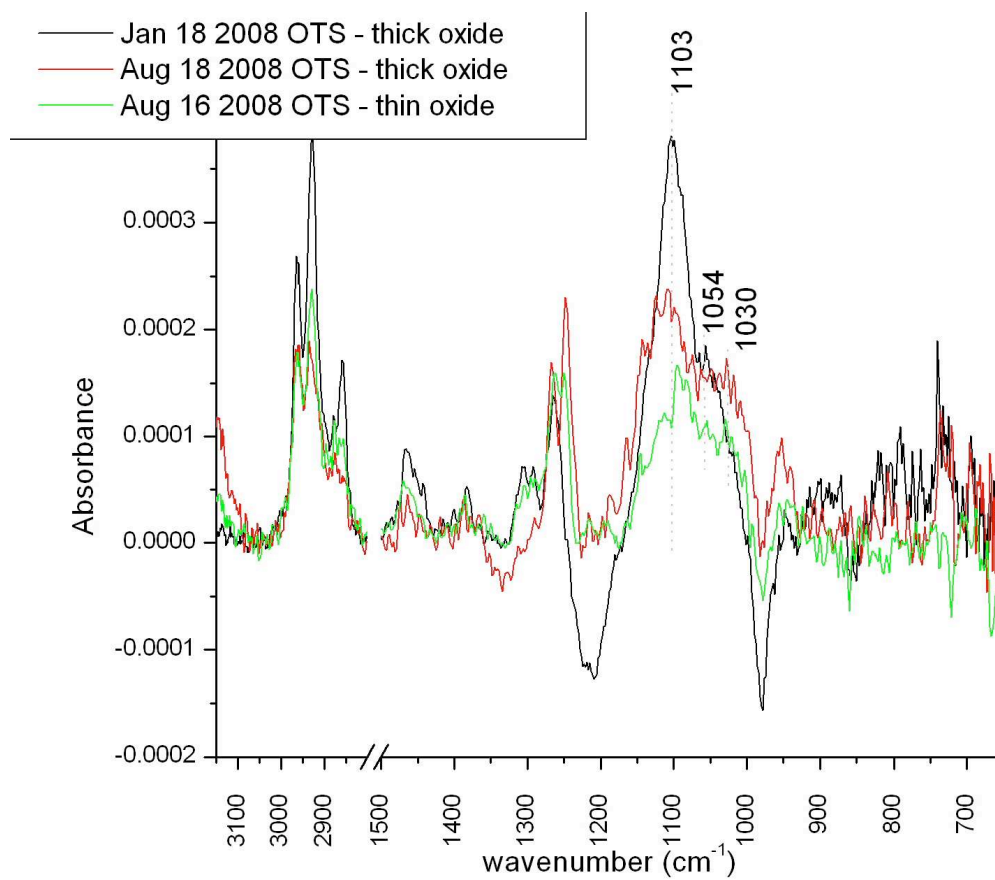


Figure A4. Reproducible infrared absorption spectroscopy of OTS referenced to thick and thin SiO_2 substrates.

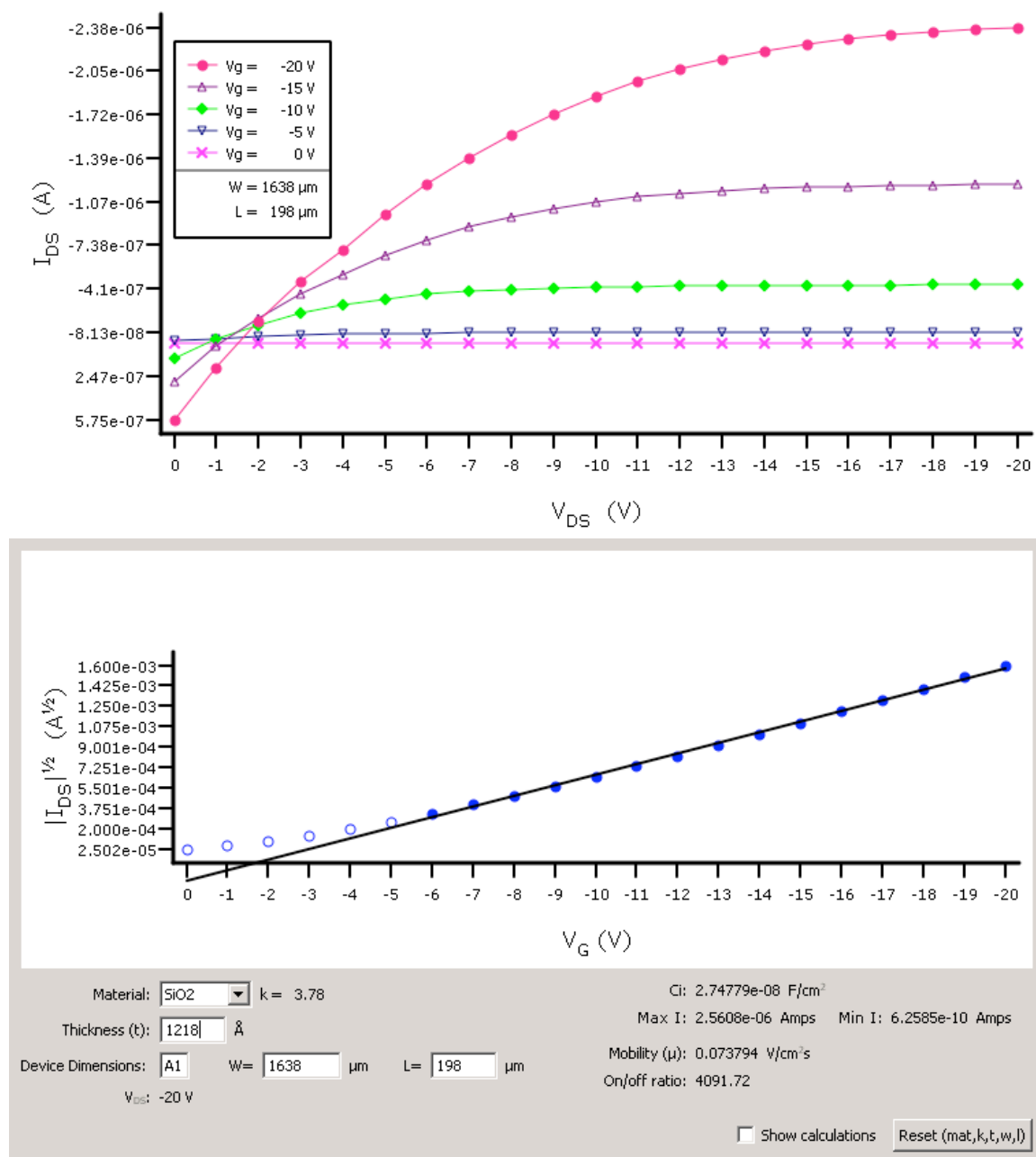


Figure A5. 1500Å Pentacene film transistor performance. Mobility: $0.074 \text{ V/cm}^2\text{s}$

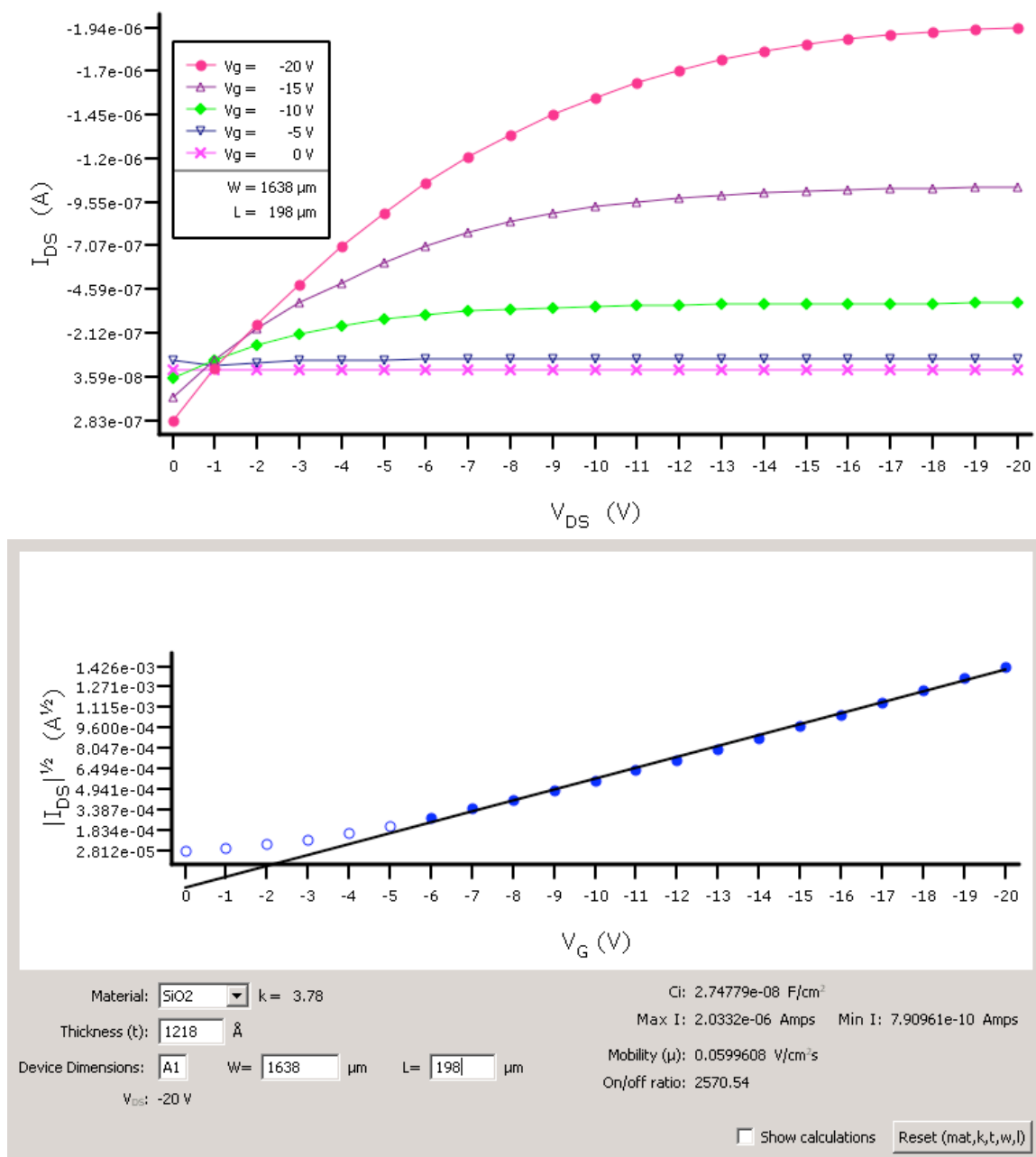


Figure A6. 1500 Å Pentacene film transistor performance after an acetone exposure.
Mobility: $0.060 \text{ V/cm}^2\text{s}$

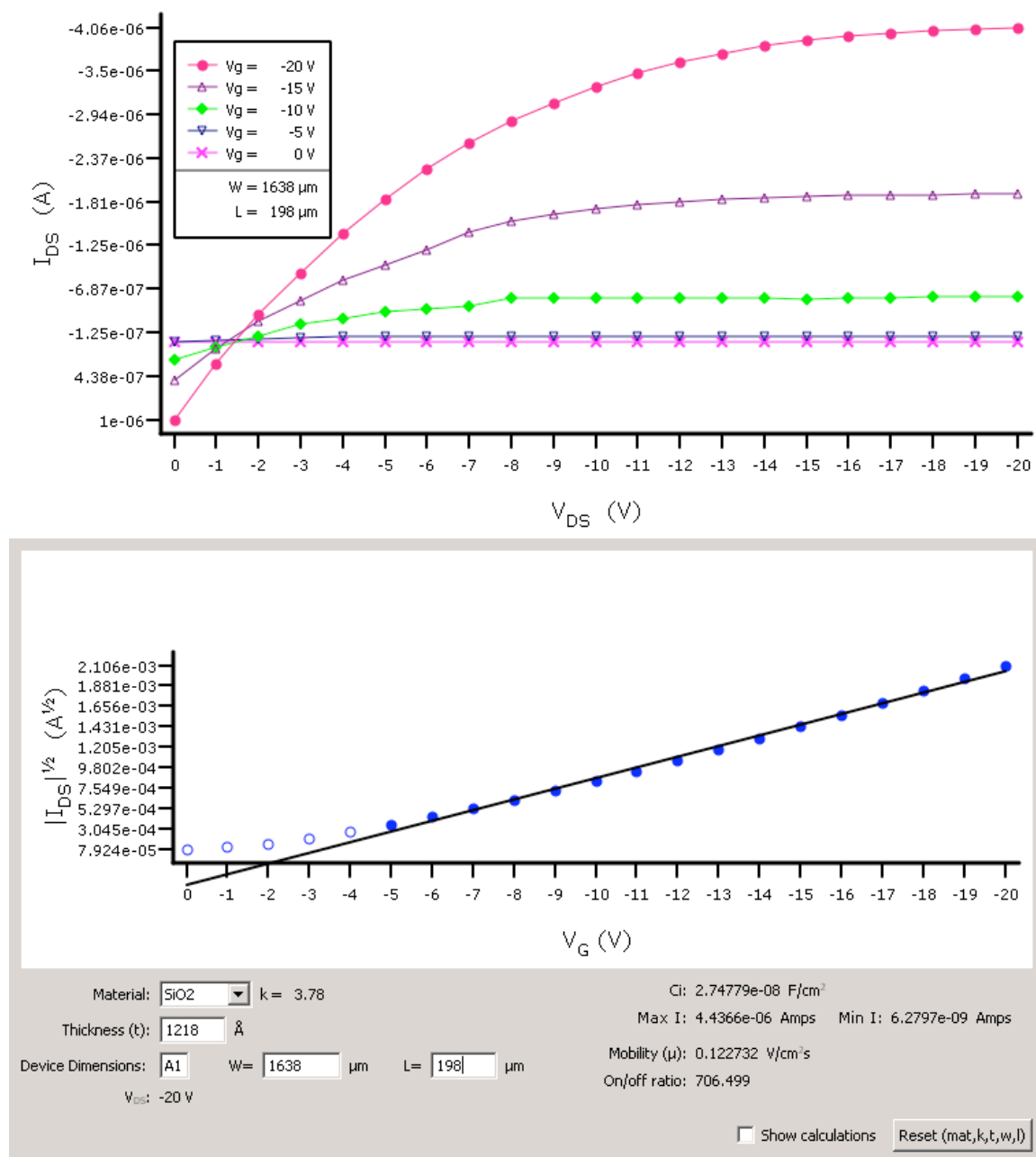


Figure A7.400 \AA Pentacene film transistor performance. Mobility: $0.123 \text{ V/cm}^2\text{s}$

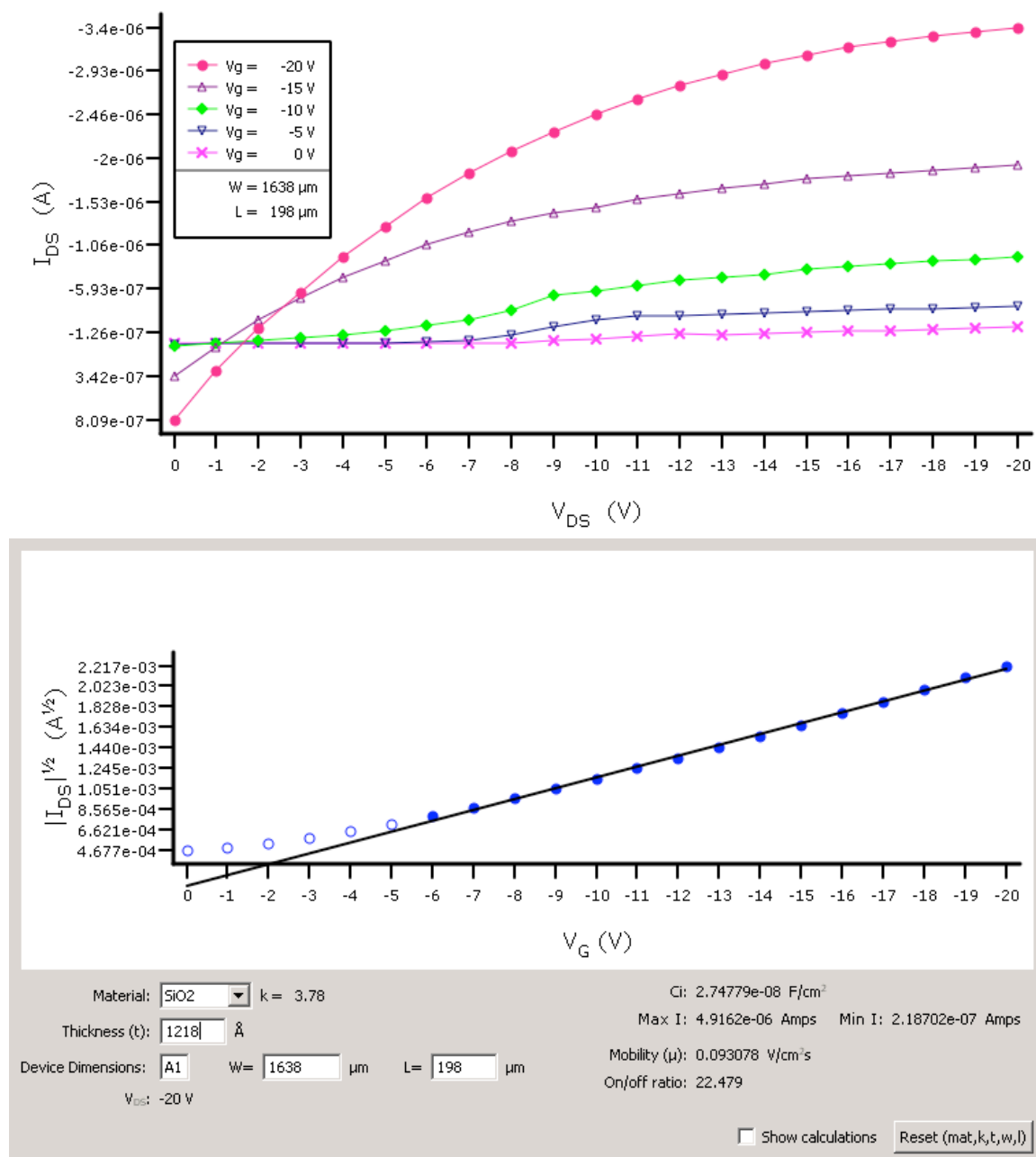


Figure A8. 80 Å pentacene film transistor performance. Mobility: $0.0931 \text{ V/cm}^2\text{s}$

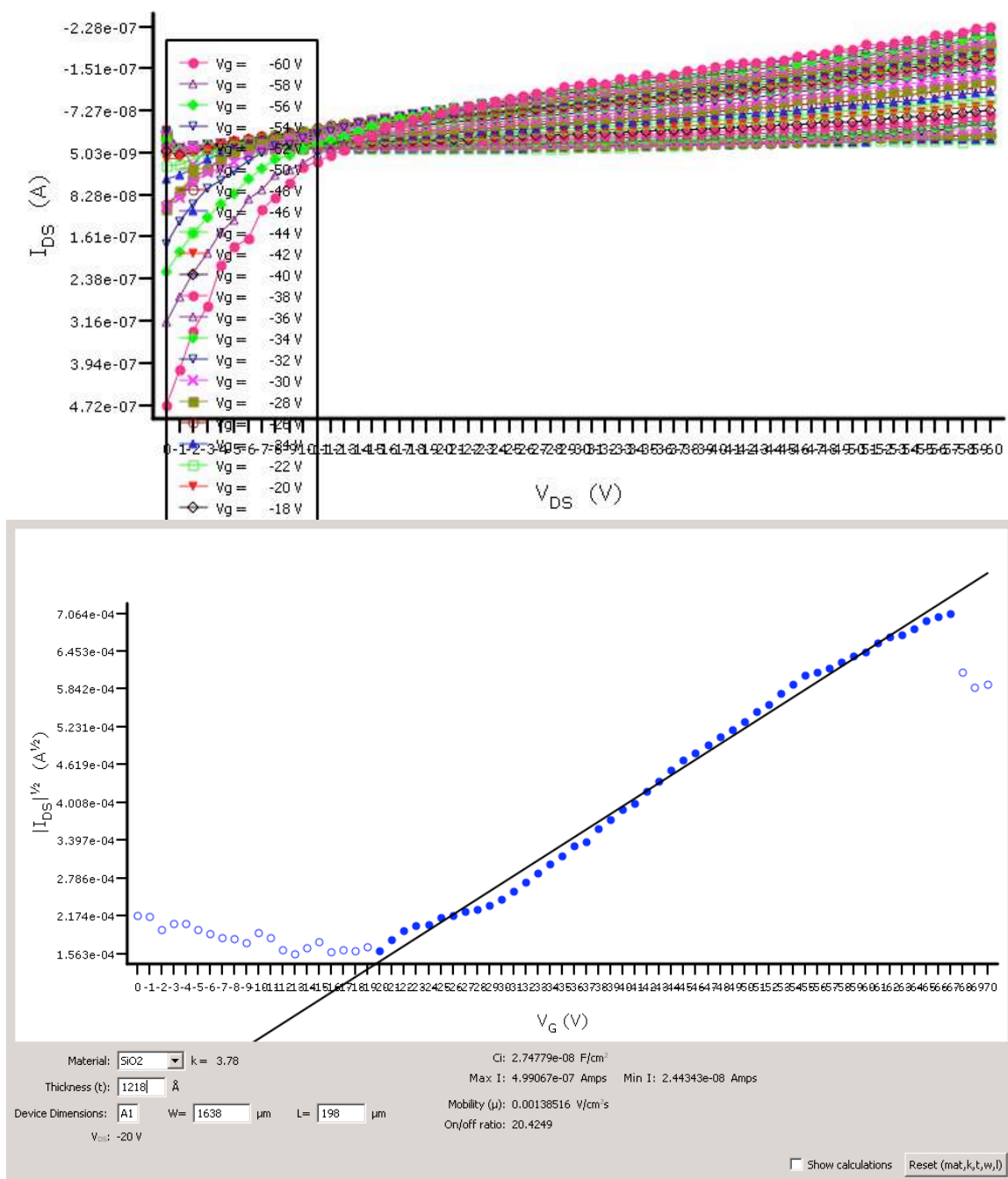


Figure A9. Transistor performance of 500A C6 thin film. Mobility: $0.00139 \text{ V/cm}^2\text{s}$, $V_{ds} = -70\text{V}$

Curriculum Vita

MELISSA A. STOKES

EDUCATION

- 10/2008 Ph.D. Biomedical Engineering
The Graduate School – New Brunswick, Rutgers University
The Graduate School of Biomedical Sciences, University of Medicine
and Dentistry of New Jersey
New Brunswick, NJ
- 05/2002 B.S. Biological and Environmental Engineering
Cornell University
College of Agriculture and Life Sciences
College of Engineering
Ithaca, NY

EXPERIENCE

- Internship IBM, TJ Watson Research Center, Yorktown Heights, NY.
- Internship Bell Laboratories, Alcatel-Lucent, Murray Hill, NJ.

PUBLICATIONS

“Molecular Ordering in Bis(phenylenyl)bithiophenes.” M. Stokes, R. Kortan, S. Rivillon, H. Katz, Y. Chabal, C. Kloc, T. Siegrist. *Journal of Materials Chemistry*, 2007, 17, 3427.

“Structural Characterization of a Functionalized Organic Semiconductor.” M. Stickle, R. Kortan, S. Rivillon, Z. Bao, H. Katz, Y. Chabal. *MRS Proceedings*, Spring 2005. Vol. 871E. I3.16.